BEILSTEIN JOURNAL OF NANOTECHNOLOGY

Photocatalysis

Edited by Rong Xu

Generated on 08 February 2026, 04:36

Imprint

Beilstein Journal of Nanotechnology
www.bjnano.org
ISSN 2190-4286
Email: journals-support@beilstein-institut.de

The *Beilstein Journal of Nanotechnology* is published by the Beilstein-Institut zur Förderung der Chemischen Wissenschaften.

Beilstein-Institut zur Förderung der Chemischen Wissenschaften
Trakehner Straße 7–9
60487 Frankfurt am Main
Germany
www.beilstein-institut.de

The copyright to this document as a whole, which is published in the *Beilstein Journal of Nanotechnology*, is held by the Beilstein-Institut zur Förderung der Chemischen Wissenschaften. The copyright to the individual articles in this document is held by the respective authors, subject to a Creative Commons Attribution license.

BEILSTEIN JOURNAL OF NANOTECHNOLOGY

Photocatalysis

Rong Xu

Editorial

Open Access

Address:
School of Chemical & Biomedical Engineering, Nanyang Technological University, 62 Nanyang Drive, Singapore 637459

Email:
Rong Xu - rxu@ntu.edu.sg

Keywords:
photocatalysis

Beilstein J. Nanotechnol. **2014,** *5,* 1071–1072.
doi:10.3762/bjnano.5.119

Received: 25 June 2014
Accepted: 08 July 2014
Published: 16 July 2014

This article is part of the Thematic Series "Photocatalysis".

Editor-in-Chief: T. Schimmel

© 2014 Xu; licensee Beilstein-Institut.
License and terms: see end of document.

Finding long-term solutions to meet the growing energy demands of the human society is one of the greatest challenges of our age. Photocatalysis, a topic of many decades of attention, has recently received renewed and more intense interest in developing innovative solutions towards achieving our sustainability goal. Though immensely inspired by natural photosynthesis, the research on artificial photosynthesis is still in its early stage, and many technological challenges must be solved before it can be applied to large-scale.

It has been widely recognized that it is necessary to develop advanced materials and new molecules assembled preferably from earth abundant elements as efficient photocatalysts to accomplish the complex process of solar energy driven water splitting and carbon dioxide reduction. Nanotechnology certainly plays a pivotal role in enabling a rational design of the structures, interfaces and surfaces with controllable features at a length scale comparable to chemical reactions. In this Thematic Series, two review articles present an excellent overview of the significance of nanostructures in visible light photocatalysis in a timely manner.

Many materials aspects of photocatalysts influence the photocatalytic performance, such as the electronic, structural, and morphological features of the semiconductors, and the interface properties between semiconductors and cocatalysts. This Thematic Series contributes to bringing together the research at the frontiers of materials science and nanotechnology to address some of these aspects. It is evidenced from several reports that structural, compositional and morphological tuning, in particular for hybrid materials systems such as Ag–ZnO, VTi/MCM-41, are important toward achieving higher solar energy conversion efficiencies. In a couple of reports, materials alternative to conventional metal oxides, for example, reduced graphene oxide, graphene quantum dots integrated with TiO_2 nanotube arrays, and carbon nitride, have been explored to construct photocatalysts with enhanced performances.

On the other hand, molecular catalysts have an advantage in design flexibility and structural tunability. A contribution based on the investigation of molecular bismuth vanadium oxide cluster exemplifies these characteristics. Besides solar fuel production, photocatalysis has a long history in water treatment. In this Thematic Series, there is also a report on the latest development in the utilization of mesoporous cerium oxide for visible light-driven dye degradation. In recent years, the interest in photocatalytic organic conversion has risen, which is reflected by a report on photo-epoxidation. And last but not

least, one of the studies of this Thematic Series aims for a fundamental understanding of the photophysical process by optical modeling.

I am grateful to all the authors for their valuable contributions. Thanks should also be given to the dedicated Beilstein team for their dependable support.

Rong Xu

Singapore, June 2014

License and Terms

This is an Open Access article under the terms of the Creative Commons Attribution License (http://creativecommons.org/licenses/by/2.0), which permits unrestricted use, distribution, and reproduction in any medium, provided the original work is properly cited.

The license is subject to the *Beilstein Journal of Nanotechnology* terms and conditions: (http://www.beilstein-journals.org/bjnano)

The definitive version of this article is the electronic one which can be found at: doi:10.3762/bjnano.5.119

Beilstein Journal of Nanotechnology

Preparation of NiS/$ZnIn_2S_4$ as a superior photocatalyst for hydrogen evolution under visible light irradiation

Liang Wei, Yongjuan Chen, Jialin Zhao and Zhaohui Li*

Full Research Paper

Open Access

Address:
Research Institute of Photocatalysis, Fujian Provincial Key Laboratory of Photocatalysis–State Key Laboratory Breeding Base, Fuzhou University, Fuzhou 350002, P. R. China

Email:
Zhaohui Li* - zhaohuili1969@yahoo.com

* Corresponding author

Keywords:
co-catalyst; hydrogen evolution; NiS; photocatalytic; photocatalysis; visible light

Beilstein J. Nanotechnol. **2013,** *4,* 949–955.
doi:10.3762/bjnano.4.107

Received: 14 October 2013
Accepted: 16 December 2013
Published: 23 December 2013

This article is part of the Thematic Series "Photocatalysis".

Guest Editor: R. Xu

© 2013 Wei et al; licensee Beilstein-Institut.
License and terms: see end of document.

Abstract

In this study, NiS/$ZnIn_2S_4$ nanocomposites were successfully prepared via a facile two-step hydrothermal process. The as-prepared samples were characterized by X-ray diffraction (XRD), X-ray photoelectron spectroscopy (XPS), transmission electron microscopy (TEM) and high-resolution transmission electron microscopy (HRTEM). Their photocatalytic performance for hydrogen evolution under visible light irradiation was also investigated. It was found that the photocatalytic hydrogen evolution activity over hexagonal $ZnIn_2S_4$ can be significantly increased by loading NiS as a co-catalyst. The formation of a good junction between $ZnIn_2S_4$ and NiS via the two step hydrothermal processes is beneficial for the directional migration of the photo-excited electrons from $ZnIn_2S_4$ to NiS. The highest photocatalytic hydrogen evolution rate (104.7 μmol/h), which is even higher than that over Pt/$ZnIn_2S_4$ nanocomposite (77.8 μmol/h), was observed over an optimum NiS loading amount of 0.5 wt %. This work demonstrates a high potential of the developing of environmental friendly, cheap noble-metal-free co-catalyst for semiconductor-based photocatalytic hydrogen evolution.

Introduction

Hydrogen is a clean and green fuel. The conversion and store of solar energy in the form of hydrogen by photocatalytic water splitting holds great promise to meet the future energy and environment requirements [1-3]. Ever since the pioneering work of a photo-electrochemical cell using Pt-TiO_2 electrodes for water splitting by Fujishima and Honda in 1972, great efforts have been devoted to the development of highly efficient semiconductor photocatalysts for hydrogen production [4]. So far, a variety of active photocatalysts for hydrogen production, including metal oxides [5-8], sulfides [9-11], oxynitrides [12-14], as well as the metal-free semiconductors [15] have already been developed.

Among the numerous types of semiconductor systems studied, metal sulfides have demonstrated promising activities towards hydrogen evolution from water containing sacrificial reagents under visible light. $ZnIn_2S_4$ is a ternary chalcogenide with a suitable band gap (2.34–2.48 eV) well corresponding to the visible light absorption. $ZnIn_2S_4$ exhibits two distinct polymorphs based on cubic and hexagonal lattices [16], which can be controlled synthesized via a facile hydrothermal method using different precursors. Previous studies revealed that both polymorphs of $ZnIn_2S_4$ are active for photocatalytic hydrogen generation under visible light irradiations and show considerable chemical stability [17-19]. However, the photocatalytic hydrogen evolution activity over pure $ZnIn_2S_4$ is low, due to the poor separation efficiency and migration ability of the photoexcited charge carriers. A variety of effects have been made to enhance the photocatalytic performance of $ZnIn_2S_4$. For example, by size control on $ZnIn_2S_4$ [20], doping with transition metals [21] and incorporation of metal sulfides [22] or RGO [23] into $ZnIn_2S_4$ nanostructures, the photocatalytic performance for hydrogen evolution over $ZnIn_2S_4$ have been enhanced to a certain degree.

Studies on semiconductor-based photocatalysts revealed that the deposition of a suitable co-catalyst on the semiconductor photocatalysts can play important roles in promoting their photocatalytic performance for hydrogen evolution. An appropriate co-catalyst can suppress the recombination of the photo-generated charge carriers, lower the overpotential for hydrogen evolution and also provide redox reaction sites for hydrogen evolution to avoid back reactions. Due to their negligible overpotential for hydrogen evolution and excellent kenetics for driving the hydrogen evolution reaction, noble metals like Pt [24-26], Rh [27], Au [28,29] and their oxides like RuO_2 [30], $Rh_xCr_{2-x}O_3$ [31-33] are generally used as the co-catalysts for photocatalytic hydrogen evolution. However, the precious metals are expensive and to reduce the cost of renewable hydrogen evolution, it is necessary to explore alternative co-catalysts based on inexpensive transition metals.

Our recent studies revealed that MoS_2, a good electrocatalyst for hydrogen evolution [34], can be an effective co-catalyst in promoting photocatalytic hydrogen evolution over $ZnIn_2S_4$ and $MoS_2/ZnIn_2S_4$ show even superior performance for hydrogen evolution than $Pt/ZnIn_2S_4$ [35]. NiS, a p-type semiconductor, is also reported to be a good electrocatalyst for cathodic hydrogen evolution in water electrolysis [36]. Although Ni and NiO have already been used as co-catalysts for hydrogen evolution over oxide semiconductor photocatalysts, the application of NiS as co-catalyst for photocatalytic hydrogen evolution is less studied [37,38]. Only until recently, Xu et al. reported that NiS can be used as co-catalyst to enhance the photocatalytic hydrogen evolution over CdS [39]. It was found that NiS/CdS photocatalysts prepared via a simple hydrothermal loading method showed high photocatalytic activity for hydrogen evolution in the presence of lactic acid as sacrificial agent and a high quantum efficiency of 51.3% at 420 nm was obtained in this system. Later on, several other reports have also reported the using of NiS as a co-catalyst for photocatalytic hydrogen evolution [40-42].

Herein, we reported the preparation of $NiS/ZnIn_2S_4$ nanocomposites via a two-step hydrothermal method and its application for photocatalytic hydrogen evolution under visible light irradiation. It was found that NiS can be an effective co-catalyst for photocatalytic hydrogen evolution over $ZnIn_2S_4$. The as-prepared $NiS/ZnIn_2S_4$ nanocomposites showed superior photocatalytic performance for hydrogen evolution under visible light irradiation and the activity of $NiS/ZnIn_2S_4$ with optimized amount of NiS is even higher than that of $Pt/ZnIn_2S_4$. A possible enhancement mechanism based on the co-catalyst and the formed junction for the improved photocatalytic activity in the $NiS/ZnIn_2S_4$ system was also proposed.

Results and Discussion

Figure 1 shows the XRD patterns of the as-prepared pure $ZnIn_2S_4$ and sample with loading amount of 0.5 wt % NiS. As shown in Figure 1, all the samples showed diffraction peaks of 2 Theta values at 21.5°, 27.6°, 30.4°, 39.8°, 47.2°, 52.4° and 55.6°, which are corresponding to the (006), (102), (104), (108), (110), (116) and (022) crystallographic planes of hexagonal $ZnIn_2S_4$ (JCPDS, No. 03-065-2023). This suggests that there is no obvious phase change in $ZnIn_2S_4$ during the hydrothermal process in the preparation of the $NiS/ZnIn_2S_4$ nanocomposites. No characteristic diffraction peaks associated with NiS are

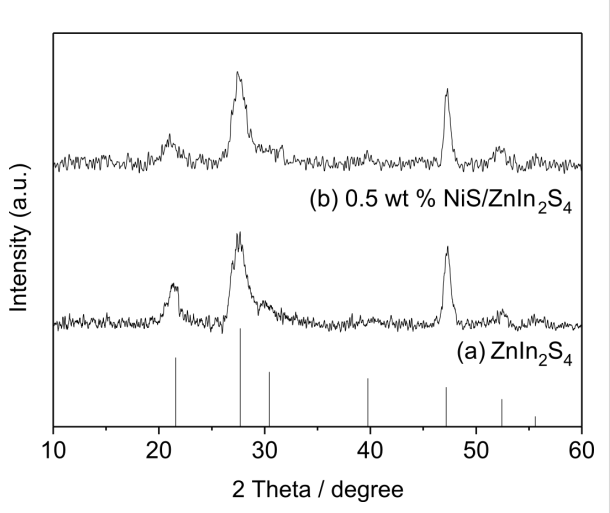

Figure 1: XRD patterns of (a) pure $ZnIn_2S_4$; (b) 0.5 wt % $NiS/ZnIn_2S_4$.

observed in these samples, probably due to the low amount of NiS loaded and its high dispersion on $ZnIn_2S_4$.

Figure 2a shows the TEM image of our previous studies that the hydrothermally prepared $ZnIn_2S_4$ sample was composed of microspheres with dimension in the range of 2–6 μm assembled by densely packed petals [16]. However, the TEM image of the current NiS/$ZnIn_2S_4$ sample shows that the $ZnIn_2S_4$ microspheres were partially decomposed after the second hydrothermal process (Figure 2b). Although no characteristic diffraction peaks corresponding to NiS nanoparticles were observed in the XRD patterns, the existence of NiS in the nanocomposite is confirmed by the HRTEM image (Figure 2c). Clear lattice fringes of 0.32 nm and 0.29 nm, which can be ascribed to the (102) plane of hexagonal $ZnIn_2S_4$ and the (300) plane of rhombohedral NiS respectively, can be observed. As shown in Figure 2b, the NiS nanoparticle has a diameter of about 5 nm and directly contact with $ZnIn_2S_4$. It is believed that the second hydrothermal treatment during the deposition of NiS on $ZnIn_2S_4$ is important for the formation of a junction between these two components. The energy-dispersive X-ray spectrometry (EDS) analysis as shown in the inset of Figure 2c also confirms the existence of Ni.

XPS analyses were carried out to evaluate the surface chemical composition and electronic state on 0.5 wt % NiS/$ZnIn_2S_4$ sample, and the results are shown in Figure 3. The survey XPS spectrum, as shown in Figure 3a, confirms the existence of Zn, In, and S. The high resolution XPS spectra of S 2p region can be deconvoluted into two peaks at around 161.7 and 162.8 eV, which can be assigned to S $2p_{3/2}$ and S $2p_{1/2}$ respectively in S^{2-} (Figure 3b). As compared to the binding energy of Zn 2p observed over pure $ZnIn_2S_4$ (1020.7 and 1043.6 eV), a higher binding energy shift is observed over NiS/$ZnIn_2S_4$ nanocoposite (1021.8 and 1044.7 eV) (Figure 3c). Similar high binding energy shift is also observed over the high resolution XPS spectra of In 3d (Figure 3d). Such a shift to high binding energy suggests a strong interaction between $ZnIn_2S_4$ and NiS. It is believed that when $ZnIn_2S_4$ are connected to NiS, the electron transfer from $ZnIn_2S_4$ to the more electronegative NiS may result in a decrease of the electron density of Zn^{2+} and In^{3+}. Therefore the binding energy of Zn 2p and In 3d shift to a high binding energy in NiS/$ZnIn_2S_4$ nanocoposite. No peaks in the Ni 2p region were observed in the XPS spectra of 0.5% NiS/$ZnIn_2S_4$, probably due to the low amount of NiS loaded and its embed within the $ZnIn_2S_4$ nanostructures.

The UV–visible diffuse reflectance spectra of NiS/$ZnIn_2S_4$ nanocomposites are displayed in Figure 4. Pure $ZnIn_2S_4$ has an absorption edge at about 540 nm with an energy gap estimated to be 2.4 eV. Although the loading of NiS onto $ZnIn_2S_4$ does not obviously change the band gap of $ZnIn_2S_4$, the resultant NiS/$ZnIn_2S_4$ nanocomposites show an enhanced absorption in the visible light region from 550 to 800 nm, attributable to the absorption of NiS.

Photocatalytic hydrogen evolution experiments were carried out over the as-prepared NiS/$ZnIn_2S_4$ nanocomposites in the presence of Na_2S/Na_2SO_3 as sacrificial agent under visible light irradiation. Figure 5 shows the amount of hydrogen evolved over 0.2 wt % NiS/$ZnIn_2S_4$ nanocomposite and is compared with that of pure $ZnIn_2S_4$ and NiS. Although NiS is a good electrocatalyst for hydrogen evolution [36], no hydrogen was evolved when NiS alone was used as the photocatalyst. Pure $ZnIn_2S_4$ only had a very low activity with the hydrogen evolution at a rate of 14.1 μmol/h. However, the doping of only 0.2 wt % NiS onto $ZnIn_2S_4$ led to its highly enhanced photocatalytic activity for hydrogen evolution. The hydrogen evolution rate over 0.2 wt % NiS/$ZnIn_2S_4$ was enhanced to 70.5 μmol/h, about 5 times of that over pure $ZnIn_2S_4$ under similar condition. This indicates that NiS deposited on the surface on $ZnIn_2S_4$ can significantly promote the photocatalytic hydrogen evolution over $ZnIn_2S_4$.

The effect of the amount of NiS loaded on the photocatalytic performance for hydrogen evolution over $ZnIn_2S_4$ has also been

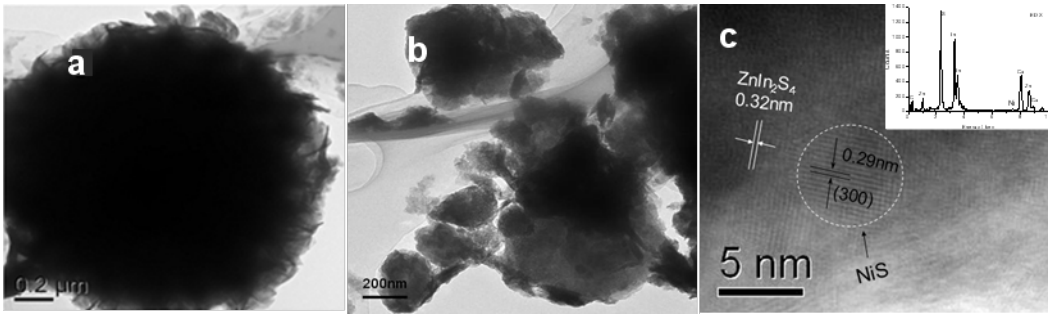

Figure 2: TEM images of (a) $ZnIn_2S_4$; (b) NiS/$ZnIn_2S_4$ and (c) HRTEM image of NiS/$ZnIn_2S_4$ (inset: EDS).

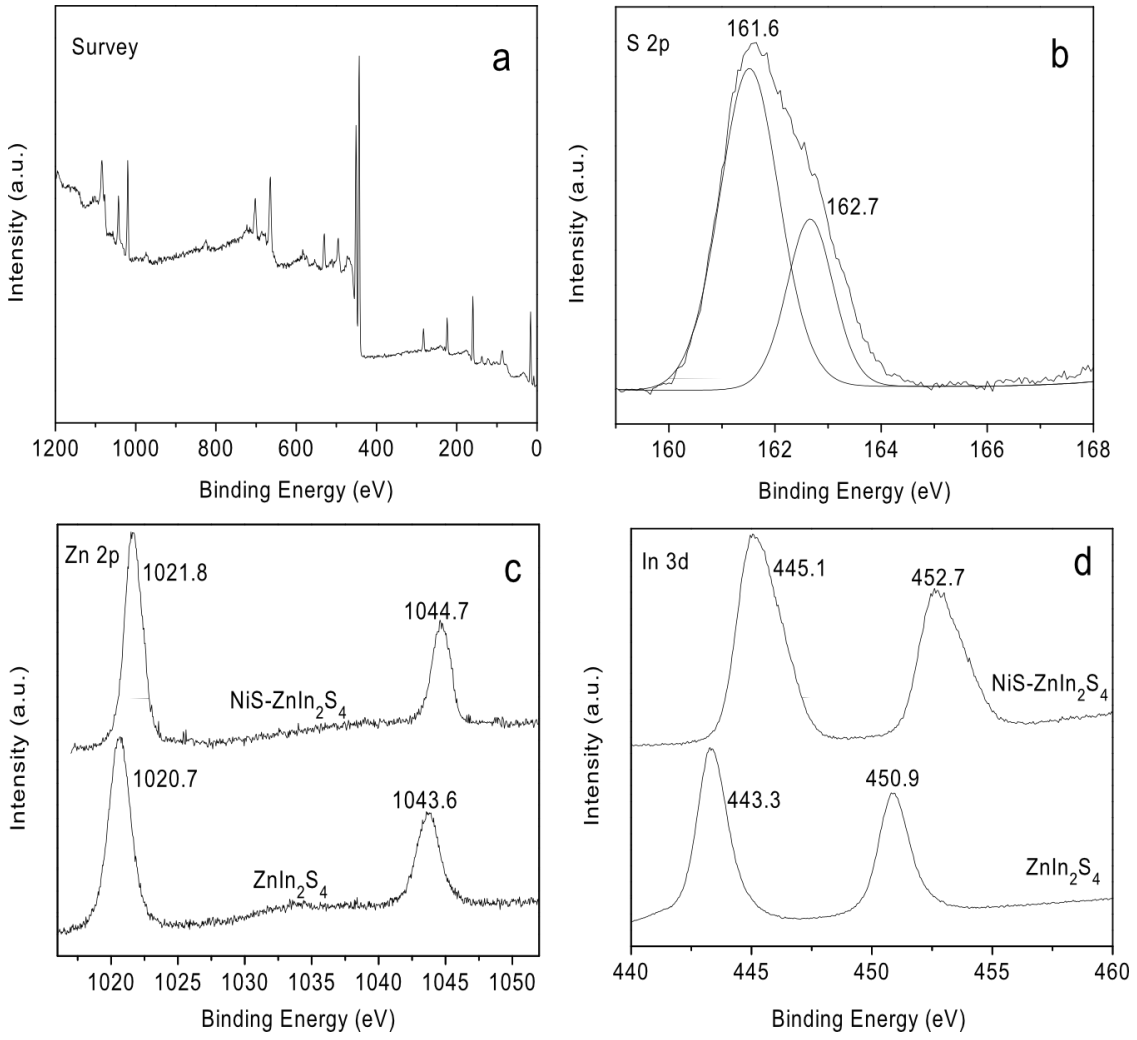

Figure 3: XPS spectra of $NiS/ZnIn_2S_4$ and $ZnIn_2S_4$ (a) survey spectrum and high-resolution spectra for (b) S 2p; (c) Zn 2p and (d) In 3d.

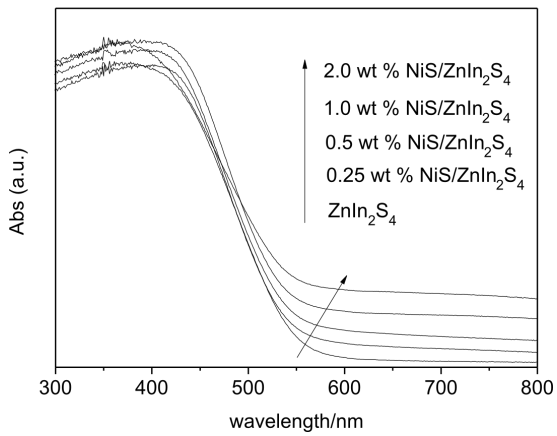

Figure 4: UV–vis diffraction spectra of the pure $ZnIn_2S_4$ and 0.25 wt %, 0.5 wt %, 1.0 wt %, 2.0 wt % $NiS/ZnIn_2S_4$.

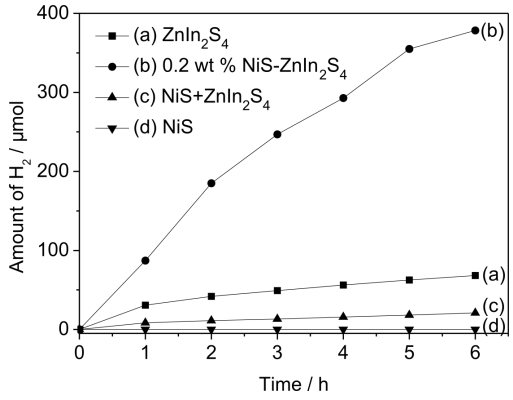

Figure 5: Amount of hydrogen evolution over (a) pure $ZnIn_2S_4$; (b) 0.2 wt % $MoS_2/ZnIn_2S_4$; (c) mechanical mixture of NiS + $ZnIn_2S_4$ and (d) NiS (Reaction conditions: catalyst, 0.05 g; 100 mL H_2O containing 0.43 M Na_2S and 0.5 M Na_2SO_3).

investigated and the results are shown in Figure 6. With increasing the amount of loaded NiS on $ZnIn_2S_4$, the rate of hydrogen evolution on 0.25 wt % NiS/$ZnIn_2S_4$ was enhanced to 98.2 μmol/h, about 7 times as that over pure $ZnIn_2S_4$. An optimum NiS loading amount is found at 0.5 wt %, which exhibits the highest photocatalytic hydrogen evolution rate of 104.7 μmol/h, almost 7.4 times as high as that obtained over the NiS-free $ZnIn_2S_4$. This value is much higher than that observed over 0.5 wt % Pt/$ZnIn_2S_4$ nanocomposite (77.8 μmol/h). A further increase in the amount of NiS resulted in a decrease in the photocatalytic hydrogen evolution rate. Such a decrease in the activity of samples with a heavy loading of NiS is likely due to the shading effect of NiS, which can block the absorption of the incident light by $ZnIn_2S_4$. Therefore, an appropriate loading amount of NiS is crucial to achieve the optimized photocatalytic activity of the $ZnIn_2S_4$ photocatalyst.

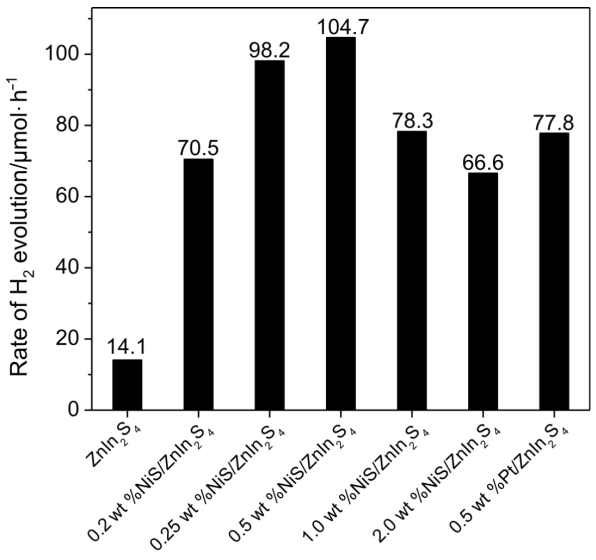

Figure 6: Photocatalytic hydrogen evolution rate over pure $ZnIn_2S_4$; $ZnIn_2S_4$ with different amounts of NiS: 0.2 wt %; 0.25 wt %; 0.5 wt %; 1.0 wt %; 2.0 wt % and 0.5 wt % Pt/$ZnIn_2S_4$. (Reaction conditions: catalyst, 0.05 g; 100 mL H_2O containing 0.43 M Na_2S and 0.5 M Na_2SO_3).

NiS/$ZnIn_2S_4$ nanocomposites show high stability during the photocatalytic hydrogen evolution reaction. A prolonged photocatalytic reaction for 15 h over 0.5 wt % NiS/$ZnIn_2S_4$ revealed that no obvious loss of the activity during the whole reaction period (Figure 7). Besides this, the unchanged XRD pattern of the photocatalyst after the long time reaction also confirms its high stability (Figure 8).

Scheme 1 shows the mechanism proposed for the enhanced photocatalytic hydrogen evolution over NiS/$ZnIn_2S_4$ nanocomposite. Although the conduction band edge of $ZnIn_2S_4$

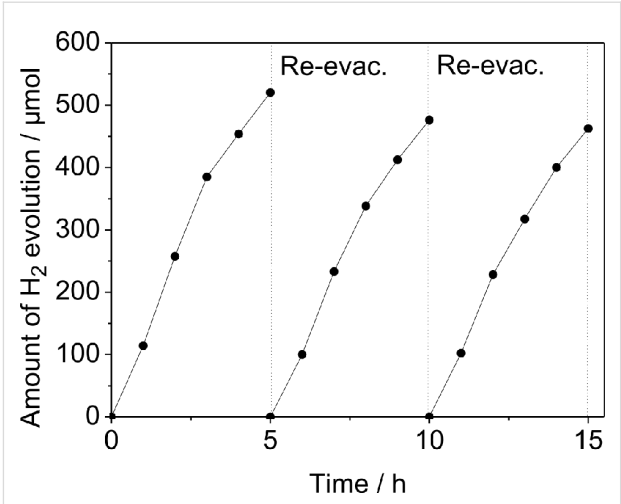

Figure 7: Amount of hydrogen evolved over 0.5 wt % NiS/$ZnIn_2S_4$ system in a 15 h photocatalytic reaction. (Reaction conditions: catalyst, 0.05 g; 100 mL H_2O containing 0.43 M Na_2S and 0.5 M Na_2SO_3).

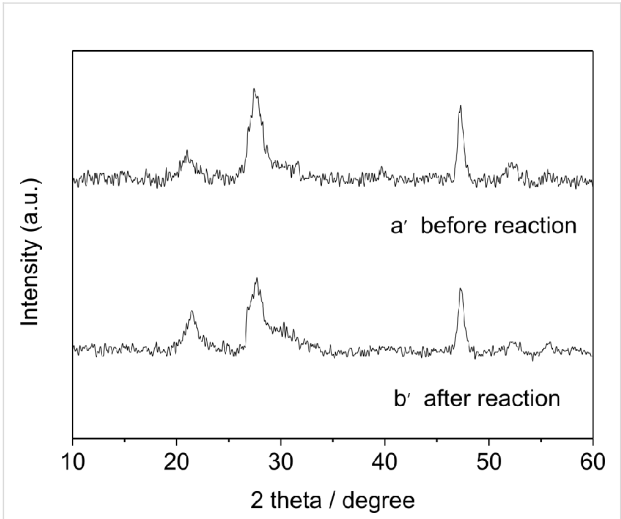

Figure 8: XRD patterns of 0.5 wt % NiS/$ZnIn_2S_4$ (a) before and (b) after photocatalytic hydrogen evolution reaction.

(−1.1 eV) is higher than the reduction potential of H^+/H_2, the rate of hydrogen evolution is low over bare $ZnIn_2S_4$ due to the rapid recombination rate of photogenerated charge carriers as well as the presence of a large hydrogen evolution overpotential. When NiS is deposited on the surface of $ZnIn_2S_4$, due to the less negative conduction band of NiS as compared to that of hexagonal $ZnIn_2S_4$ [43], a directional transfer of the photogenerated electrons from the conduction band of $ZnIn_2S_4$ to NiS is feasible. Since NiS is a good electrocatalyst for hydrogen evolution [36], NiS can adsorb H^+ from water and act as the active sites for hydrogen evolution. An efficient electron transfer from the conduction band of $ZnIn_2S_4$ to NiS in which the hydrogen evolution occurs is crucial for the enhanced hydrogen evolution

over the NiS/$ZnIn_2S_4$ nanocomposites since controlled experiments performed over a mixture of NiS and $ZnIn_2S_4$ shows a much lower photocatalytic activity under similar condition (Figure 5d). Therefore, the formation of a good junction between $ZnIn_2S_4$ and NiS via the two step hydrothermal processes is important for achieving the highly efficient NiS/$ZnIn_2S_4$ nanocomposites with enhanced photocatalytic hydrogen evolution activity.

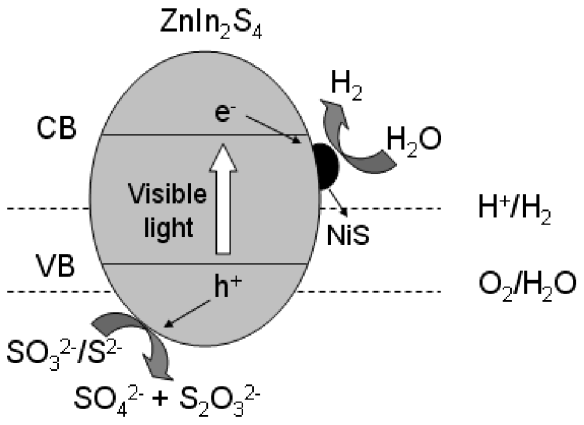

Scheme 1: Schematic illustration of proposed mechanism for photocatalytic hydrogen evolution over NiS/$ZnIn_2S_4$ nanocomposite under visible light irradiations.

Conclusion

In summary, NiS/$ZnIn_2S_4$ nanocomposites were facilely synthesized via a two-step hydrothermal method. The as-prepared NiS/$ZnIn_2S_4$ nanocomposites showed highly enhanced photocatalytic performance for hydrogen evolution under visible light irradiation. The highest photocatalytic hydrogen evolution rate (104.7 μmol/h), which is even higher than that over Pt/$ZnIn_2S_4$ nanocomposite (77.8 μmol/h), was observed over an optimum NiS loading amount of 0.5 wt %. This work demonstrates a high potential of developing the environmental friendly, cheap non-noble-metal co-catalyst for semiconductor-based photocatalytic hydrogen evolution.

Experimental

Preparations. All the reagents are analytical grade and used without further purifications. Hexagonal $ZnIn_2S_4$ powder was synthesized according to our previously reported method [16]. In a typical synthesis of 0.5 wt % NiS/$ZnIn_2S_4$ photocatalyst, 0.2 g $ZnIn_2S_4$, 2.8 mg nickel acetate and 0.9 mg thioacetamide (TAA) were dispersed in 70 mL of de-ionized water by stirring and ultra-sonication for 2 h. The resultant solution was transferred to a 100 mL Teflon liner, sealed in the stainless steel autoclave and heated at 120 °C for 4 h. After the autoclave was cooled to room temperature, the product was collected and washed with de-ionized water several times before it was dried at 60 °C to obtain the final product. Samples with different amount of NiS (0.2, 0.25, 1.0, 2.0 wt %) were prepared by using different amounts of nickel acetate and TAA precursor during the hydrothermal treatment at 120 °C, while keeping other conditions the same.

0.5 wt % Pt/$ZnIn_2S_4$ was prepared by a photo-deposited method using $H_2PtCl_6{\cdot}6H_2O$ as the starting material. Pure NiS was prepared by hydrothermal using nickel acetate and TAA as precursors at 120 °C for 4 h.

Characterizations. X-ray diffraction (XRD) patterns were collected on a Bruker D8 Advance X-ray diffractometer with Cu Kα radiation. The transmission electron microscopy (TEM) and high-resolution transmission electron microscopy (HRTEM) images were measured by a JEOL model JEM 2010 EX instrument at an accelerating voltage of 200 kV. The powder particles were supported on a carbon film coated on a 3 mm diameter fine-mesh copper grid. A suspension in ethanol was sonicated and a drop was dripped on the support film. X-ray photoelectron spectroscopy (XPS) measurements were performed on a PHI Quantum 2000 XPS system with a monochromatic Al Kα source and a charge neutralizer. All of the binding energies were referred to the C 1s peak at 284.8 eV of the surface adventitious carbon. UV–visible diffraction spectra (UV–vis DRS) of the powders were obtained for the dry pressed disk samples using a UV–visible spectrophotometer (Cary 500 Scan Spectrophotometers, Varian). $BaSO_4$ was used as a reflectance standard.

Photocatalytic hydrogen evolution. Photocatalytic hydrogen evolution experiments were carried out in a closed gas circulation and evacuation system fitted with a top Pyrex window. 50 mg of photocatalyst was dispersed in 100 mL of aqueous solution containing 0.5 M Na_2SO_3 and 0.43 M Na_2S as sacrificial reagents. The suspension was irradiated with a 300 W Xe lamp equipped with a 420 nm cutoff filter to provide the visible light irradiation. The temperature of the reactant solution was maintained at room temperature by a flow of cooling water during the photocatalytic reaction. The amount of hydrogen evolved was determined with an on-line gas chromatography equipped with a TCD detector.

Acknowledgments

The work was supported by NSFC (21273035), 973 Programs (2014CB239303) and Specialized Research Fund for the Doctoral Program of Higher Education (20123514110002). Z. Li thanks the Award Program for Minjiang Scholar Professorship for financial support.

References

1. Chen, X.; Shen, S.; Guo, L.; Mao, S. S. *Chem. Rev.* **2010,** *110,* 6503–6570. doi:10.1021/cr1001645
2. Tong, H.; Ouyang, S.; Bi, Y.; Umezawa, N.; Oshikiri, M.; Ye, J. *Adv. Mater.* **2012,** *24,* 229–251. doi:10.1002/adma.201102752
3. Lewis, N. S.; Nocera, D. G. *Proc. Natl. Acad. Sci. U. S. A.* **2006,** *103,* 15729–15735. doi:10.1073/pnas.0603395103
4. Fujishima, A.; Honda, K. *Nature* **1972,** *238,* 37–38. doi:10.1038/238037a0
5. Kamegawa, T.; Matsuura, S.; Seto, H.; Yamashita, H. *Angew. Chem., Int. Ed.* **2013,** *52,* 916–919. doi:10.1002/anie.201206839
6. Zuo, F.; Bozhilov, K.; Dillon, R. J.; Wang, L.; Smith, P.; Zhao, X.; Bardeen, C.; Feng, P. *Angew. Chem., Int. Ed.* **2012,** *51,* 6223–6226. doi:10.1002/anie.201202191
7. Ouyang, S.; Tong, H.; Umezawa, N.; Cao, J.; Li, P.; Bi, Y.; Zhang, Y.; Ye, J. *J. Am. Chem. Soc.* **2012,** *134,* 1974–1977. doi:10.1021/ja210610h
8. Seo, S. W.; Park, S.; Jeong, H.-Y.; Kim, S. H.; Sim, U.; Lee, C. W.; Nam, K. T.; Hong, K. S. *Chem. Commun.* **2012,** *48,* 10452–10454. doi:10.1039/c2cc36216c
9. Jin, J.; Yu, J.; Liu, G.; Wong, P. K. *J. Mater. Chem. A* **2013,** *1,* 10927–10934. doi:10.1039/c3ta12301d
10. Kim, H. N.; Kim, T. W.; Choi, K.-H.; Kim, I. Y.; Kim, Y.-R.; Hwang, S.-J. *Chem.–Eur. J.* **2011,** *17,* 9626–9633. doi:10.1002/chem.201100583
11. Tsuji, I.; Shimodaira, Y.; Kato, H.; Kobayashi, H.; Kudo, A. *Chem. Mater.* **2010,** *22,* 1402–1409. doi:10.1021/cm9022024
12. Higashi, M.; Domen, K.; Abe, R. *J. Am. Chem. Soc.* **2013,** *135,* 10238–10241. doi:10.1021/ja404030x
13. Wang, Z.; Hou, J.; Yang, C.; Jiao, S.; Huang, K.; Zhu, H. *Energy Environ. Sci.* **2013,** *6,* 2134–2144. doi:10.1039/c3ee24370b
14. Ida, S.; Okamoto, Y.; Matsuka, M.; Hagiwara, H.; Ishihara, T. *J. Am. Chem. Soc.* **2012,** *134,* 15773–15782. doi:10.1021/ja3043678
15. Wang, X.; Maeda, K.; Thomas, A.; Takanabe, K.; Xin, G.; Carlssom, J. M.; Domen, K.; Antonietti, M. *Nat. Mater.* **2009,** *8,* 76–82. doi:10.1038/nmat2317
16. Chen, Y.; Hu, S.; Liu, W.; Chen, X.; Wu, L.; Wang, X.; Liu, P.; Li, Z. *Dalton Trans.* **2011,** *40,* 2607–2613. doi:10.1039/c0dt01435d
17. Lei, Z.; You, W.; Liu, M.; Zhou, G.; Takata, T.; Hara, M.; Domen, K.; Li, C. *Chem. Commun.* **2003,** 2142–2143. doi:10.1039/b306813g
18. Shen, S.; Zhao, L.; Guo, L. *Int. J. Hydrogen Energy* **2008,** *33,* 4501–4510. doi:10.1016/j.ijhydene.2008.05.043
19. Shen, J.; Zai, J.; Yuan, Y.; Qian, X. *Int. J. Hydrogen Energy* **2012,** *37,* 16986–16993. doi:10.1016/j.ijhydene.2012.08.038
20. Chai, B.; Peng, T.; Zeng, P.; Zhang, X.; Liu, X. *J. Phys. Chem. C* **2011,** *115,* 6149–6155. doi:10.1021/jp1112729
21. Shen, S.; Zhao, L.; Zhou, Z.; Guo, L. *J. Phys. Chem. C* **2008,** *112,* 16148–16155. doi:10.1021/jp804525q
22. Mei, Z.; Ouyang, S.; Tang, D.-M.; Kako, T.; Golberg, D.; Ye, J. *Dalton Trans.* **2013,** *42,* 2687–2690. doi:10.1039/c2dt32271d
23. Chen, Y.; Ge, H.; Wei, L.; Li, Z.; Yuan, R.; Liu, P.; Fu, X. *Catal. Sci. Technol.* **2013,** *3,* 1712–1717. doi:10.1039/c2cy20710a
24. Wang, Y.; Wang, Y.; Xu, R. *J. Phys. Chem. C* **2013,** *117,* 783–790. doi:10.1021/jp309603c
25. Yang, J.; Yan, H.; Wang, X.; Wen, F.; Wang, Z.; Fan, D.; Shi, J.; Li, C. *J. Catal.* **2012,** *290,* 151–157. doi:10.1016/j.jcat.2012.03.008
26. Maeda, K.; Lu, D. L.; Domen, K. *ACS Catal.* **2013,** *3,* 1026–1033. doi:10.1021/cs400156m
27. Shimura, K.; Kawai, H.; Yoshida, T.; Yoshida, H. *Chem. Commun.* **2011,** *47,* 8958–8960. doi:10.1039/c1cc12287h
28. Tanaka, A.; Sakaguchi, S.; Hashimoto, K.; Kominami, H. *ACS Catal.* **2013,** *3,* 79–85. doi:10.1021/cs3006499
29. Iwase, A.; Kato, H.; Kudo, A. *Appl. Catal., B: Environ.* **2013,** *136–137,* 89–93. doi:10.1016/j.apcatb.2013.02.006
30. Inoue, Y. *Energy Environ. Sci.* **2009,** *2,* 364–386. doi:10.1039/B816677N
31. Ohno, T.; Bai, L.; Hisatomi, T.; Maeda, K.; Domen, K. *J. Am. Chem. Soc.* **2012,** *134,* 8254–8259. doi:10.1021/ja302479f
32. Lee, Y.; Teramura, K.; Hara, M.; Domen, K. *Chem. Mater.* **2007,** *19,* 2120–2127. doi:10.1021/cm062980d
33. Maeda, K.; Teramura, K.; Masuda, H.; Takata, T.; Saito, N.; Inoue, Y.; Domen, K. *J. Phys. Chem. B* **2006,** *110,* 13107–13112. doi:10.1021/jp0616563
34. Hinnemann, B.; Moses, P. G.; Bonde, J.; Jørgensen, K. P.; Nielsen, J. H.; Horch, S.; Chorkendorff, I.; Nørskov, J. K. *J. Am. Chem. Soc.* **2005,** *127,* 5308–5309. doi:10.1021/ja0504690
35. Wei, L.; Chen, Y.; Lin, Y.; Wu, H.; Yuan, R.; Li, Z. *Appl. Catal., B: Environ.* **2014,** *144,* 521–527. doi:10.1016/j.apcatb.2013.07.064
36. Borucinsky, T.; Rausch, S.; Wendt, H. *J. Appl. Electrochem.* **1997,** *27,* 762–773. doi:10.1023/A:1018460425956
37. Zou, Z.; Ye, J.; Sayama, K.; Arakawa, H. *Nature* **2001,** *414,* 625–627. doi:10.1038/414625a
38. Kato, H.; Asakura, K.; Kudo, A. *J. Am. Chem. Soc.* **2003,** *125,* 3082–3089. doi:10.1021/ja027751g
39. Zhang, W.; Wang, Y.; Wang, Z.; Zhong, Z.; Xu, R. *Chem. Commun.* **2010,** *46,* 7631–7633. doi:10.1039/c0cc01562h
40. Zhang, L.; Tian, B.; Chen, F.; Zhang, J. *Int. J. Hydrogen Energy* **2012,** *37,* 17060–17067. doi:10.1016/j.ijhydene.2012.08.120
41. Zhang, J.; Qiao, S. Z.; Qi, L.; Yu, J. *Phys. Chem. Chem. Phys.* **2013,** *15,* 12088–12094. doi:10.1039/c3cp50734c
42. Li, N.; Zhou, B.; Guo, P.; Zhou, J.; Jing, D. *Int. J. Hydrogen Energy* **2013,** *38,* 11268–11277. doi:10.1016/j.ijhydene.2013.06.067
43. Xu, Y.; Schoonen, M. A. A. *Am. Mineral.* **2000,** *85,* 543–556.

License and Terms

This is an Open Access article under the terms of the Creative Commons Attribution License (http://creativecommons.org/licenses/by/2.0), which permits unrestricted use, distribution, and reproduction in any medium, provided the original work is properly cited.

The license is subject to the *Beilstein Journal of Nanotechnology* terms and conditions: (http://www.beilstein-journals.org/bjnano)

The definitive version of this article is the electronic one which can be found at: doi:10.3762/bjnano.4.107

Beilstein Journal of Nanotechnology

Dye-sensitized Pt@TiO_2 core–shell nanostructures for the efficient photocatalytic generation of hydrogen

Jun Fang, Lisha Yin, Shaowen Cao, Yusen Liao and Can Xue*

Full Research Paper

Open Access

Address:
Solar Fuels Laboratory, School of Materials Science and Engineering, Nanyang Technological University, 50 Nanyang Avenue, Singapore 639798, Singapore

Email:
Can Xue* - cxue@ntu.edu.sg

* Corresponding author

Keywords:
charge transfer; dye-sensitization; photocatalysis; photocatalyst; solar fuels; water splitting

Beilstein J. Nanotechnol. **2014,** *5,* 360–364.
doi:10.3762/bjnano.5.41

Received: 10 November 2013
Accepted: 04 March 2014
Published: 26 March 2014

This article is part of the Thematic Series "Photocatalysis".

Guest Editor: R. Xu

© 2014 Fang et al; licensee Beilstein-Institut.
License and terms: see end of document.

Abstract

Pt@TiO_2 core–shell nanostructures were prepared through a hydrothermal method. The dye-sensitization of these Pt@TiO_2 core–shell structures allows for a high photocatalytic activity for the generation of hydrogen from proton reduction under visible-light irradiation. When the dyes and TiO_2 were co-excited through the combination of two irradiation beams with different wavelengths, a synergic effect was observed, which led to a greatly enhanced H_2 generation yield. This is attributed to the rational spatial distribution of the three components (dye, TiO_2, Pt), and the vectored transport of photogenerated electrons from the dye to the Pt particles via the TiO_2 particle bridge.

Introduction

Since Honda and Fujishima reported the effective hydrogen evolution from water splitting by a TiO_2 and Pt electrode in a photoelectrochemical cell in the early 1970s [1], TiO_2 has received extensive attention as one of the promising semiconductor photocatalysts, because of its high chemical stability, low cost and non-toxicity [2-5]. However, it suffers from the wide band gap (3.2–3.4 eV), which restricts the utilization of visible light, and the high recombination rate of photogenerated electrons and holes often leads to low quantum yields and a poor photocatalytic activity [6]. Tremendous efforts have been made to improve the photocatalytic performance of TiO_2. One typical strategy is prolonging the lifetime of the electron–hole pair through deposition of noble metal (e.g., Pt) nanoparticles as co-catalysts that can act as electron-sinks to achieve effective charge separation on TiO_2 [7-11]. Dye-sensitization has been widely used to enable visible light harvesting by wide band gap semiconductors. Since the seminal work reported by O'Regan and Grätzel in 1991 [12], various types of dyes have been explored, and some of them allow for the reduction of protons into hydrogen gas through visible-light-driven photocatalytic processes [13-17]. Herein, we use erythrosin B (ErB) sensitized Pt@TiO_2 core–shell nanoparticles for the highly-efficient

photocatalytic generation of hydrogen under visible-light irradiation. In this rational design of the ternary structure, the TiO_2 particle acts as a bridge that allows for the effective electron transfer pathway of excited ErB→TiO_2→Pt. Importantly, we found that when the TiO_2 bridges are excited simultaneously, the dye-sensitization-driven H_2 evolution showed a much higher efficiency as compared to the situation with no excitation of TiO_2. This kind of synergic effect reveals a new direction for improving the efficiency of composite photocatalysts by using selective excitation wavelengths.

Results and Discussion

The Pt@TiO_2 core–shell nanoparticles were prepared trough a hydrothermal process by using Pt nanoparticles and TiF_4 as the precursor. The crystalline structure was determined by XRD, as shown in Figure 1. After the hydrothermal reaction, the TiO_2 was transformed into anatase phase, which could be well indexed to the standard anatase TiO_2 (JCPDS Card No. 83-2243). The three additional diffraction peaks shown in Figure 1 could be assigned to the face-centered metallic Pt phase, with the positions at 40.0°, 46.6° and 67.9° representing the spacing of the (111), (200) and (220) planes, respectively. This indicates the retaining of the Pt nanoparticle cores after the hydrothermal reaction. As a control sample, Pt/TiO_2 was prepared through the photodeposition of Pt (1% in mole fraction) onto pure TiO_2 particles that were prepared through the same hydrothermal method without using Pt nanoparticles. Due to the low Pt loading, we could only observe a weak diffraction peak at 40° corresponding to the Pt (111) lattice spacing, which could indicate successful loading of metallic Pt nanoparticles onto TiO_2 particles. The molar ratio of Pt to Ti was estimated to be about 6.7% according to EDX analysis (Figure S1, Supporting Information File 1).

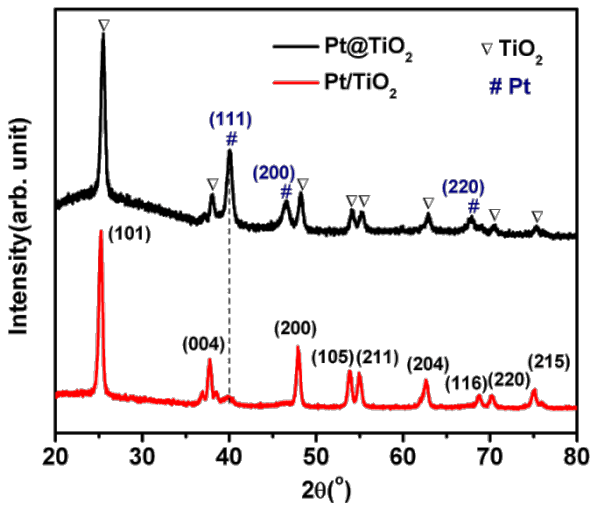

Figure 1: XRD patterns of Pt@TiO_2 and Pt/TiO_2 samples.

The core–shell morphology of the prepared Pt@TiO_2 nanostructures was confirmed by TEM and SEM examination. As shown in Figure 2A and 2B, the core–shell particles appear as flower-like structures, in which the Pt nanoparticles as the cores show an average diameter of 30 nm, and the TiO_2 shell thickness is around 60 nm. The HRTEM image (Figure 2C) indicates lattice distances of 0.228 nm and 0.341 nm, which correspond to the (111) spacing of the core Pt particle and the (101) spacing of the anatase TiO_2 shell. The SEM image (Figure 2D) reveals that these core–shell Pt@TiO2 structures appear like a large particle with scraggy surfaces and an average diameter of about 150 nm. These observations confirm that all Pt nanoparticles are well encapsulated by TiO_2 shells. Nevertheless, we note that the TiO_2 shell does not compactly cover all Pt surfaces, which allows for the proton reduction and H_2 evolution on the uncovered surface area of Pt. For the control sample Pt/TiO_2, the TiO_2 particles were synthesized through a hydrothermal method that was followed by the photodeposition of Pt nanoparticles, as shown in Figure S2 (Supporting Information File 1). The TiO_2 particles are in a solid spherical shape and composed by nanoparticle aggregation, and the average diameter of deposited Pt nanoparticles is about 5 nm.

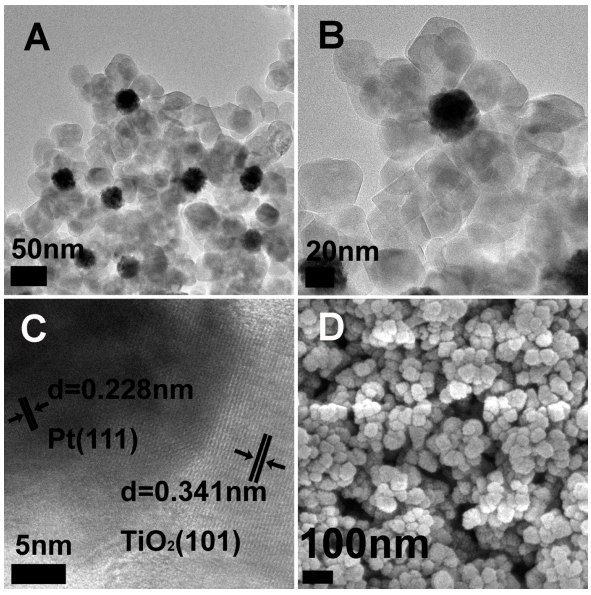

Figure 2: TEM and SEM images of the Pt@TiO_2 sample. (A) (B) TEM images of Pt@TiO_2, (C) HRTEM images of Pt@TiO_2, (D) SEM image of Pt@TiO_2.

Figure 3 shows the UV–vis diffuse reflectance spectra of the Pt@TiO_2 core–shell nanostructures and the Pt/TiO_2 control sample. The absorption from 250 to ca. 380 nm can be attributed to the band edge absorption of anatase TiO_2. The band gaps of both samples are calculated according to the modified

Kubelka–Munk function $\left[F\left(R_{\infty}\right)E\right]^{1/2}$ vs the energy the of absorbed light, E [18]. And the plots shown in the inset of Figure 3 reveal the band gap value as 3.3 eV for Pt@TiO_2 and 3.2 eV for Pt/TiO_2, which indicates that the combination of Pt nanoparticles with TiO_2 did not significantly influence the band gap energy of the TiO_2 component.

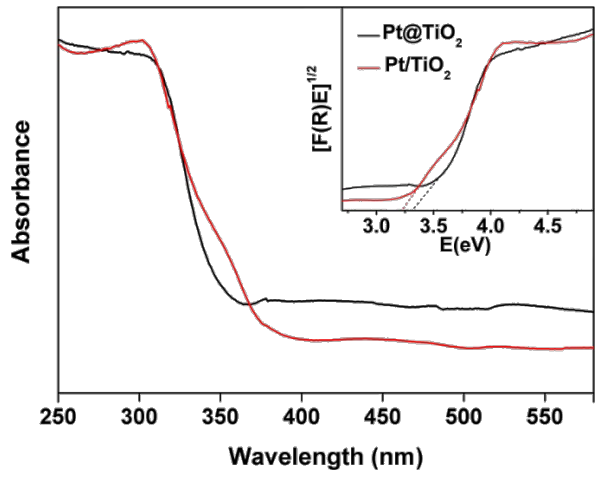

Figure 3: UV–vis diffuse reflectance spectra of the Pt@TiO_2 and Pt/TiO_2 samples.

The photocatalytic tests were carried out by suspending the Pt@TiO_2 sample (5 mg) in an aqueous solution containing 0.2 wt % ErB and 15 wt % triethanolamine (TEOA) that acts as the electron donor. In this study, we employed two different irradiation wavelengths for the purpose of separating the excitation of TiO_2 and ErB, which will help us to explore the potential synergic effect between the two excitations. The primary irradiation with a wavelength of 550 ± 20 nm (light A) is to excite ErB since the main absorbance peak of ErB is located at about 550 nm. A secondary irradiation with a wavelength of 400 ± 10 nm (light B) is to excite the defect/impurity states of TiO_2, while ErB exhibit a minimum absorption in this range.

As shown in Figure 4, after the individual irradiation with light A (550 ± 20 nm) or light B (400 ± 10 nm) for 2 h, the ErB-sensitized Pt@TiO_2 core–shell structure showed generated H_2 amounts of 4.5 µmol and 5.3 µmol, respectively. However, when light A and light B are used simultaneously, to our surprise, the 2 h irradiation led to a H_2 amount of 15.9 µmol, which is significantly higher than the sum of the two generated H_2 amounts under individual irradiation of light A and B (9.8 µmol). This observation suggests that in the ErB-sensitized Pt@TiO_2 core–shell structure, a synergic effect exists between the excitation of ErB and TiO_2, which plays an important role in the photocatalytic hydrogen generation.

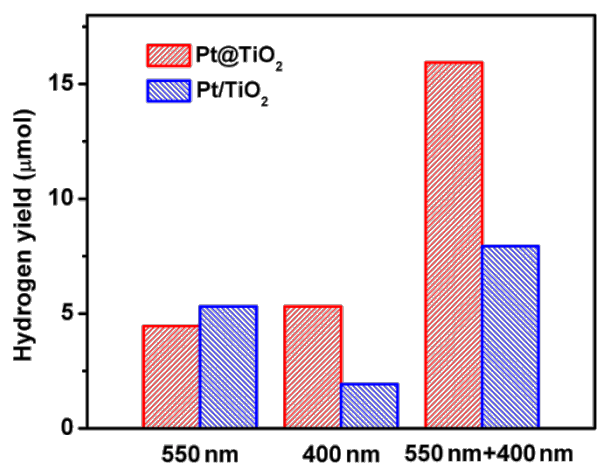

Figure 4: The H_2 yield from Pt@TiO_2 and Pt/TiO_2 for water splitting under irridiation with the given for 2 h while using TEOA as the sacrificial reagent.

The observed synergic effect could be attributed to the electron transport in TiO_2 particles. Since the dye-sensitization induces an electron transfer from the excited ErB to TiO_2, these electrons have to be transported through the TiO_2 particles with a maximum distance of ca. 60 nm to reach the Pt surface for the reduction of protons to H_2. When TiO_2 is simultaneously excited by the 400 ± 10 nm light, though it is weak, the charge carrier concentration in TiO_2 becomes higher, which increases the conductivity of TiO_2. Thereby, the vectored electron transfer from ErB to the core Pt particle via TiO_2 bridges becomes more effective, which leading to enhanced yield of H_2. The principle is depicted in Figure 5, and the energy diagram is shown in Figure S3 (Supporting Information File 1).

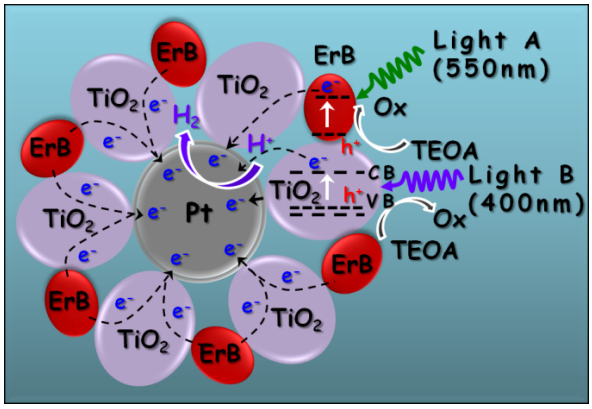

Figure 5: Schematic illustration of the photocatalytic H_2 generation by ErB-sensitized Pt@TiO_2 core–shell nanostructures under irradiation of light A (550 ± 20 nm) and/or light B (400 ± 10 nm).

In comparison, under individual irradiation of light A or light B for 2 h, the Pt/TiO_2 sample showed a H_2 generation of 5.3 µmol

and 1.9 μmol, respectively. While the simultaneous irradiation with light A and B for 2 h led to the generation of 7.9 μmol H_2, which is only slightly higher than the sum of the H_2 generation amount under individual irradiation of light A and B (7.2 μmol). This indicates that the synergic effect may also exist in the Pt-loaded TiO_2 particles, but with a less significant role as compared to the Pt@TiO_2 core–shell structure. This may be because the post-loaded Pt nanoparticles are randomly distributed on the outer surfaces of TiO_2 particles, thus the electron transfer path from ErB to Pt becomes less oriented through TiO_2. In addition, the Pt nanoparticles would occupy some reactive sites on the TiO_2 surface, which also reduces the efficiency of the dye-sensitization.

Conclusion

We have prepared Pt@TiO_2 core–shell nanostructures through a one-step hydrothermal method. Upon ErB sensitization, the Pt@TiO_2 core–shell photocatalysts exhibit high visible-light activity for the generation of H_2 from proton reduction. Significantly, we observed a synergic effect that allows for a greatly enhanced activity for the H_2 generation when the ErB and TiO_2 are co-excited through the combination of two irradiation beams at different wavelengths. The enhancement is attributed to the rational spatial distribution of three components (ErB, TiO_2, Pt), and the vectored transport of photogenerated electrons from ErB to Pt particles via the TiO_2 particle bridge. The presented core–shell structures and the observed synergic effect would provide a new direction for improving the efficiency of composite photocatalysts by using selective excitation wavelengths.

Experimental

Seed growth of 30 nm Pt nanoparticles: Seed Pt nanoparticles were prepared first. Typically, an aqueous solution of H_2PtCl_6 (3.8 mM, 7 mL) was added into 90 mL deionized (DI) water and heated to boil under stirring. After that, 2.2 mL aqueous solution containing 1% trisodium citrate and 0.05% citrate acid was added, followed by a quick injection of freshly prepared $NaBH_4$ solution (0.08%, 1.1 mL). After 10 min, the solution was cooled down to room temperature, and used as the solution of seed nanoparticles (≈4 nm). For further growth into 16 nm Pt nanoparticles, 1 mL of this Pt seed solution was added into 29 mL DI water, followed by the addition of 0.09 mL solution of H_2PtCl_6 (0.2 M) and 0.5 mL of a solution containing 1% sodium citrate and 1.25% L-ascorbic acid. The solution was kept under stirring and heated to boil. After 30 min, the solution was cooled down to the room temperature and used as the 16 nm Pt seed solution for further growth into 30 nm Pt nanoparticles. In a typical run, 4 mL of the 16 nm Pt particle solution was mixed with 26 mL DI water. Then 0.09 mL solution of H_2PtCl_6 (0.2 M) was added, followed by addition of 0.5 mL solution containing 1% trisodium citrate and 1.25% L-ascorbic acid. The solution was kept stirring and heated to boil, and after 30 min of boiling, the solution was cooled down to room temperature and used the solution of 30 nm Pt nanoparticles.

Preparation of Pt@TiO_2 core–shell nanostructures: The Pt@TiO_2 core–shell nanostructures were synthesized through a hydrothermal method. Typically, 15 mL solution of the as-prepared 30 nm Pt nanoparticles was mixed with 4.5 mL aqueous solution of TiF_4 (0.04 M). The mixture was kept stirring for 10 min, diluted into 80 mL DI water, and then transferred into a 100 mL Teflon-lined stainless steel autoclave, which was treated at 180 °C for 24 h. After that, the product was cooled down to room temperature, centrifuged and washed with deionized water for three times, and dried in a vacuum oven.

Characterizations: The crystalline phases of the samples were examined by powder X-ray diffraction (XRD) on a Shimazu XRD-6000 X-ray diffractometer (Cu Kα radiation) with a scanning speed of 2°/min in the 2θ range from 20 to 80°. Diffuse reflectance UV–vis spectra were acquired on a Lambda 750 UV–vis–NIR spectrophotometer (Perkin Elmer, USA). The morphology of the Pt@TiO_2 nanocomposites were investigated by field emission scanning electron microscopy (SEM, JEOL JSM-7600F) with energy-dispersive X-ray analysis system and transmission electron microscopy (TEM, JEOL JEM-2100) at an accelerating voltage at 200 kV.

Photocatalytic generation of H_2 with erythrosin B-sensitized Pt@TiO_2 core–shell particles: In a typical run, 5 mg Pt@TiO_2 photocatalyst was dispersed into 10 mL of an aqueous solution containing triethanolamine (TEOA, 15 wt %) as electron donor and erythrosin B (0.2 wt %) as the photo-sensitizing dye. The suspension was sealed in a quartz vessel and purged with Argon for 30 min to remove the residual oxygen. After that, the vessel was exposed under a 300 W Xenon lamp (MAX-302, Asahi Spectra Co. Ltd.) coupled with a band pass filter ($\lambda = 400 \pm 10$ nm or 550 ± 20 nm) to evaluate the photocatalytic H_2 generation yield. The gas products were analyzed periodically by an Agilent 7890A gas chromatograph (GC) with a thermal conductivity detector (TCD).

Supporting Information

Supporting Information File 1

Additional experimental data.
[http://www.beilstein-journals.org/bjnano/content/supplementary/2190-4286-5-41-S1.pdf]

Acknowledgements

This work was financially supported by NTU seed funding for Solar Fuels Laboratory, MOE AcRF-Tier1 RG 44/11, MOE AcRF-Tier2 (MOE2012-T2-2-041, ARC 5/13), and CRP program (NRF-CRP5-2009-04) from the Singapore National Research Foundation.

References

1. Fujishima, A.; Honda, K. *Nature* **1972,** *238,* 37–38. doi:10.1038/238037a0
2. Chen, X.; Shen, S.; Guo, L.; Mao, S. S. *Chem. Rev.* **2010,** *110,* 6503–6570. doi:10.1021/cr1001645
3. Kudo, A.; Miseki, Y. *Chem. Soc. Rev.* **2009,** *38,* 253–278. doi:10.1039/b800489g
4. Kubacka, A.; Fernández-García, M.; Colón, G. *Chem. Rev.* **2012,** *112,* 1555–1614. doi:10.1021/cr100454n
5. Thompson, T. L.; Yates, J. T., Jr. *Chem. Rev.* **2006,** *106,* 4428–4453. doi:10.1021/cr050172k
6. Asahi, R.; Morikawa, T.; Ohwaki, T.; Aoki, K.; Taga, Y. *Science* **2001,** *293,* 269–271. doi:10.1126/science.1061051
7. Jing, D.; Zhang, Y.; Guo, L. *Chem. Phys. Lett.* **2005,** *415,* 74–78. doi:10.1016/j.cplett.2005.08.080
8. Ebina, Y.; Sasaki, T.; Harada, M.; Watanabe, M. *Chem. Mater.* **2002,** *14,* 4390–4395. doi:10.1021/cm020622e
9. Ikuma, Y.; Bessho, H. *Int. J. Hydrogen Energy* **2007,** *32,* 2689–2692. doi:10.1016/j.ijhydene.2006.09.024
10. Chiarello, G. L.; Selli, E.; Forni, L. *Appl. Catal., B: Environ.* **2008,** *84,* 332–339. doi:10.1016/j.apcatb.2008.04.012
11. Bae, E.; Choi, W. *Environ. Sci. Technol.* **2003,** *37,* 147–152. doi:10.1021/es025617q
12. O'Regan, B.; Grätzel, M. *Nature* **1991,** *353,* 737–740. doi:10.1038/353737a0
13. Anderson, S.; Constable, E. C.; Dare-Edwards, M. P.; Goodenough, J. B.; Hamnett, A.; Seddon, K. R.; Wright, R. D. *Nature* **1979,** *280,* 571–573. doi:10.1038/280571a0
14. Borgarello, E.; Kiwi, J.; Pelizzetti, E.; Visca, M.; Grätzel, M. *J. Am. Chem. Soc.* **1981,** *103,* 6324–6329. doi:10.1021/ja00411a010
15. Nguyen, T.-V.; Wu, J. C. S.; Chiou, C.-H. *Catal. Commun.* **2008,** *9,* 2073–2076. doi:10.1016/j.catcom.2008.04.004
16. Nazeeruddin, M. K.; De Angelis, F.; Fantacci, S.; Selloni, A.; Viscardi, G.; Liska, P.; Ito, S.; Takeru, B.; Grätzel, M. *J. Am. Chem. Soc.* **2005,** *127,* 16835–16847. doi:10.1021/ja052467l
17. Wang, Z.-S.; Yamaguchi, T.; Sugihara, H.; Arakawa, H. *Langmuir* **2005,** *21,* 4272–4276. doi:10.1021/la050134w
18. Lin, H.; Huang, C. P.; Li, W.; Ni, C.; Ismat Shah, S.; Tseng, Y.-H. *Appl. Catal., B: Environ.* **2006,** *68,* 1–11. doi:10.1016/j.apcatb.2006.07.018

License and Terms

This is an Open Access article under the terms of the Creative Commons Attribution License (http://creativecommons.org/licenses/by/2.0), which permits unrestricted use, distribution, and reproduction in any medium, provided the original work is properly cited.

The license is subject to the *Beilstein Journal of Nanotechnology* terms and conditions: (http://www.beilstein-journals.org/bjnano)

The definitive version of this article is the electronic one which can be found at: doi:10.3762/bjnano.5.41

Beilstein Journal of Nanotechnology

Mesoporous cerium oxide nanospheres for the visible-light driven photocatalytic degradation of dyes

Subas K. Muduli[‡1], Songling Wang[‡2], Shi Chen[3], Chin Fan Ng[3], Cheng Hon Alfred Huan[3,4], Tze Chien Sum[*3,5,6] and Han Sen Soo[*1,6]

Letter

Open Access

Address:
[1]Division of Chemistry and Biological Chemistry, School of Physical and Mathematical Sciences, Nanyang Technological University, Singapore 637371, [2]Department of Chemistry, National University of Singapore, 10 Kent Ridge, Singapore 119260, [3]Division of Physics and Applied Physics, School of Physical and Mathematical Sciences, Nanyang Technological University, Singapore 637371, [4]Institute of High Performance Computing, Agency for Science, Technology and Research, 1 Fusionopolis Way, #16-16 Connexis, Singapore 138632, [5]Energy Research Institute @ NTU (ERI@N), 1 CleanTech Loop, Singapore 637141 and [6]Singapore-Berkeley Research Initiative for Sustainable Energy (SinBeRISE), 1 Create Way, Singapore 138602

Email:
Tze Chien Sum[*] - tzechien@ntu.edu.sg; Han Sen Soo[*] - hansen@ntu.edu.sg

* Corresponding author ‡ Equal contributors

Keywords:
cerium oxide; dye degradation; mesoporous; photocatalysis; visible light

Beilstein J. Nanotechnol. **2014,** *5,* 517–523.
doi:10.3762/bjnano.5.60

Received: 13 December 2013
Accepted: 29 March 2014
Published: 24 April 2014

This article is part of the Thematic Series "Photocatalysis".

Guest Editor: R. Xu

© 2014 Muduli et al; licensee Beilstein-Institut.
License and terms: see end of document.

Abstract

A facile, solvothermal synthesis of mesoporous cerium oxide nanospheres is reported for the purpose of the photocatalytic degradation of organic dyes and future applications in sustainable energy research. The earth-abundant, relatively affordable, mixed valence cerium oxide sample, which consists of predominantly Ce_7O_{12}, has been characterized by powder X-ray diffraction, X-ray photoelectron and UV–vis spectroscopy, and transmission electron microscopy. Together with N_2 sorption experiments, the data confirms that the new cerium oxide material is mesoporous and absorbs visible light. The photocatalytic degradation of rhodamin B is investigated with a series of radical scavengers, suggesting that the mechanism of photocatalytic activity under visible-light irradiation involves predominantly hydroxyl radicals as the active species.

Introduction

The degradation of organic pollutants by affordable and effective chemical methods is an acute problem that has been tackled by advanced oxidation processes [1]. The photocatalytic production of reactive oxygen species by using semiconductor technology has emerged as a sustainable and promising route for such advanced oxidation processes [2-6]. In these photocatalytic processes, based on TiO_2 for example, radiation larger than the band gap is absorbed to promote an electron from the valence to the conduction band [2-4]. The resultant strongly oxidizing, valence band holes (h^+) and reducing, conduction band electrons (e^-) are short-lived under ambient conditions and react with water and air to form reactive oxygen species such as $^{\bullet}OH$, $^{\bullet}OOH$, H_2O_2, and O_2^- for example [1,2,4-6]. These reactive oxygen species can subsequently decompose organic pollutants. Recent developments in nanotechnology have enhanced the performance of photocatalytic and solar energy absorption processes by providing higher surface areas and more effective charge separation in semiconductor materials on the nanoscale. In fact, the commercially available Degussa P25 mixed-phase TiO_2 is commonly employed as a benchmark in photocatalysis for applications ranging from dye-sensitized solar cells to the oxidative degradation of pollutants [7-11]. Despite being cheap, chemically robust, and generally non-toxic, TiO_2 has a wide band gap of more than 3.0 eV, which means that photocatalytic processes that use TiO_2 as the sensitizer can only absorb UV radiation (≈5% of the solar spectrum) [2-4,7,8]. Moreover, the valence band of TiO_2 is strongly oxidizing whereas the conduction band level is only mildly reducing, which results in a low energy-conversion efficiency since most of the oxidation potential is wasted thermally. A number of other metal oxide semiconductors have been explored for the visible-light driven photocatalytic degradation of pollutants and microbes, such as bismuth oxides [5,6] and cerium oxides [12,13]. CeO_2 specifically has been applied in a number of sustainable energy applications lately, including oxidative catalysis, hydrogen storage, and solar thermal dissociation of water and CO_2 [14-18].

Cerium oxides with oxygen vacancies represent an underexplored area of nanotechnology with the potential to provide visible-light absorbing photocatalysts [13,19-21]. Cerium is relatively earth-abundant and the oxides, including Ce_2O_3 and Ce_7O_{12}, are known to have band gaps in the visible region [13,19-21]. Our team has maintained a keen interest in alternative affordable, earth-abundant, visible light absorbing metal oxides to be used in two-photon 'Z-schemes' for dye-sensitized photoelectrosynthesis cells (DSPECs) [22-24]. To be employed in DSPECs, high surface areas for dye adsorption and an efficient charge conduction are critical properties [22-24]. As part of the preliminary investigations into this field, we communicate herein the preparation of high surface area, mesoporous cerium oxide nanospheres, which is a mixed phase of Ce_7O_{12} and CeO_2, and can absorb visible light to photocatalytically degrade dyes such as rhodamine B (RhB). The materials characterization of the cerium oxide nanospheres and some mechanistic insights into the photocatalytic process are presented.

Findings

Polycrystalline Ce_7O_{12} samples have been previously synthesized, but harsh conditions (up to 1030 °C) by reduction of CeO_2 with CO were employed [25,26]. Instead, mild, surfactant-free solvothermal conditions were used to prepare mesoporous cerium oxide with oxygen vacancies. A solution of ceric ammonium nitrate (CAN) in ethylene glycol and isopropanol as the solvent and reductant was heated up to 130 °C to yield mesoporous cerium oxide nanospheres after work-up. The powder X-ray diffraction (XRD) pattern (Figure 1a) indicates that the as-prepared cerium oxide material can be indexed to a superposition of hexagonal Ce_7O_{12} (JCPDS File No. 71-0567) and cubic CeO_2 (JCPDS File No. 81-0792) phases [14,26,27]. The peaks cannot be attributed to $Ce(OH)_3$ or Ce_2O_3 phases [13,28], and confirm that the material contains a mixed phase. The considerable broadening of the peaks suggest that the domain sizes of the nanocrystalites are small, and has been estimated to be 4.8 nm ((211) plane, $2\theta = 28.3°$) by the Scherrer equation [29].

In order to confirm the valence states of Ce and quantify their relative ratios in the prepared cerium oxide, X-ray photoelectron spectroscopy (XPS) experiments with monochromatic Al Kα radiation ($h\nu$ = 1486.7 eV) were conducted. Unlike CeO_2, in which the Ce atoms are all in the oxidation state 4+, the Ce atoms in Ce_7O_{12} consist of both Ce^{3+} and Ce^{4+} valence states. The wide-scan survey spectrum in Figure 1b only shows Ce 3d, O 1s, and C 1s signals, and no other signals. The presence of the C 1s signal is probably from residual organic solvents or from air. This C 1s signal was used to calibrate the binding energy of the Ce 3d peaks. The high-resolution spectrum of the Ce 3d core states is illustrated in Figure 1c. Neither Ce^{4+} nor Ce^{3+} alone could give a satisfactory fitting to the spectrum in Figure 1c. Instead, the fitting of the Ce 3d spectrum required five components derived from both Ce^{3+} and Ce^{4+}. There are two components (red) from Ce^{3+}. The principal peak is at 886.4 eV and a $4f^0$ to $4f^1\underline{v}$ ($\underline{v}$ denotes valence hole) shake-down peak is at 879.9 eV [30]. The Ce^{4+} component consists of three peaks (blue). The peaks at 889.3 eV and 883.0 eV are the principal and $4f^1\underline{v}$ to $4f^2\underline{v}^2$ shake-down peaks from the $4f^1\underline{v}$ electronic configuration. The highest binding energy peak at 898.7 eV is from the $4f^0$ electronic configuration [30]. The binding energy of these peaks is in good agreement with those found in the literature [19,20,31]. However, by integrating the

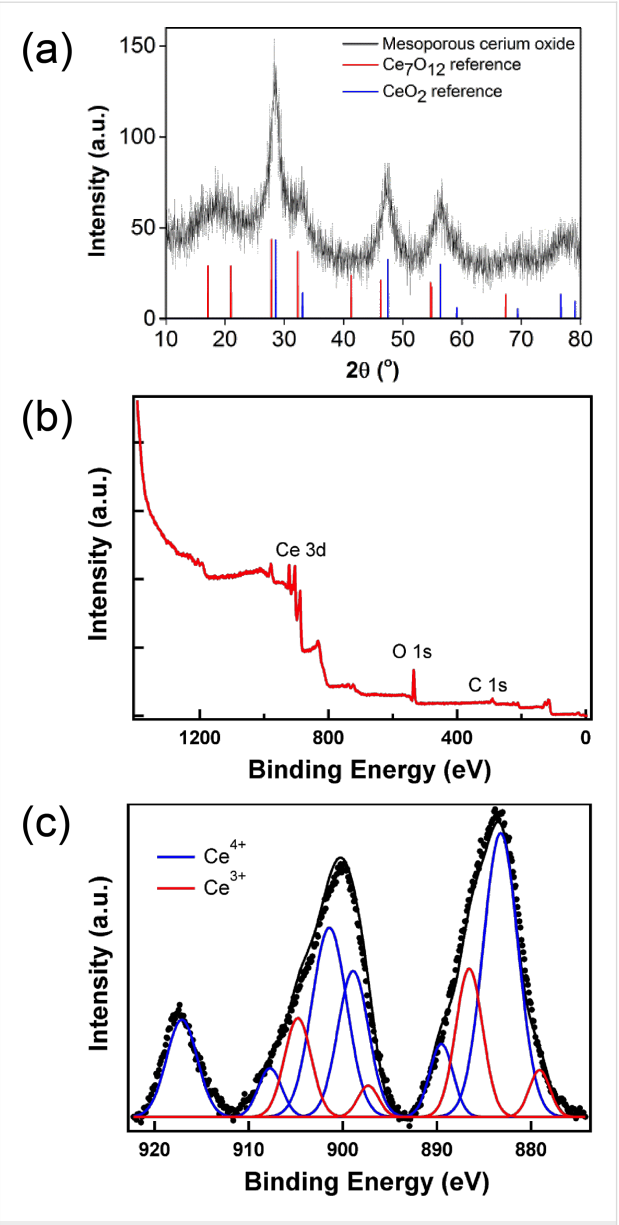

Figure 1: (a) Powder XRD pattern of cerium oxide nanospheres. (b) Wide-scan XPS survey spectrum. (c) High-resolution XPS spectrum of mesoporous cerium oxide (black circles) with the overall fit (black) and the fits to Ce^{4+} (blue) and Ce^{3+} (red).

spheres, CeO_2 (commercially available 7 nm) nanopowder, and TiO_2 (commercially available Degussa P25) nanoparticles are illustrated in Figure 2a. As expected, the cerium oxide sample displayed stronger visible light absorption than both commercially available 7 nm CeO_2 and P25 TiO_2 nanomaterials. The estimated band gap from the Tauc plot is approximately 2.7 eV (Figure 2b), which corresponds to an absorption edge in the blue region (460 nm). The reduced band gap compared to CeO_2 can be attributed to the presence of oxygen vacancies, as previously reported [32]. The enhanced visible light absorption has been exploited for driving the photocatalytic degradation of RhB in aqueous solutions (vide infra).

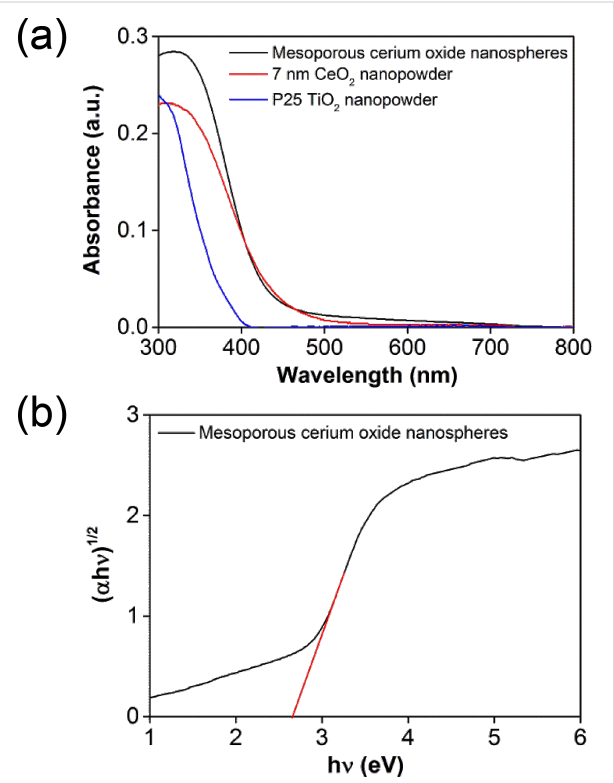

Figure 2: (a) UV–vis diffuse reflectance spectra of cerium oxide nanospheres (black), 7 nm CeO_2 (red) nanopowder, and P25 TiO_2 (blue). (b) Tauc plot for cerium oxide to obtain the band gap.

area under the fitted peaks, the concentration of Ce^{3+} is only 23%, which deviates from the predicted stoichiometric value (57%). This observation suggests that the Ce_7O_{12} phase is mixed with some CeO_2 phase on the surface. The nominal molecular formula of the material based on the XPS data is $CeO_{1.89}$, comprising of around 54% Ce_7O_{12} and 46% CeO_2. The mixture of two crystalline forms is also observed in our XRD measurements and TEM results (vide infra).

The UV–vis diffuse reflectance spectra (subjected to a Kubelka–Munck transformation) of the cerium oxide nano-

The transmission electron microscopy (TEM) images of the cerium oxide sample supported the mesoporous nature and nanosphere morphology of the material (Figure 3a). The material has fairly monodisperse nanospheres with diameters of 50–70 nm. Each nanosphere consists of an irregular mesoporous structure that is an aggregate of small nanocrystalline domains. The high-resolution TEM images confirm that the cerium oxide consists of crystalline domains, 4–5 nm in size (red dotted ring), that can be indexed to Ce_7O_{12} and CeO_2 (Figure 3b). Nitrogen sorption experiments were conducted to ascertain the average surface area and pore size distribution of

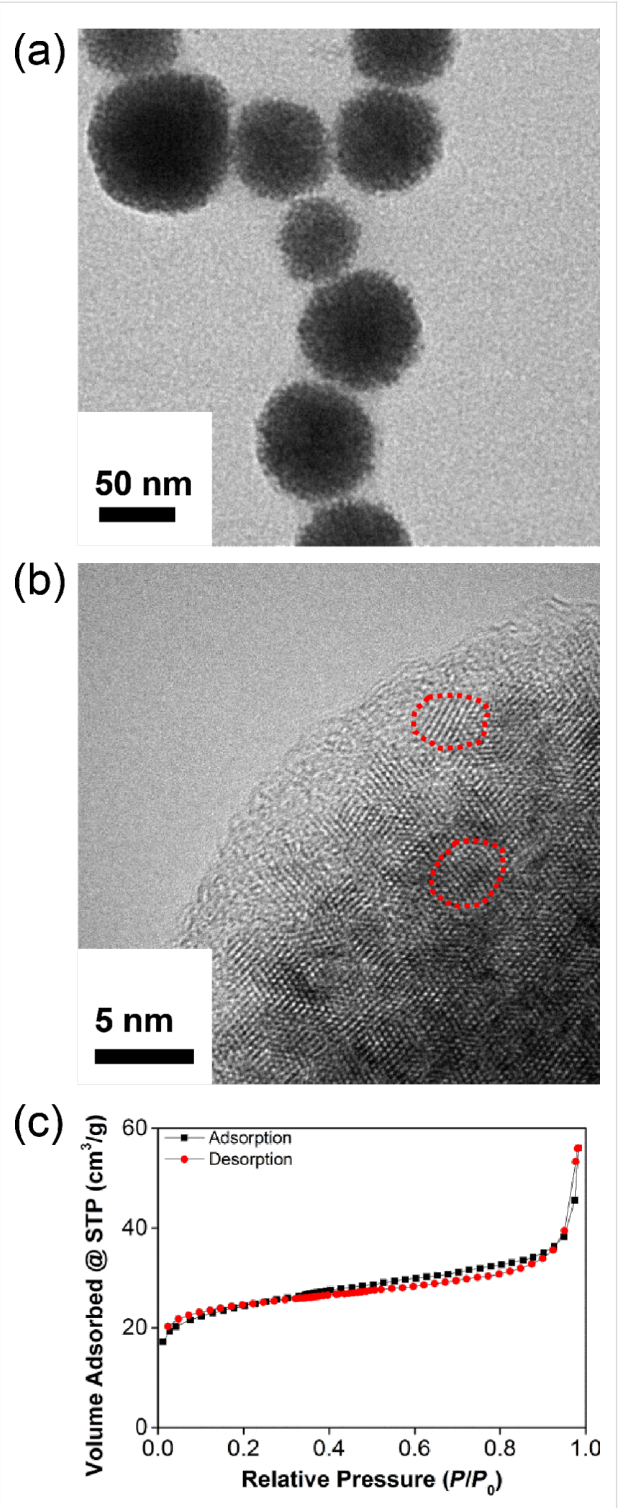

Figure 3: (a) TEM and (b) HRTEM images of the mesoporous cerium oxide nanospheres. (c) Nitrogen adsorption–desorption isotherm of the mesoporous cerium oxide nanospheres.

the material. The nitrogen adsorption–desorption isotherm of the cerium oxide sample (Figure 3c) shows a type-II curve and the surface area of the sample is 93 m^2 g^{-1} as calculated by the Brunauer–Emmett–Teller (BET) method. The average pore size determined by a Barrett–Joyner–Halenda (BJH) analysis is 3 nm, confirming the mesoporous nature of the cerium oxide sample.

The photocatalytic behavior at visible-light irradiation of the cerium oxide sample has been probed by the photodegradation of the suspected carcinogenic dye rhodamine B (RhB). A colloidal mixture of cerium oxide and RhB has been stirred and irradiated with AM 1.5 solar intensity light after equilibration in the dark for 30 min. A standard glass filter has been applied to transmit only wavelengths larger than 420 nm, to demonstrate photocatalytic properties under ambient conditions. The UV–vis spectral changes of the colloidal mixture illustrated in Figure 4 clearly shows the degradation of RhB over time, with the dye being completely decomposed within 6 h. In comparison, RhB is only decomposed to 50% or less after irradiation under the same conditions with the commercially available P25 TiO_2 and 7 nm CeO_2 nanopowder. The visible-light photocatalytic degradation of organic compounds with wide band-gap materials, by a ligand-to-metal charge-transfer mechanism after adsorption [33], has been reported and may be a contributing factor for the activity of TiO_2 and CeO_2. In the absence of light, some of the RhB adsorbs on the cerium oxide (green). The mesoporous cerium oxide sample is patently a more effective agent for the photocatalytic degradation of RhB under visible light and ambient conditions after equilibration, and the activity cannot be accounted to the presence of CeO_2 or adsorption alone. Gas chromatography mass spectrometry (GC–MS) and electrospray ionisation mass spectrometry (ESI–MS) were used to identify some of the organic products during the course of the 6 h irradiation (see Supporting Information File 1). These included *N*-hydroxylated desethyl rhodamine B, phthalic acid, and even

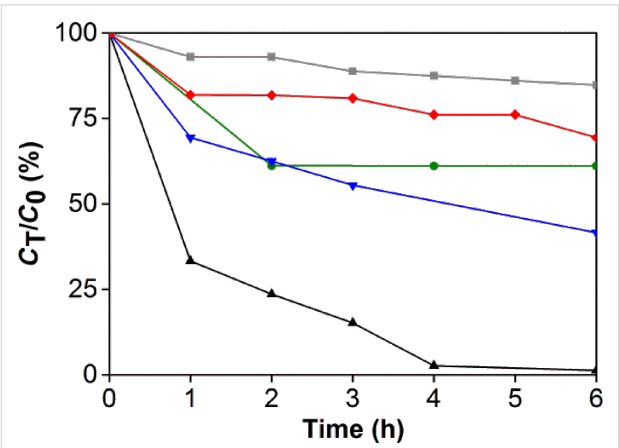

Figure 4: Comparison of RhB concentrations over time at 554 nm, after photocatalytic degradation with mesoporous cerium oxide under light (black) and in the dark with no equilibration (green), 7 nm CeO_2 (red), P25 TiO_2 (blue), and with no catalyst (grey).

ring-opened products [6]. The composition of the degradation products alludes to oxidative decomposition by reactive oxygen species, such as hydroxyl radicals.

Chemical scavengers were employed to investigate the mechanism of the photocatalytic processes and to identify the major contributors to the photocatalytic processes. The concentration of RhB, monitored at 554 nm, was used as the proxy to identify the active agent in the decomposition of RhB. Control experiments were performed in the absence of scavengers (black line, Figure 5a). The established scavengers used include sodium oxalate for h^+ (red), CrO_3 for e^- (green), isopropanol for $^\bullet OH$ (blue), and 1,4-benzoquinone for $^\bullet OOH/^\bullet O_2^-$ (grey, Figure 5a) [5]. The inhibition of photocatalytic activity is most pronounced in the presence of the hole scavenger, with impaired activity in the presence of both $^\bullet OH$ and $^\bullet OOH/^\bullet O_2^-$ scavengers. Interestingly, the electron scavenger does not significantly affect the photodegradation experiments. The participation of $^\bullet OH$ radicals was confirmed with the use of sodium terephthalate as a fluorescence probe [34]. Over the course of 6 h, the fluorescence intensity due to formation of 2-hydroxyterephthalate grew [35], with a blue shift possibly due to coordination to the mesoporous cerium oxide nanoparticles (Figure 5b). These results indicate that the photocatalytic mechanism can be summarized as depicted in Figure 5c, in which h^+, and downstream reactive oxygen species $^\bullet OH$ and $^\bullet OOH/^\bullet O_2^-$, are the active agents for the chemical destruction of RhB. Superoxide radicals from the reduction of O_2 or direct reduction by electrons from the cerium oxide appear to play secondary roles in the photocatalytic destruction of RhB.

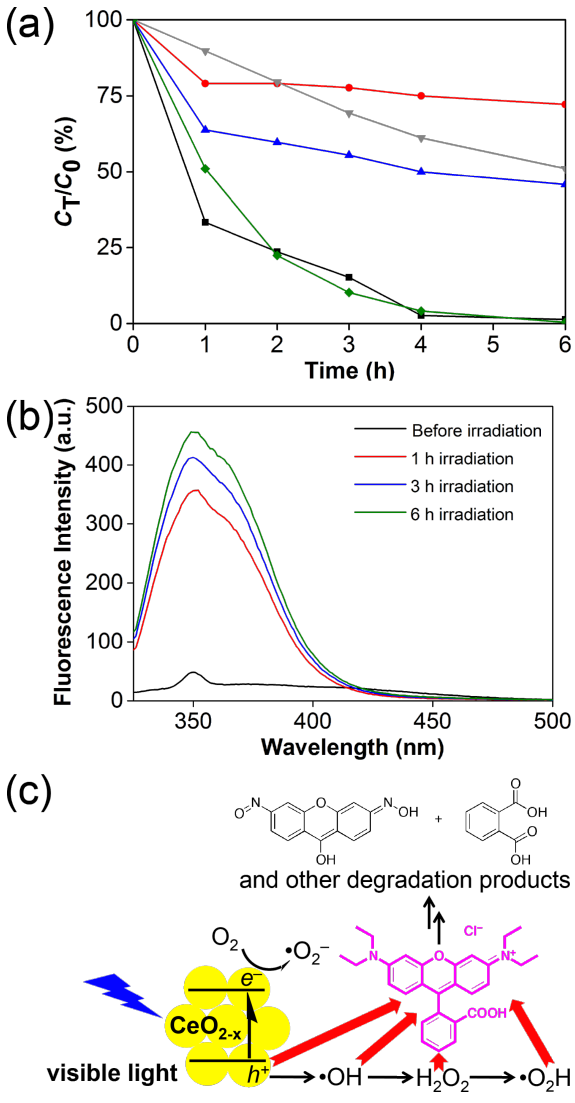

Figure 5: (a) Photocatalytic degradation of RhB over time at 554 nm, in the absence of scavengers (black), and the presence of h^+ (red), $^\bullet OH$ (blue), e^- (green), and $^\bullet OOH/^\bullet O_2^-$ scavengers (grey). (b) Growth of the fluorescence intensity of 2-hydroxyterephthlate as a probe for hydroxyl radicals. (c) Proposed pathway for photocatalytic RhB degradation.

Conclusion

In summary, we have presented a facile, solvothermal synthesis of new mesoporous cerium oxide nanospheres, with isopropanol and ethylene glycol as the solvents and reducing agents. No expensive surfactants and templates have been used in the preparation of the earth-abundant, relatively affordable, mixed valence cerium oxide. The cerium oxide has been characterized with a suite of structural, spectroscopic, and electron microscopy techniques, confirming the high surface area, mesoporous nature, and visible-light absorption properties of the material. The visible-light photocatalytic activity in the degradation of RhB surpasses that of the commercially available CeO_2 and P25 TiO_2 nanopowders. With a series of radical scavengers, the mechanism of the photocatalytic activity is proposed to involve a prominent role of $^\bullet OH$ radicals as the active species in RhB degradation. This new material is a promising candidate as a robust, earth-abundant, visible-light absorbing metal oxide scaffold to be used in DSPECs and other sustainable energy applications.

Supporting Information

The Supporting Information provides details about the synthesis of the nanospheres as well as additional experimental data.

Supporting Information File 1

Synthesis procedure, characterization, and dye degradation studies.
[http://www.beilstein-journals.org/bjnano/content/supplementary/2190-4286-5-60-S1.pdf]

Acknowledgements

H. S. Soo is supported by a NTU start-up grant (M4081012) and the Nanyang Assistant Professorship (M4081154). T. C. Sum is supported by a NTU start-up grant (M4080514), and the SPMS collaborative Research Award (M4080536). H. S. Soo and T. C. Sum also acknowledge the funding support from the Singapore-Berkeley Research Initiative for Sustainable Energy (SinBeRISE) CREATE Programme. This research programme/project is funded by the National Research Foundation (NRF), Prime Minister's Office, Singapore under its Campus for Research Excellence and Technological Enterprise (CREATE) programme. S.K. Muduli and H.S. Soo thank Nanyang Asst. Prof. Ling Xing Yi for the use of her solar simulator, and Nanyang Asst. Prof. Zhao Yanli for the use of his gas sorption analyzer. The authors also thank Dr. Wei Fengxia for her assistance with HRTEM measurements and Dr. Sarifuddin Gazi for his help with EPR experiments.

References

1. Andreozzi, R.; Caprio, V.; Insola, A.; Marotta, R. *Catal. Today* **1999,** *53,* 51–59. doi:10.1016/S0920-5861(99)00102-9
2. Hoffmann, M. R.; Martin, S. T.; Choi, W.; Bahnemann, D. W. *Chem. Rev.* **1995,** *95,* 69–96. doi:10.1021/cr00033a004
3. Chalasani, R.; Vasudevan, S. *ACS Nano* **2013,** *7,* 4093–4104. doi:10.1021/nn400287k
4. Kisch, H. *Angew. Chem., Int. Ed.* **2013,** *52,* 812–847. doi:10.1002/anie.201201200
5. Wang, W.; Yu, Y.; An, T.; Li, G.; Yip, H. Y.; Yu, J. C.; Wong, P. K. *Environ. Sci. Technol.* **2012,** *46,* 4599–4606. doi:10.1021/es2042977
6. Yu, K.; Yang, S.; He, H.; Sun, C.; Gu, C.; Ju, Y. *J. Phys. Chem. A* **2009,** *113,* 10024–10032. doi:10.1021/jp905173e
7. Chen, H.; Nanayakkara, C. E.; Grassian, V. H. *Chem. Rev.* **2012,** *112,* 5919–5948. doi:10.1021/cr3002092
8. Chen, X.; Mao, S. S. *Chem. Rev.* **2007,** *107,* 2891–2959. doi:10.1021/cr0500535
9. Hagfeldt, A.; Boschloo, G.; Sun, L.; Kloo, L.; Pettersson, H. *Chem. Rev.* **2010,** *110,* 6595–6663. doi:10.1021/cr900356p
10. Hodes, G.; Cahen, D. *Acc. Chem. Res.* **2012,** *45,* 705–713. doi:10.1021/ar200219h
11. Kubacka, A.; Fernández-García, M.; Colón, G. *Chem. Rev.* **2012,** *112,* 1555–1614. doi:10.1021/cr100454n
12. Pouretedal, H. R.; Kadkhodaie, A. *Chin. J. Catal.* **2010,** *31,* 1328–1334. doi:10.1016/S1872-2067(10)60121-0
13. Vuppala, V.; Motappa, M. G.; Venkata, S. S.; Sadashivaiah, P. H. *Eur. J. Chem.* **2012,** *3,* 191–195. doi:10.5155/eurjchem.3.2.191-195.564
14. Chueh, W. C.; Falter, C.; Abbott, M.; Scipio, D.; Furler, P.; Haile, S. M.; Steinfeld, A. *Science* **2010,** *330,* 1797–1801. doi:10.1126/science.1197834
15. Chueh, W. C.; Haile, S. M. *ChemSusChem* **2009,** *2,* 735–739. doi:10.1002/cssc.200900138
16. Scheffe, J. R.; Steinfeld, A. *Energy Fuels* **2012,** *26,* 1928–1936. doi:10.1021/ef201875v
17. Zhang, D.; Du, X.; Shi, L.; Gao, R. *Dalton Trans.* **2012,** *41,* 14455–14475. doi:10.1039/c2dt31759a
18. Muhich, C. L.; Evanko, B. W.; Weston, K. C.; Lichty, P.; Liang, X.; Martinek, J.; Musgrave, C. B.; Weimer, A. W. *Science* **2013,** *341,* 540–542. doi:10.1126/science.1239454
19. Ghoshal, T.; Fleming, P. G.; Holmes, J. D.; Morris, M. A. *J. Mater. Chem.* **2012,** *22,* 22949–22957. doi:10.1039/c2jm35073d
20. Stetsovych, V.; Pagliuca, F.; Dvořák, F.; Duchoň, T.; Vorokhta, M.; Aulická, M.; Lachnitt, J.; Schernich, S.; Matolinová, I.; Veltruská, K.; Skála, T.; Mazur, D.; Mysliveček, J.; Libuda, J.; Matolín, V. *J. Phys. Chem. Lett.* **2013,** *4,* 866–871. doi:10.1021/jz400187j
21. Wilkens, H.; Schuckmann, O.; Oelke, R.; Gevers, S.; Schaefer, A.; Bäumer, M.; Zoellner, M. H.; Schroeder, T.; Wollschläger, J. *Appl. Phys. Lett.* **2013,** *102,* 111602. doi:10.1063/1.4795867
22. Luo, H.; Song, W.; Hoertz, P. G.; Hanson, K.; Ghosh, R.; Rangan, S.; Brennaman, M. K.; Concepcion, J. J.; Binstead, R. A.; Bartynski, R. A.; Lopez, R.; Meyer, T. J. *Chem. Mater.* **2013,** *25,* 122–131. doi:10.1021/cm3027972
23. Song, W.; Chen, Z.; Glasson, C. R. K.; Hanson, K.; Luo, H.; Norris, M. R.; Ashford, D. L.; Concepcion, J. J.; Brennaman, M. K.; Meyer, T. J. *ChemPhysChem* **2012,** *13,* 2882–2890. doi:10.1002/cphc.201200100
24. Alibabaei, L.; Luo, H.; House, R. L.; Hoertz, P. G.; Lopez, R.; Meyer, T. J. *J. Mater. Chem. A* **2013,** *1,* 4133–4145. doi:10.1039/c2ta00935h
25. Ray, S. P.; Cox, D. E. *J. Solid State Chem.* **1975,** *15,* 333–343. doi:10.1016/0022-4596(75)90289-3
26. Kümmerle, E. A.; Heger, G. *J. Solid State Chem.* **1999,** *147,* 485–500. doi:10.1006/jssc.1999.8403
27. Ray, S. P.; Nowick, A. S.; Cox, D. E. *J. Solid State Chem.* **1975,** *15,* 344–351. doi:10.1016/0022-4596(75)90290-X
28. Suresh, R.; Ponnuswamy, V.; Mariappan, R. *Appl. Surf. Sci.* **2013,** *273,* 457–464. doi:10.1016/j.apsusc.2013.02.062
29. Patterson, A. L. *Phys. Rev.* **1939,** *56,* 978–982. doi:10.1103/PhysRev.56.978
30. Kotani, A.; Ogasawara, H. *J. Electron Spectrosc. Relat. Phenom.* **1992,** *60,* 257–299. doi:10.1016/0368-2048(92)80024-3
31. Trudeau, M. L.; Tschöpe, A.; Ying, J. Y. *Surf. Interface Anal.* **1995,** *23,* 219–226. doi:10.1002/sia.740230405
32. Corma, A.; Atienzar, P.; Garcia, H.; Chane-Ching, J.-Y. *Nat. Mater.* **2004,** *3,* 394–397. doi:10.1038/nmat1129
33. Liang, S.; Wen, L.; Lin, S.; Bi, J.; Feng, P.; Fu, X.; Wu, L. *Angew. Chem., Int. Ed.* **2014,** *53,* 2951–2955. doi:10.1002/anie.201311280
34. Gomes, A.; Fernandes, E.; Lima, J. L. F. C. *J. Biochem. Biophys. Methods* **2005,** *65,* 45–80. doi:10.1016/j.jbbm.2005.10.003
35. Ishibashi, K.; Fujishima, A.; Watanabe, T.; Hashimoto, K. *J. Photochem. Photobiol., A: Chem.* **2000,** *134,* 139–142. doi:10.1016/S1010-6030(00)00264-1

License and Terms

This is an Open Access article under the terms of the Creative Commons Attribution License (http://creativecommons.org/licenses/by/2.0), which permits unrestricted use, distribution, and reproduction in any medium, provided the original work is properly cited.

The license is subject to the *Beilstein Journal of Nanotechnology* terms and conditions: (http://www.beilstein-journals.org/bjnano)

The definitive version of this article is the electronic one which can be found at: doi:10.3762/bjnano.5.60

Beilstein Journal of Nanotechnology

Artificial sunlight and ultraviolet light induced photo-epoxidation of propylene over V-Ti/MCM-41 photocatalyst

Van-Huy Nguyen[1], Shawn D. Lin[*1,§], Jeffrey Chi-Sheng Wu[*2,¶] and Hsunling Bai[3]

Full Research Paper

Open Access

Address:
[1]Department of Chemical Engineering, National Taiwan University of Science and Technology, Taipei 106, Taiwan, [2]Department of Chemical Engineering, National Taiwan University, Taipei 10617, Taiwan and [3]Institute of Environmental Engineering, National Chiao Tung University, Hsin Chu 300, Taiwan

Email:
Shawn D. Lin[*] - sdlin@mail.ntust.edu.tw; Jeffrey Chi-Sheng Wu[*] - cswu@ntu.edu.tw

* Corresponding author
§ Phone: +886-2-27376984, Fax: +886-2-27376644
¶ Phone: +886-2-23631994, Fax: +886-2-23623040

Keywords:
artificial sunlight; light irradiation effects; photo-epoxidation; ultraviolet (UV) light; V-Ti/MCM-41 photocatalyst

Beilstein J. Nanotechnol. **2014,** *5,* 566–576.
doi:10.3762/bjnano.5.67

Received: 20 December 2013
Accepted: 10 April 2014
Published: 05 May 2014

This article is part of the Thematic Series "Photocatalysis".

Guest Editor: R. Xu

© 2014 Nguyen et al; licensee Beilstein-Institut.
License and terms: see end of document.

Abstract

The light irradiation parameters, including the wavelength spectrum and intensity of light source, can significantly influence a photocatalytic reaction. This study examines the propylene photo-epoxidation over V-Ti/MCM-41 photocatalyst by using artificial sunlight (Xe lamp with/without an Air Mass 1.5 Global Filter at 1.6/18.5 mW·cm^{-2}) and ultraviolet light (Mercury Arc lamp with different filters in the range of 0.1–0.8 mW·cm^{-2}). This is the first report of using artificial sunlight to drive the photo-epoxidation of propylene. Over V-Ti/MCM-41 photocatalyst, the propylene oxide (PO) formation rate is 193.0 and 112.1 μmol·g_{cat}^{-1}·h^{-1} with a PO selectivity of 35.0 and 53.7% under UV light and artificial sunlight, respectively. A normalized light utilization (NLU) index is defined and found to correlate well with the rate of both PO formation and C_3H_6 consumption in log–log scale. The light utilization with a mercury arc lamp is better than with a xenon lamp. The selectivity to PO remains practically unchanged with respect to NLU, suggesting that the photo-epoxidation occurs through the same mechanism under the conditions tested in this study.

Introduction

It is agreed that light, especially its wavelength spectrum and intensity, is a crucial factor for efficient photocatalysis. A photocatalytic reaction occurs only when the illumination with light enables the generation of highly reactive species such as hydroxyl radicals (OH•) and oxy radicals (O•) [1]. The light intensity in photocatalysis has attracted considerable attention.

The positive effect of increasing the light intensity on photocatalytic reactions is a common phenomenon, which has been observed in, e.g., the photo-degradation of gaseous formaldehyde [2], dye [3-5] and polychlorinated dibenzo-*p*-dioxins [6], and the disinfection of *Escherichia coli* [7-9]. How the light energy can be effectively utilized in a heterogeneous photocatalysis process is under debate, and both the intensity and the exposure time to light irradiation need to be considered [4,10]. In the photo-decomposition of organic species and the inactivation of bacteria under ultraviolet sources (UV-A and UV-C), low-intensity light with long exposure times resulted in a better light-utilization efficiency than light of high intensity with short exposure times [10]. In addition, the wavelength of the irradiation is another important factor that can affect the efficiency of photocatalysis. It is believed that the shorter wavelength of irradiation can promote the electron–hole generation and consequently enhance the efficiency of the catalyst. This has been observed in the CO_2 photo-reduction over Ag/TiO_2 or TiO_2 [11], the photo-degradation of 4-chlorophenol over TiO_2 [12] and the photo-decomposition of organic contaminants over $CaBi_2O_4$ [13]. No previous study discusses that the suitable wavelength needs to match the absorbance range of the catalyst and also needs to be energetic enough to generate active species.

Propylene oxide (PO) is an intermediate chemical widely used in the chemical industry, and its market size is predicted to have an average annual growth of 5% [14]. However, the current commercial processes to produce PO are not environmentally friendly because of the significant amounts of byproducts [15,16]. Much effort has been devoted to develop green PO production processes and photo-epoxidation utilizing light energy and O_2 oxidant under mild conditions attracts much attention. Differently designed photocatalysts were examined [17-24], and the reaction conditions such as reaction temperature [18], light irradiation [25,26] and oxygen/propylene ratio [23,27] were also tested. Yoshida and co-workers reported the first systematic investigation of the photo-epoxidation of propylene over more than 50 silica-supported metal oxides, in which TiO_x/SiO_2 was the most effective photocatalyst [20]. Amano et al. reported that Rb-ion-modified V_2O_5/SiO_2 was their best photo-epoxidation catalyst under UV-C light [24]. In our previous study, V-Ti/MCM-41 photocatalyst showed good PO yield under UV light [17]. However, the effects of light irradiation on the photo-epoxidation of propylene have not been systematically examined. Yamashita et al. carried out photo-epoxidation experiments by using a high-pressure mercury lamp equipped with 3 UV cut-filters, but they did not discuss the effect of light wavelengths [28]. Xenon lamps are the most commonly used light sources in these studies [24,29]. No previous work, to the best of our knowledge, attempts the use of artificial sunlight to drive the photocatalytic epoxidation [30].

In this study, we compared the photo-epoxidation over V-Ti/MCM-41 photocatalyst with different wavelengths (365, 320–500 and 250–400 nm) and different light intensities in the range of 0.1–0.8 $mW \cdot cm^{-2}$. In addition, artificial sunlight from a solar simulator with/without an Air Mass 1.5 Global (AM1.5G) filter was also used to drive the photo-epoxidation reaction. The performances of photo-epoxidation under different light sources are compared and discussed.

Results and Discussion

Photocatalyst characterization

Figure 1 compares the absorbance spectrum of the prepared photocatalyst and the light emission spectrum from a Hg arc lamp, and a Xe lamp without filter [22] and with AM1.5G filter [31], respectively. The emission spectrum from the Hg arc lamp is in the range of 260–650 nm while those spectra from Xe lamp without filter and with AM1.5G filter are 200–2400 nm and 310–2400 nm (not shown in the range of Figure 1), respectively. The UV–vis absorbance confirms the absorption band of 200–380 nm. The strong absorbance at about 220 nm is attributed to the charge transfer band of tetra-coordinated titanium in the framework while the weaker band at 340 nm is attributed to the charge transfer band of tetra-coordinated vanadium in the V^{5+} state [32]. The overlap of catalyst absorbance and light emission spectra, in the wavelength range from 260 to 380 nm, is the main contribution to the photo-reaction activity.

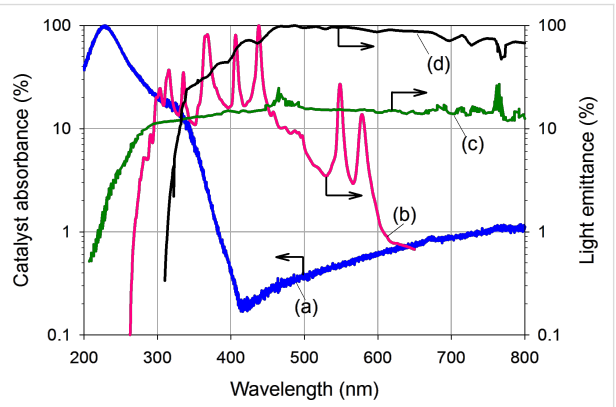

Figure 1: The spectrum of: (a) UV–vis absorption of V-Ti/MCM-41, and emission of (b) 200 W mercury arc lamp, (c) 300 W Xe lamp (extracted from [22]) and (d) AM1.5G filter [31].

Figure 2 shows the low-angle XRD pattern of V-Ti/MCM-41 photocatalyst. The XRD pattern indicates a mesoporous hexagonal lattice with a clear feature of (100). The (110) and (200) peaks are not well-separated, maybe due to the high calcination temperature of 823 K [33]. The HRTEM image of V-Ti/MCM-

41 in Figure 3 reveals a uniform hexagonal structure, which is a distinctive feature of MCM-41. The pore diameters of catalyst estimated from TEM was approximately 3 nm.

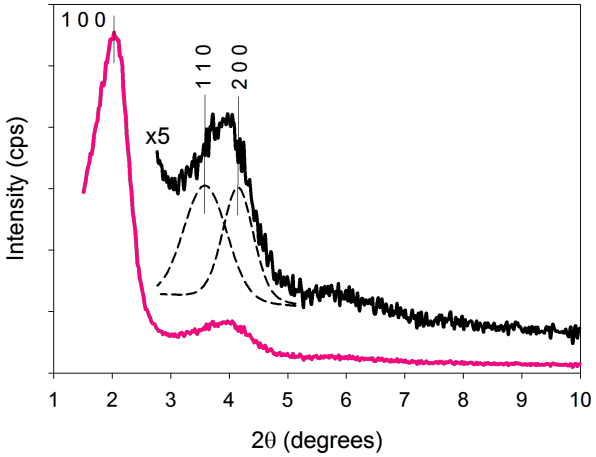

Figure 2: The low-angle XRD pattern of V-Ti/MCM-41.

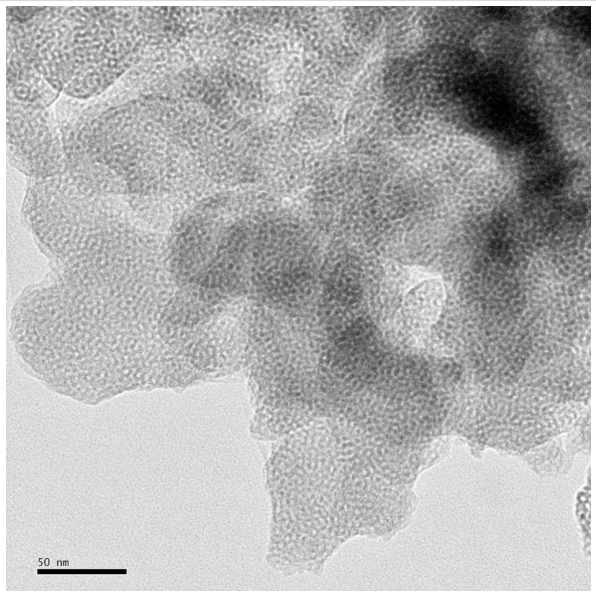

Figure 3: The HRTEM images of V-Ti/MCM-41 photocatalyst.

We previously proposed that the titanium in V-Ti/MCM-41 should be Ti^{4+} with a tetrahedral coordination [17]. The K-edge XANES of vanadium (Figure 4) suggests its oxidation state to be V^{5+}. A possible local structure of tetra-coordinated V- and Ti-oxides in V-Ti/MCM-41 is proposed in the inset of Figure 4. Both Ti^{4+} and V^{5+} are anchored by three oxygen atoms (each linked to silicon) and with an exposed (Ti^{4+}–OH) or an exposed (V^{5+}–O^{2-}). We expect that the design of V-Ti/MCM-41 can lead not only to the direct excitation of (Ti–O) moieties by UV irradiation but also to the indirect excitation through a charge transition from (V^{4+}–O_L^-)* states as proposed in [34,35], which brings up a high photocatalytic activity [34]. Furthermore, Amano et al. reported that the lattice oxygen in the excited triplet state (V^{4+}–O_L^-)* is considered to exhibit electrophilic character, which preferably attacks the double bonds in propylene [35]. Hence, the V-Ti/MCM-41 is expected to perform a selective photocatalytic epoxidation of propylene.

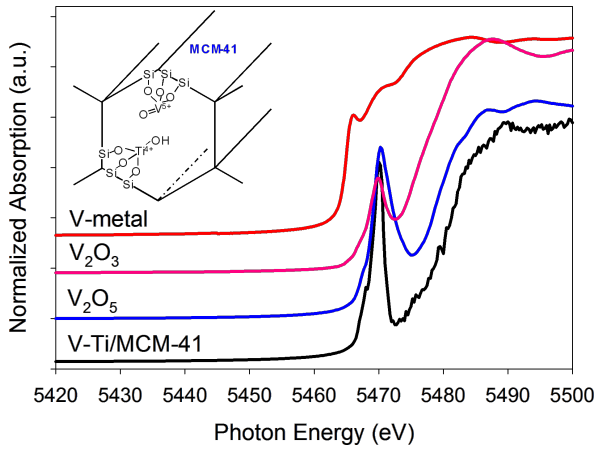

Figure 4: Summary of the V K-edge characterization of V-Ti/MCM-41 with references by XANES and proposed structures of V-Ti/MCM-41 (inset).

Photocatalytic epoxidation of propylene

There is no activity observed if the experiment is conducted in the absence of either the photocatalyst or light irradiation. Evidently, the propylene epoxidation over V-Ti/MCM-41 is mainly photo-catalysed. Table 1 summarizes the consumption rate of C_3H_6, the formation rate of PO and the product selectivity under different irradiation conditions. These values are averages obtained on stream within 3–6 h of photoreaction. The major products included propylene oxide (PO), propionaldehyde (PA) and acetaldehyde (AA) while the minor products were acetone (AC) and ethanol (EtOH).

Artificial sunlight irradiation

Recently, sun-light-driven photocatalysis has received much attention. In this section, we examined the photo-epoxidation of propylene over V-Ti/MCM-41 by utilizing UV-visible light (without an AM1.5G filter) and artificial sunlight (with an AM1.5G filter). With UV–visible light, the C_3H_6 consumption rate and the PO formation rate with time on stream are shown in Figure 5a. Within a 6 h test, its performance decreased monotonously with time, but the selectivity of products on stream did not change as shown in Figure 5b, which indicates PO as the dominant product with a selectivity of 59.9%. This PO selectivity is significantly higher that of experiments using only UV light.

Table 1: Overview of the photocatalytic epoxidation of propylene.[a]

entry	light sources			C_3H_6 consumption rate ($\mu mol \cdot g^{-1} \cdot h^{-1}$)	PO formation rate ($\mu mol \cdot g^{-1} \cdot h^{-1}$)	selectivity (%)				
	lamp	filter	intensity ($mW \cdot cm^{-2}$)			AA	EtOH	PO	PA	AC
1	200 W Mercury Arc	365 nm	0.1	89.2 ± 2.2	25.8 ± 1.1	38.9	2.5	29.0	20.5	9.1
2			0.2	145.4 ± 1.8	42.9 ± 0.2	39.5	3.5	29.5	19.9	7.6
3		320–500 nm	0.1	136.3 ± 1.8	48.4 ± 1.1	30.3	ND	35.5	27.0	7.2
4			0.2	269.3 ± 11.6	114.2 ± 7.8	28.9	ND	42.3	23.7	5.1
5			0.4	276.7 ± 10.5	80.6 ± 3.2	42.7	4.5	29.1	17.5	6.8
6			0.6	285.3 ± 3.3	92.9 ± 1.6	38.9	4.4	32.6	16.9	7.2
7			0.8	340.9 ± 2.7	108.4 ± 1.2	38.8	4.7	31.8	17.4	7.3
8		250–400 nm	0.2	329.9 ± 9.3	100.5 ± 2.0	35.4	2.3	30.5	23.6	8.2
9			0.4	424.4 ± 21.0	140.6 ± 6.2	32.9	2.4	33.2	24.1	7.4
10			0.8	551.9 ± 2.4	193.0 ± 1.2	30.7	2.3	35.0	25.9	6.1
11	300 W Xe	AM1.5G	1.6	208.4 ± 14.3	112.1 ± 8.9	13.0	ND	53.7	23.1	10.3
12		—	18.5	287.3 ± 14.4	172.1 ± 8.9	15.9	ND	59.9	21.0	3.2

[a]Reaction conditions: 0.01–0.02 g photocatalyst; feed gas $C_3H_6/O_2/N_2$ = 1:1:16 in vol % at GHSV = 6000 h^{-1} and T = 312–323 K. The data were obtained on stream within a cycle (3–6 h in reaction). AA: acetaldehyde, EtOH: ethanol, PO: propylene oxide, PA: propionaldehyde, AC: acetone, and ND: not detected.

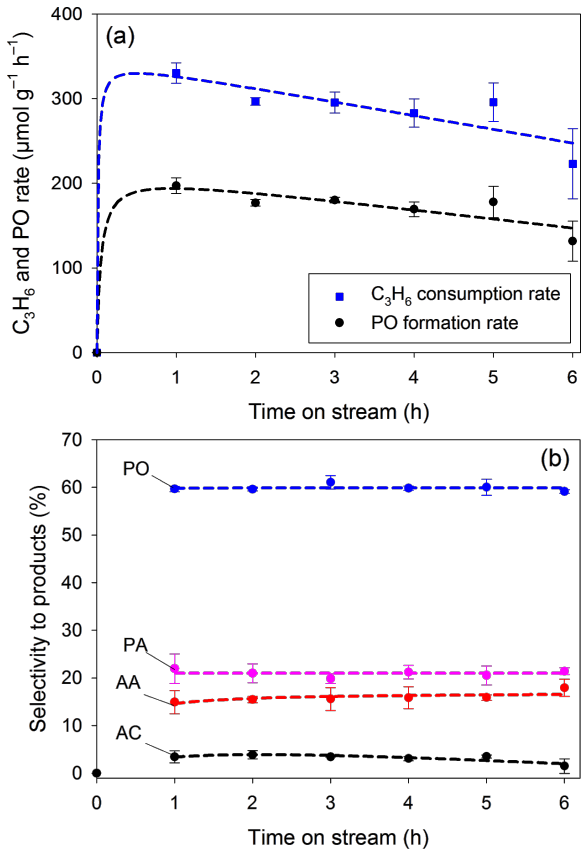

Figure 5: Time course of the photo-epoxidation of propylene with molecular oxygen under UV–visible light irradiation (without an AM1.5G filter; 18.5 $mW \cdot cm^{-2}$): (a) C_3H_6 consumption rate and PO formation rate, (b) Selectivity to products. Lines are presented for guiding and are not based on a kinetic model.

Figure 6 shows the time-dependent behavior of the photocatalytic reaction when using artificial sunlight. With respect to time on stream, the PO formation rate increased to a peak value of 151 $\mu mol \cdot g_{cat}^{-1} \cdot h^{-1}$ after 1 h and then it decayed to 81 $\mu mol \cdot g_{cat}^{-1} \cdot h^{-1}$ after 24 h reaction time (Figure 6a). The product distribution was not significantly changed by the inclusion of the AM1.5 filter. The main product PO still maintained a selectivity of approximately 60% (Figure 6b). To the best of our knowledge, this is the first report of using artificial sunlight to drive the photocatalytic epoxidation of propylene.

Both of UV–visible light and artificial sunlight show a similar and stable product distribution (Figure 5b and Figure 6b). The use of AM1.5G filter decreased the photo-activity but similar trends in PO formation rate and C_3H_6 consumption rate with time on stream are also found in Figure 5a and Figure 6a. The similar product distribution implies that the reaction mechanism was not changed by the presence of the AM1.5G filter. The filter reduced the light intensity significantly from 18.5 to 1.6 $mW \cdot cm^{-2}$. Therefore, we believe that the decreased photo-activity when using the AM1.5 G filter is mainly attributed to the decreased light intensity.

UV-light irradiation

Among the UV-irradiation experiments shown in Table 1, entry 4 shows a good selectivity to PO (42.3%) while entry 10 shows excellent performance of both C_3H_6 consumption rate and PO formation rate, 551.9 and 193.0 $\mu mol \cdot g_{cat}^{-1} \cdot h^{-1}$, respectively. Figure 7 shows that the illumination of shorter wavelengths (250–400 nm) resulted in a better performance (higher C_3H_6

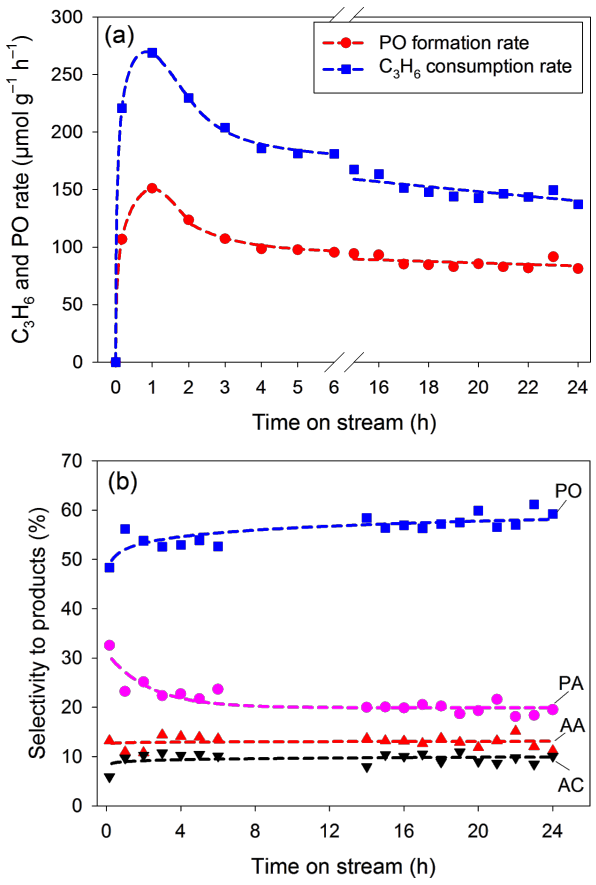

Figure 6: Time course of the photo-epoxidation of propylene with molecular oxygen under artificial sunlight (with an AM1.5G filter; 1.6 mW·cm^{-2}): (a) C_3H_6 consumption rate and PO formation rate. (b) Selectivity to products. Lines are presented for guiding and are not based on a kinetic model.

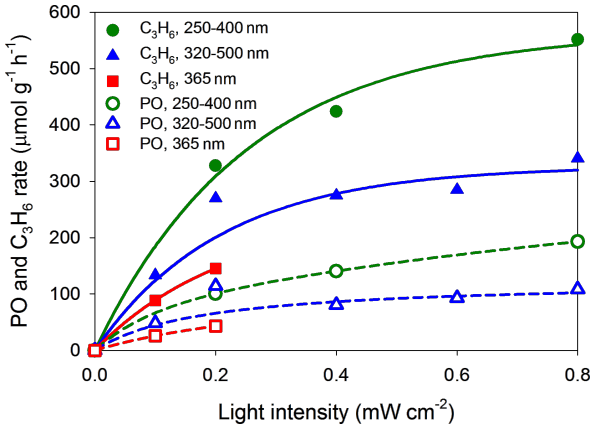

Figure 7: The correlation between UV-light intensity (200 W mercury arc lamp) and C_3H_6 consumption rate and PO formation rate. Lines are presented for guiding and are not based on a kinetic model.

consumption rate and higher PO formation rate) than that with 365 nm or 320–500 nm illumination. In response to intensity, both C_3H_6 consumption rate and PO formation rate show an initial linear increase and then the increase gradually levels off at strong intensities. The nonlinear behavior can be explained by either that the effect of light scattering becomes significant or that the reactions strongly compete with processes involving electron–hole pair recombination and with those involving the participation of photo-generated holes in surface photo-reactions at high-intensity illumination [6,36,37]. On the other hand, the initial linear behavior suggests that the recombination of electron–hole pairs is negligible at low intensity illumination.

Figure 8 shows the time-dependent behavior of the photocatalytic reaction when using different filters with UV light. The PO selectivity was stable even under UV-C range of 250–400 nm. On the whole, an increase in light intensity promoted the activity and resulted in increased C_3H_6 consumption rate.

Comparison of artificial sunlight and UV light irradiation

To understand how photo-epoxidation efficiency changed with wavelength, we compared the effect of photon absorption based on the spectra of different lamps and/or filters. Since not all the light delivered to the photocatalyst can be absorbed, we defined the normalized light utilization (NLU) of V-Ti/MCM-41 photocatalyst as the fraction of light that can possibly activate the photoreaction by Equation 1.

$$\text{NLU} = \text{intensity of light emitted} \times \text{normalized absorption capability of photocatalyst} \quad (1)$$

The total absorption capability of V-Ti/MCM-41 photocatalyst was calculated by integrating the normalized UV–vis spectrum from the lower cut-off wavelength of irradiation light (260 nm for UV, 200 nm for visible light and 310 nm for artificial light) to the cut-off absorbance of the catalyst (380 nm). The ratio of the integrated absorbance over the filtered range of the light source to the total absorption capacity is defined as the normalized absorption capability. Table 2 shows the calculated NLU of V-Ti/MCM-41 photocatalyst for visible light, artificial sunlight and UV light at three filtered wavelength range (365 nm, 320–500 nm and 250–400 nm).

Figure 9 shows that both C_3H_6 consumption rate and PO formation rate increased with the calculated NLU, regardless of the filtered wavelength range. For the UV light source (Figure 9a), it suggests that the photon flux, i.e., the light intensity, is equally efficient for the photo-epoxidation of propylene when the wavelengths of photon were filtered to 365, 350–500, or 250–400 nm range. This also implies that the energy in these

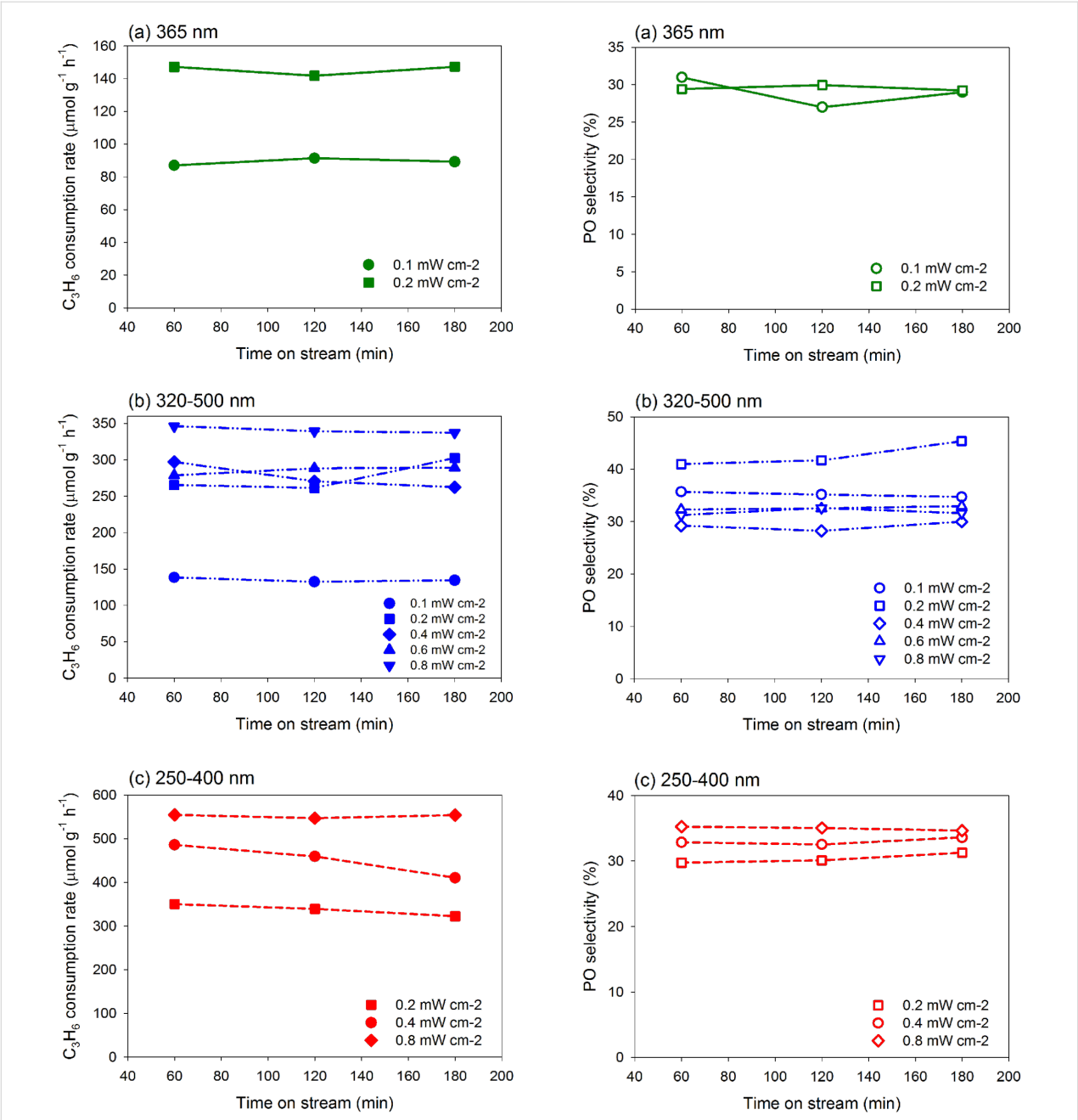

Figure 8: Time course of the photo-epoxidation of propylene with molecular oxygen under UV light for C_3H_6 consumption rate and PO selectivity under different filters conditions: (a) 365 nm, (b) 320–500 nm and 250–400 nm.

three filtered ranges is sufficient to activate oxygen and/or propylene. The correlation between the rate of PO formation or of C_3H_6 consumption versus NLU in the log–log scale can be expressed by Equation 2 and Equation 3 as the rate expression for the UV-irradiated photo-epoxidation. The ratio of these two rate expressions indicates a constant PO selectivity of 40%.

$$\text{PO formation rate} = 240 \times \text{NLU}^{0.36} \quad (2)$$

$$C_3H_6\text{consumption rate} = 600 \times \text{NLU}^{0.36} \quad (3)$$

The rate expressions of both PO formation and C_3H_6 consumption with a Xe lamp were estimated by the data with and without AM1.5G filter as shown in Figure 9b, and the results are shown in Equation 4 and Equation 5. These rates are lower but the PO selectivity is higher than that of using mercury arc lamp.

Table 2: A quantitative evaluations of normalized light utilization by V-Ti/MCM-41 photocatalyst.

entry	light sources lamp	filter	intensity of light emitted ($mW \cdot cm^{-2}$)	normalized active absorbed light by catalyst[a] (a.u.)	normalized light utilization[b] ($mW \cdot cm^{-2}$)
1	200 W mercury arc	365 nm	0.1	0.03	0.003
2			0.2		0.006
3		320–500 nm	0.1	0.21	0.021
4			0.2		0.042
5			0.4		0.084
6			0.6		0.126
7			0.8		0.168
8		250–400 nm	0.2	1.00	0.200
9			0.4		0.400
10			0.8		0.800
11	300 W Xe	AM1.5G	1.6	0.29	0.464
12		—	18.5	1.00	18.500

[a]The normalized absorption capability is the ratio between area of irradiation at different wavelength and the area of full UV–vis absorbance spectrum.
[b]Normalized light utilization was calculated directly by Equation 1.

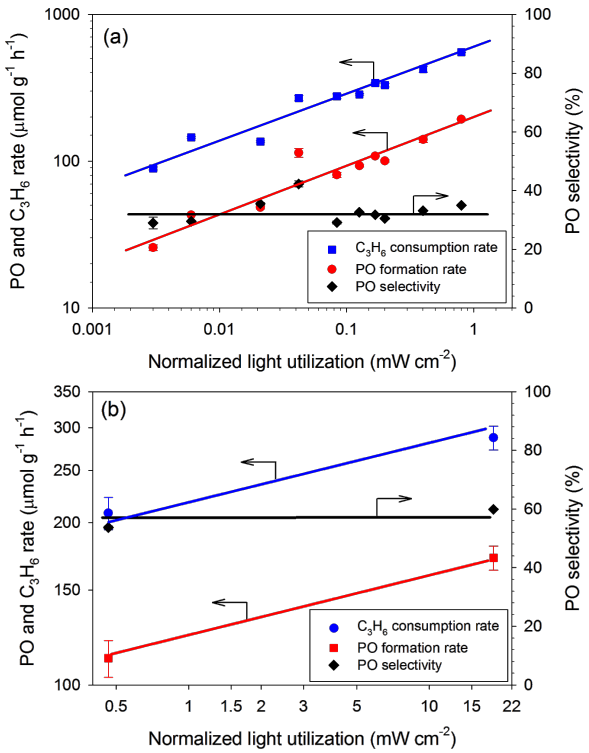

Figure 9: The PO formation rate, C_3H_6 consumption rate and PO selectivity over V-Ti/MCM-41 versus the normalized light utilization by V-Ti/MCM-41 photocatalyst over (a) a mercury arc lamp and (b) a xenon lamp (see Table 2). Lines are presented for guiding and are not based on a kinetic model.

$$\text{PO formation rate} = 124 \times \text{NLU}^{0.11} \quad (4)$$

$$C_3H_6\text{consumption rate} = 219 \times \text{NLU}^{0.11} \quad (5)$$

The different dependency on NLU in these rate equations of PO formation and C_3H_6 consumption between UV and UV–visible/artificial sunlight may be due to the difference in light wavelength and intensity. Both UV and UV-visible/artificial sunlight resulted in a nearly constant PO selectivity, regardless of the filter or the light intensity. Based on this fact, we believe that the photocatalytic epoxidation of propylene over V-Ti/MCM-41 photocatalyst occurred through the same mechanism regardless of the absorbed wavelengths within the range of study.

We have compared the C_3H_6 consumption rate of V-Ti/MCM-41 when using UV (0.8 $mW \cdot cm^{-2}$, 250–400 nm), artificial sunlight (1.6 $mW \cdot cm^{-2}$ when with AM1.5G filter) and UV–visible light without AM1.5G filter (18.5 $mW \cdot cm^{-2}$) from entry 10, 11 and 12, respectively. Although the light intensity differed strongly when comparing both UV–visible light and artificial sunlight, the C_3H_6 consumption rate (551.9, 287.3 and 208.4 μmol g_{cat}^{-1} h^{-1}, respectively) did not significantly change. A possible explanation is that the emission wavelength of UV light fits better with the spectral absorption of V-Ti/MCM-41 than the other irradiation types (Figure 1). Wendl et al. reported a similar observation when they compared the effects of various lamps [38]. The non-fitting wavelengths of the visible light source may provide an additional heating to the catalyst.

The decay in the photo-activity with time on stream may be due to fouling caused by strongly adsorbed organic species. Comparing to UV-irradiation conditions, the selectivity to AA was lower when using artificial sunlight (Table 1). Takeuchi et al. reported that products with a carbonyl group such as AA can easily adsorb on active Ti^{4+} sites [39]. Therefore, the low selectivity to AA might be due to its accumulation on catalyst surface, which can consequently cause the higher standard error on the C_3H_6 consumption rate observed with both UV–visible light and artificial sunlight. The condensation of AA molecules may lead to larger and heavier species such as hexa-2,4-dienal and 3-methylpentanedial [40]. The TGA weight loss curves of the spent and the fresh V-Ti/MCM-41 are compared in Figure 10. The weight loss below 400 K is attributed to the removal of adsorbed water while that above 400 K can be attributed to burn-off of the remaining organic species [41]. The different decay rates observed with UV and UV–visible light/artificial sunlight may come from the different fouling level of strongly adsorbed organic species.

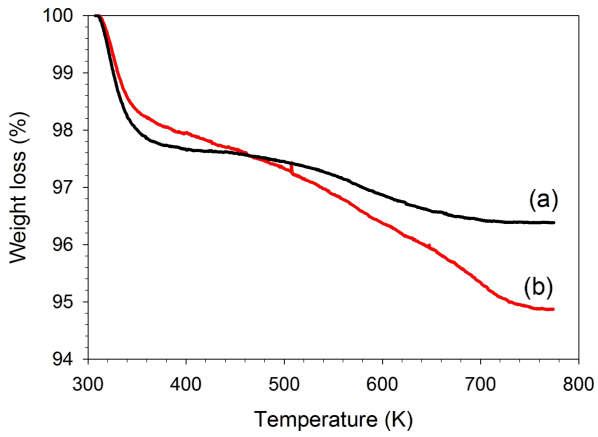

Figure 10: The TGA weight loss curves V-Ti/MCM-41 photocatalyst using O_2 as the sweep gas: (a) fresh catalyst and (b) catalyst deactivated by the photo-epoxidation of propylene.

Current status of photo-epoxidation of propylene

Table 3 compares the propylene photo-epoxidation performance of this study and those reported in the literature. Entries 1–4 show that V_2O_5/SiO_2 exhibits visible-light-driven photocatalytic activities when using a solar simulator; Rb ion-modified V_2O_5/SiO_2 performs well with a high C_3H_6 consumption rate of 563.5 $\mu mol \cdot g_{cat}^{-1} \cdot h^{-1}$. Rubidium ions can effectively modify isolated VO_4 via a mono-oxo terminal oxygen, which is proposed to improve the PO formation rate [24]. The V-Ti/MCM-41 used in this study had only half of that C_3H_6 consumption rate (entry 5) under light from solar simulator, but both V-Ti/MCM-41 and Rb-V_2O_5/SiO_2 had nearly the same PO formation rate. Although the two experiments were carried out under different conditions, both demonstrate good performance of propylene photo-epoxidation. Artificial sunlight has been successfully used and it showed interesting photo-activity (112.1 $\mu mol \cdot g_{cat}^{-1} \cdot h^{-1}$ of PO formation rate). In this contribution, 193.0 $\mu mol \cdot g_{cat}^{-1}\ h^{-1}$ (with 0.8 $mW \cdot cm^{-2}$ UV in the range of 250–400 nm) is the highest PO formation rate achieved among a variety of conditions.

Conclusion

Artificial sunlight has been successfully used to drive the photo-epoxidation of propylene for the first time, with a PO formation rate of 112.1 $\mu mol \cdot g_{cat}^{-1} \cdot h^{-1}$ and a PO selectivity of 53.7% over V-Ti/MCM-41. Without AM1.5G filter, UV–visible light with higher intensity results in higher PO formation rate with a similar PO selectivity but a faster deactivation rate. UV light only with different filter (365, 320–500 and 250–400 nm, respectively) and intensity over the ranges of 0.1–0.8 $mW \cdot cm^{-2}$ are also examined. Among a variety of conditions,

Table 3: Comparison of artificial sunlight and other light sources.

entry	photocatalyst	lamp	reactants	C_3H_6 consumption rate ($\mu mol \cdot g^{-1} \cdot h^{-1}$)	PO formation rate ($\mu mol \cdot g^{-1} \cdot h^{-1}$)	PO selectivity (%)	ref.
1	0.18 wt % V_2O_5/SiO_2	300 W Xe	C_3H_6/O_2/He = 2:1:7 (GHSV 8000 h^{-1})	141.9	61.0	43.0	[29]
2	0.1 mol % V_2O_5/SiO_2			229.7	85.0	37.0	[21]
3	0.1 mol % V_2O_5/HMS			208.1	77.0	37.0	
4	Rb ion-modified 0.5wt% V_2O_5/SiO_2			563.5	173.0	30.7	[24]
5[a]	V-Ti/MCM-41	300 W Xe with AM1.5G	$C_3H_6/O_2/N_2$ = 1:1:16 (GHSV 6000 h^{-1})	208.4	112.1	53.7	this study
6[b]		300 W Xe		287.3	172.1	59.9	
7[c]		200 W Hg arc		551.9	193.0	35.0	

[a]300 W Xe lamp equipped with AM1.5G filter (artificial sunlight): 1.6 $mW \cdot cm^{-2}$; [b]300 W Xe lamp: 18.5 $mW \cdot cm^{-2}$; [c]200 W Hg arc lamp (250–400 nm): 0.8 $mW \cdot cm^{-2}$. The data is the mean value obtained on stream in 6 h. V-Ti/MCM-41 photocatalyst: V/Ti/Si = 0.05:0.53:46.29, based on ICP–AES.

193.0 μmol·g_{cat}^{-1}·h^{-1} was observed as the highest PO formation rate for propylene photo-epoxidation with a minimal deactivation rate. Data analysis suggests that the rate of PO formation and of C_3H_6 consumption under either UV light or UV–visible light/artificial sunlight can be correlated with NLU in log–log scale. This indicates a similar reaction mechanism under UV light and under UV–visible light/artificial sunlight, which is also supported by the same products observed under the different light source used in this study.

Experimental

Preparation and characterizations of photocatalyst

The procedure of V-Ti/MCM-41 preparation was described in details previously [17]. Typically, 21.2 g of sodium metasilicate monohydrate was dissolved in 100 mL deionized (DI) water and then combined with an appropriate amount of titanium oxysulfate hydrate and vanadyl sulfate hydrate (dissolved in 20 mL of 2 M H_2SO_4) to form a uniform gel. Next, 7.28 g of cetyltrimethylammonium bromide (CTAB) was dissolved in 25 mL of DI water and added slowly into the mixture. After stirring for 3 h, the gel mixture was transferred to an autoclave and heated to 418 K for 36 h. The resulting solid was washed with DI water after cooling to the room temperature, then dried at 383 K for 8 h, and calcined at 823 K for 10 h.

A powder X-ray diffractometer (XRD, Xray-M03XHF, Ultima IV) was used to verify the crystalline structure of the photocatalyst. Diffraction peaks were assigned by comparison to known crystalline phases. The light absorption of the photocatalyst was characterized by ultraviolet–visible light spectroscopy (Varian Cary-100). The X-ray absorption near edge spectroscopy (XANES) of the vanadium K-edge was carried out with synchrotron radiation at the beam line 16A, National Synchrotron Radiation Research Center, Taiwan. The standard metal foil and V oxides (V_2O_5 and V_2O_3) powders were used as references. High resolution transmission electron microscope (HRTEM) was performed with a JEOL JEM-2100 instrument operating at 200 kV. Thermal gravimetric analysis (TGA, PYRIS Diamond TG-DTA, high temperature 115V) was carried out in the range of 300–773 K. About 30 mg samples were placed in an alumina sample holder and heated under air (20 mL·min^{-1}) with a heating rate of 3 K·min^{-1}. Due to the small amount of catalyst used for the reaction, the spent is a mixture of all the photocatalysts after reaction.

Photocatalytic epoxidation of propylene

The apparatus for carrying out the photocatalytic epoxidation of propylene with a reactant gas mixture of $C_3H_6/O_2/N_2$ = 1:1:16 at GHSV = 6000 h^{-1} was mentioned in our previous study [17]. Around 0.01–0.02 g of photocatalyst was packed in a photoreactor (0.55 cm^3 in volume) with a quartz window for light transmission. A hot-plate was used to maintain the temperature at 323 K for the UV-irradiated reaction while no heating was provided with artificial sunlight when the temperature of the photocatalyst bed was typically sustained at 312–315 K. We demonstrated previously that the photocatalytic propylene epoxidation was not sensitive to temperature in the range of 312–323 K [20]. The light sources were set up as follows: (1) **UV light:** 200 W mercury arc lamp (Exfo S1500) with three different interference filters, i.e., 365, 320–500, and 250–400 nm. The light intensity, adjustable in the range of 0.1–0.8 mW cm^{-2}, was measured at the quartz window of the reactor by using a GOLDILUX radiometer/photometer (UV-A Probe/UV-C Probe). (2) **UV–visible light:** 300 W xenon lamp (Newport, USA) was directly used; the influx in the range of 200–380 nm was 18.5 mW·cm^{-2}. (3) **Artificial sunlight:** A 300 W xenon lamp (Newport, USA) was used with an AM1.5G filter to simulate the sunlight that has the same power and spectral distribution of the sun at 48.5° zenith angle. The influx in the range of 310–380 nm with the AM1.5G filter was 1.6 mW·cm^{-2}.

Product analysis

The effluent stream was analyzed with a gas chromatograph (GC, Young Lin, YL6100) via an on-line 6-port sampling valve (Valco, with 1 mL loop). The GC was equipped with a flame ionization detector (FID) and a thermal conductivity detector (TCD) and the analysis was performed with both molecular sieve 5 Å and Porapak-N columns. The product formation rate, propylene consumption rate and the product selectivity were defined according to the following equations.

$$\text{specific formation rate of product} = \frac{\text{concentration of product detected on stream} \times \text{flow rate}}{\text{weight of photocatalyst}} \quad (6)$$

$$\text{specific consumption rate of } C_3H_6 = \sum \text{specific formation rate of all products} \quad (7)$$

$$\text{product selectivity} = \left(\frac{\text{specific formation rate of product}}{\text{specific consumption rate of } C_3H_6} \right) \times 100\% \quad (8)$$

Acknowledgements

This work was supported by National Science Council of Taiwan under grant number NSC 99-2923-E-002-002-MY2. Lumen Dynamics is gratefully acknowledged for providing the emission spectrum of the 200 W mercury arc lamp.

References

1. Nakata, K.; Fujishima, A. *J. Photochem. Photobiol., C* **2012,** *13,* 169–189. doi:10.1016/j.jphotochemrev.2012.06.001
2. Yang, L.; Liu, Z. *Energy Convers. Manage.* **2007,** *48,* 882–889. doi:10.1016/j.enconman.2006.08.023
3. Behnajady, M. A.; Modirshahla, N.; Hamzavi, R. *J. Hazard. Mater.* **2006,** *133,* 226–232. doi:10.1016/j.jhazmat.2005.10.022
4. Sakthivel, S.; Neppolian, B.; Shankar, M. V.; Arabindoo, B.; Palanichamy, M.; Murugesan, V. *Sol. Energy Mater. Sol. Cells* **2003,** *77,* 65–82. doi:10.1016/S0927-0248(02)00255-6
5. Akyol, A.; Yatmaz, H. C.; Bayramoglu, M. *Appl. Catal., B* **2004,** *54,* 19–24. doi:10.1016/j.apcatb.2004.05.021
6. Choi, W.; Hong, S. J.; Chang, Y.-S.; Cho, Y. *Environ. Sci. Technol.* **2000,** *34,* 4810–4815. doi:10.1021/es0011461
7. Rincón, A. G.; Pulgarin, C. *Appl. Catal., B* **2003,** *44,* 263–284. doi:10.1016/S0926-3373(03)00076-6
8. Cho, M.; Chung, H.; Choi, W.; Yoon, J. *Water Res.* **2004,** *38,* 1069–1077. doi:10.1016/j.watres.2003.10.029
9. Dunlop, P. S. M.; Byrne, J. A.; Manga, N.; Eggins, B. R. *J. Photochem. Photobiol., A* **2002,** *148,* 355–363. doi:10.1016/S1010-6030(02)00063-1
10. Chen, F.; Yang, X.; Wu, Q. *Environ. Sci. Technol.* **2009,** *43,* 4606–4611. doi:10.1021/es900505h
11. Koči, K.; Zatloukalová, K.; Obalová, L.; Krejčiková, S.; Lacný, Z.; Čapek, L.; Hospodková, A.; Šolcová, O. *Chin. J. Catal.* **2011,** *32,* 812–815. doi:10.1016/S1872-2067(10)60199-4
12. Stafford, U.; Gray, K. A.; Kamat, P. V. *J. Catal.* **1997,** *167,* 25–32. doi:10.1006/jcat.1997.1511
13. Tang, J.; Zou, Z.; Ye, J. *Angew. Chem., Int. Ed.* **2004,** *43,* 4463–4466. doi:10.1002/anie.200353594
14. Hauser, S. A.; Cokoja, M.; Kühn, F. E. *Catal. Sci. Technol.* **2013,** *3,* 552–561. doi:10.1039/c2cy20595e
15. Nijhuis, T. A.; Makkee, M.; Moulijn, J. A.; Weckhuysen, B. M. *Ind. Eng. Chem. Res.* **2006,** *45,* 3447–3459. doi:10.1021/ie0513090
16. Vernimmen, J.; Meynen, V.; Cool, P. *Beilstein J. Nanotechnol.* **2011,** *2,* 785–801. doi:10.3762/bjnano.2.87
17. Nguyen, V.-H.; Chan, H.-Y.; Wu, J. C. S.; Bai, H. *Chem. Eng. J.* **2012,** *179,* 285–294. doi:10.1016/j.cej.2011.11.003
18. Nguyen, V.-H.; Chan, H.-Y.; Wu, J. C. S. *J. Chem. Sci.* **2013,** *125,* 859–867. doi:10.1007/s12039-013-0449-z
19. Murata, C.; Yoshida, H.; Kumagai, J.; Hattori, T. *J. Phys. Chem. B* **2003,** *107,* 4364–4373. doi:10.1021/jp0277006
20. Yoshida, H.; Murata, C.; Hattori, T. *J. Catal.* **2000,** *194,* 364–372. doi:10.1006/jcat.2000.2952
21. Amano, F.; Yamaguchi, T.; Tanaka, T. *J. Phys. Chem. B* **2006,** *110,* 281–288. doi:10.1021/jp0557868
22. Yoshida, H.; Murata, C.; Hattori, T. *Chem. Commun.* **1999,** 1551–1552. doi:10.1039/a904886c
23. Yoshida, H.; Tanaka, T.; Yamamoto, M.; Funabiki, T.; Yoshida, S. *Chem. Commun.* **1996,** 2125–2126. doi:10.1039/cc9960002125
24. Amano, F.; Tanaka, T. *Catal. Commun.* **2005,** *6,* 269–273. doi:10.1016/j.catcom.2005.01.007
25. *Catalyst laboratory of National Taiwan University - Research*. http://homepage.ntu.edu.tw/~cswu/research/english_research.html (accessed March 11, 2014).
26. Nguyen, V.-H.; Chan, H.-Y.; Wu, J.C.S.; Bai, H. Photo-epoxidation of Propylene to Propylene Oxide over V-Ti/MCM-41: A Wavelength Effect on Photocatalytic Activities. In *14th Asia Pacific Confederation of Chemical Engineering Congress.* Feb 21–24, 2012. Singapore.
27. Yoshida, H.; Tanaka, T.; Yamamoto, M.; Yoshida, T.; Funabiki, T.; Yoshida, S. *J. Catal.* **1997,** *171,* 351–357. doi:10.1006/jcat.1997.1813
28. Yamashita, H.; Kida, K.; Ikeue, K.; Kanazawa, Y.; Yoshizawa, K.; Anpo, M. Photocatalytic epoxidation of propene with molecular oxygen under visible light irradiation on V ion-implanted Ti-HMS and Cr-HMS mesoporous molecular sieves. In *Studies in Surface Science and Catalysis;* Park, S.-E.; Ryoo, R.; Ahn, W.-S.; Lee, C. W., Eds.; Elsevier, 2003; Vol. 146, pp 597–600.
29. Amano, F.; Tanaka, T.; Funabiki, T. *Langmuir* **2004,** *20,* 4236–4240. doi:10.1021/la0359981
30. Molinari, R.; Argurio, P.; Lavorato, C. *Curr. Org. Chem.* **2013,** *17,* 2516–2537. doi:10.2174/13852728113179990063
31. *ASTM Standard G173 - 03 (Reapproved 2012), Standard Tables for Reference Solar Spectral Irradiances: Direct Normal and Hemispherical on 37° Tilted Surface;* ASTM International: West Conshohocken, PA, 2012. doi:10.1520/G0173-03R12
32. Laha, S. C.; Kumar, R. *Microporous Mesoporous Mater.* **2002,** *53,* 163–177. doi:10.1016/S1387-1811(02)00337-2
33. Maschmeyer, T.; Rey, F.; Sankar, G.; Thomas, J. M. *Nature* **1995,** *378,* 159–162. doi:10.1038/378159a0
34. Zou, J.-J.; Liu, Y.; Pan, L.; Wang, L.; Zhang, X. *Appl. Catal., B* **2010,** *95,* 439–445. doi:10.1016/j.apcatb.2010.01.024
35. Amano, F.; Yamaguchi, T.; Tanaka, T. *J. Phys. Chem. B* **2006,** *110,* 281–288. doi:10.1021/jp0557868
36. Thakur, R. S.; Chaudhary, R.; Singh, C. *J. Renewable Sustainable Energy* **2010,** *2,* 042701. doi:10.1063/1.3467511
37. Al-Ekabi, H.; Serpone, N. Mechanistic implications in surface photochemistry. In *Photocatalysis: Fundamentals and Applications;* Serpone, N.; Pelizzetti, E., Eds.; Wiley: New York, 1989; pp 457–488.
38. Wendl, B.; Droschl, H.; Kern, W. *Eur. J. Orthod.* **2004,** *26,* 545–551. doi:10.1093/ejo/26.5.545
39. Takeuchi, M.; Deguchi, J.; Sakai, S.; Anpo, M. *Appl. Catal., B* **2010,** *96,* 218–223. doi:10.1016/j.apcatb.2010.02.024
40. Luo, S.; Falconer, J. L. *J. Catal.* **1999,** *185,* 393–407. doi:10.1006/jcat.1999.2511
41. Airoldi, C.; Arakaki, L. N. H. *J. Colloid Interface Sci.* **2002,** *249,* 1–7. doi:10.1006/jcis.2001.8192

License and Terms

This is an Open Access article under the terms of the Creative Commons Attribution License (http://creativecommons.org/licenses/by/2.0), which permits unrestricted use, distribution, and reproduction in any medium, provided the original work is properly cited.

The license is subject to the *Beilstein Journal of Nanotechnology* terms and conditions: (http://www.beilstein-journals.org/bjnano)

The definitive version of this article is the electronic one which can be found at: doi:10.3762/bjnano.5.67

Beilstein Journal of Nanotechnology

High activity of Ag-doped $Cd_{0.1}Zn_{0.9}S$ photocatalyst prepared by the hydrothermal method for hydrogen production under visible-light irradiation

Leny Yuliati[*1,§], Melody Kimi[2,3] and Mustaffa Shamsuddin[2]

Full Research Paper

Open Access

Address:
[1]Ibnu Sina Institute for Fundamental Science Studies, Universiti Teknologi Malaysia, 81310 UTM Johor Bahru, Johor, Malaysia, [2]Department of Chemistry, Faculty of Science, Universiti Teknologi Malaysia, 81310 UTM Johor Bahru, Johor, Malaysia and [3]Centre for Pre-University Studies, Universiti Malaysia Sarawak, 94300 Kota Samarahan, Sarawak, Malaysia

Email:
Leny Yuliati[*] - leny@ibnusina.utm.my

* Corresponding author
§ Tel: +60-7-5536272; Fax: +60-7-5536080

Keywords:
Ag doping; $Cd_{0.1}Zn_{0.9}S$; hydrogen production; hydrothermal; visible light

Beilstein J. Nanotechnol. **2014,** *5,* 587–595.
doi:10.3762/bjnano.5.69

Received: 31 December 2013
Accepted: 14 April 2014
Published: 07 May 2014

This article is part of the Thematic Series "Photocatalysis".

Guest Editor: R. Xu

© 2014 Yuliati et al; licensee Beilstein-Institut.
License and terms: see end of document.

Abstract

Background: The hydrothermal method was used as a new approach to prepare a series of Ag-doped $Cd_{0.1}Zn_{0.9}S$ photocatalysts. The effect of Ag doping on the properties and photocatalytic activity of $Cd_{0.1}Zn_{0.9}S$ was studied for the hydrogen production from water reduction under visible light irradiation.

Results: Compared to the series prepared by the co-precipitation method, samples prepared by the hydrothermal method performed with a better photocatalytic activity. The sample with the optimum amount of Ag doping showed the highest hydrogen production rate of 3.91 mmol/h, which was 1.7 times higher than that of undoped $Cd_{0.1}Zn_{0.9}S$. With the Ag doping, a red shift in the optical response was observed, leading to a larger portion of the visible light absorption than that of without doping. In addition to the larger absorption in the visible-light region, the increase in photocatalytic activity of samples with Ag doping may also come from the Ag species facilitating electron–hole separation.

Conclusion: This study demonstrated that Ag doping is a promising way to enhance the activity of $Cd_{0.1}Zn_{0.9}S$ photocatalyst.

Introduction

The development of clean and renewable hydrogen energy through a sustainable production process is still a big issue to be addressed. Solar energy is a very attractive option as it is the most abundant energy. The conversion of solar energy to chemical energy by photocatalytic processes, such as photocatalytic water reduction in the presence of semiconductor photocata-

lysts, would be an opportunity to produce clean hydrogen energy. Recently, special attention has been paid to the use of visible light-driven photocatalysts [1-4]. One of the promising photocatalysts is $Cd_{1-x}Zn_xS$ solid solution [5-8]. The successful formation of a solid solution of ZnS and CdS resulted in an absorption shift of ZnS to the visible-light range, while maintaining the high conduction band energy required for hydrogen production. However, in order to utilize solar energy in the future, a further red shift to a range of even longer wavelengths is still highly desired.

The modification of $Cd_{1-x}Zn_xS$ photocatalyst with metal ions, such as Cu [9-13], Ni [14,15], Sn [16], and Sr [17] has been a good attempt to increase the visible-light absorption of the $Cd_{1-x}Zn_xS$ photocatalyst. The use of Ag species as a good dopant for various types of photocatalysts has been also reported [18-20], including its use to modify $Cd_{1-x}Zn_xS$ [21-23]. $Cd_{1-x}Zn_xS$ modified by Ag_2S was reported to show activity for hydrogen production from water [21] and hydrogen sulfide [22]. On the other hand, the properties of Ag^+-doped $Cd_{1-x}Zn_xS$ have been investigated by spectroscopic and photochemical studies [23]. It was proposed that the Ag^+ might act as a hole trapping site. Since the electron–hole recombination rate may increase as a result of defect sites created by the doping element, reducing electron–hole recombination and promoting interfacial charge transfer should be optimized in order to improve the efficiency of the photocatalysts.

The most widely used method to prepare Ag-doped $Cd_{1-x}Zn_xS$ is the co-precipitation method [21]. However, the co-precipitation method usually produces materials with low crystallinity. Since high crystallinity is beneficial for photocatalytic hydrogen production [1-4], it is worth to further investigate an alternative method to prepare the Ag-doped $Cd_{1-x}Zn_xS$ with high crystallinity. It has been reported that compared to the co-precipitation method, the hydrothermal method produced sulfide photocatalysts with better crystallinity, which gave higher activity for hydrogen production [9,16]. In the present work, the Ag(x)-doped $Cd_{0.1}Zn_{0.9}S$ samples were prepared by both hydrothermal and co-precipitation methods. The superior activity of Ag(x)-doped $Cd_{0.1}Zn_{0.9}S$ prepared by hydrothermal method is discussed.

Results and Discussion

Figure 1 shows the X-ray diffraction (XRD) patterns of $Cd_{0.1}Zn_{0.9}S$ and Ag(x)-doped $Cd_{0.1}Zn_{0.9}S$ samples prepared by using the hydrothermal method. The diffraction peaks for all samples, except for Ag(0.05)-doped $Cd_{0.1}Zn_{0.9}S$, were in good agreement with the diffraction peaks of ZnS cubic zinc-blende phase (JCPDS No. 772100) with major diffraction peaks at 2θ of 28.6, 32.5, 47.6 and 56.3°, corresponding to the (111), (200), (220) and (311) planes respectively. On the other hand, in addition to the cubic zinc blende phase, the Ag(0.05)-doped $Cd_{0.1}Zn_{0.9}S$ also showed the presence of small diffraction peaks of the hexagonal phase at 2θ of ca. 27 and 31° (Figure 1d). A similar phenomenon was also reported when Cu was used as a dopant [9]. There are no diffraction peaks corresponding to Ag or other crystal phases. This could be due to the fact that the content of Ag might be too small to be detected or Ag was well dispersed in $Cd_{0.1}Zn_{0.9}S$. This result also indicated that no detectable impurity phases existed in the prepared samples. The small amount of Ag dopant increased remarkably the intensity of the diffraction peaks compared to the undoped $Cd_{0.1}Zn_{0.9}S$ (Figure 1a,b), which suggests that a small amount of Ag might induce the crystal growth. However, further increase of the Ag dopant did not further increase the intensity of the diffraction peaks. With increasing amount of Ag dopant, the peaks became slightly broader (Figure 1b–d) since Ag might be clustered and in turn gave a slightly increased disorder. As the diffraction peaks were only slightly shifted to higher values of 2θ with increasing amount of Ag, it can be suggested that Ag could be doped into the lattice without causing much crystal distortion.

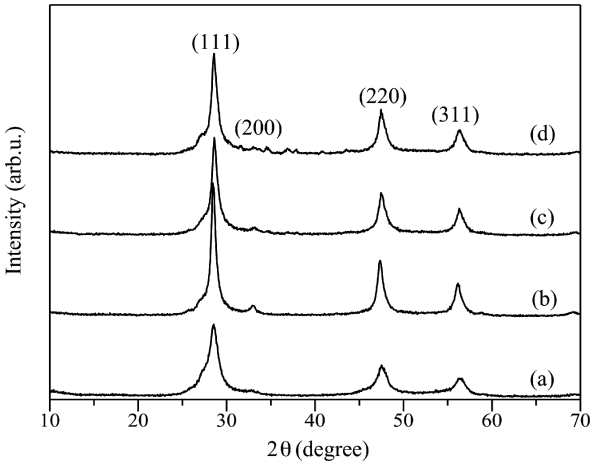

Figure 1: XRD patterns of (a) $Cd_{0.1}Zn_{0.9}S$, (b) Ag(0.01)-doped $Cd_{0.1}Zn_{0.9}S$, (c) Ag(0.03)-doped $Cd_{0.1}Zn_{0.9}S$, and (d) Ag(0.05)-doped $Cd_{0.1}Zn_{0.9}S$ prepared by the hydrothermal method.

The XRD patterns for $Cd_{0.1}Zn_{0.9}S$ and Ag(x)-doped $Cd_{0.1}Zn_{0.9}S$ samples prepared by the co-precipitation method are shown in Figure 2. For all samples, only diffraction peaks of ZnS cubic zinc-blende phase could be observed and no other phases could be detected. Different from the series prepared by hydrothermal method, there was no obvious change in the intensities of diffraction peaks after Ag was doped into the $Cd_{0.1}Zn_{0.9}S$. Broadening and shifting of the diffraction peaks were not observed, suggesting that Ag might not be doped

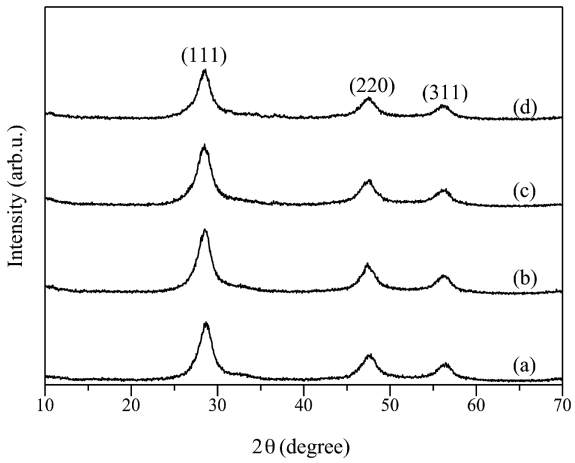

Figure 2: XRD patterns of (a) $Cd_{0.1}Zn_{0.9}S$, (b) Ag(0.01)-doped $Cd_{0.1}Zn_{0.9}S$, (c) Ag(0.03)-doped $Cd_{0.1}Zn_{0.9}S$, and (d) Ag(0.05)-doped $Cd_{0.1}Zn_{0.9}S$ prepared by the co-precipitation method.

inside but existed on the surface of $Cd_{0.1}Zn_{0.9}S$. Samples prepared by the co-precipitation method showed less intense and broader diffraction peaks than those prepared by the hydrothermal method, suggesting the less crystallinity and/or less crystallite size. This result was reasonable since co-precipitation method did not involve crystal growth by heating process.

Figure 3 and Figure 4 show field emission scanning electron microscopy (FESEM) images of $Cd_{0.1}Zn_{0.9}S$ and Ag(x)-doped $Cd_{0.1}Zn_{0.9}S$ samples prepared by hydrothermal and co-precipitation methods, respectively. For samples prepared by the hydrothermal method, all samples have a spherical shape with particle sizes in the range of 20–120 nm that are further agglomerated into bigger particles with no uniform size. The samples prepared by the co-precipitation method also have spherical shapes with slightly lower particle sizes in the range of 10–70 nm. For all samples, the morphology of $Cd_{0.1}Zn_{0.9}S$ was not affected by the added Ag.

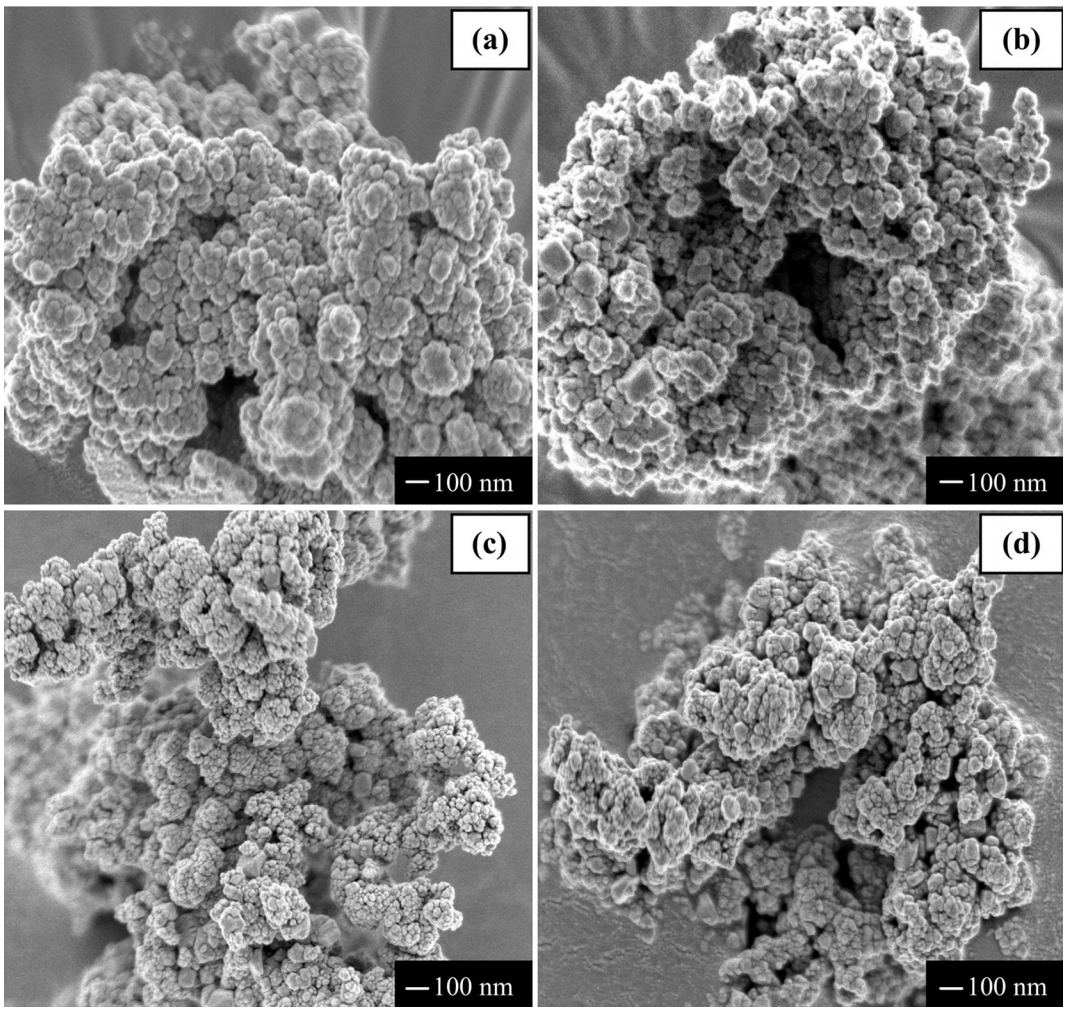

Figure 3: FESEM images of (a) $Cd_{0.1}Zn_{0.9}S$, (b) Ag(0.01)-doped $Cd_{0.1}Zn_{0.9}S$, (c) Ag(0.03)-doped $Cd_{0.1}Zn_{0.9}S$ (d) Ag(0.05)-doped $Cd_{0.1}Zn_{0.9}S$ prepared by the hydrothermal method.

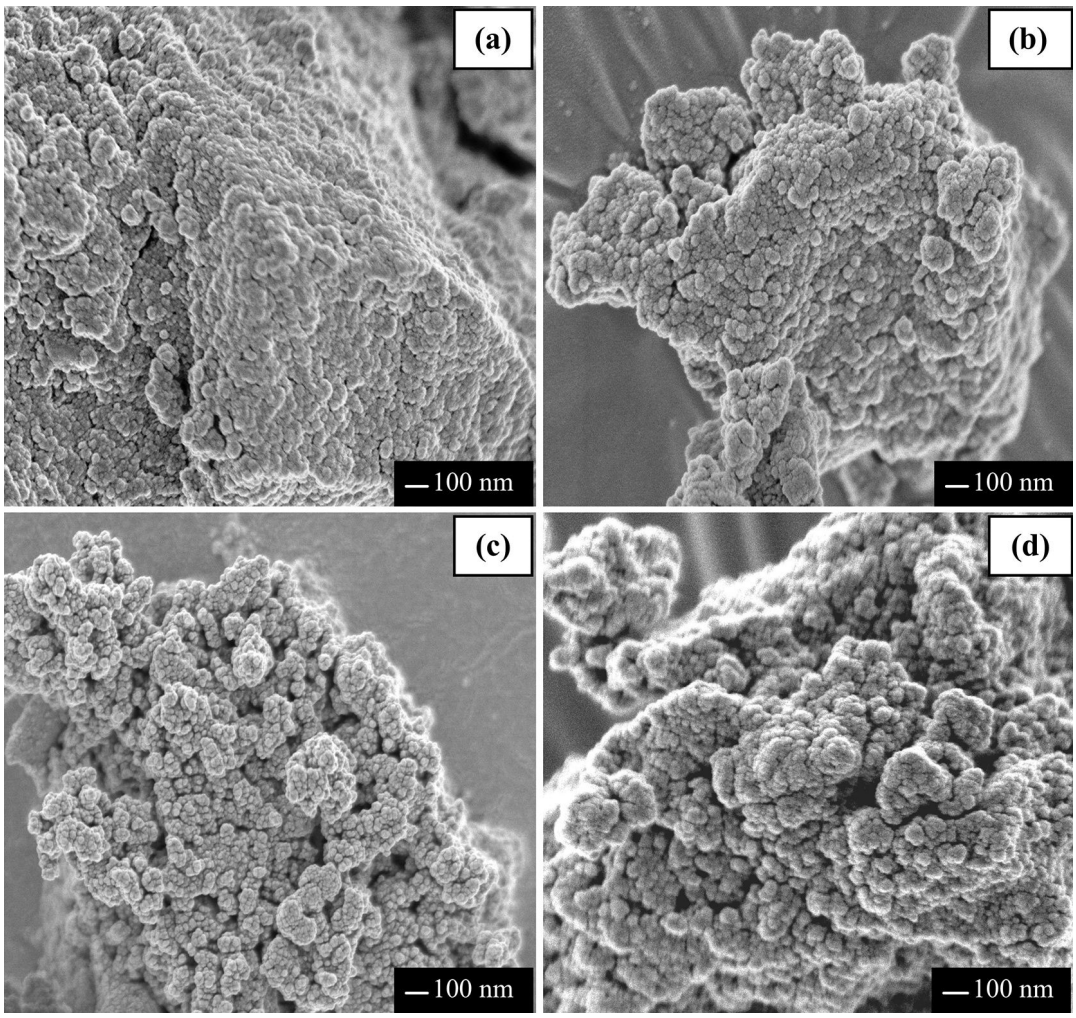

Figure 4: FESEM images of (a) $Cd_{0.1}Zn_{0.9}S$, (b) Ag(0.01)-doped $Cd_{0.1}Zn_{0.9}S$, (c) Ag(0.03)-doped $Cd_{0.1}Zn_{0.9}S$ (d) Ag(0.05)-doped $Cd_{0.1}Zn_{0.9}S$ prepared by the co-precipitation method.

Figure 5 shows the diffuse reflectance UV–visible (DR UV–vis) spectra of samples prepared by the hydrothermal method. The $Cd_{0.1}Zn_{0.9}S$ showed a shoulder peak around 400–500 nm (Figure 5a), similar to previous studies [9,16]. The addition of Ag shifted the absorption edge toward longer wavelengths, suggesting the formation of Ag-doped $Cd_{0.1}Zn_{0.9}S$ samples. The values of the band gap energy for the samples are listed in Table 1. The band gap energy was determined by taking the intersection between the linear tangent line with the *x*-axis from a plot of $F(\%R)h\nu^{1/n}$ versus hν, in which F(%R) is the Kubelka–Munk function, *h* is Planck's constant, ν is the frequency of vibration, and *n* is 1/2 for a direct allowed transition. As shown in Table 1, the addition of a small amount of Ag decreased the band gap energy of the $Cd_{0.1}Zn_{0.9}S$ samples (Table 1, entries 1 and 2). A further increase of Ag did not give a monotonous decrease in the band gap energy, even though these samples still showed lower band gap energy than the $Cd_{0.1}Zn_{0.9}S$ sample (Table 1, entries 3 and 4).

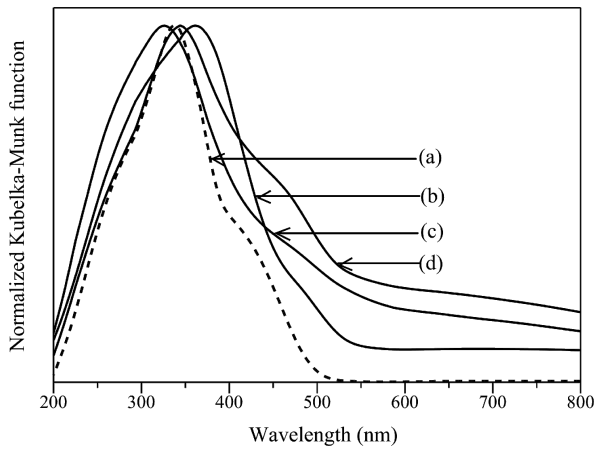

Figure 5: DR UV–visible spectra of (a) $Cd_{0.1}Zn_{0.9}S$, (b) Ag(0.01)-doped $Cd_{0.1}Zn_{0.9}S$, (c) Ag(0.03)-doped $Cd_{0.1}Zn_{0.9}S$ (d) Ag(0.05)-doped $Cd_{0.1}Zn_{0.9}S$ prepared by the hydrothermal method.

Table 1: Band gap energy values for $Cd_{0.1}Zn_{0.9}S$ and Ag-doped $Cd_{0.1}Zn_{0.9}S$ samples.

entry	sample	band gap energy/eV	preparation method
1	$Cd_{0.1}Zn_{0.9}S$	3.11	hydrothermal
2	Ag(0.01)-doped $Cd_{0.1}Zn_{0.9}S$	2.81	
3	Ag(0.03)-doped $Cd_{0.1}Zn_{0.9}S$	3.01	
4	Ag(0.05)-doped $Cd_{0.1}Zn_{0.9}S$	2.88	
5	$Cd_{0.1}Zn_{0.9}S$	2.94	co-precipitation
6	Ag(0.01)-doped $Cd_{0.1}Zn_{0.9}S$	3.06	
7	Ag(0.03)-doped $Cd_{0.1}Zn_{0.9}S$	2.99	
8	Ag(0.05)-doped $Cd_{0.1}Zn_{0.9}S$	2.66	

In addition to the shifted absorption edge and the decreased band gap energy, Ag doping caused an absorption tail in the range of 600–800 nm. The absorption in this area has been assigned to the formation of Ag_2S [21,24]. Even though the Ag_2S formation could not be detected by XRD owing to the low sensitivity, it can be suggested that the added Ag was not completely doped in the $Cd_{0.1}Zn_{0.9}S$. The addition of Ag also caused a new absorption appearing at about 295 nm for Ag(0.01)-doped $Cd_{0.1}Zn_{0.9}S$ and Ag(0.03)-doped $Cd_{0.1}Zn_{0.9}S$ (Figure 5b,c), corresponding to the presence of Ag metal nanoparticles [25] that can be formed catalytically through the reduction of Ag^+ by the Ag_2S as the catalyst [26]. On the other hand, even though Ag(0.05)-doped $Cd_{0.1}Zn_{0.9}S$ did not show such an absorption at 295 nm (Figure 5d), its maximum peak was shifted to longer wavelengths, which might occur due to the increase in the particle size of the formed Ag metal [26]. Even though the mechanism could not be revealed in this paper, these results showed that the addition of Ag was not only simply doped into the $Cd_{0.1}Zn_{0.9}S$, but also was used to form other Ag species such as Ag metal and Ag_2S. The formation of the later species was obviously increased with the increase of the added Ag amount. Various possible formations of Ag species mentioned above led to the non-monotonous red shift and non-monotonous decrease in the band gap energy with the increase of Ag doping.

The absorption spectra of samples synthesized by co-precipitation method are shown in Figure 6. The $Cd_{0.1}Zn_{0.9}S$ sample showed a smooth absorption edge around 450 nm (Figure 6a). The addition of Ag shifted the absorption edge toward longer wavelengths when the amount of Ag was large (Figure 6d). As shown in Table 1, a small amount of Ag slightly increased the band gap energy of $Cd_{0.1}Zn_{0.9}S$ sample (Table 1, entries 5–7), while a large amount of Ag decreased the band gap energy (Table 1, entry 8). The increase in Ag doping also gave an increase in the absorption level above 600 nm due to the formation of Ag_2S [21,24]. The formation of Ag_2S on the samples prepared by the co-precipitation method was found to be larger than that on the samples prepared by the hydrothermal method. Even though the formation of a new absorption below 300 nm was not as clear as those observed on the samples prepared by the hydrothermal method, it could be observed that the peak maximum of $Cd_{0.1}Zn_{0.9}S$ was shifted from 348 to 325–326 nm (Figure 6b,c), which would be due to formation of Ag metal on Ag(0.01)-doped $Cd_{0.1}Zn_{0.9}S$ and Ag(0.03)-doped $Cd_{0.1}Zn_{0.9}S$. A further increase of the amount of added Ag caused the peak maximum to be shifted from 326 to 339 nm (Figure 6d), owing to the formation of larger particles of Ag metal, similar to the samples prepared by hydrothermal method mentioned above.

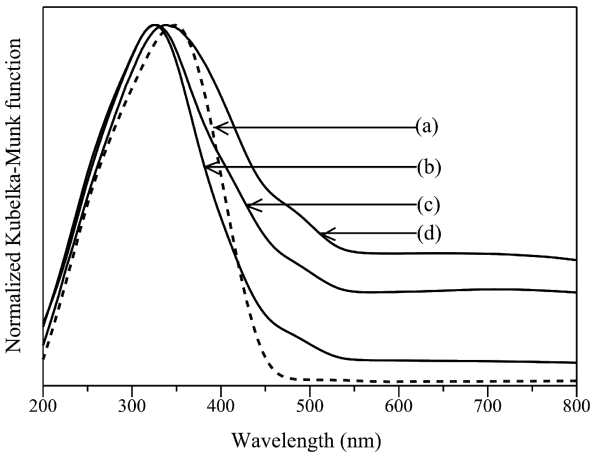

Figure 6: DR UV–visible spectra of (a) $Cd_{0.1}Zn_{0.9}S$, (b) Ag(0.01)-doped $Cd_{0.1}Zn_{0.9}S$, (c) Ag(0.03)-doped $Cd_{0.1}Zn_{0.9}S$ (d) Ag(0.05)-doped $Cd_{0.1}Zn_{0.9}S$ prepared by the co-precipitation method.

The photocatalytic performances of $Cd_{0.1}Zn_{0.9}S$ and Ag(x)-doped $Cd_{0.1}Zn_{0.9}S$ samples prepared by the hydrothermal method were examined for hydrogen production under visible-light irradiation as shown in Figure 7. All samples showed visible-light activity for hydrogen production. The undoped $Cd_{0.1}Zn_{0.9}S$ sample produced hydrogen at a rate of 2.49 mmol/h. The Ag(0.01)-doped $Cd_{0.1}Zn_{0.9}S$ showed an increased rate of hydrogen production of 3.68 mmol/h.

However, unfortunately, when the amount of Ag increased, the activity was not improved. After 5 h of reaction, Ag(0.03)-doped $Cd_{0.1}Zn_{0.9}S$ and Ag(0.05)-doped $Cd_{0.1}Zn_{0.9}S$ even showed a lower rate than that obtained from the undoped $Cd_{0.1}Zn_{0.9}S$. The enhancement in the photocatalytic activity of Ag(0.01)-doped $Cd_{0.1}Zn_{0.9}S$ might be attributed to the better crystallinity, the improved absorption in the visible-light region, as well as the presence of Ag species. Regarding the latter it has been proposed that both Ag^0 and Ag^+ played an important role in facilitating the charge separation and suppressing the recombination of photoexcited charge carries [18,19], while the Ag_2S could also act as a hole-transfer catalyst [21,24] for the oxidation of sulfide ions, which in turn promoted the activity. As shown in the DR UV–vis spectra (Figure 5), the formation of Ag_2S could not be avoided and it increased with the increase of Ag amount. However, since the activity did not increase but decreased with the increase of Ag amount, the Ag_2S would not be the main species responsible for the high activity on Ag(0.01)-doped $Cd_{0.1}Zn_{0.9}S$. Indeed, the decrease of the activity of Ag(0.03)-doped $Cd_{0.1}Zn_{0.9}S$ and Ag(*0.05*)-doped $Cd_{0.1}Zn_{0.9}S$ showed that the Ag_2S might block the incident light, reduce the reaction sites for oxidation, and thus suppress the photocatalytic reaction [24].

The stability of the samples prepared by the hydrothermal method was investigated by reusing the samples for two consecutive runs. The photocatalytic activity results for first and second runs are also shown in Figure 7. The undoped $Cd_{0.1}Zn_{0.9}S$ showed a lower photocatalytic activity in the second run due to poor stability. On the other hand, all Ag-doped $Cd_{0.1}Zn_{0.9}S$ samples showed a relatively stable activity. This result suggested that the presence of Ag was important to maintain the stability of the photocatalysts. Among the samples, the Ag(0.01)-doped $Cd_{0.1}Zn_{0.9}S$ sample showed the highest activity for hydrogen production. The rate for hydrogen production was slightly increased in the second run, suggesting that the Ag(0.01)-doped $Cd_{0.1}Zn_{0.9}S$ sample might experience a photochemical activation process. The similar phenomenon was also reported to occur on $CdS/ZnFe_2O_4$ photocatalyst during the photocatalytic hydrogen production [27]. In order to understand the possible photochemical activation process occurred on the Ag(0.01)-doped $Cd_{0.1}Zn_{0.9}S$ sample, the used sample was characterized by DR UV–visible spectroscopy. As shown in Figure 8, the absorption peak of the

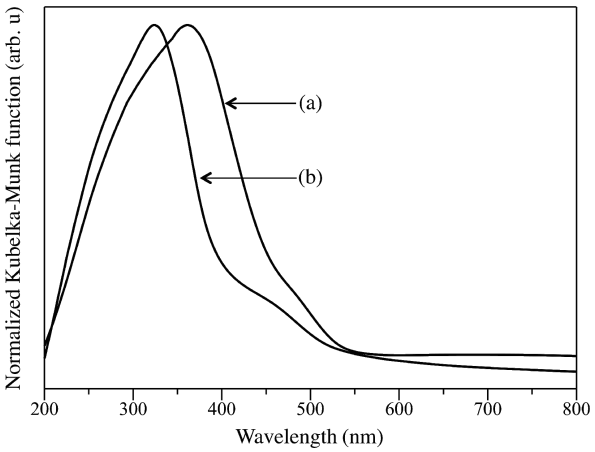

Figure 8: DR UV–visible spectra of (a) fresh and (b) used Ag(0.01)-doped $Cd_{0.1}Zn_{0.9}S$ prepared by the hydrothermal method after second run.

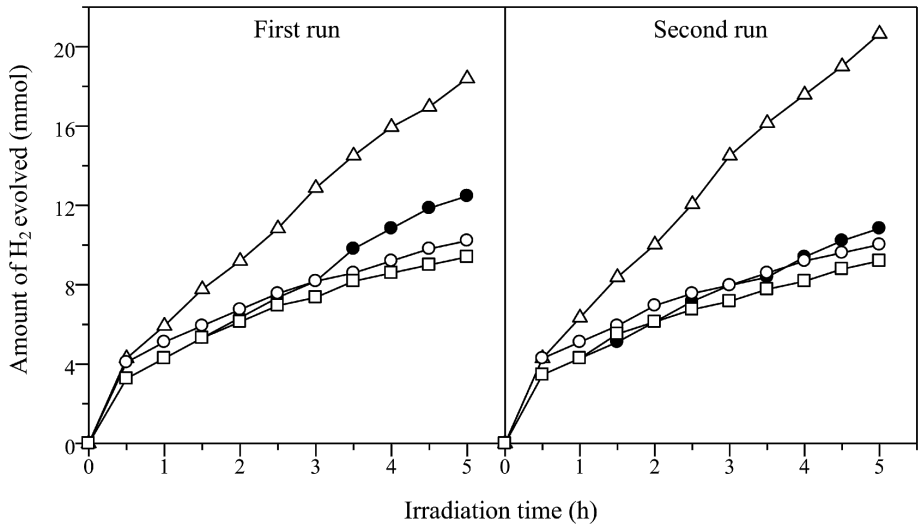

Figure 7: Photocatalytic hydrogen evolution on $Cd_{0.1}Zn_{0.9}S$ (filled circles), Ag(0.01)-doped $Cd_{0.1}Zn_{0.9}S$ (empty triangles), Ag(0.03)-doped $Cd_{0.1}Zn_{0.9}S$ (empty circles), and Ag(0.05)-doped $Cd_{0.1}Zn_{0.9}S$ (empty squares) prepared by the hydrothermal method under visible-light irradiation.

Ag(0.01)-doped $Cd_{0.1}Zn_{0.9}S$ sample was shifted to lower wavelengths centred around 323 nm and the absorption intensity above 550 nm was decreased after the second run. These changes showed that the amount of Ag metal on the surface might be increased via photoreduction during the reaction. As a result, the photocatalytic activity of the Ag(0.01)-doped $Cd_{0.1}Zn_{0.9}S$ sample increased within the reaction time. The average hydrogen production rate from both runs was determined to be 3.91 mmol/h and the value was 1.7 times better than the average rate observed on the undoped $Cd_{0.1}Zn_{0.9}S$.

Figure 9 shows the photocatalytic activities of $Cd_{0.1}Zn_{0.9}S$ and Ag(x)-doped $Cd_{0.1}Zn_{0.9}S$ samples prepared by co-precipitation method. The Ag(0.01)-doped $Cd_{0.1}Zn_{0.9}S$ and Ag(0.03)-doped $Cd_{0.1}Zn_{0.9}S$ showed a higher activity than the undoped $Cd_{0.1}Zn_{0.9}S$. The highest photocatalytic activity was recorded for the Ag(0.01)-doped $Cd_{0.1}Zn_{0.9}S$ with a hydrogen production rate of 2.19 mmol/h. As for Ag(0.05)-doped $Cd_{0.1}Zn_{0.9}S$, the activity was higher than that of the undoped compound in the first 3.5 hours, but the activity decreased over time. The samples prepared by the co-precipitation method showed less activity than those prepared by the hydrothermal method, which might be due to the lower crystallinity as discussed above. The stability of the samples was also tested for the second run. It was observed that undoped $Cd_{0.1}Zn_{0.9}S$ and Ag(0.01)-doped $Cd_{0.1}Zn_{0.9}S$ showed a slightly decreased photocatalytic activity as compared to activity obtained in the first run. The decrease in the activity is stronger in Ag(0.03)-doped $Cd_{0.1}Zn_{0.9}S$ and Ag(0.05)-doped $Cd_{0.1}Zn_{0.9}S$. Both samples showed a lower activity than the undoped one in the second run. The Ag(x)-doped $Cd_{0.1}Zn_{0.9}S$ samples prepared by the co-precipitation method were found to be less stable than those prepared by the hydrothermal method that might be due to the formation of more Ag_2S and less doping of Ag.

Conclusion

Two series of Ag-doped $Cd_{0.1}Zn_{0.9}S$ samples were prepared by hydrothermal and co-precipitation methods, respectively. The Ag(0.01)-doped $Cd_{0.1}Zn_{0.9}S$ prepared by the hydrothermal method showed the highest photocatalytic activity and stability under visible light irradiation with a hydrogen production rate of 3.91 mmol/h, which was 1.7 times higher than that of the undoped $Cd_{0.1}Zn_{0.9}S$. The better photocatalytic activity observed for the Ag(0.01)-doped $Cd_{0.1}Zn_{0.9}S$ was proposed due to higher crystallinity, better absorption of visible light, and the formation of an optimum amount of Ag species, which facilitates the electron–hole separation and increase the stability of the catalyst, and the formation of less Ag_2S, which would suppress the reaction.

Experimental

Preparation of Ag-doped $Cd_{0.1}Zn_{0.9}S$. Hydrothermal and co-precipitation methods were used to prepare the Ag-doped $Cd_{0.1}Zn_{0.9}S$ samples, which were labeled as Ag(x)-doped $Cd_{0.1}Zn_{0.9}S$, with x showed the doping amount of Ag (x = 0.01, 0.03, or 0.05 mol). For the hydrothermal method, a series of Ag(x)-doped $Cd_{0.1}Zn_{0.9}S$ samples was synthesized similarly to the previous studies [9,16]. In a typical synthesis for Ag(0.01)-doped $Cd_{0.1}Zn_{0.9}S$, $AgNO_3$ (Unilab, 99.9%), $Cd(NO_3)_2{\cdot}4H_2O$ (Aldrich, 98%), $Zn(CH_3COO)_2{\cdot}2H_2O$ (GCE chemicals, 98%) and CH_3CSNH_2 (Merck, 99%) with molar ratios of 0.01:0.1:0.9:1 were dissolved in distilled water at room

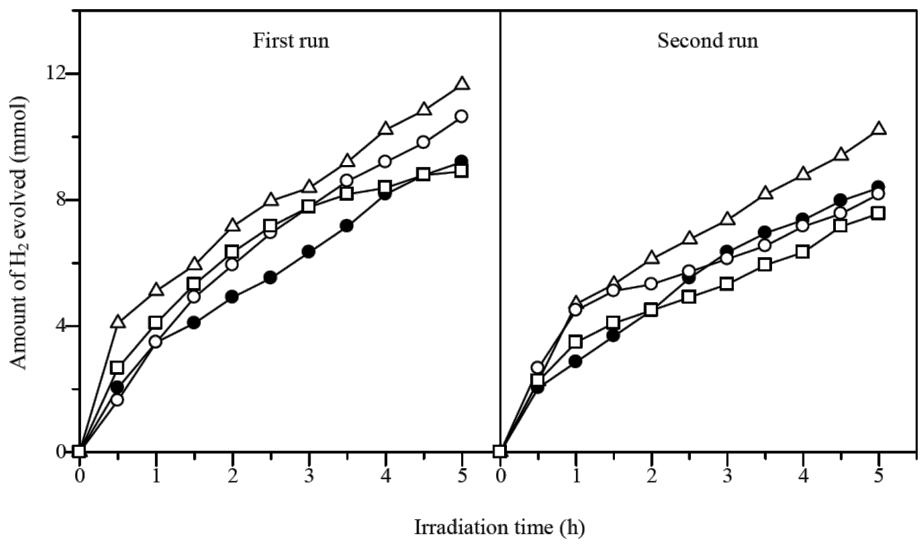

Figure 9: Photocatalytic hydrogen evolution on $Cd_{0.1}Zn_{0.9}S$ (filled circles), Ag(0.01)-doped $Cd_{0.1}Zn_{0.9}S$ (empty triangles), Ag(0.03)-doped $Cd_{0.1}Zn_{0.9}S$ (empty circles), and Ag(0.05)-doped $Cd_{0.1}Zn_{0.9}S$ (empty squares) prepared by the co-precipitation method under visible-light irradiation.

temperature. The solution was then transferred into an autoclave with an inner Teflon lining, sealed and heated in an oven at 433 K for 8 h. The solution was left to reach room temperature naturally. The precipitate was separated by using a centrifuge and washed by using distilled water. The sample was then dried at room temperature under vacuum conditions. For the co-precipitation method, the series of Ag(x)-doped $Cd_{0.1}Zn_{0.9}S$ was prepared similarly to the previous studies [9,16]. Typically, to synthesize Ag(0.01)-doped $Cd_{0.1}Zn_{0.9}S$, $Na_2S{\cdot}xH_2O$ (QRëc, 98%) solution was added dropwise to an aqueous solution containing $AgNO_3$ (Unilab, 99.9%), $Cd(NO_3)_2{\cdot}4H_2O$ (Aldrich, 98%) and $Zn(CH_3COO)_2{\cdot}2H_2O$ (GCE chemicals, 98%) with molar ratios of 0.01:0.1:0.9. The solution was stirred for 12 h at room temperature. The resulting precipitate was filtered and washed several times with distilled water. The product then was dried in air at 343 K for 12 h.

Characterizations. XRD patterns were obtained on an X-ray diffractometer (Bruker Advance D8) using Cu Kα radiation (40 kV, 40 mA). The morphologies and size of the samples were observed by using field emission scanning electron microscopy (FESEM) with JEOL JSM 6701F at an accelerating voltage of 2 kV with platinum coating prior to analysis. DR UV–vis spectra were recorded at room temperature using a UV–visible spectrometer (Perkin Elmer Lambda 900). $BaSO_4$ was used as a reflectance standard.

Photocatalytic testing. As described in the previous studies [9,16], photocatalytic hydrogen evolution was performed in a closed side irradiated-Pyrex cell equipped with a water condenser to maintain the temperature constant during the reaction. A 500 W halogen lamp was used as the visible-light source. Hydrogen gas evolved was identified by an online system with thermal conductivity detector (TCD) gas chromatography (GC, Agilent 7890A) using Supelco 13X molecular sieves and argon carrier gas, which amount was measured by volumetric method. In all experiments, the powder sample (0.2 g) was dispersed by magnetic stirring in an aqueous solution (50 mL) containing 0.25 M Na_2SO_3 and 0.35 M Na_2S as the sacrificial agents. Nitrogen gas was flushed through the reaction cell for 30 min before reaction to remove air. In order to check the photocatalytic stability, the sample was reused without washing or drying. Before another 5 h irradiation in the second run, the reactor containing the tested sample was purged with nitrogen gas for 30 min to ensure that there was no residual hydrogen in the reactor.

Acknowledgements

This work was financially supported by the Ministry of Higher Education (MOHE, Malaysia) and the Universiti Teknologi Malaysia (UTM, Malaysia) through a Tier-1 Research University Grant (cost center code: Q.J130000.2526.02H95). Financial support from the Ministry of Science, Technology and Innovation through the National Science Fellowship is greatly acknowledged (MK).

References

1. Navarro, R. M.; Alvarez-Galván, M. C.; Villoria de la Mano, J. A.; Al-Zahrani, S. M.; Fierro, J. L. G. *Energy Environ. Sci.* **2010,** *3,* 1865–1882. doi:10.1039/c001123a
2. Maeda, K. *J. Photochem. Photobiol., C: Photochem. Rev.* **2011,** *12,* 237–268. doi:10.1016/j.jphotochemrev.2011.07.001
3. Zhang, K.; Guo, L. *Catal. Sci. Technol.* **2013,** *3,* 1672–1690. doi:10.1039/c3cy00018d
4. Abe, R. *J. Photochem. Photobiol., C: Photochem. Rev.* **2010,** *11,* 179–209. doi:10.1016/j.jphotochemrev.2011.02.003
5. Xing, C.; Zhang, Y.; Yan, W.; Guo, L. *Int. J. Hydrogen Energy* **2006,** *31,* 2018–2024. doi:10.1016/j.ijhydene.2006.02.003
6. del Valle, F.; Ishikawa, A.; Domen, K.; Villoria de la Mano, J. A.; Sánchez-Sánchez, M. C.; González, I. D.; Herreras, S.; Mota, N.; Rivas, M. E.; Álvarez Galván, M. C.; Fierro, J. L. G.; Navarro, R. M. *Catal. Today* **2009,** *143,* 51–56. doi:10.1016/j.cattod.2008.09.024
7. Wang, L.; Wang, W.; Shang, M.; Yin, W.; Sun, S.; Zhang, L. *Int. J. Hydrogen Energy* **2010,** *35,* 19–25. doi:10.1016/j.ijhydene.2009.10.084
8. Liu, M.; Wang, L.; Lu, G. (M.); Yao, X.; Guo, L. *Energy Environ. Sci.* **2011,** *4,* 1372–1378. doi:10.1039/c0ee00604a
9. Kimi, M.; Yuliati, L.; Shamsuddin, M. *J. Photochem. Photobiol., A: Chem.* **2012,** *230,* 15–22. doi:10.1016/j.jphotochem.2012.01.004
10. Zhang, W.; Zhong, Z.; Wang, Y.; Xu, R. *J. Phys. Chem. C* **2008,** *112,* 17635–17642. doi:10.1021/jp8059008
11. Liu, G.; Zhao, L.; Ma, L.; Guo, L. *Catal. Commun.* **2008,** *9,* 126–130. doi:10.1016/j.catcom.2007.05.036
12. Zhang, W.; Xu, R. *Int. J. Hydrogen Energy* **2009,** *34,* 8495–8503. doi:10.1016/j.ijhydene.2009.08.041
13. Liu, G.; Zhou, Z.; Guo, L. *Chem. Phys. Lett.* **2011,** *509,* 43–47. doi:10.1016/j.cplett.2011.04.073
14. Zhang, X.; Jing, D.; Liu, M.; Guo, L. *Catal. Commun.* **2008,** *9,* 1720–1724. doi:10.1016/j.catcom.2008.01.032
15. Zhang, X.; Jing, D.; Guo, L. *Int. J. Hydrogen Energy* **2010,** *35,* 7051–7057. doi:10.1016/j.ijhydene.2009.12.132
16. Kimi, M.; Yuliati, L.; Shamsuddin, M. *Int. J. Hydrogen Energy* **2011,** *36,* 9453–9461. doi:10.1016/j.ijhydene.2011.05.044
17. Zhang, K.; Jing, D.; Chen, Q.; Guo, L. *Int. J. Hydrogen Energy* **2010,** *35,* 2048–2057. doi:10.1016/j.ijhydene.2009.12.143
18. Liao, L.; Ingram, C. W. *Appl. Catal., A: Gen.* **2012,** *433–434,* 18–25. doi:10.1016/j.apcata.2012.04.033
19. Li, Y.; Ma, M.; Chen, W.; Li, L.; Zen, M. *Mater. Chem. Phys.* **2011,** *129,* 501–505. doi:10.1016/j.matchemphys.2011.04.055
20. Lin, Y.-J.; Chang, Y.-H.; Chen, G.-J.; Chang, Y.-S.; Chang, Y.-C. *J. Alloys Compd.* **2009,** *479,* 785–790. doi:10.1016/j.jallcom.2009.01.061
21. Reber, J. F.; Rusek, M. *J. Phys. Chem.* **1986,** *90,* 824–834. doi:10.1021/j100277a024
22. Khan, M. M. T.; Bhardwaj, R. C.; Bhardwaj, C. *Int. J. Hydrogen Energy* **1988,** *13,* 7–10. doi:10.1016/0360-3199(88)90003-1

23. Dzhagan, V. M.; Stroyuk, O. L.; Rayevska, O. E.; Kuchmiy, S. Y.; Valakh, M. Y.; Azhniuk, Y. M.; von Borczyskowski, C.; Zahn, D. R. T. *J. Colloid Interface Sci.* **2010,** *345,* 515–523. doi:10.1016/j.jcis.2010.02.001
24. Shen, S.; Guo, L.; Chen, X.; Ren, F.; Mao, S. S. *Int. J. Hydrogen Energy* **2010,** *35,* 7110–7115. doi:10.1016/j.ijhydene.2010.02.013
25. Zhou, Z.; Long, M.; Cai, W.; Cai, J. *J. Mol. Catal. A: Chem.* **2012,** *353–354,* 22–28. doi:10.1016/j.molcata.2011.10.025
26. Kryukov, A. I.; Stroyuk, A. L.; Zin'chuk, N. N.; Korzhak, A. V.; Kuchmii, S. Y. *J. Mol. Catal. A: Chem.* **2004,** *221,* 209–221. doi:10.1016/j.molcata.2004.07.009
27. Yu, T.-H.; Cheng, W.-Y.; Chao, K.-J.; Lu, S.-Y. *Nanoscale* **2013,** *5,* 7356–7360. doi:10.1039/c3nr02658b

License and Terms

This is an Open Access article under the terms of the Creative Commons Attribution License (http://creativecommons.org/licenses/by/2.0), which permits unrestricted use, distribution, and reproduction in any medium, provided the original work is properly cited.

The license is subject to the *Beilstein Journal of Nanotechnology* terms and conditions: (http://www.beilstein-journals.org/bjnano)

The definitive version of this article is the electronic one which can be found at: doi:10.3762/bjnano.5.69

Beilstein Journal of Nanotechnology

Enhanced photocatalytic activity of Ag–ZnO hybrid plasmonic nanostructures prepared by a facile wet chemical method

Sini Kuriakose[1], Vandana Choudhary[1], Biswarup Satpati[2] and Satyabrata Mohapatra[*1,§]

Full Research Paper

Open Access

Address:
[1]School of Basic and Applied Sciences, Guru Gobind Singh Indraprastha University, Dwarka, New Delhi 110078, India and [2]Saha Institute of Nuclear Physics, 1/AF Bidhannagar, Kolkata 700064, India

Email:
Satyabrata Mohapatra[*] - smiuac@gmail.com

* Corresponding author
§ Phone: +91 11 25302414

Keywords:
Ag–ZnO; hybrid plasmonic nanostructures; photocatalysis

Beilstein J. Nanotechnol. **2014,** *5,* 639–650.
doi:10.3762/bjnano.5.75

Received: 20 December 2013
Accepted: 24 April 2014
Published: 15 May 2014

This article is part of the Thematic Series "Photocatalysis".

Guest Editor: R. Xu

© 2014 Kuriakose et al; licensee Beilstein-Institut.
License and terms: see end of document.

Abstract

We report the synthesis of Ag–ZnO hybrid plasmonic nanostructures with enhanced photocatalytic activity by a facile wet-chemical method. The structural, optical, plasmonic and photocatalytic properties of the Ag–ZnO hybrid nanostructures were studied by X-ray diffraction (XRD), field emission scanning electron microscopy (FESEM), transmission electron microscopy (TEM), photoluminescence (PL) and UV–visible absorption spectroscopy. The effects of citrate concentration and Ag nanoparticle loading on the photocatalytic activity of Ag–ZnO hybrid nanostructures towards sun-light driven degradation of methylene blue (MB) have been investigated. Increase in citrate concentration has been found to result in the formation of nanodisk-like structures, due to citrate-assisted oriented attachment of ZnO nanoparticles. The decoration of ZnO nanostructures with Ag nanoparticles resulted in a significant enhancement of the photocatalytic degradation efficiency, which has been found to increase with the extent of Ag nanoparticle loading.

Introduction

The removal of hazardous materials such as dyes and organic compounds from waste water has attracted ever increasing attention over the years. Semiconductor photocatalysis is one of the most important technologies used for the complete mineralization of a wide range of organic dyes and toxic chemicals. ZnO, a wide band gap semiconductor with large excitonic binding energy is suitable for diverse applications including UV lasers [1], field effect transistors [2], dye sensitized solar cells [3,4], surface enhanced Raman spectroscopy (SERS) [5] and biomedical applications [6-10]. ZnO nanostructures are

promising photocatalysts because of their high quantum efficiency, high redox potential, superior physical and chemical stability, non-toxicity and low cost [11-16]. However, ZnO nanostructures suffer from drawbacks such as a high electron–hole recombination rate and the inefficient utilization of sun light, which limit their photocatalytic activity [17,18]. Several attempts have been made to improve the photocatalytic efficiency of ZnO by decreasing the rate of recombination of electrons and holes by surface modification with noble metal nanoparticles [19-24]. Surface modification of ZnO nanostructures with noble metal nanoparticles improves the photocatalytic efficiency, since the noble metal–ZnO system has two distinct features. Firstly, noble metal–ZnO contacts result in a Schottky junction, which creates an internal electric field close to the interface causing the photogenerated electrons and holes to move in different directions, which results in a decrease of their recombination rate [19]. Secondly, noble metal nanoparticles on ZnO exhibit localized surface plasmon resonance (LSPR) absorption of light which can have significant impact on semiconductor photocatalysis. The LSPR wavelength of noble metal nanoparticles can be tuned from near UV to the visible region by controlling their size, shape, inter-particle spacing and surrounding medium [25]. In case of ZnO modified with noble metal nanoparticles, LSPR absorption can lead to enhanced utilization of UV–visible light as compared to pure ZnO [26-28]. Silver nanoparticles decorated ZnO nanostructures of various morphology have shown considerable increase in the photocatalytic efficiency for the degradation of organic dyes [19,23,29-34]. Xie et al. [23] have shown that Ag loading on ZnO nanostructures improves its photostability and enhances the photocatalytic activity due to increased efficiency for separation of photogenerated electrons and holes. It has been shown that Ag–ZnO nanostructures take 80 min for the complete photocatalytic degradation of 0.2 μM crystal violet dye under UV irradiation. Liu et al. [30] have studied the effects of Ag loading on ZnO on the photocatalytic degradation of rhodamine B (RhB) and showed that the degradation of RhB over pure Ag nanowires was negligible as compared to ZnO, the degradation efficiency of which further was increased due to the decoration with Ag nanoparticles. Deng et al. [19] fabricated Ag nanoparticles decorated ZnO microrods, by photoreduction of Ag ions onto the surface of the ZnO microrods prepared through a solvothermal-assisted method, which showed enhanced sun light active photocatalytic activity. In this paper, we report the synthesis of Ag–ZnO hybrid plasmonic nanostructures by a two-step facile wet chemical method involving the trisodium citrate assisted photoreduction of Ag ions onto the surface of ZnO nanostructures, prepared by a facile wet chemical method. The effects of citrate concentration and Ag nanoparticle loading on the photocatalytic activity of Ag–ZnO hybrid plasmonic nanostructures towards sun-light driven degradation of methylene blue (MB) dye have been investigated.

Results and Discussion

Morphology and crystal structure

FESEM images of as-synthesized ZnO and Ag–ZnO samples with varying citrate concentrations for different $[Ag^+]$/[citrate] ratios are shown in Figure 1. The presence of aggregates of ZnO nanoparticles of anisotropic shapes can be seen in the FESEM image (Figure 1a) of the pristine ZnO sample. Addition of citrate at 0.2 mM concentration resulted in an increased aggregation of the nanoparticles, as shown in Figure 1b. As the citrate concentration is increased to 10 mM, the oriented attachment of the aggregated nanoparticles resulted in complex nanostructures (Figure 1c). In Figure 1d we show the FESEM image of Ag–ZnO sample AZ510, which was prepared by using citrate a concentration of 20 mM and a $AgNO_3$ concentration of 2 mM. It can be clearly seen that as the citrate concentration is increased to 20 mM, nanodisk-like structures formed due to oriented attachment of aggregating nanoparticles. It is evident from the FESEM images that above a threshold concentration trisodium citrate assists in the oriented attachment of ZnO nanoparticles and leads to the formation of nanodisk-like structures, even at room temperature. Cao et al. [35] have studied the effects of citrate on the morphology of the ZnO nanostructures. It has been shown that citrate ions bind to the ZnO(0001) surface through the –COOH and –OH groups and suppress the growth along the <0001> direction. Thus, growth proceeds sideways, which leads to the formation of nanodisk-like structures. Our FESM results showing formation of nanodisk-like structures at higher citrate concentration go in line with this.

Figure 2 shows the XRD patterns of as-synthesized ZnO and Ag–ZnO samples (sample nomenclature shown in Table 1, see section Experimental) prepared with varying $[Ag^+]$/[citrate] ratios and $AgNO_3$ concentrations. The observed peaks can be well indexed to the hexagonal wurtzite structure of bulk crystalline ZnO [JCPDS no. 36-1451] and the face centred cubic structure of Ag [JCPDS card no. 04-0783]. Appearance of Ag peaks in the diffraction patterns clearly indicates the formation of crystalline Ag nanoparticles by photoreduction onto ZnO nanostructures. No extra peaks related to any impurity or silver oxides were observed, which confirms that the as-synthesized products are pure wurtzite ZnO and Ag–ZnO hybrid nanostructures. The average crystallite size of the ZnO nanoparticles was estimated to be about 20 nm, while that of Ag nanoparticles varied from 8 to 20 nm in different as-synthesized Ag–ZnO samples.

In-depth structural information was further obtained using TEM studies. From a low-magnification TEM image (Figure 3a) of

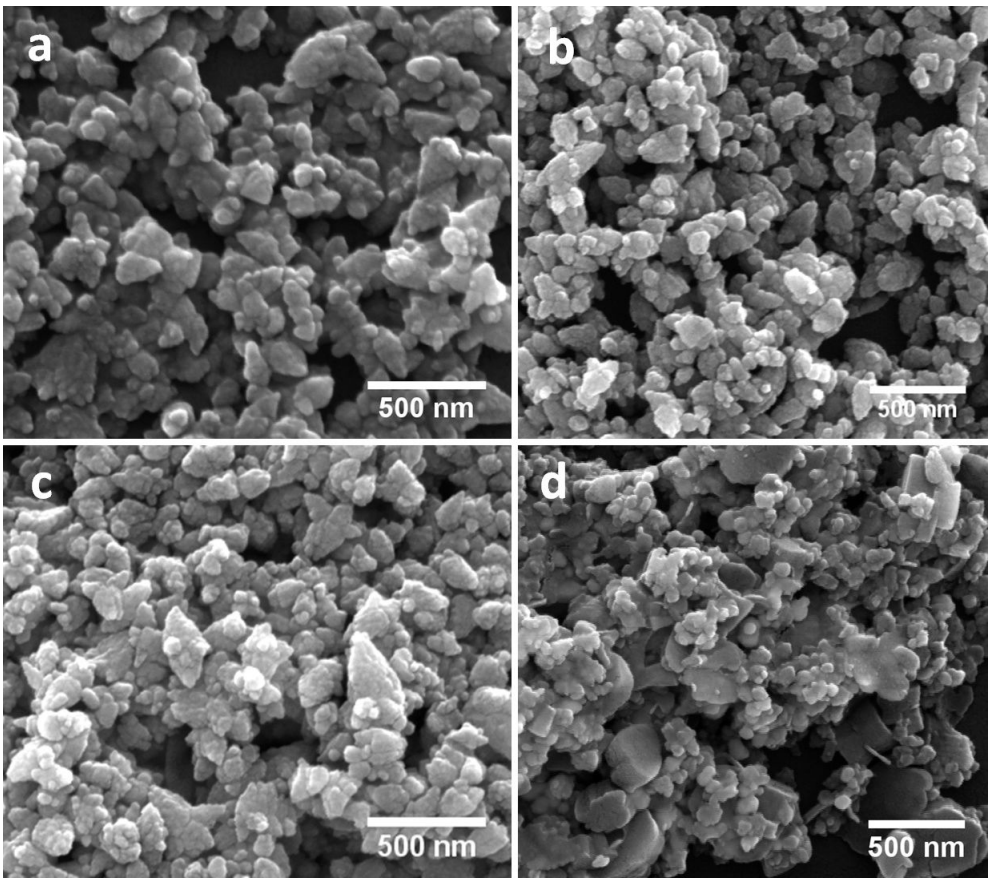

Figure 1: FESEM images of as-synthesized samples (a) PZ, (b) AZ21, (c) AZ410 and (d) AZ510 showing the effect of citrate concentration on the morphology of the samples.

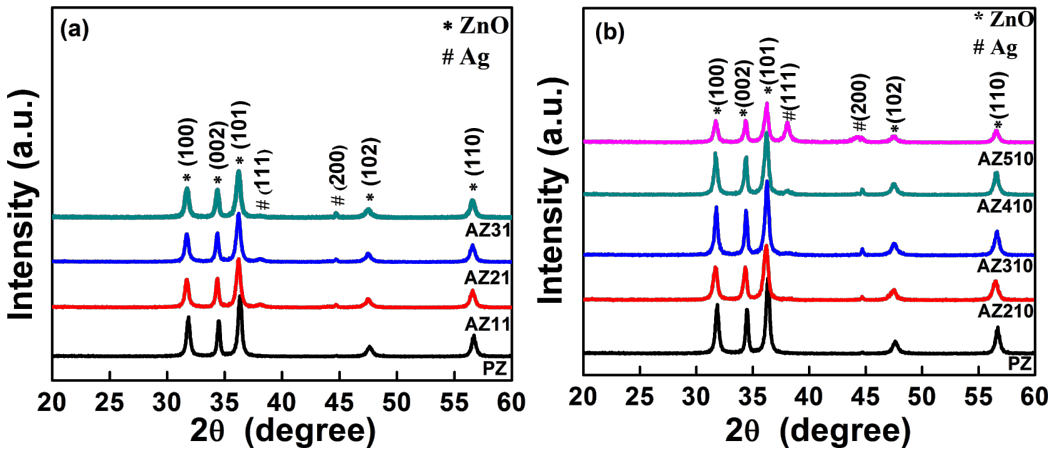

Figure 2: XRD patterns of as-synthesized ZnO and Ag–ZnO samples prepared with varying $AgNO_3$ concentrations and different $[Ag^+]$/[citrate] ratios (a) 1:1, (b) 1:10.

sample PZ, the presence of ZnO nanostructures of anisotropic shapes can be clearly seen. Higher magnification images revealed that these anisotropic nanostructures consist of smaller nanoparticles and are formed through aggregation. TEM images of AZ510 sample revealed the presence of anisotropic nanostructures decorated with nanoparticles. HRTEM study of these

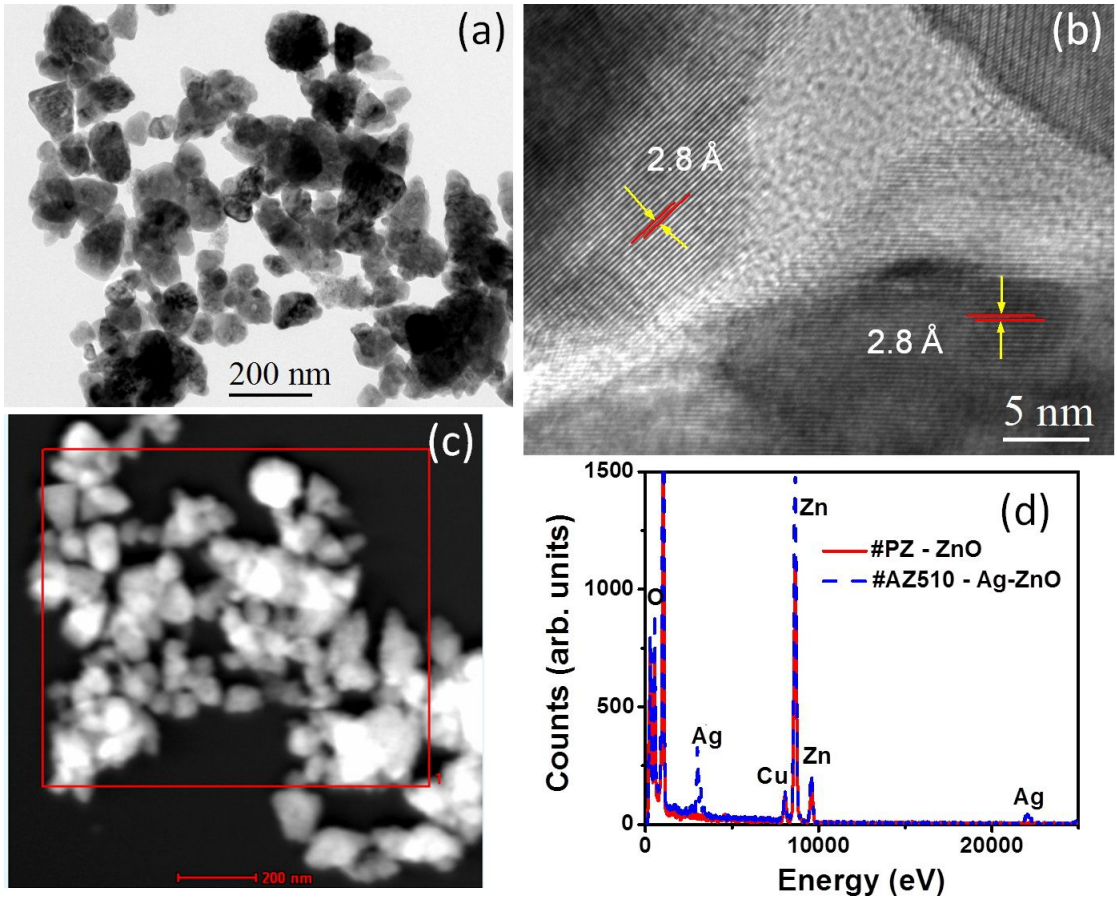

Figure 3: (a) Low-magnification TEM image of ZnO nanostructures in sample PZ. (b) HRTEM image showing lattice fringes. (c) STEM-HAADF image from the same area of TEM image. (d) EDX spectra from a region marked by area 1 in (c) and from area 2 in Figure 4c.

decorating nanoparticles confirmed them to be of Ag. Figure 4b shows the selected area diffraction (SAD) pattern from a region marked by a dotted circle. The SAD pattern shows concentric rings consisting of distinct spots, which is because of the presence of many small crystals and suggests the crystalline nature of heterostructures. The SAD pattern further confirms the formation of crystalline hexagonal phase of Ag–ZnO hybrid nanostructures. The high-resolution TEM image of ZnO nanostructures in Figure 3b clearly shows lattice fringes and the measured lattice spacing is 2.8 Å. The HRTEM image of of Ag–ZnO hybrid nanostructures shown in Figure 4b reveals lattice fringes of 2.3 Å and 2.8 Å, which correspond to the (111) and (100) interplanar spacing (*d*-spacings) of Ag and ZnO, respectively. Some of the measured *d*-spacings from the SAD pattern of Figure 4a are 2.84 Å, 2.50 Å, 1.49 Å, and 1.39 Å and these may be assigned as (100), (101), (103) and (112) interplanar spacing of hexagonal ZnO (*d*(100), *d*(101), *d*(103) and *d*(112) of ZnO are 2.81 Å, 2.47 Å, 1.47 Å, 1.37 Å, respectively) [JCPDS 36-1451]. In the SAD pattern there are also spots corresponding to Ag and one of them is marked in Figure 4a.

STEM-HAADF analysis was carried out to investigate the chemical composition of the Ag–ZnO hybrid nanostructures. STEM-HAADF analysis provides the *Z*-contrast image, where the intensity of scattered electrons is proportional to the square of the atomic number *Z*. Figure 3c shows the STEM-HAADF image of ZnO nanostructures in sample PZ. Energy dispersive X-ray spectroscopy (EDX) data from the regions marked by area 1 in Figure 3c and area 2 in Figure 4c is plotted in Figure 3d for ZnO and Ag–ZnO. The C and Cu signals in the EDX spectra are due to carbon-coated copper grid. The drift corrected EDX line profile was used to obtain the spatial distributions of the atomic contents across the Ag–ZnO nanostructures. Figure 4d shows the EDX profiles for Zn, O and Ag across the line marked in Figure 4c.

Figure 5 show the elemental mapping using EFTEM for obtaining the distributions of Zn, O and Ag atoms in the Ag–ZnO hybrid nanostructures. Chemical maps from Zn M (87 eV), O K (532 eV) and Ag N (56 eV) edges were obtained using the jump-ratio method by acquiring two images (one post-

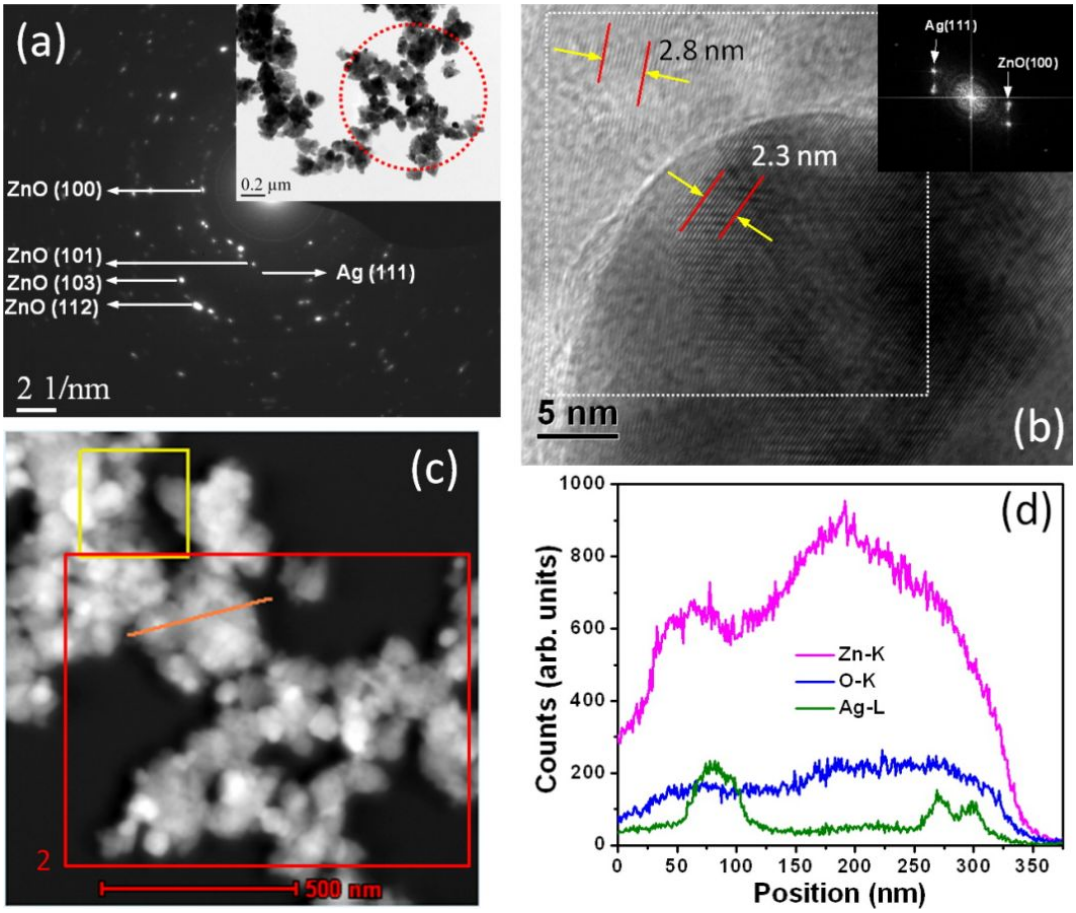

Figure 4: (a) Selected area diffraction pattern from Ag–ZnO hybrid nanostructures and in the inset low magnification TEM image of sample AZ510. (b) HRTEM image showing lattice fringes and in the inset FFT from a region marked by dotted box. (c) STEM-HAADF image from the same area of the TEM image. (d) EDX line profile from a region marked by line in (c) showing the distribution of different constituent elements across the nanostructures.

edge and one pre-edge), respectively, to extract the background, with an energy slit of 8 eV for Zn, 30 eV for O and 2 eV for Ag. The observed EFTEM images confirmed the decoration of ZnO nanostructures with Ag nanoparticles.

Optical absorption and photoluminescence

The UV–visible absorption spectra of samples with varying Ag concentration are shown in Figure 6a. It can be seen that Ag–ZnO samples exhibit two prominent absorption peaks. The first peak around 375 nm is attributed to the excitonic absorption peak of ZnO nanostructures. A weak and broad band around 480 nm has been found to emerge as the Ag concentration is increased. This band has been found to red shift, broaden and increase in intensity with increase in the extent of Ag nanoparticles loading onto ZnO nanostructures. It can be clearly seen that the sample AZ510 with the highest Ag concentration (2 mM) and citrate concentration (20 mM) exhibits a very broad band around 500 nm with much higher intensity as compared to other samples.

The observed broad bands around 480–500 nm are the characteristic SPR peak of Ag nanoparticles [23] and confirm the formation of Ag nanoparticles by photoreduction onto ZnO nanostructures. It should be pointed out here that Ag nanoparticles prepared by citrate-assisted reduction in aqueous solution shows SPR peaks around 400 nm. It is known that the SPR wavelength of noble metal nanoparticles can be tuned by tailoring the size, shape, inter-particle spacing and the surrounding medium [25]. Deposition of Ag nanoparticles onto ZnO nanostructures with higher refractive index leads to red shift in SPR. In addition, reduced inter-particle spacing due to increased Ag loading is expected to contribute to the observed red shift and significant broadening of the SPR peak, due to stronger electromagnetic coupling within the Ag nanoparticles deposited onto ZnO nanostructures.

The room-temperature PL spectra of Ag–ZnO samples with varying Ag concentrations are shown in Figure 6b. The peak at 375 nm is the near band edge emission peak of ZnO [19]. It is

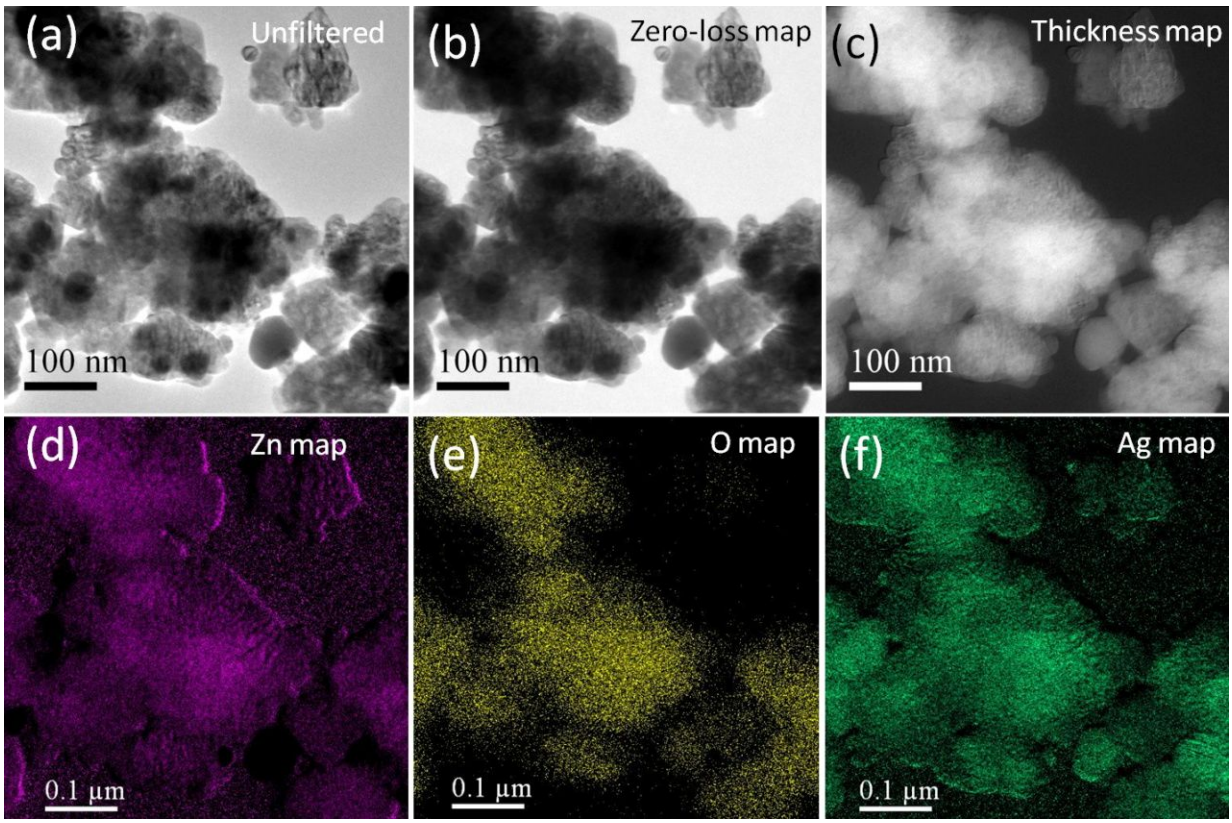

Figure 5: EFTEM images taken from the same area of a TEM image indicating the locations of different atoms across the nanostructure in sample AZ510. (a) Unfiltered image. (b) Zero-loss image. (c) Relative thickness map. (d) Chemical map of Zn (pink). (e) Chemical map of O (yellow). (f) Chemical map of Ag (green).

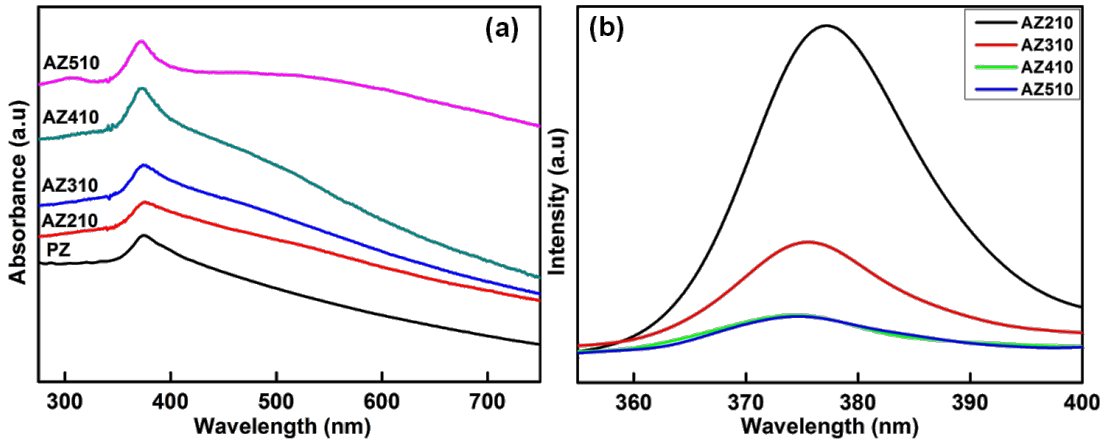

Figure 6: (a) UV-visible absorption spectra of samples AZ210, AZ310, AZ410 and AZ510 with varying Ag concentrations and [Ag]/[citrate] ratio of 1:10 and (b) corresponding room temperature PL spectra of these samples.

observed that the intensity of UV emission decreased with an increase in the Ag content of the samples. The decrease of intensity in UV region clearly indicates that the recombination of electrons and holes is suppressed [36]. The Ag nanoparticles deposited on the ZnO nanostructures act as sinks for the photo-generated electrons and hence result in the suppression of their recombination with the holes. Increase in Ag nanoparticle loading onto ZnO nanostructures leads to an efficient suppression of recombination of photogenerated electrons and holes, which, in turn, improves the photocatalytic efficiency.

Mechanism of citrate assisted growth of nanodisks

The formation of ZnO nanoparticles from aqueous solutions of zinc nitrate and KOH involves the following reactions [37]:

$$Zn^{2+} + 2OH^- \rightarrow Zn(OH)_2$$
$$Zn(OH)_2 \rightarrow ZnO + H_2O$$
$$Zn(OH)_2 + 2OH^- \leftrightarrow [Zn(OH)_4]^{2-}$$
$$ZnO + H_2O + 2OH^- \leftrightarrow [Zn(OH)_4]^{2-}$$

The concentration of KOH is an important factor in deciding the morphology of the ZnO nanostructures that are formed. The addition of aqueous KOH into Zn salt solution leads to formation of white precipitates of $Zn(OH)_2$, which decompose to form ZnO nuclei. Depending on the Zn^{2+} concentration and synthesis conditions, ZnO nuclei grow into nanoparticles. In the presence of excess OH^- ions (because of a higher KOH concentration) $[Zn(OH)_4]^{2-}$ ions form, which help in formation of aggregates of ZnO nanoparticles. As seen from the FESEM results (Figure 1), the amount of trisodium citrate has a significant effect on the morphology of the Ag–ZnO nanostructures. When the concentration of citrate is 1 mM, there is almost no change in the morphology of the sample as compared to that of pristine ZnO. However, when the citrate concentration was increased to 5 mM oriented attachment of the nanoparticles led to formation of complex shaped nanostructures. With the further increase of citrate concentration to 20 mM, nanodisk-like structures formed. Citrate ions with –COOH and –OH groups preferentially get adsorbed on the (0001) surface and prevent the accumulation of growth units on the (0001) surface. Because of this the growth of ZnO crystallites occurs along the six symmetric directions, producing ZnO nanodisks [38]. Thus the morphology of ZnO nanostructures can be easily altered by using trisodium citrate [39]. Detailed studies on the effects of trisodium citrate on the shape evolution of ZnO nanostructures will be reported elsewhere.

Photocatalytic studies

Figure 7 shows the UV–visible absorption spectra of 10 μM MB aqueous solutions with different photocatalysts AZ210, AZ310, AZ410 and AZ510 following the irradiation with sun

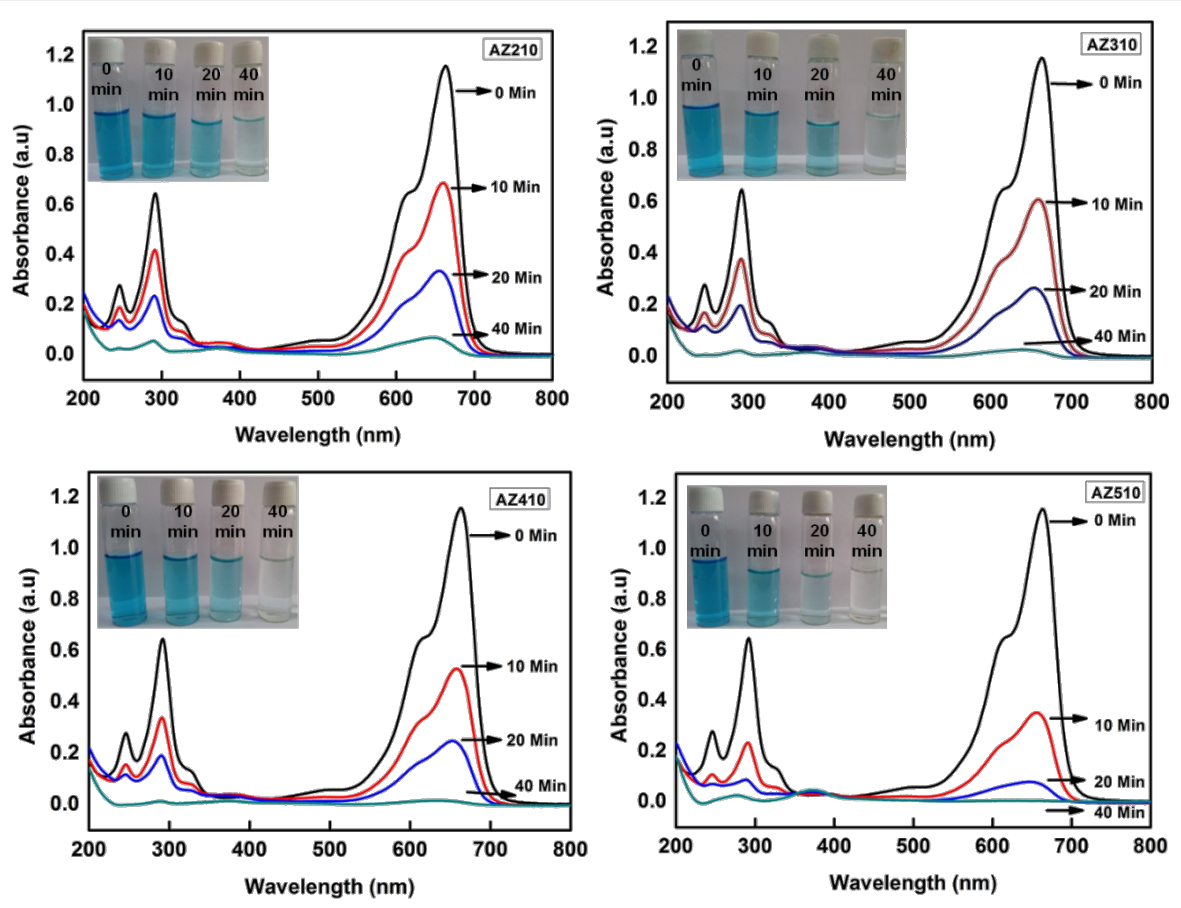

Figure 7: UV–visible absorption spectra showing the temporal evolution of the degradation of MB upon sun-light irradiation using Ag–ZnO samples AZ210, AZ310, AZ410 and AZ510, prepared with different $AgNO_3$ concentrations and a $[Ag^+]$/[citrate] ratio of 1: 10, as photocatalysts.

light for different durations of time. The characteristic absorption peak of MB at 664 nm is monitored as a function of sun-light exposure time. From Figure 7, it is clear that Ag–ZnO samples with higher Ag content lead to more efficient degradation of MB for the same exposure time. It can also be clearly seen that the photocatalytic efficiency is highest for AZ510, which has the maximum Ag nanoparticles loading and nanodisk-like structures, formed because of the higher citrate concentration.

The mechanisms underlying the enhanced photocatalytic activity of Ag–ZnO hybrid plasmonic nanostructures towards the degradation of MB can be understood as follows: The SPR of Ag nanoparticles helps in extending the light absorption of ZnO from near UV to the visible region, leading to an improved sun-light utilization efficiency. In addition, decoration with Ag nanoparticles significantly improves the charge separation in ZnO. When ZnO absorbs photons of energy greater than or equal to its band gap, electrons are promoted from its valence band to conduction band, creating an equal number of holes in the valence band. Since the energy level of conduction band of ZnO is higher than the Fermi level of Ag–ZnO hybrid structure, electrons flow from ZnO nanostructures to Ag nanoparticles. This way Ag nanoparticles act as efficient sinks for the photogenerated electrons, preventing their recombination with holes. This process, known as the direct electron transfer from semiconductor to the plasmonic nanostructures, is dependent on the alignment of electronic band structure of the noble metal and semiconductor. Furthermore, irradiation with sun light leads to the excitation of MB dye molecules adsorbed onto the ZnO nanostructures. The photoexcited MB molecules transfer electrons into the conduction band of ZnO [40]. The photogenerated electrons created by the above mentioned processes react with dissolved O_2 molecules forming superoxide anion radicals, while holes react with H_2O leading to the formation of hydroxyl radicals, both of which cause the degradation of the MB dye. These reactions can be summarized as follows [29,30] and are schematically illustrated in Figure 8.

$$\mathrm{ZnO} + h\nu \rightarrow e^- \left(\mathrm{CB}\right) + h^+ \left(\mathrm{VB}\right)$$

$$e^- + \mathrm{O_2} \rightarrow \bullet\mathrm{O_2^-}$$

$$\mathrm{Ag^+} + e^- \left(\mathrm{CB}\right) \rightarrow \mathrm{Ag}$$

$$h^+ + \mathrm{OH^-} \rightarrow \bullet\mathrm{OH}$$

$$\bullet\mathrm{OH} + \text{organic dye} \rightarrow \text{degradation products}$$

$$\bullet\mathrm{O_2^-} + \text{organic dye} \rightarrow \text{degradation products}$$

Yin et al. [41] prepared nanocomposites with Ag nanoparticle decorated ZnO nanorods with a core–shell structure by seed-mediated method. They have shown that Ag–ZnO is a better

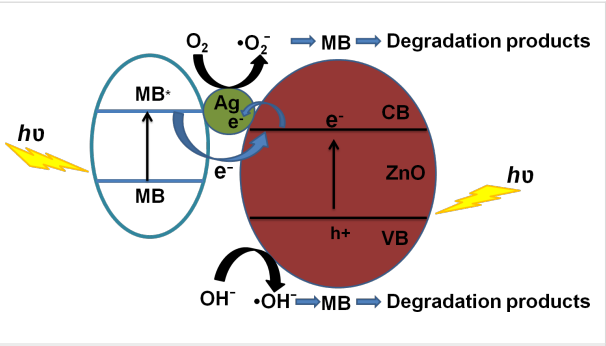

Figure 8: Schematic band diagram of Ag–ZnO hybrid nanostructure showing the charge redistribution processes that lead to the photocatalytic degradation of MB dye.

photocatalyst than ZnO because, firstly, the nanocomposites have a larger surface area as compared to ZnO, which leads to enhanced adsorption of dye. Secondly, due to the decoration of ZnO with Ag nanoparticles, the recombination of electrons and holes are inhibited. Gao et al. [42] synthesized Ag–ZnO nanocomposites by a biomolecule assisted hydrothermal method and studied their photocatalytic properties. They concluded that Ag nanoparticles improve the separation of electron and holes by acting as electron sinks. In our case, the photocatalytic efficiency is highest for sample AZ510, with nanodisk-like structures having higher surface area, and maximum Ag nanoparticle loading. The BET surface area of the pristine sample PZ and the sample AZ510 prepared with the highest citrate concentration were found out to be 13.5 and 15.9 $m^2 \cdot g^{-1}$, respectively.

Figure 9 shows the kinetics of MB degradation by using different Ag–ZnO hybrid nanostructures as photocatalysts under sun-light exposure. Figure 9a,b show the kinetics of MB degradation for photocatalysts with different Ag nanoparticles loading by using different $[Ag^+]$/[citrate] ratios 1:1 and 1:10. It can be seen that pristine ZnO nanostructures degraded only 52% of MB following 20 min of sun-light exposure, whereas all the Ag–ZnO hybrid plasmonic nanostructures led to enhanced photodegradation for the same exposure time. Among the various Ag–ZnO photocatalysts used, sample AZ510 exhibited the highest photocatalytic efficiency of 94% for the same exposure time of 20 min. Figure 9c shows the results of repetitive tests of the photocatalytic activity of AZ510 sample for four runs. It can be clearly seen that the efficiency of the photocatalyst remains high even after four runs.

The effects of citrate concentration and Ag loading on the photocatalytic efficiency can be summarized as follows. It can be clearly seen from that for the same citrate concentration, the photocatalytic efficiency increases with increasing Ag loading. Also, for the same Ag concentration, an increase in citrate

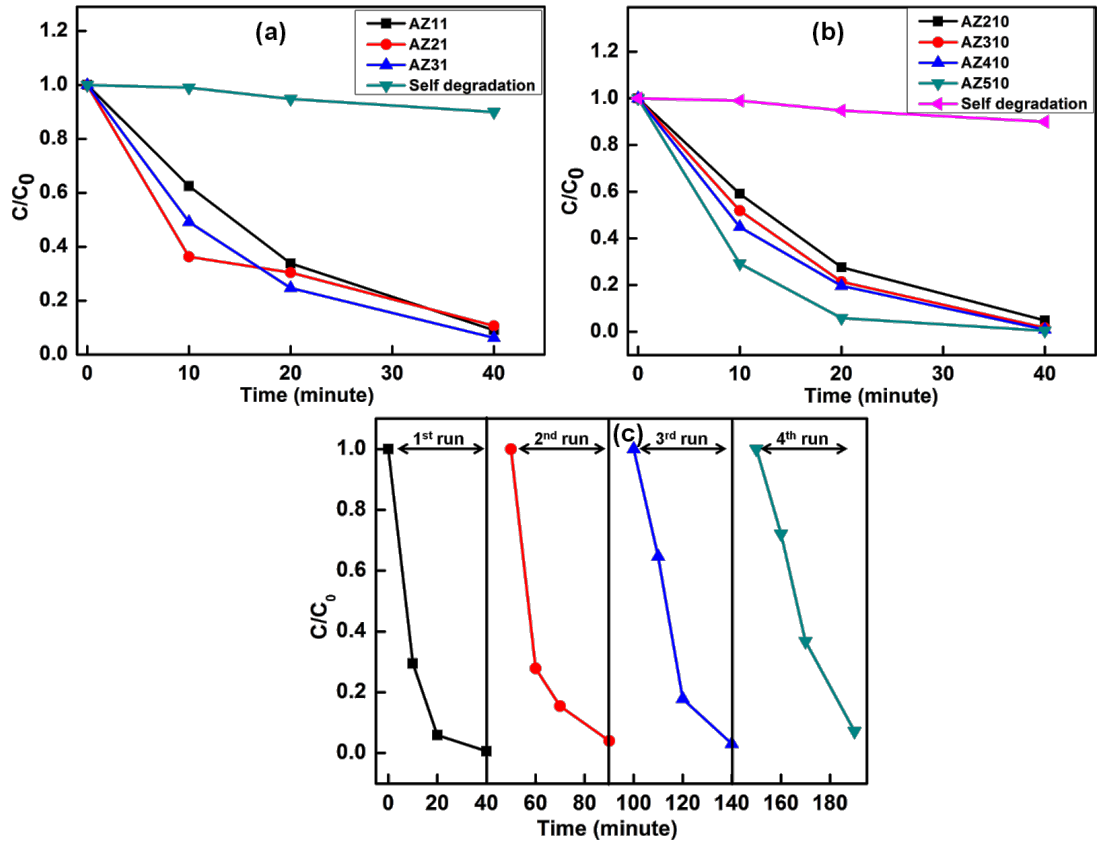

Figure 9: (a,b) Kinetics of MB photodegradation by Ag–ZnO hybrid plasmonic nanostructures with different Ag nanoparticle loading for different $[Ag^+]$/[citrate] concentrations. (c) Repetitive test for AZ510 photocatalyst for four runs.

concentration has been found to result in an increased efficiency of the photodegradation of MB. This clearly indicates that increase in the photocatalytic efficiency of the synthesized Ag–ZnO hybrid plasmonic nanostructures is mainly due to citrate-assisted morphological changes and changes in plasmonic coupling due to different level of Ag nanoparticle decoration. Beyond a threshold concentration, citrate plays an important role in changing the morphology of ZnO nanostructures so that it has a larger surface area as compared to the pristine sample. The sample AZ510, prepared with highest citrate concentration and with maximum Ag nanoparticles loading, exhibited higher BET surface area as compared to other samples. The larger surface area of nanodisk-like structures in AZ510 facilitates enhanced dye adsorption. In addition, Ag nanoparticles act as sinks for the photogenerated electrons and hence suppress the recombination of electrons and holes. The observed enhanced photocatalytic activity of Ag–ZnO hybrid plasmonic nanostructures is mainly due to citrate-assisted formation of nanodisks with better photocatalytic efficiency and improved sun-light utilization due to the plasmonic response of Ag nanoparticles, which suppress the recombination of photodegenerated electrons and holes.

Conclusion

We have successfully synthesized the Ag–ZnO plasmonic nanohybrids with enhanced photocatalytic activity by a facile wet chemical method. ZnO nanostructures were decorated with Ag nanoparticles by citrate assisted photoreduction. Higher citrate concentrations resulted in the formation of nanodisks due to citrate-assisted oriented attachment of ZnO nanostructures. The photocatalytic efficiency of ZnO nanostructures has been found to increase with extent of Ag nanoparticles loading. We have demonstrated that the photocatalytic activity of ZnO nanostructures can be significantly enhanced upon decoration with Ag nanoparticles, which suppress the recombination of photodegenerated electrons and holes and improve sun-light utilization due to plasmonic response of Ag nanoparticles.

Experimental

Materials

Zinc nitrate hexahydrate ($Zn(NO_3)\cdot 6H_2O$, Merck, Germany) and potassium hydroxide (KOH, SRL, India) were used as the starting materials for the synthesis of ZnO nanostructures. Silver nitrate ($AgNO_3$, Spectrochem, India) and trisodium citrate ($Na_3C_6H_5O_7$, CDH, India) were used for the photodepo-

sition of Ag nanoparticles onto ZnO nanostructures. Methylene blue (MB, SRL India) was used as dye for photocatalysis studies. All chemicals were of analytical grade and were used as received without any further purification.

Synthesis of ZnO nanoparticles

ZnO nanoparticles were prepared by a water-based facile wet chemical method by slowly adding an aqueous KOH solution to a $Zn(NO_3)\cdot 6H_2O$ solution at room temperature under stirring. In a typical synthesis, 200 mL aqueous solution of 0.1 M $Zn(NO_3)\cdot 6H_2O$ and 100 mL of 2 M KOH solution were prepared and separately stirred until they became clear. The KOH solution was then added drop-wise into the Zn salt solution under continuous stirring so as to reach pH ≈ 12. The mixture with white precipitates was continuously stirred for 2 h and aged overnight at room temperature. The precipitate was then filtered out, thoroughly washed with deionized water and then dried in an oven for 20 h at 80 °C leading to the formation of ZnO nanoparticles in powder form.

Synthesis of Ag–ZnO hybrid nanostructures

For the synthesis of Ag–ZnO hybrid nanostructures, synthesized ZnO nanoparticles were redispersed in 100 mL of deionized water under sonication. To this aqueous solution, different concentrations of trisodium citrate ranging from 0.1 to 20 mM were added and continuously stirred overnight. Silver nitrate of concentrations varying from 0.1 to 2 mM was added into these solutions under stirring for 30 min in the dark. The $[Ag^+]$/[citrate] concentration ratios in these solutions were chosen to be 1:1 and 1:10 for different $AgNO_3$ concentrations. Photoreduction of Ag ions was carried out by irradiation of these suspensions with sun light for 2 h for the photodeposition of Ag nanoparticles onto the surface of ZnO nanostructures. The color of the suspensions changed rapidly from white to pale yellow and in some cases to grey depending on the Ag concentration. The colored precipitates formed were centrifuged, thoroughly washed with deionized water and dried in an oven at 80 °C for 20 h. The nomenclature of the synthesized samples obtained with different $[Ag^+]$/[citrate] concentration ratios and $AgNO_3$ concentrations are given in Table 1.

Characterization

The structural properties of the synthesized samples were determined by powder X-ray diffraction (XRD) at room temperature by using a Panalytical X'pert Pro diffractometer with Cu Kα radiation (λ = 0.1542 nm). Field emission scanning electron microscopy (FESEM) was used for studying the morphology of ZnO and Ag–ZnO nanostructures. Transmission electron microscopy (TEM) investigations were carried out using a FEI, TECNAI G^2 F30, S-TWIN microscope operating at 300 kV. TEM machine is equipped with an Orius CCD camera from Gatan Inc., a HAADF detector from Fischione (Model 3000), an EDS detector from EDAX Inc., and a post-column Imaging Filter (Quantum SE, Model 963) from Gatan Inc. The sample was dispersed in ethanol by using an ultrasonic bath, mounted on a carbon coated Cu grid, dried, and used for TEM measurements. The optical properties of the samples were studied by UV–visible absorption spectroscopy and photoluminescence (PL) spectroscopy at room temperature. The powder samples were dispersed in deionized water by sonication and their optical properties were studied by UV–visible absorption spectroscopy by using a dual beam spectrophotometer HITACHI U3300 in the wavelength range of 200–800 nm, with deionized water as the reference medium. PL studies using excitation at 325 nm were carried out on samples coated onto Si substrates. The surface area of selected samples was determined by N_2 adsorption/desorption measurements by using a BET 2375 surface area analyzer.

Photocatalytic measurements

The photocatalytic activity of ZnO nanostructures and Ag–ZnO hybrid plasmonic nanostructures was evaluated by the degradation of methylene blue (MB) dye under sun-light irradiation. For the photocatalytic studies, typically 5 mg of as-synthesized

Table 1: Sample nomenclature and the estimated photocatalytic efficiency.

sample	experimental conditions		photocatalytic Efficiency η (%) (*t* = 20 min)
	$AgNO_3$ concentration (mM)	$[Ag^+]$/[citrate] ratio	
PZ	0	—	52.1
AZ11	0.1	1:1	66.3
AZ21	0.2		69.7
AZ31	0.5		75.3
AZ210	0.2	1:10	73.1
AZ310	0.5		78.7
AZ410	1		80.3
AZ510	2		94.1

ZnO and Ag–ZnO nanostructures were ultrasonically dispersed in 5 mL deionized water. Aqueous MB solution was added to the photocatalyst mixture and thoroughly mixed. The reaction suspensions containing 10 μM MB and different (ZnO, Ag–ZnO) photocatalysts were irradiated with sun light for different times (10, 20, 40 min) with intermittent shaking for uniform mixing of the photocatalysts with the MB solution. The photocatalysts were removed from the suspensions by centrifugation following the sun light exposure. The concentration of MB in the resultant solutions were monitored by UV–visible absorption spectroscopy studies in the wavelength range of 200–800 nm, with deionized water as the reference medium. The photocatalytic degradation efficiency of the photocatalysts for MB dye was calculated using the following formula:

$$\eta = (C_0 - C)/C_0 ,$$

where C_0 is the concentration of aqueous MB solution before addition of any photocatalyst and C is the concentration of MB in the reaction suspension with photocatalyst following sunlight exposure for time t.

Acknowledgements

The authors are thankful to Ankush Vij, Saif A. Khan and Srikanth for their help in PL, SEM and XRD measurements, respectively. The authors are grateful to Prof. S. M. Manocha and Prof. L. M. Manocha for extending the facility for surface area measuments. SM is thankful to Department of Science and Technology (DST), New Delhi for providing XRD facility under Nano Mission program. SM is thankful to University Grants Commission (UGC), New Delhi for funding under Major Research Project (F.No: 41-865/2012 (SR)). SK is thankful to Guru Gobind Singh Indraprastha University, New Delhi for providing financial assistance through IP Research Fellowship.

References

1. Chu, S.; Wang, G.; Zhou, W.; Lin, Y.; Chernyak, L.; Zhao, J.; Kong, J.; Li, L.; Ren, J.; Liu, J. *Nat. Nanotechnol.* **2011,** *6,* 506–510. doi:10.1038/nnano.2011.97
2. Park, Y. K.; Choi, H. S.; Kim, J.-H.; Kim, J.-H.; Hahn, Y.-B. *Nanotechnology* **2011,** *22,* 185310. doi:10.1088/0957-4484/22/18/185310
3. Zhang, Q.; Dandeneau, C. S.; Zhou, X.; Cao, G. *Adv. Mater.* **2009,** *21,* 4087–4108. doi:10.1002/adma.200803827
4. Seow, Z. L. S.; Wong, A. S. W.; Thavasi, V.; Jose, R.; Ramakrishna, S.; Ho, G. W. *Nanotechnology* **2009,** *20,* 045604. doi:10.1088/0957-4484/20/4/045604
5. Wang, Y.; Ruan, W.; Zhang, J.; Yang, B.; Xu, W.; Zhao, B.; Lombardi, J. R. *J. Raman Spectrosc.* **2009,** *40,* 1072–1077. doi:10.1002/jrs.2241
6. Papavlassopoulos, H.; Mishra, Y. K.; Kaps, S.; Paulowicz, I.; Abdelaziz, R.; Elbahri, M.; Maser, E.; Adelung, R.; Röhl, C. *PLoS One* **2014,** *9,* e84983. doi:10.1371/journal.pone.0084983
7. Wahab, R.; Kaushik, N. K.; Kaushik, N.; Choi, E. H.; Umar, A.; Dwivedi, S.; Musarrat, J.; Al-Khedhairy, A. A. *J. Biomed. Nanotechnol.* **2013,** *9,* 1181–1189.
8. Antoine, T. E.; Mishra, Y. K.; Trigilio, J.; Tiwari, V.; Adelung, R.; Shukla, D. *Antiviral Res.* **2012,** *96,* 363–375. doi:10.1016/j.antiviral.2012.09.020
9. Mishra, Y. K.; Adelung, R.; Röhl, C.; Shukla, D.; Spors, F.; Tiwari, V. *Antiviral Res.* **2011,** *92,* 305–312. doi:10.1016/j.antiviral.2011.08.017
10. Ul-Islam, M.; Khattak, W. A.; Ullah, M. W.; Khan, S.; Park, J. K. *Cellulose* **2014,** *21,* 433–447. doi:10.1007/s10570-013-0109-y
11. Vayssieres, L. *Adv. Mater.* **2003,** *15,* 464–466. doi:10.1002/adma.200390108
12. Kamat, P. V. *J. Phys. Chem. C* **2007,** *111,* 2834–2860. doi:10.1021/jp066952u
13. Umar, A.; Chauhan, M. S.; Chauhan, S.; Kumar, R.; Kumar, G.; Al-Sayari, S. A.; Hwang, S. W.; Al-Hajry, A. *J. Colloid Interface Sci.* **2011,** *363,* 521–528. doi:10.1016/j.jcis.2011.07.058
14. Kaneva, N.; Stambolova, I.; Blaskov, V.; Dimitriev, Y.; Bojinova, A.; Dushkin, C. *Surf. Coat. Technol.* **2012,** *207,* 5–10. doi:10.1016/j.surfcoat.2011.10.020
15. Liu, Z.; Zhang, Q.; Li, Y.; Wang, H. *J. Phys. Chem. Solids* **2012,** *73,* 651–655. doi:10.1016/j.jpcs.2012.01.003
16. Yassıtepe, E.; Yatmaz, H. C.; Öztürk, C.; Öztürk, K.; Duran, C. *J. Photochem. Photobiol., A* **2008,** *198,* 1–6. doi:10.1016/j.jphotochem.2008.02.007
17. Yıldırım, Ö. A.; Unalan, H. E.; Durucan, C. *J. Am. Ceram. Soc.* **2013,** *96,* 766–773. doi:10.1111/jace.12218
18. Lu, Y.; Lin, Y.; Wang, D.; Wang, L.; Xie, T.; Jiang, T. *J. Phys. D: Appl. Phys.* **2011,** *44,* 315502. doi:10.1088/0022-3727/44/31/315502
19. Deng, Q.; Duan, X.; Ng, D. H. L.; Tang, H.; Yang, Y.; Kong, M.; Wu, Z.; Cai, W.; Wang, G. *ACS Appl. Mater. Interfaces* **2012,** *4,* 6030–6037. doi:10.1021/am301682g
20. Wang, Q.; Geng, B.; Wang, S. *Environ. Sci. Technol.* **2009,** *43,* 8968–8973. doi:10.1021/es902568h
21. Zeng, H.; Liu, P.; Cai, W.; Yang, S.; Xu, X. *J. Phys. Chem. C* **2008,** *112,* 19620–19624. doi:10.1021/jp807309s
22. Jing, L.; Wang, D.; Wang, B.; Li, S.; Xin, B.; Fu, H.; Sun, J. *J. Mol. Catal. A: Chem.* **2006,** *244,* 193–200. doi:10.1016/j.molcata.2005.09.020
23. Xie, W.; Li, Y.; Sun, W.; Huang, J.; Xie, H.; Zhao, X. *J. Photochem. Photobiol., A* **2010,** *216,* 149–155. doi:10.1016/j.jphotochem.2010.06.032
24. Zheng, Y.; Zheng, L.; Zhan, Y.; Lin, X.; Zheng, Q.; Wei, K. *Inorg. Chem.* **2007,** *46,* 6980–6986. doi:10.1021/ic700688f
25. Kelly, K. L.; Coronado, E.; Zhao, L. L.; Schatz, G. C. *J. Phys. Chem. B* **2003,** *107,* 668–677. doi:10.1021/jp026731y
26. Mishra, Y. K.; Mohapatra, S.; Singhal, R.; Avasthi, D. K.; Agarwal, D. C.; Ogale, S. B. *Appl. Phys. Lett.* **2008,** *92,* 043107. doi:10.1063/1.2838302
27. Mishra, Y. K.; Chakravadhanula, V. S. K.; Hrkac, V.; Jebril, S.; Agarwal, D. C.; Mohapatra, S.; Avasthi, D. K.; Kienle, L.; Adelung, R. *J. Appl. Phys.* **2012,** *112,* 064308. doi:10.1063/1.4752469
28. Thomann, I.; Pinaud, B. A.; Chen, Z.; Clemens, B. M.; Jaramillo, T. F.; Brongersma, M. L. *Nano Lett.* **2011,** *11,* 3440–3446. doi:10.1021/nl201908s

29. Gu, C.; Cheng, C.; Huang, H.; Wong, T.; Wang, N.; Zhang, T.-Y. *Cryst. Growth Des.* **2009,** *9,* 3278–3285. doi:10.1021/cg900043k
30. Liu, H. R.; Shao, G. X.; Zhao, J. F.; Zhang, Z. X.; Zhang, Y.; Liang, J.; Liu, X. G.; Jia, H. S.; Xu, B. S. *J. Phys. Chem. C* **2012,** *116,* 16182–16190. doi:10.1021/jp2115143
31. Height, M. J.; Pratsinis, S. E.; Mekasuwandumrong, O.; Praserthdam, P. *Appl. Catal., B: Environ.* **2006,** *63,* 305–312. doi:10.1016/j.apcatb.2005.10.018
32. Lin, D.; Wu, H.; Zhang, R.; Pan, W. *Chem. Mater.* **2009,** *21,* 3479–3484. doi:10.1021/cm900225p
33. Georgekutty, R.; Seery, M. K.; Pillai, S. C. *J. Phys. Chem. C* **2008,** *112,* 13563–13570. doi:10.1021/jp802729a
34. Zheng, Y.; Chen, C.; Zhan, Y.; Lin, X.; Zheng, Q.; Wei, K.; Zhu, J. *J. Phys. Chem. C* **2008,** *112,* 10773–10777. doi:10.1021/jp8027275
35. Cao, X.; Zeng, H.; Wang, M.; Xu, X.; Fang, M.; Ji, S.; Zhang, L. *J. Phys. Chem. C* **2008,** *112,* 5267–5270. doi:10.1021/jp800499r
36. Liu, X.; Wu, X.; Cao, H.; Chang, R. P. H. *J. Appl. Phys.* **2004,** *95,* 3141. doi:10.1063/1.1646440
37. Bian, S.-W.; Mudunkotuwa, I. A.; Rupasinghe, T.; Grassian, V. H. *Langmuir* **2011,** *27,* 6059–6068. doi:10.1021/la200570n
38. Cho, S.; Jung, S.-H.; Lee, K.-H. *J. Phys. Chem. C* **2008,** *112,* 12769–12776. doi:10.1021/jp803783s
39. Sun, Y.; Wang, L.; Yu, X.; Chen, K. *CrystEngComm* **2012,** *14,* 3199–3204. doi:10.1039/c2ce06335b
40. Rehman, S.; Ullah, R.; Butt, A. M.; Gohar, N. D. *J. Hazard. Mater.* **2009,** *170,* 560–569. doi:10.1016/j.jhazmat.2009.05.064
41. Yin, X.; Que, W.; Fei, D.; Shen, F.; Guo, Q. *J. Alloys Compd.* **2012,** *524,* 13–21. doi:10.1016/j.jallcom.2012.02.052
42. Gao, S.; Jia, X.; Yang, S.; Li, Z.; Jiang, K. *J. Solid State Chem.* **2011,** *184,* 764–769. doi:10.1016/j.jssc.2011.01.025

License and Terms

This is an Open Access article under the terms of the Creative Commons Attribution License (http://creativecommons.org/licenses/by/2.0), which permits unrestricted use, distribution, and reproduction in any medium, provided the original work is properly cited.

The license is subject to the *Beilstein Journal of Nanotechnology* terms and conditions: (http://www.beilstein-journals.org/bjnano)

The definitive version of this article is the electronic one which can be found at: doi:10.3762/bjnano.5.75

Beilstein Journal of Nanotechnology

Effects of the preparation method on the structure and the visible-light photocatalytic activity of Ag_2CrO_4

Difa Xu[1,2], Shaowen Cao[1], Jinfeng Zhang[1], Bei Cheng[1] and Jiaguo Yu[*1]

Full Research Paper

Open Access

Address:
[1]State Key Laboratory of Advanced Technology for Materials Synthesis and Processing, Wuhan University of Technology, Wuhan 430070, P. R. China and [2]Department of Biological and Environmental Science, Changsha University, Changsha 410022, P.R. China

Email:
Jiaguo Yu[*] - jiaguoyu@yahoo.com

* Corresponding author

Keywords:
microemulsion method; nanoparticles; photocatalysis; photocatalytic activity; silver chromate; visible-light-driven

Beilstein J. Nanotechnol. **2014,** *5,* 658–666.
doi:10.3762/bjnano.5.77

Received: 06 January 2014
Accepted: 22 April 2014
Published: 19 May 2014

This article is part of the Thematic Series "Photocatalysis".

Guest Editor: R. Xu

© 2014 Xu et al; licensee Beilstein-Institut.
License and terms: see end of document.

Abstract

Silver chromate (Ag_2CrO_4) photocatalysts are prepared by microemulsion, precipitation, and hydrothermal methods, in order to investigate the effect of preparation methods on the structure and the visible-light photocatalytic activity. It is found that the photocatalytic activity of the prepared $Ag_2CrO_4$was highly dependent on the preparation methods. The sample prepared by microemulsion method exhibits the highest photocatalytic efficiency on the degradation of methylene blue (MB) under visible-light irradiation. The enhanced photocatalytic activity could be ascribed to the smaller particle size, higher surface area, relatively stronger light absorption, and blue-shift absorption edge, which result in the adsorption of more MB molecules, a shorter diffusion process of more photogenerated excitons, and a stronger oxidation ability of the photogenerated holes. Considering the universalities of microemulsion, precipitation, and hydrothermal methods, this work may also provide a prototype for the comparative study of semiconductor based photocatalysis for water purification and environmental remediation.

Introduction

Semiconductor photocatalysis has been considered as a potential solution to the worldwide energy shortage and for counteracting environmental degradation [1-5]. Numerous efforts have been made to develop efficient and stable photocatalysts during the past decades. TiO_2 is most widely studied because of its low cost, non-toxicity, high efficiency and long-time photostability [6-11]. However, due to its large band gap of about 3.2 eV, TiO_2 is only active in the ultraviolet (UV) region that corresponds to 3–4% of the solar light. Therefore, the development of visible-light-driven photocatalysts has received considerable attention as visible light (400–800 nm) is abundant in the solar spectrum [12-16]. Some semiconductors such as $BiVO_4$ [17-19], Bi_2O_3 [20,21], Fe_2O_3 [22-25], and Cu_2O [26-28] have been developed as photocatalysts with visible-light activities.

Recently, a family of Ag-based salts, including Ag_3PO_4 [29,30], Ag_2CO_3 [31,32], $AgVO_3$ [33,34], $AgGaO_2$ [35,36], has attracted particular interests due to their ability to split water, as well as decompose organic contaminants both in air and aqueous solution. However, Ag_2CrO_4 is neglected although it has been explored as cathode for lithium cells in early years [37-39]. Actually, the band gap of Ag_2CrO_4 is narrow enough (about 1.75 eV) to obtain strong absorption in visible-light region [40], and thus may enable it to perform excellent visible-light photocatalytic activity. However, up to now, the photocatalytic studies on Ag_2CrO_4 are still limited with only few reports [40-42].

So far, several methods have been employed for the preparation of Ag_2CrO_4 crystals, such as precipitation [43], reversed-micellar [44], hydrothermal [45], sonochemical [41], and template methods [46]. It is known that the photocatalytic activity of semiconductor photocatalysts relies heavily on their structures, which are commonly determined by the preparation methods [47-49]. Nevertheless, to our knowledge, there is no comparative study about the effect of the preparation methods on the structure and photocatalytic performance of Ag_2CrO_4. Herein, for the first time, special attention is paid to evaluate the effect of preparation methods on the structure and visible-light photocatalytic activity of Ag_2CrO_4. Microemulsion, precipitation, and hydrothermal methods are selected for preparing Ag_2CrO_4 photocatalysts, as they are simple, efficient, and extensively used preparation methods for semiconductor crystals. In this case, the present work can also provide a prototype for comparative study of other semiconductor photocatalysts. The performance of the developed Ag_2CrO_4 is evaluated by the photocatalytic degradation of methylene blue under visible-light irradiation. The effect of the three preparation methods on the structure, optical properties and photocatalytic activity are investigated and discussed.

Results and Discussion

Phase structure and morphology

The X-ray diffraction (XRD) patterns are shown in Figure 1. All the diffraction peaks for the S-M, S-P, and S-H samples respectively prepared by microemulsion, precipitation, and hydrothermal methods can be indexed to the orthorhombic phase of Ag_2CrO_4 (JCPDS No. 26-0952). It is noted that the diffraction peaks of S-H sample exhibit the highest intensity (Figure 1c), resulting from the improved crystallinity of Ag_2CrO_4 promoted by hydrothermal reaction at the high temperature and pressure conditions [45]. While the crystal growth in microemulsion is restricted due to the effect of steric barrier [50,51], it is not surprising that the lowest intensity is observed for the diffraction peaks of S-M sample (Figure 1a).

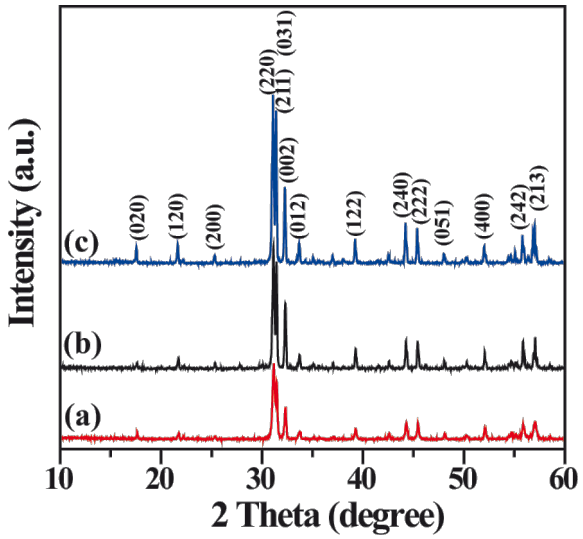

Figure 1: XRD patterns of Ag_2CrO_4 samples prepared by different methods: (a) microemulsion, (b) precipitation, and (c) hydrothermal.

Scanning electron microscope (SEM) images are taken to directly analyze the structure of the prepared Ag_2CrO_4 samples and particularly the effect of the preparation methods on the morphology changes. Figure 2 indicates that the S-M sample has a more homogenous morphology, and the average particle size is much smaller than those of S-P (ca. 800 nm) and S-H (ca. 1.2 μm) samples. For an in-depth investigation of the morphology and particle size of the S-M sample, transmission electron microscopy (TEM) observation is carried out. As

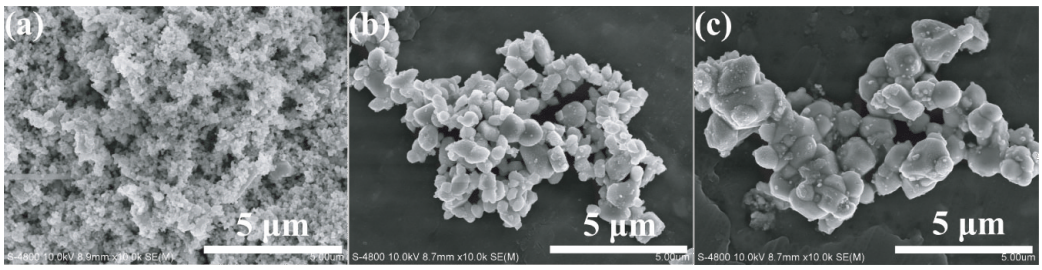

Figure 2: SEM images of Ag_2CrO_4 samples obtained from different methods: (a) microemulsion, (b) precipitation, and (c) hydrothermal.

shown in Figure 3a, the S-M sample is composed of nanoparticles with an average particle size of about 30 nm. The high-resolution transmission electron microscopy (HRTEM) image in Figure 3b clearly shows the lattice fringes with *d* spacings of 0.503 and 0.288 nm, which can be assigned to the (020) and (220), respectively, crystal planes of orthorhombic Ag_2CrO_4. The corresponding fast Fourier transform (FFT) image suggests a single-crystalline nature. This also indicates that the S-M sample is well-crystallized, although its XRD pattern exhibits a relatively lower intensity (Figure 1a). In our experiment, a dynamically stable and isotropic W/O reverse microemulsion system is established by using cyclohexane as oil phase, Triton X-100 as surfactant, and *n*-hexanol as co-surfactant, respectively. Hence a more homogeneous morphology and smaller particle size of Ag_2CrO_4 can be achieved since the precipitation reaction is restricted in nanosized water droplets, which are dispersed as liquid entities in a continuous oil media and act as nanoreactors for the synthesis of nanoparticles [52-55]. Furthermore, Triton X-100 serves as a nonionic surfactant in the W/O reverse microemulsion system to avoid the introduction of ionic impurities. These results suggest that the microemulsion method is superior for preparing Ag_2CrO_4 nanoparticles with homogenous distribution, as compared to the precipitation and hydrothermal methods.

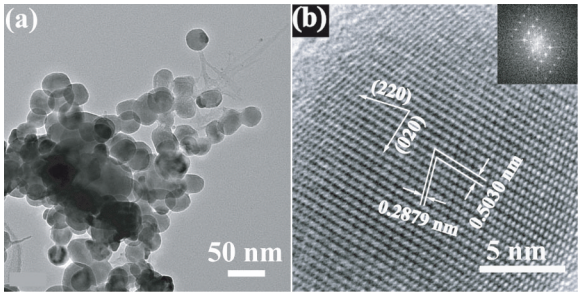

Figure 3: TEM (a) and HRTEM (b) images of Ag_2CrO_4 sample prepared by microemulsion method. The inset of (b) is the corresponding FFT image.

Brunauer–Emmett–Teller (BET) surface area and pore size distributions

Figure 4 shows the nitrogen adsorption–desorption isotherms and the corresponding pore size distributions of the as-prepared Ag_2CrO_4 photocatalysts. According to the Brunauer–Deming–Deming–Teller classification, the isotherms of all Ag_2CrO_4 samples are of type IV, indicating the presence of mesopores (2–50 nm) [56-58]. Moreover, the shapes of the hysteresis loops are of type H3 at the high relative pressure range from 0.8 to 1.0, which suggests the formation of large mesopores and macropores [56]. The pore size distributions (inset of Figure 4) are very broad, further confirming the presence of large mesopores and macropores. Considering the absence of a pore structure inside the individual nanoparticles on the basis of SEM and TEM results, these pores can be related to the pores between the aggregated Ag_2CrO_4 particles. The Ag_2CrO_4 samples show decreasing specific surface areas in the sequence S-M, S-P, and S-H, which are listed in Table 1. This is because the S-M sample has the smallest particle size, whereas the S-H sample has the largest particle size. Usually, photocatalysts with higher specific surface areas are beneficial for the enhancement of photocatalytic performance by facilitating the absorption of pollutants for degradation.

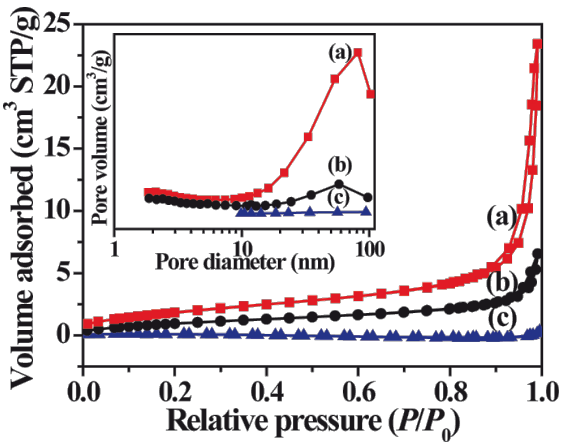

Figure 4: Nitrogen adsorption-desorption isotherms and corresponding pore size distribution curves (inset) of Ag_2CrO_4 samples prepared by different methods: (a) microemulsion, (b) precipitation, and (c) hydrothermal.

UV–vis spectroscopy measurements

A comparison of UV–vis diffuse reflectance spectra (DRS) and the corresponding colours of the Ag_2CrO_4 samples are

Table 1: Physical properties and photocatalytic performance of as-prepared samples.

sample	preparation method	particle size (nm)	S_{BET}[a] (m^2/g)	band gap (eV)	rate constant *k* (min^{-1})
S-M	microemulsion	30	7.0	1.85	0.033
S-P	precipitation	800	4.0	1.82	0.020
S-H	hydrothermal	1200	0.3	1.76	0.015

[a]BET specific surface area.

displayed in Figure 5. An enhanced absorption of visible light in the range of 400–600 nm and 700–900 nm can be observed for the S-M sample (Figure 5a), as compared to that for the S-P sample (Figure 5c), which may be attributed to the increased intensity of the scattered light in the sample with smaller particle size [59]. Moreover, there is an obvious blue shift of the absorption edge for the S-M sample, which should be explained in terms of the small size effect [60,61]. In contrast, a weaker light absorption and red shift of the absorption edge are observed for the S-H sample (Figure 5b), because it has the largest particle size among the three samples. The indirect band gaps of the Ag_2CrO_4 samples are calculated according to the Kubelka–Munk (KM) method by the following equation [62]:

$$\alpha h\nu = \mathrm{A}\left(h\nu - E_\mathrm{g}\right)^2, \qquad (1)$$

where α is the absorption coefficient, $h\nu$ is the photon energy, E_g is the indirect band gap, and A is a constant. As shown in the inset of Figure 5, the calculated band gap energies of the S-M, S-P and S-H samples are 1.85, 1.82 and 1.76 eV, respectively (Table 1). In spite of the little difference of the band gaps, it is clear that all the three Ag_2CrO_4 samples exhibit an excellent visible-light response for photocatalytic applications.

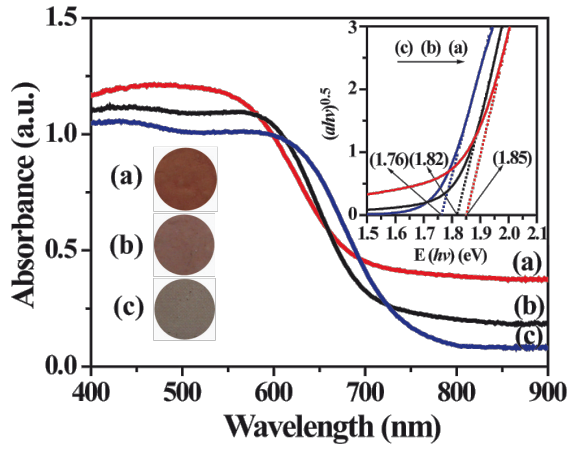

Figure 5: UV–visible diffuse reflectance spectra, the calculated band gaps (upper right inset) and the corresponding colours (lower left inset) of Ag_2CrO_4 samples prepared by different methods: (a) micro-emulsion, (b) precipitation, and (c) hydrothermal.

Calculation

Theoretically, the band structure of the Ag_2CrO_4 is also calculated by density function theory (DFT) (Figure 6). As shown in the band structure plots, the calculated band gap energy of Ag_2CrO_4 is 1.37 eV, which is lower than the experimental values, which is due to the well-known limitation of DFT calculation [63,64]. The electronic structure of Ag_2CrO_4 indicates that the valence band mainly consists of occupied Ag 4d and O 2p orbitals, and the conduction band mainly comes from the empty Cr 3d orbital, which means that Cr makes an important contribution to the bottom of the conduction band. It has been found that Ag is one of the elements that are able to form a valence band position higher than the O 2p orbital [65]. It has been demonstrated that Cr has the potential ability to lower down the bottom of the conduction band [40,66]. Thereby the synergistic effect of Ag and Cr elements results in the narrow band gap of Ag_2CrO_4. The calculated results also show that the top of the valence band is at the G point but the bottom of the conduction band is near the Z point, which confirms that Ag_2CrO_4 has an indirect band gap structure. These results indicate that Ag_2CrO_4 can potentially serve as a visible-light-driven photocatalyst.

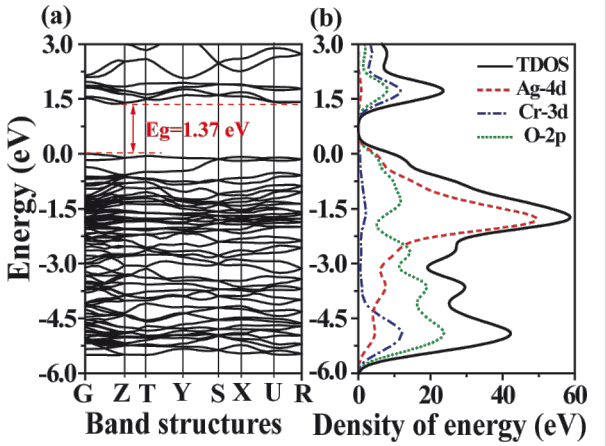

Figure 6: Band structure plots (a) and density of states (b) for Ag_2CrO_4.

Photocatalytic activity

We have measured the zeta potential of Ag_2CrO_4 as −15.8 mV at pH 6.8, suggesting that it is electronegative in neutral solutions. Since MB is a cationic dye, it can be easily adsorbed on the surface of Ag_2CrO_4 through electrostatic interaction. Therefore, the photocatalytic activity of the as-prepared Ag_2CrO_4 samples is evaluated through MB degradation under visible-light irradiation. Without any photocatalyst, no obvious MB degradation is observed under visible-light irradiation. For comparison, P25 (commercial TiO_2, Degussa, Germany) is also used as a reference. Figure 7 shows that all Ag_2CrO_4 samples exhibit a much better photocatalytic performance than P25 in the MB degradation. In particular, the S-M Ag_2CrO_4 sample shows the highest activity with a rate constant of 0.033 min^{-1}, and MB is almost completely degraded within 90 min. The S-P and S-H samples exhibit a lower activity with rate constants of 0.020 and 0.012 min^{-1}, respectively. P25 is a mixed-phase TiO_2 containing 25% rutile, whit a band gap of 3.0 eV, which results

in a weak visible-light absorption up to about 413 nm. Therefore, P25 still shows some photocatalytic activity under visible-light irradiation. But it is not surprising that the rate constant for P25 is only 0.007 min^{-1} because the other phase anatase (75%) is not active in the visible region.

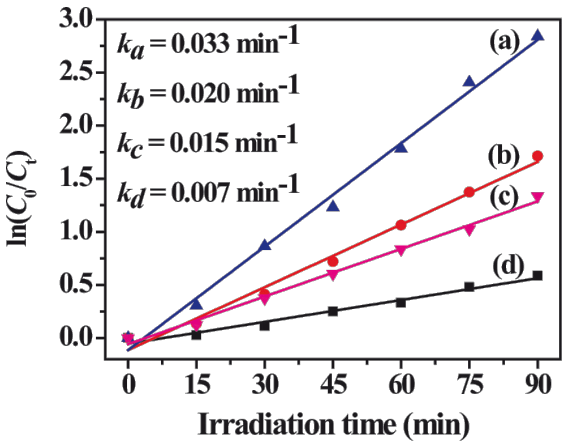

Figure 7: Photocatalytic degradation of MB aqueous solution over Ag_2CrO_4 samples prepared by (a) microemulsion, (b) precipitation, and (c) hydrothermal methods, and (d) P25 sample under visible-light irradiation.

Generally, the photocatalytic degradation of dyes in water is mainly attributed to the photogenerated holes, and the active oxygen species, including superoxide radicals ($O_2^{\bullet -}$) and hydroxyl radicals ($OH^{\bullet}$). In order to understand the possible mechanism of the photocatalytic degradation of MB over Ag_2CrO_4, we have determined the CB and VB position at the point of zero charge by a widely accepted approach based on the following equation [67,68]:

$$E_{CB} = \chi - E^C - 0.5E_g\ , \qquad (2)$$

where E_{CB} is the CB edge potential, χ is the absolute electronegativity of the semiconductor. E^C is the energy of free electrons on the hydrogen scale (ca. 4.5 eV), and $E_g$is the band gap of the semiconductor. Accordingly, the CB energy level of Ag_2CrO_4 is calculated to be ca. 0.46 eV (vs NHE), which is less negative than the $O_2/O_2^{\bullet -}$ potential; and the VB energy level of Ag_2CrO_4 is calculated to be ca. 2.26 eV (vs NHE), which is less positive than $OH^{\bullet}/OH^-$ potential [69]. As a result, the photogenerated electrons on the CB of Ag_2CrO_4 are not able to reduce the adsorbed O_2 to yield $O_2^{\bullet -}$, meanwhile the photogenerated holes on the VB of Ag_2CrO_4 also can not oxidize H_2O to form $OH^{\bullet}$ due to their insufficient reduction (for electron) and oxidation ability (for hole). In addition, the energy level of the lowest unoccupied molecular orbital (LUMO) and the highest occupied molecular orbital (HOMO) of MB are reported as ca. −0.25 and 1.6 eV [70,71], respectively. As such, the direct decomposition of MB molecules by the photogenerated holes on the VB of Ag_2CrO_4 is expected, since the VB of Ag_2CrO_4 is more positive than the HOMO of MB. Therefore, we assume that the main active species for the photocatalytic degradation of MB over Ag_2CrO_4 should be photogenerated holes.

The highest photocatalytic efficiency for the S-M sample is attributed to several major factors. First, the S-M sample has the highest surface area. Its photocatalytic efficiency is improved by adsorbing more MB molecules for a more efficient interaction between MB and Ag_2CrO_4. Second, the smaller particle size of the S-M sample can shorten the diffusion process of photogenerated electrons and holes to the surface of Ag_2CrO_4, thus reducing the rate of recombination [72]. Third, the enhanced visible-light absorption in the range of 400–600 nm for the S-M sample (Figure 5) can allow for a more efficient utilization of the solar energy to generate more electrons and holes and to further promote the catalytic process. Finally, the relatively wider band gap, compared to those of the S-P and S-H samples, calculated from the obvious blue-shift absorption edge of the S-M sample (Figure 5) can lead to a higher redox potential, thereby resulting in a stronger oxidation ability of the photogenerated holes [73,74]. Overall the results suggest that the photocatalytic efficiency of the Ag_2CrO_4 samples is influenced by the surface area, particle size and optical property, which originate from the different structure caused by different preparation methods.

We further explore the photocatalytic stability of the S-M Ag_2CrO_4 sample by a cycling test of photocatalytic degradation of a MB aqueous solution under visible-light irradi-

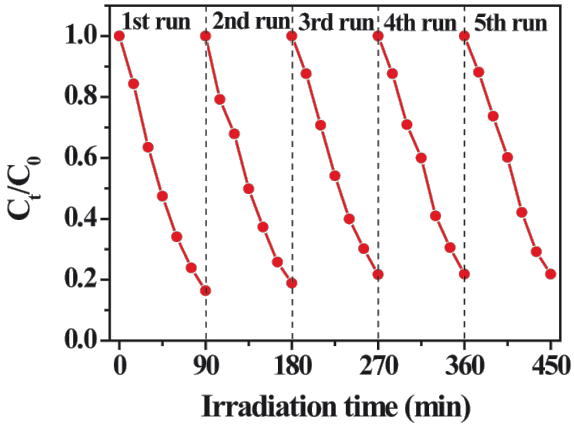

Figure 8: Cycling test of the photocatalytic degradation under visible-light irradiation of a MB aqueous solution in the presence of the Ag_2CrO_4 sample prepared by microemulsion method.

ation. Figure 8 reveals that no obvious decrease of the photocatalytic activity was observed after five cycles, suggesting the excellent photocatalytic stability of the S-M Ag_2CrO_4 sample in the reactions.

To investigate the structure of Ag_2CrO_4 after five circles of the photocatalytic reaction, the corresponding SEM and TEM images, XRD pattern, and UV–vis diffuse reflectance spectrum were collected. Figure 9a and Figure 9b show that the overall morphology and average particle size of Ag_2CrO_4 were not changed significantly. However, some homogenously distributed Ag nanoparticles could be observed on the surface of Ag_2CrO_4 (Figure 9b). The existence of metallic Ag could be further demonstrated by the XRD pattern (Figure 9c), which displayed a new peak located at $2\theta = 38.1°$ corresponding to the (111) plane of silver (JCPDS No. 65-2871). The UV–visible spectrum with the corresponding colour of Ag_2CrO_4 after five circles of photocatalytic reaction is displayed in Figure 9d. It was found that the absorbance intensity in the visible-light region largely increased, which could be ascribed to the darkened colour of Ag_2CrO_4 after photocatalysis, resulting from the silver nanoparticles [32]. These results indicate that Ag_2CrO_4 was partially reduced to metallic Ag and formed an Ag–Ag_2CrO_4 composite. However, the majority of Ag_2CrO_4 was still preserved, and the formed Ag particles may further promote the photocatalytic activity in terms of surface plasmon resonance [75,76] and electron-sink effect [30]. Therefore, the photocatalytic activity of Ag_2CrO_4 did not show obvious decrease after 5-circle reaction.

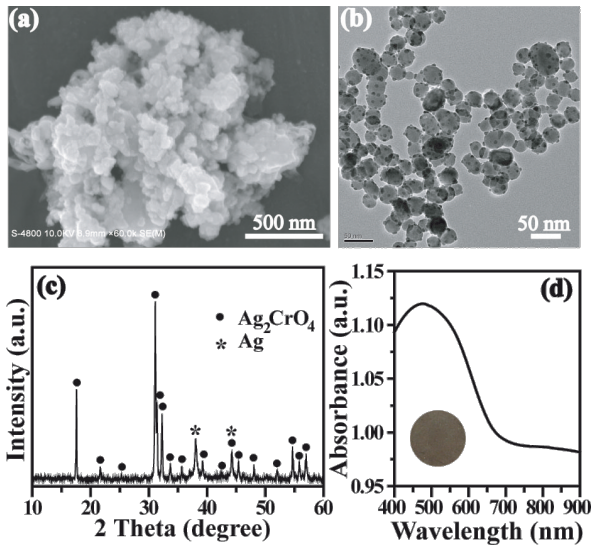

Figure 9: (a) SEM image, (b) TEM image, (c) XRD pattern, and (d) UV–visible spectrum of Ag_2CrO_4 after five circles of photocatalytic reaction.

Conclusion

In summary, a range of Ag_2CrO_4 photocatalysts are prepared by microemulsion, precipitation, and hydrothermal methods. The preparation methods exhibit a great influence on the structure, optical properties and photocatalytic activity of the Ag_2CrO_4 crystals. The sample prepared by microemulsion method has the smallest particle size, highest surface area, most efficient light absorption, and a blue-shifted absorption edge. Consequently, the microemulsion prepared Ag_2CrO_4photocatalyst shows the best activity in the photodegradation of a MB aqueous solution, because of the higher adsorption of MB molecules, shorter diffusion process of more photogenerated excitons, and stronger oxidation ability of the photogenerated holes. The current investigation may provide new insight into the effect of preparation methods on the structure and photocatalytic activity of photocatalysts. Future work may focus on the study of the visible-light photocatalytic mechanism and the stability promoting methods of Ag_2CrO_4. Moreover, it is also possible to investigate the photocatalytic activity of Ag_2CrO_4 toward the degradation of other organic pollutants under visible-light irradiation.

Experimental

Preparation of Ag_2CrO_4 photocatalysts

All chemicals were analytical grade and used without further purification. Deionized (DI) water was used in all experiments. The Ag_2CrO_4 photocatalysts were prepared by the microemulsion, precipitation, and hydrothermal methods. The corresponding samples were labeled as S-M, S-P and S-H, respectively, as listed in Table 1. The detailed experimental procedures for the preparation of the samples are described as follows:

Sample S-M: Under stirring, cyclohexane (16 mL), Triton X-100 (5.2 mL) and *n*-hexanol (3 mL) were mixed at room temperature. Then K_2CrO_4 aqueous solution (0.5 mL, 0.5 M) was dripped into the mixture under continuous stirring to form a clarified and transparent W/O reversed-micellar solution, followed by the dropwise addition of $AgNO_3$ aqueous solution (0.5 mL, 0.25 M) and kept for 1 h under stirring. The resultant suspension was aged for 24 h.

Sample S-P: $AgNO_3$ (1000 mL, 0.5 M) and K_2CrO_4 (1000 mL, 0.25 M) aqueous solutions were mixed together under vigorous stirring. The resultant suspension was then aged for 24 h.

Sample S-H: The sample prepared by precipitation method was loaded into a Teflon-lined stainless steel autoclave with a capacity of 100 mL, sealed, heated to and maintained at 160 °C for 16 h, and subsequently cooled to room temperature naturally.

All the samples were collected and washed by centrifugation–redispersion cycles with ethanol and water, and then dried at 70 °C for 4 h.

Characterization

The XRD were recorded on an X-ray diffractometer (type HZG41BPC) with Cu Kα irradiation source at a scan rate (2θ) of $0.05°\cdot s^{-1}$. The accelerating voltage and applied current were 40 kV and 80 mA, respectively. The morphology observation was carried out by SEM (S4800, Hitachi, Japan) at an accelerating voltage of 5 kV. TEM and HRTEM analysis were conducted by the transmission electron microscopy (JEM-2100F, JEOL, Japan) at an accelerating voltage of 200 kV. The DRS were taken with a UV–vis spectrophotometer (UV2550, Shimadzu, Japan). $BaSO_4$ was used as a reflectance standard. The nitrogen adsorption and desorption isotherms were measured by using an ASAP 2020 system (Micromertitics instruments, USA) after the samples were degassed at 180 °C. The S_{BET} was determined by a multipoint BET method using the adsorption data in the relative pressure (P/P_0) range of 0.05–0.3. The desorption data was used to determine the pore size distribution through the Barret–Joyner–Halenda (BJH) method. The nitrogen adsorption volume at P/P_0 of 0.994 was used to determine the average pore size. Zeta potential was measured by electrophoretic light scattering with a zetasizer (Nano ZS90, Malvern, UK).

Computational details

The DFT calculations were carried out to investigate the band structure and density of states (DOS) of Ag_2CrO_4 model by using the CASTEP Packages on the basis of the plane-wave-pseudo-potential approach [77,78]. Combined with ultrasoft pseudo-potentials, the Perdew–Burke–Ernzerhof (PBE) of generalized gradient approximation (GGA) was applied as the exchange–correlation function [79,80]. The plane-wave cut-off energy was set to be 500 eV, the Monkhorst–Pack *k*-point in the Brilliouin Zone to be 3 × 5 × 6, and the self-consistent field (SCF) convergence accuracy to be 1×10^{-6} eV/atom. For the geometric optimization, the convergence criteria were set as follows: 1×10^{-5} eV/atom for total energy, 0.03 eV/Å for maximum force, 0.05 GPa for maximum stress, and 1×10^{-3} Å for maximum displacement. The energy and geometry structure showed no obvious change when higher cut-off energy and more *k*-points were adopted. The electronic structure calculation was carried out by using the optimized geometric structure.

Measurements of photocatalytic activity

The photocatalytic activity of the as-prepared samples was evaluated by the photocatalytic degradation of MB under visible-light irradiation in water at ambient temperature. The prepared photocatalysts (50 mg) were firstly dispersed into water in a reactor with a diameter of 7.0 cm and then dried at 80 °C for 4 h, giving rise to the formation of Ag_2CrO_4 films at the bottom of the reactor. MB aqueous solution (50 mL, 2.5×10^{-5} M) was added into the reactor and kept in the dark for 30 min to ensure an adsorption–desorption equilibrium prior to irradiation. A 300 W xenon arc lamp coupled with a UV cut-off filter ($\lambda \geq 400$ nm), which was positioned 20 cm away from the reactor, was used as a visible-light source to drive the photocatalytic reaction. The concentration of MB was determined by a UV–vis spectrophotometer (UV2550, Shimadzu, Japan). After irradiation for every 15 min, the reaction solution was taken out to measure the concentration change of MB. As for the MB aqueous solution with low concentration, its photocatalytic degradation was a pseudo-fist-order reaction and its kinetics was expressed as [81-83]:

$$\ln\left(C_0 / C_t\right) = k \cdot t \tag{3}$$

Where k is the apparent rate constant, C_0 and C_t are the initial and reaction concentrations of MB, respectively.

Acknowledgements

This work was supported by the 973 program (2013CB632402), 863 Program (2012AA062701), and NSFC (51272199, 51320105001, 51372190 and 21177100). Also, this work was financially supported by the Fundamental Research Funds for the Central Universities (2013-VII-030) and Self-determined and Innovative Research Funds of SKLWUT (2013-ZD-1).

References

1. Xiang, Q.; Yu, J. *J. Phys. Chem. Lett.* **2013,** *4,* 753–759. doi:10.1021/jz302048d
2. Kudo, A.; Miseki, Y. *Chem. Soc. Rev.* **2009,** *38,* 253–278. doi:10.1039/b800489g
3. Jin, J.; Yu, J.; Liu, G.; Wong, P. K. *J. Mater. Chem. A* **2013,** *1,* 10927–10934. doi:10.1039/c3ta12301d
4. Tong, H.; Ouyang, S.; Bi, Y.; Umezawa, N.; Oshikiri, M.; Ye, J. *Adv. Mater.* **2012,** *24,* 229–251. doi:10.1002/adma.201102752
5. Xiang, Q.; Yu, J.; Jaroniec, M. *Chem. Soc. Rev.* **2012,** *41,* 782–796. doi:10.1039/c1cs15172j
6. Linsebigler, A. L.; Lu, G.; Yates, J. T. *Chem. Rev.* **1995,** *95,* 735–758. doi:10.1021/cr00035a013
7. Wen, C. Z.; Zhou, J. Z.; Jiang, H. B.; Hu, Q. H.; Qiao, S. Z.; Yang, H. G. *Chem. Commun.* **2011,** *47,* 4400–4402. doi:10.1039/c0cc05798c
8. Yu, J.; Wang, Y.; Xiao, W. *J. Mater. Chem. A* **2013,** *1,* 10727–10735. doi:10.1039/c3ta12218b
9. Chatterjee, D.; Dasgupta, S. *J. Photochem. Photobiol., C* **2005,** *6,* 186–205. doi:10.1016/j.jphotochemrev.2005.09.001
10. Mitsionis, A.; Vaimakis, T.; Trapalis, C.; Todorova, N.; Bahnemann, D.; Dillert, R. *Appl. Catal., B* **2011,** *106,* 398–404. doi:10.1016/j.apcatb.2011.05.047

11. Hernández-Alonso, M. D.; Fresno, F.; Suárez, S.; Coronado, J. M. *Energy Environ. Sci.* **2009,** *2,* 1231–1257. doi:10.1039/b907933e
12. Yang, X.; Cao, C. D.; Erickson, L.; Hohn, K.; Maghirang, R.; Klabunde, K. *Appl. Catal., B* **2009,** *91,* 657–662. doi:10.1016/j.apcatb.2009.07.006
13. Asahi, R.; Morikawa, T.; Ohwaki, T.; Aoki, K.; Taga, Y. *Science* **2001,** *293,* 269–271. doi:10.1126/science.1061051
14. Low, J.; Yu, J.; Li, Q.; Cheng, B. *Phys. Chem. Chem. Phys.* **2014,** *16,* 1111–1120. doi:10.1039/c3cp53820f
15. Yu, J.; Zhou, P.; Li, Q. *Phys. Chem. Chem. Phys.* **2013,** *15,* 12040–12047. doi:10.1039/c3cp44651d
16. Yu, J.; Wang, S.; Low, J.; Xiao, W. *Phys. Chem. Chem. Phys.* **2013,** *15,* 16883–16890. doi:10.1039/c3cp53131g
17. Li, R.; Zhang, F.; Wang, D.; Yang, J.; Li, M.; Zhu, J.; Zhou, X.; Han, H.; Li, C. *Nat. Commun.* **2013,** *4,* No. 1432. doi:10.1038/ncomms2401
18. Cao, S.-W.; Yin, Z.; Barber, J.; Boey, F. Y. C.; Loo, S. C. J.; Xue, C. *ACS Appl. Mater. Interfaces* **2012,** *4,* 418–423. doi:10.1021/am201481b
19. Puttaswamy, M.; Ran, J.; Zhang, J.; Yu, J.; Liu, G. *Appl. Catal., B: Environ.* **2011,** *110,* 286–295. doi:10.1016/j.apcatb.2011.09.014
20. Liu, H.; Luo, M.; Hu, J.; Zhou, T.; Chen, R.; Li, J. *Appl. Catal., B: Environ.* **2013,** *140-141,* 141–150. doi:10.1016/j.apcatb.2013.04.009
21. Hu, J.; Li, H.; Huang, C.; Liu, M.; Qiu, X. *Appl. Catal., B: Environ.* **2013,** *142-143,* 598–603. doi:10.1016/j.apcatb.2013.05.079
22. Qu, J.; Yu, Y.; Cao, C.-Y.; Song, W.-G. *Chem.–Eur. J.* **2013,** *19,* 11172–11177. doi:10.1002/chem.201301295
23. Yu, J.; Yu, X.; Huang, B.; Zhang, X.; Dai, Y. *Cryst. Growth Des.* **2009,** *9,* 1474–1480. doi:10.1021/cg800941d
24. Zhou, X.; Xu, Q.; Lei, W.; Zhang, T.; Qi, X.; Liu, G.; Deng, K.; Yu, J. *Small* **2014,** *10,* 674–679. doi:10.1002/smll.201370001
25. Sun, W.; Meng, Q.; Jing, L.; Liu, D.; Cao, Y. *J. Phys. Chem. C* **2013,** *117,* 1358–1365. doi:10.1021/jp309599d
26. Huang, W.-C.; Lyu, L.-M.; Yang, Y.-C.; Huang, M. H. *J. Am. Chem. Soc.* **2012,** *134,* 1261–1267. doi:10.1021/ja209662v
27. Yu, H.; Yu, J.; Liu, S.; Mann, S. *Chem. Mater.* **2007,** *19,* 4327–4334. doi:10.1021/cm070386d
28. Li, J.; Cushing, S. K.; Bright, J.; Meng, F.; Senty, T. R.; Zheng, P.; Bristow, A. D.; Wu, N. *ACS Catal.* **2013,** *3,* 47–51. doi:10.1021/cs300672f
29. Yi, Z.; Ye, J.; Kikugawa, N.; Kako, T.; Ouyang, S.; Stuart-Williams, H.; Yang, H.; Cao, J.; Luo, W.; Li, Z.; Liu, Y.; Withers, R. L. *Nat. Mater.* **2010,** *9,* 559–564. doi:10.1038/nmat2780
30. Wang, W.; Cheng, B.; Yu, J.; Liu, G.; Fan, W. *Chem.–Asian J.* **2012,** *7,* 1902–1908. doi:10.1002/asia.201200197
31. Xu, C.; Liu, Y.; Huang, B.; Li, H.; Qin, X.; Zhang, X.; Dai, Y. *Appl. Surf. Sci.* **2011,** *257,* 8732–8736. doi:10.1016/j.apsusc.2011.05.060
32. Dai, G.; Yu, J.; Liu, G. *J. Phys. Chem. C* **2012,** *116,* 15519–15524. doi:10.1021/jp305669f
33. Ju, P.; Fan, H.; Zhang, B.; Shang, K.; Liu, T.; Ai, S.; Zhang, D. *Sep. Purif. Technol.* **2013,** *109,* 107–110. doi:10.1016/j.seppur.2013.01.057
34. Xu, J.; Hu, C.; Xi, Y.; Wan, B.; Zhang, C.; Zhang, Y. *Solid State Sci.* **2012,** *14,* 535–539. doi:10.1016/j.solidstatesciences.2012.01.013
35. Dong, H.; Li, Z.; Xu, X.; Ding, Z.; Wu, L.; Wang, X.; Fu, X. *Appl. Catal., B: Environ.* **2009,** *89,* 551–556. doi:10.1016/j.apcatb.2009.01.018
36. Maruyama, Y.; Irie, H.; Hashimoto, K. *J. Phys. Chem. B* **2006,** *110,* 23274–23278. doi:10.1021/jp063406s
37. Eichinger, G.; Besenhard, J. O. *J. Electroanal. Chem. Interfacial Electrochem.* **1976,** *72,* 1–31. doi:10.1016/S0022-0728(76)80072-1
38. Cignini, P. *J. Power Sources* **1978,** *3,* 347–357. doi:10.1016/0378-7753(78)80023-8
39. Messina, R.; Perichon, J. *J. Electroanal. Chem. Interfacial Electrochem.* **1982,** *133,* 115–123. doi:10.1016/0022-0728(82)87010-1
40. Ouyang, S.; Li, Z.; Ouyang, Z.; Yu, T.; Ye, J.; Zou, Z. *J. Phys. Chem. C* **2008,** *112,* 3134–3141. doi:10.1021/jp077127w
41. Soofivand, F.; Mohandes, F.; Salavati-Niasari, M. *Mater. Res. Bull.* **2013,** *48,* 2084–2094. doi:10.1016/j.materresbull.2013.02.025
42. Liu, Y.; Yu, H.; Cai, M.; Sun, J. *Catal. Commun.* **2012,** *26,* 63–67. doi:10.1016/j.catcom.2012.04.017
43. Alamdari, R. F.; Hajimirsadeghi, S. S.; Kohsari, I. *Inorg. Mater.* **2010,** *46,* 60–64. doi:10.1134/S0020168510010140
44. Demidova, M. G.; Bulavchenko, A. I.; Alekseev, A. V. *Russ. J. Inorg. Chem.* **2008,** *53,* 1446–1454. doi:10.1134/S0036023608090167
45. Cheng, L.; Shao, Q.; Shao, M.; Wei, X.; Wu, Z. *J. Phys. Chem. C* **2009,** *113,* 1764–1768. doi:10.1021/jp808907e
46. Liu, J.-K.; Luo, C.-X.; Quan, N.-J. *J. Nanopart. Res.* **2008,** *10,* 531–535. doi:10.1007/s11051-007-9277-8
47. Yu, J.; Dai, G.; Cheng, B. *J. Phys. Chem. C* **2010,** *114,* 19378–19385. doi:10.1021/jp106324x
48. Zhang, X.; Lei, L. *J. Hazard. Mater.* **2008,** *153,* 827–833. doi:10.1016/j.jhazmat.2007.09.052
49. Park, H.; Choi, W.; Hoffmann, M. R. *J. Mater. Chem.* **2008,** *18,* 2379–2385. doi:10.1039/b718759a
50. Bagwe, R. P.; Khilar, K. C. *Langmuir* **1997,** *13,* 6432–6438. doi:10.1021/la9700681
51. Bagwe, R. P.; Khilar, K. C. *Langmuir* **2000,** *16,* 905–910. doi:10.1021/la980248q
52. Bagwe, R. P.; Yang, C.; Hilliard, L. R.; Tan, W. *Langmuir* **2004,** *20,* 8336–8342. doi:10.1021/la049137j
53. Xiong, L.; He, T. *Chem. Mater.* **2006,** *18,* 2211–2218. doi:10.1021/cm052320t
54. Xu, Z.; Yu, J.; Xiao, W. *Chem.–Eur. J.* **2013,** *19,* 9592–9598. doi:10.1002/chem.201300438
55. Xu, Z.; Yu, J.; Liu, G.; Cheng, B.; Zhou, P.; Li, X. *Dalton Trans.* **2013,** *42,* 10190–10197. doi:10.1039/c3dt51067k
56. Sing, K. S. W. *Pure Appl. Chem.* **1982,** *54,* 2201–2218. doi:10.1351/pac198254112201
57. Sing, K. S. W. *Pure Appl. Chem.* **1985,** *57,* 603–619. doi:10.1351/pac198557040603
58. Kruk, M.; Jaroniec, M. *Chem. Mater.* **2001,** *13,* 3169–3183. doi:10.1021/cm0101069
59. Jeevanandam, P.; Mulukutla, R. S.; Phillips, M.; Chaudhuri, S.; Erickson, L. E.; Klabunde, K. J. *J. Phys. Chem. C* **2007,** *111,* 1912–1918. doi:10.1021/jp066363o
60. Dhara, S.; Giri, P. K. *Nanoscale Res. Lett.* **2011,** *6,* 320–326. doi:10.1186/1556-276X-6-320
61. Zhang, H.; Bayne, M.; Fernando, S.; Legg, B.; Zhu, M.; Penn, R. L.; Banfield, J. F. *J. Phys. Chem. C* **2011,** *115,* 17704–17710. doi:10.1021/jp205192a
62. Ran, F.; Miao, L.; Tanemura, S.; Tanemura, M.; Cao, Y.; Tanaka, S.; Shibata, N. *Mater. Sci. Eng., B* **2008,** *148,* 35–39. doi:10.1016/j.mseb.2007.09.029

63. Wu, J.-C.; Zheng, J.; Zacherl, C. L.; Wu, P.; Liu, Z.-K.; Xu, R. *J. Phys. Chem. C* **2011,** *115,* 19741–19748. doi:10.1021/jp204799q
64. Li, Q.; Meng, H.; Zhou, P.; Zheng, Y.; Wang, J.; Yu, J.; Gong, J. *ACS Catal.* **2013,** *3,* 882–889. doi:10.1021/cs4000975
65. Kato, H.; Kobayashi, H.; Kudo, A. *J. Phys. Chem. B* **2002,** *106,* 12441–12447. doi:10.1021/jp025974n
66. Santamaría-Pérez, D.; Bandiello, E.; Errandonea, D.; Ruiz-Fuertes, J.; Gomis, O.; Sans, J. A.; Manjón, F. J.; Rodríguez-Hernández, P.; Muñoz, A. *J. Phys. Chem. C* **2013,** *117,* 12239–12248. doi:10.1021/jp401524s
67. Jiang, H.-Q.; Endo, H.; Natori, H.; Nagai, M.; Kobayashi, K. *Mater. Res. Bull.* **2009,** *44,* 700–706. doi:10.1016/j.materresbull.2008.06.007
68. Yu, J.; Ran, J. *Energy Environ. Sci.* **2011,** *4,* 1364–1371. doi:10.1039/C0EE00729C
69. Wu, L.; Yu, J. C.; Fu, X. *J. Mol. Catal. A: Chem.* **2006,** *244,* 25–32. doi:10.1016/j.molcata.2005.08.047
70. Takizawa, T.; Watanabe, T.; Honda, K. *J. Phys. Chem.* **1978,** *82,* 1391–1396. doi:10.1021/j100501a014
71. Ji, K. H.; Jang, D. M.; Cho, Y. J.; Myung, Y.; Kim, H. S.; Kim, Y.; Park, J. *J. Phys. Chem. C* **2009,** *113,* 19966–19972. doi:10.1021/jp906476m
72. Hagfeldt, A.; Grätzel, M. *Chem. Rev.* **1995,** *95,* 49–68. doi:10.1021/cr00033a003
73. Hoffmann, M. R.; Martin, S. T.; Choi, W.; Bahnemann, D. W. *Chem. Rev.* **1995,** *95,* 69–96. doi:10.1021/cr00033a004
74. Lee, H.-S.; Woo, C.-S.; Youn, B.-K.; Kim, S.-Y.; Oh, S.-T.; Sung, Y.-E.; Lee, H.-I. *Top. Catal.* **2005,** *35,* 255–260. doi:10.1007/s11244-005-3832-2
75. Wang, P.; Huang, B.; Qin, X.; Zhang, X.; Dai, Y.; Wei, J.; Whangbo, M.-H. *Angew. Chem., Int. Ed.* **2008,** *47,* 7931–7993. doi:10.1002/anie.200802483
76. Wang, P.; Huang, B.; Zhang, X.; Qin, X.; Jin, H.; Dai, Y.; Wang, Z.; Wei, J.; Zhan, J.; Wang, S.; Wang, J.; Whangbo, M.-H. *Chem.–Eur. J.* **2009,** *15,* 1821–1824. doi:10.1002/chem.200802327
77. Segall, M. D.; Lindan, P. J. D.; Probert, M. J.; Pickard, C. J.; Hasnip, P. J.; Clark, S. J.; Payne, M. C. *J. Phys.: Condens. Matter* **2002,** *14,* 2717–2744. doi:10.1088/0953-8984/14/11/301
78. Zhou, P.; Yu, J.; Wang, Y. *Appl. Catal., B: Environ.* **2013,** *142-143,* 45–53. doi:10.1016/j.apcatb.2013.04.063
79. Perdew, J. P.; Burke, K.; Ernzerhof, M. *Phys. Rev. Lett.* **1996,** *77,* 3865–3868. doi:10.1103/PhysRevLett.77.3865
80. Perdew, J. P.; Wang, Y. *Phys. Rev. B* **1992,** *45,* 13244–13249. doi:10.1103/PhysRevB.45.13244
81. Kumazawa, H.; Inoue, M.; Kasuya, T. *Ind. Eng. Chem. Res.* **2003,** *42,* 3237–3244. doi:10.1021/ie020723m
82. Yu, J.-G.; Yu, H.-G.; Cheng, B.; Zhao, X.-J.; Yu, J. C.; Ho, W.-K. *J. Phys. Chem. B* **2003,** *107,* 13871–13879. doi:10.1021/jp036158y
83. Yu, J.; Li, Q.; Liu, S.; Jaroniec, M. *Chem.–Eur. J.* **2013,** *19,* 2433–2441. doi:10.1002/chem.201202778

License and Terms

This is an Open Access article under the terms of the Creative Commons Attribution License (http://creativecommons.org/licenses/by/2.0), which permits unrestricted use, distribution, and reproduction in any medium, provided the original work is properly cited.

The license is subject to the *Beilstein Journal of Nanotechnology* terms and conditions: (http://www.beilstein-journals.org/bjnano)

The definitive version of this article is the electronic one which can be found at: doi:10.3762/bjnano.5.77

Beilstein Journal of Nanotechnology

A visible-light-driven composite photocatalyst of TiO_2 nanotube arrays and graphene quantum dots

Donald K. L. Chan, Po Ling Cheung and Jimmy C. Yu*

Full Research Paper

Open Access

Address:
Department of Chemistry and Shenzhen Research Institute, The Chinese University of Hong Kong, Shatin, New Territories, Hong Kong, China

Email:
Jimmy C. Yu* - jimyu@cuhk.edu.hk

* Corresponding author

Keywords:
anodic oxidation; graphene quantum dots; photocatalyst; photodegradation; TiO_2 nanotube arrays

Beilstein J. Nanotechnol. **2014,** *5,* 689–695.
doi:10.3762/bjnano.5.81

Received: 31 December 2013
Accepted: 25 April 2014
Published: 22 May 2014

This article is part of the Thematic Series "Photocatalysis".

Guest Editor: R. Xu

© 2014 Chan et al; licensee Beilstein-Institut.
License and terms: see end of document.

Abstract

TiO_2 nanotube arrays are well-known efficient UV-driven photocatalysts. The incorporation of graphene quantum dots could extend the photo-response of the nanotubes to the visible-light range. Graphene quantum dot-sensitized TiO_2 nanotube arrays were synthesized by covalently coupling these two materials. The product was characterized by Fourier-transform infrared spectrometry (FTIR), scanning electron microscopy (SEM), transmission electron microscopy (TEM), X-ray diffraction (XRD), thermogravimetric analysis (TGA) and UV–vis absorption spectroscopy. The product exhibited high photocatalytic performance in the photodegradation of methylene blue and enhanced photocurrent under visible light irradiation.

Introduction

Semiconductor-mediated photocatalysis is a promising technique for the conversion of solar energy as well as degradation of organic pollutants in air and water [1,2]. Among various photocatalysts, nanostructured titanium dioxide (TiO_2) is the most widely used because of its high activity, long-term stability and low production cost [3,4]. However, pure TiO_2 is not efficient for solar-driven applications because it requires UV excitation [5]. Belonging to one-dimensional nanostructures, TiO_2 nanotube arrays (TNAs) synthesized by anodic oxidation of titanium had attracted particular interests [6,7]. Comparing with bulk nanoparticles, smooth walls of nanotubes provide a lower surface state density hence lowering recombination probability. Random walk of charges is suppressed because of the one-dimensional nature of the tubes [8]. Moreover, nanotube layers do have higher surface area for more active reaction sites over the bulk nanoparticle layers [9] and they were shown to be more efficient in photocatalysis [10]. Since TNAs can be grown directly on a conducting Ti substrate, they can be used directly as photoanodes for various applications. The activity of TNAs can be further enhanced by applying a potential bias [11]. In the recent years, TNAs have been widely studied for their applications in solar cells [12-14] or photoreactors [15,16]. Various approaches have been developed to achieve photoresponse of TiO_2-based catalysts towards

visible light, for example, doping with metal or non-metal [7,17-20], coupling with other semiconductor materials to form composite catalysts [4,21-24]. Two-dimensional graphene has attracted immense attention due to its large specific area, high intrinsic electron mobility and good electrical conductivity [3]. As an excellent electron acceptor, graphene has been combined with semiconductor photocatalysts such as TiO_2 [25], ZnO [26] and CdS [27] to enhance their photocatalytic activities. However, graphene sheets are usually micrometer-sized and they can hardly be introduced into efficient nano-sized photocatalysts on a solid support, for example, TNAs.

Zero-dimensional graphene quantum dots (GQDs) are defined as few-layered graphene with lateral dimensions smaller than 100 nm [28]. Due to quantum confinement and edge effects, GQDs possess a size-dependent band gap and other interesting properties [29,30]. In recent years, GQDs have been explored for their potential applications in bioimaging [31], sensing [32], photovoltaics [33,34]. Besides, they have been coupled with TiO_2 nanoparticles to achieve visible-light-driven photocatalysis [35,36]. Very recently, the combination of GQDs with CdS-modified TNAs was reported for photoelectrochemical hydrogen production. However, GQDs did not enhance the activity of bare TNAs in the study [37]. GQDs have also been chemically coupled with ZnO nanowires for photoelectrochemical water splitting [38].

In the present work, a composite photocatalyst of graphene quantum dots and TiO_2 nanotube arrays (GQDs/TNAs) was fabricated by the coupling reaction between carboxyl-containing GQDs and amine-functionalized TNAs (Scheme 1). The experimental data revealed that sensitization of TNAs with GQDs not only extended the optical absorption spectrum of TNAs over the visible range, but also enhanced the photocatalytic and photoelectrochemical performances of TNAs under visible light.

Results and Discussion

Figure 1a shows a TEM image of GQDs with diameters of about 10 nm. The AFM image and a corresponding height profile in Figure 1b suggest that the thickness of the GQDs were between 0.5 and 3 nm, corresponding to one to few layers of graphene [39]. According to the UV–vis absorption spectrum in Figure 1c, GQDs show a broad absorption below 600 nm and a small peak at ca. 340 nm. The result agrees with typical absorption spectra of GQDs being reported [28]. Figure 1d shows the excitation-dependent emission of GQDs. This behavior could be explained by the differences in size and emissive states of GQDs [40]. To provide evidence for the existence of carboxyl groups in GQDs, Fourier-transform infrared (FTIR) spectra of GO and GQDs were obtained (Figure S1, Supporting Information File 1).

FESEM and TEM were used to examine the morphology of the TNAs. Figure 2 shows typical FESEM images with top (a, c) and side (b, d) views of the prepared TNAs films. The nanotube arrays are highly ordered and vertically aligned. Each nanotube has an inner diameter of approximately 110 nm and a length of about 18 μm. As shown in Figure 2c and Figure 2d, the TNAs retain the morphology after coupling with GQDs. In Figure 2e, the hollow structure of nanotubes can be observed clearly. In Figure 2f, dark spots with diameters of about 10 nm can be found, suggesting the successful loading of GQDs onto TNAs.

The structures of the products were investigated by using XRD. Figure 3 shows the XRD pattern of a pure Ti foil, which is consistent with the standard (JCPDS 44-1294). Figure 3 also shows that TNAs and GQDs/TNAs exhibit the same diffraction peaks at 2θ of 25.3°, 36.9°, 37.8°, 38.5°, 48.0°, 53.9°, 55.0°, 62.7°, 68.8° and 70.6°. These peaks match very well with anatase TiO_2 (JCPDS 21-1272). FTIR spectra were also obtained to study the chemical structures of the products (Figure S2, Supporting Information File 1).

Figure 4 shows the UV–vis absorption spectra of the samples. For pristine TNAs, the absorption edge extends up to about 550 nm instead of a typical value of TiO_2 (400 nm). This phenomenon can be explained by the incorporation of nitrogen into the nanotubes from NH_4F during anodization. A subsequent annealing at 450 °C resulted in the formation of N 2p

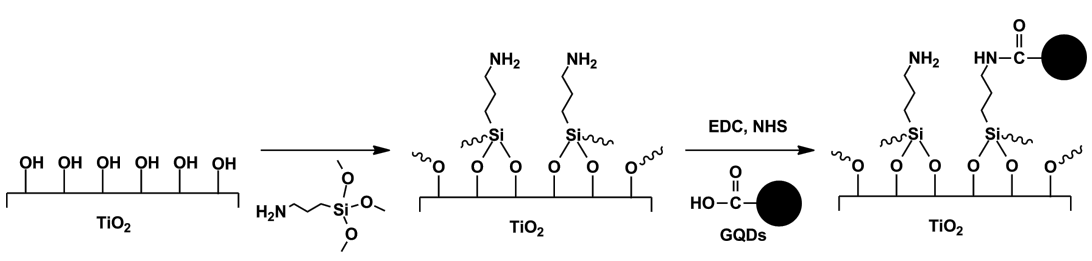

Scheme 1: Reaction scheme for the loading of GQDs onto TNAs via covalent bonding.

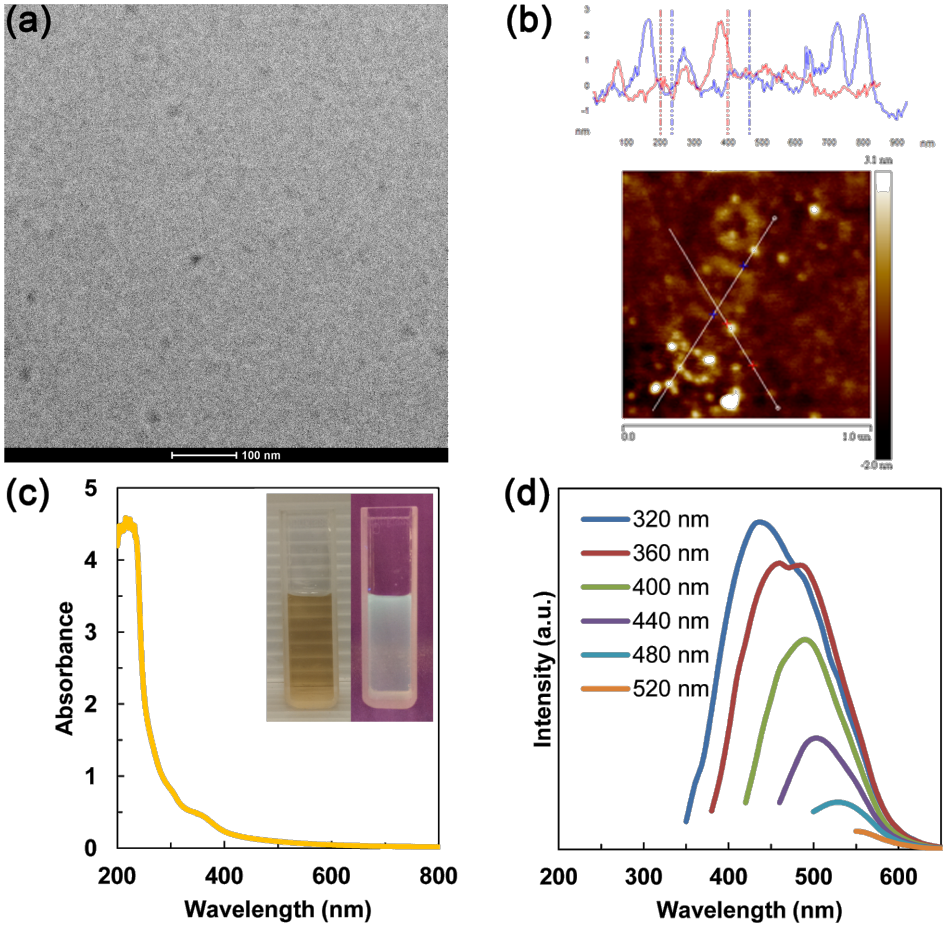

Figure 1: (a) TEM image of GQDs, (b) AFM image of GQDs with corresponding height profile, (c) UV–vis absorption spectrum of GQDs, inset: photos of GQDs in aqueous solution under ambient light (left) and 365 nm UV light (right), (d) PL spectra of GQDs at different excitation wavelengths.

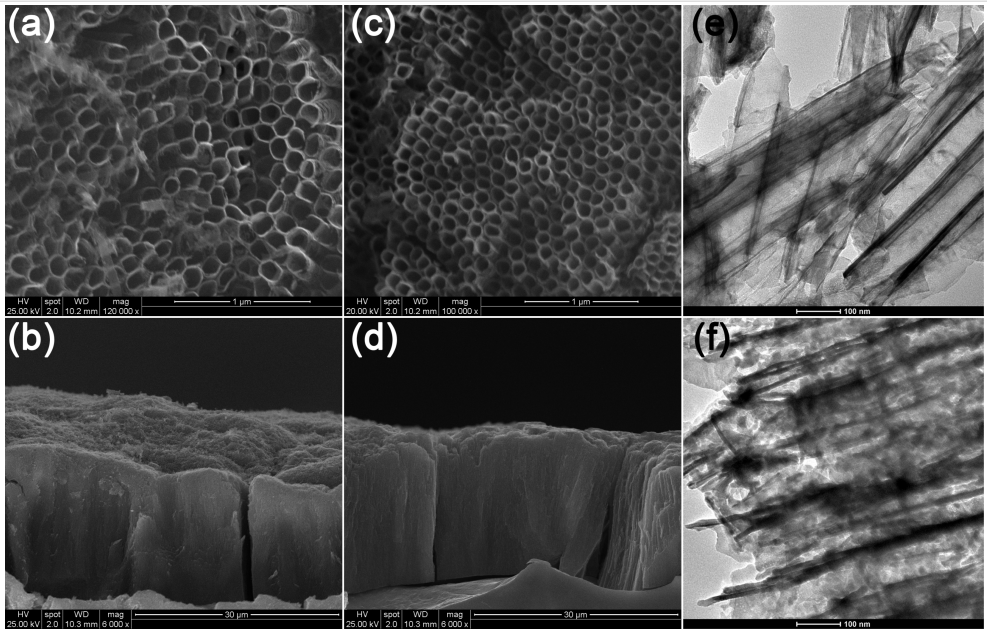

Figure 2: FESEM images of (a,b) pristine TNAs and (c,d) GQDs/TNAs; TEM images of (e) pristine TNAs and (f) GQDs/TNAs.

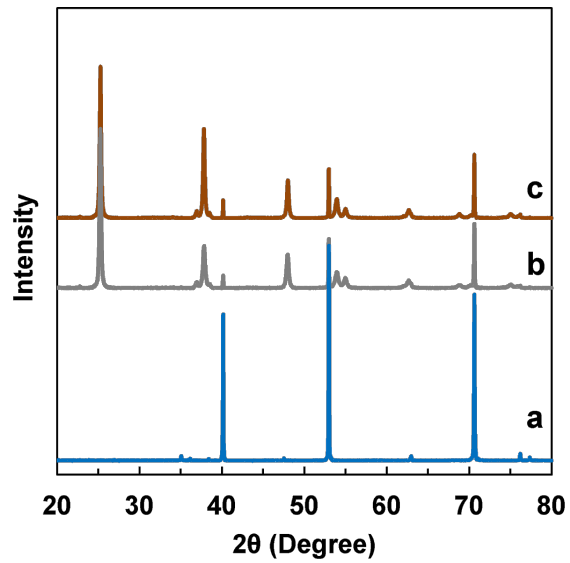

Figure 3: XRD patterns of (a) Ti foil, (b) TNAs and (c) GQDs/TNAs.

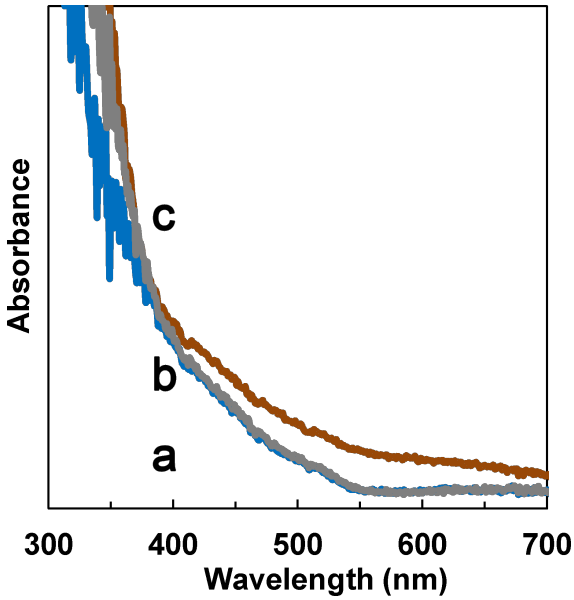

Figure 4: UV–vis absorption spectra of (a) TNAs, (b) amine-functionalized TNAs and (c) GQDs/TNAs.

states above the valence band of TiO_2 and hence in a red shift of the absorption edge [41]. The absorption spectrum of amine-functionalized TNAs is similar to that of pristine TNAs. For GQDs/TNAs, higher absorption intensity at wavelengths from 400 to 600 nm is observed, indicating the visible light response of TNAs is enhanced by loading GQDs.

The photocatalytic activities of the catalysts were evaluated by the degradation of MB under visible light irradiation. Figure 5

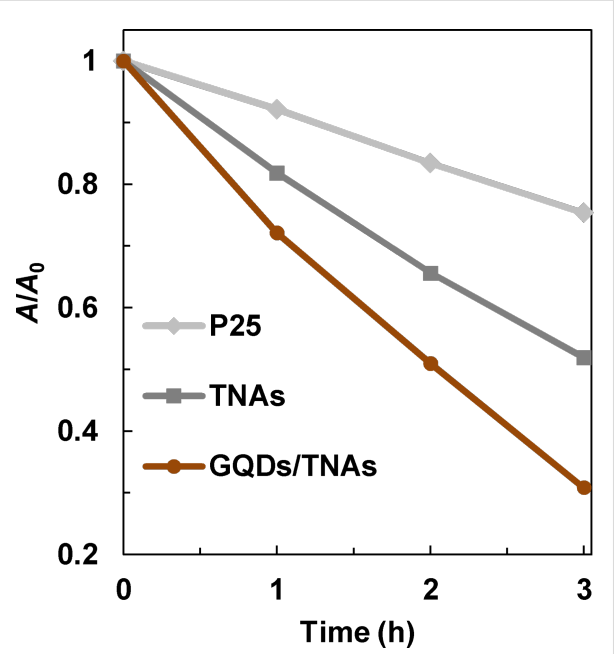

Figure 5: Photodegradation of methylene blue for TNAs and GQDs/TNAs under visible light irradiation.

shows that pristine TNAs have a relatively low activity. The concentration of MB dropped slowly to about 52 % after 3 h irradiation. The activity of pristine TNAs under visible light can be explained by nitrogen-doping as described previously. For GQDs/TNAs, an enhanced activity is achieved. The concentration of MB dropped to about 31% after 3 h irradiation. For comparison, the activity of pure TiO_2 (P25) was tested under the same conditions and it was found to be low.

TNAs were stably grown on a conducting Ti substrate, so the entire foil can be directly used for photoelectrochemical applications. Photocurrent responses of the catalysts were measured under visible light irradiation. Figure 6 clearly shows a significant enhancement of photocurrent after the loading of GQDs, indicating the charge separation efficiency of TNAs is greatly enhanced. The stable current reveals that GQDs are covalently bonded to TNAs instead of adsorbed onto the surface of TNAs.

The improved photocatalytic performance of GQDs/TNAs over TNAs can be simply explained by the photosensitization of TNAs by GQDs [38]. Upon visible light irradiation, electron–hole pairs are generated by the GQDs. Typically, the conduction band level of GQDs is higher than that of TiO_2 [36,42]. Thus, an interfacial electron transfer from GQDs to TNAs is possible. Meanwhile, such a directional charge transfer promotes charge separation and reduces the probability of charge recombination, then further increases the activity of the photocatalyst.

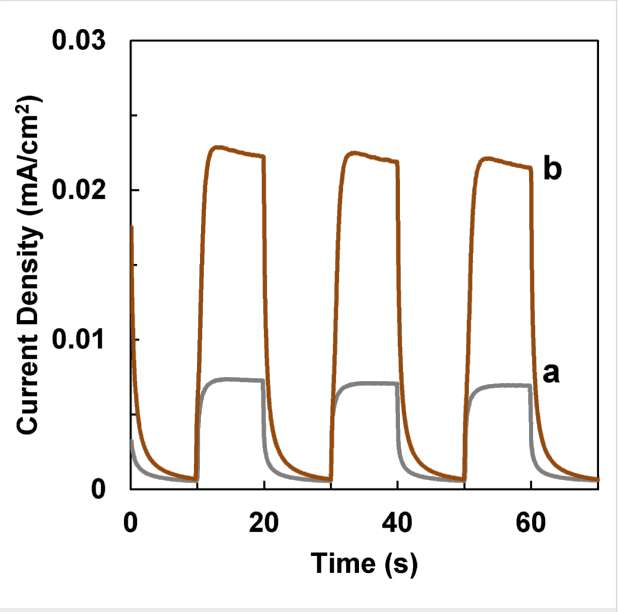

Figure 6: Photocurrent responses of (a) TNAs and (b) GQDs/TNAs under visible-light irradiation. The potential bias was 0.417 V.

Conclusion

In summary, a visible-light-driven photocatalyst was fabricated by covalently bonding GQDs onto amine-modified TNAs. The GQDs/TNAs composite retains the highly ordered nanotube morphology and well crystallized anatase phase. The high visible-light photocatalytic activity could be attributed to photosensitization of TNAs by GQDs. This research shows the potential of GQD-based photocatalysts for visible-light-driven photocatalytic and photoelectrochemical applications.

Experimental

Synthesis of TiO_2 nanotube arrays (TNAs): Highly ordered TNAs were fabricated by an anodic oxidation approach [43]. Ethylene glycol (99+%) containing 0.5 wt % NH_4F and 2.0 wt % deionized (DI) water was used as electrolyte. Ti foil (2 cm × 3 cm) was used as a working electrode, and a Pt foil (1 cm × 1 cm) served as a counter electrode. Prior to anodization, Ti foils were washed with ethanol, acetone by ultrasonication to remove contaminants, subsequently rinsed with DI water and dried in air. At room temperature, anodization is carried out by immersing a Ti foil in as-prepared electrolyte for 3 h at 60 V. Afterwards, the sample was removed from the electrochemical cell, rinsed with DI water, sonicated in ethanol for 2 min to remove surface debris. A subsequent heating to 450 °C for 1 h with a temperature increasing rate of 1 °C·min^{-1} in air was applied to improve crystallization.

Synthesis of graphene quantum dots (GQDs): GQDs were synthesized from graphene oxide (GO) by heating with a solution of hydrogen peroxide and ammonia [44]. 20 mg of GO was dispersed into 5 mL of water and sonicated for 10 minutes. 40 mL of H_2O_2 (30%) and 10 mL of NH_3 (28–30%) were added to the dispersion. The mixture was then stirred at 80 °C for 24 h followed by centrifugation for 10 minutes to remove large GO. The supernatant was heated at 60 °C under reduced pressure to remove H_2O_2, NH_3 and water. The solid GQDs were re-dispersed into water for further use.

Synthesis of GQDs/TNAs: TNAs were firstly immersed in 0.2 wt % (3-aminopropyl)trimethoxysilane (APTMS) in toluene for 3 h, rinsed with toluene and dried. The modified TNAs were then immersed in a beaker containing a solution of GQDs (1 mg·mL^{-1}), ethyl(dimethylaminopropyl)carbodiimide (EDC) and *N*-hydroxysuccinimide (NHS) for 4 h. The foils were then sonicated in DI water, rinsed with DI water and dried in air.

Characterization: The morphologies of the products were characterized by transmission electron microscopy (Philips, CM120) and field-emission scanning electron microscopy (FEI, Quanta 400 FEG). AFM images were obtained using a tapping mode with an atomic force microscope (Bruker, Dimension Icon). UV–vis spectra were recorded on a UV–vis spectrometer (Varian, Cary 100). The PL measurements were performed using a fluorescence spectrometer (Hitachi, F-4500). X-ray diffraction (XRD) patterns were recorded using a diffractometer (Bruker, D8 Advance) with high-intensity Cu Kα1 irradiation (λ = 1.5406 Å). The chemical structures of the products were characterized using a Fourier-transform infrared spectrometer (Nicolet, Magna 560). Thermogravimetric analysis was performed in air using a thermogravimetric analyzer (Perkin Elmer, TGA 6). The samples were heated from 50 °C to 800 °C at a rate of 10 °C·min^{-1}.

Photocatalytic activity measurements: The photocatalytic activities of catalysts were evaluated by measuring the photodegradation of methylene blue (MB). In a typical measurement, 10 mg photocatalyst were mechanically detached from Ti foils and suspended in 20 mL of 10 ppm aqueous solution of MB. The solution was stirred in the dark for 12 h to reach the adsorption/desorption equilibrium. The suspension was then illuminated with a 300 W tungsten halogen lamp with a 400 nm cutoff filter. Photodegradation of MB was monitored by measuring the UV–vis absorption of the suspensions at regular time intervals. The suspension was centrifuged for 2 min to remove the photocatalyst before measurement. The peak absorbance of MB at 664 nm was used to determine its concentration.

Photocurrent response measurements: The photo-electrochemical measurements were performed in a three-electrode electrochemical cell by using a CHI 660D electrochemical workstation. The as-prepared TNAs, Pt foil (1.0 cm × 1.0 cm)

and Ag/AgCl were the working, counter and reference electrodes. The electrolyte was a 0.1 M Na_2SO_4 aqueous solution. A 300 W xenon arc lamp was used as the irradiation source and the average light intensity was about 100 $mW \cdot cm^{-2}$. The photocurrent responses under illumination of visible light (AM 1.5G plus a 400 nm cutoff filter) were analyzed.

Supporting Information

Supporting information features FTIR spectra, TGA profiles of the samples and UV–vis absorption spectra of methylene blue.

Supporting Information File 1

Additional figures.
[http://www.beilstein-journals.org/bjnano/content/supplementary/2190-4286-5-81-S1.pdf]

Acknowledgements

The authors acknowledge support from the National Natural Science Foundation of China (Project 21173179) and Shenzhen Basic Research Program-JCYJ20120619151417947.

References

1. Ravelli, D.; Dondi, D.; Fagnoni, M.; Albini, A. *Chem. Soc. Rev.* **2009,** *38,* 1999–2011. doi:10.1039/b714786b
2. Hu, X.; Li, G.; Yu, J. C. *Langmuir* **2010,** *26,* 3031–3039. doi:10.1021/la902142b
3. Zhao, W.; Feng, L.; Yang, R.; Zheng, J.; Li, X. *Appl. Catal., B* **2011,** *103,* 181–189. doi:10.1016/j.apcatb.2011.01.025
4. An, X.; Yu, J. C. *RSC Adv.* **2011,** *1,* 1426–1434. doi:10.1039/c1ra00382h
5. Zhang, J.; Wu, Y.; Xing, M.; Leghari, S. A. K.; Sajjad, S. *Energy Environ. Sci.* **2010,** *3,* 715–726. doi:10.1039/b927575d
6. Shankar, K.; Basham, J. I.; Allam, N. K.; Varghese, O. K.; Mor, G. K.; Feng, X.; Paulose, M.; Seabold, J. A.; Choi, K.-S.; Grimes, C. A. *J. Phys. Chem. C* **2009,** *113,* 6327–6359. doi:10.1021/jp809385x
7. Roy, P.; Berger, S.; Schmuki, P. *Angew. Chem., Int. Ed.* **2011,** *50,* 2904–2939. doi:10.1002/anie.201001374
8. Ghicov, A.; Schmuki, P. *Chem. Commun.* **2009,** 2791–2808. doi:10.1039/b822726h
9. Shankar, K.; Mor, G. K.; Prakasam, H. E.; Yoriya, S.; Paulose, M.; Varghese, O. K.; Grimes, C. A. *Nanotechnology* **2007,** *18,* 065707. doi:10.1088/0957-4484/18/6/065707
10. Macak, J. M.; Zlamal, M.; Krysa, J.; Schmuki, P. *Small* **2007,** *3,* 300–304. doi:10.1002/smll.200600426
11. Zlamal, M.; Macak, J. M.; Schmuki, P.; Krýsa, J. *Electrochem. Commun.* **2007,** *9,* 2822–2826. doi:10.1016/j.elecom.2007.10.002
12. Shankar, K.; Bandara, J.; Paulose, M.; Wietasch, H.; Varghese, O. K.; Mor, G. K.; LaTempa, T. J.; Thelakkat, M.; Grimes, C. A. *Nano Lett.* **2008,** *8,* 1654–1659. doi:10.1021/nl080421v
13. Varghese, O. K.; Paulose, M.; Grimes, C. A. *Nat. Nanotechnol.* **2009,** *4,* 592–597. doi:10.1038/nnano.2009.226
14. Jen, H.-P.; Lin, M.-H.; Li, L.-L.; Wu, H.-P.; Huang, W.-K.; Cheng, P.-J.; Diau, E. W.-G. *ACS Appl. Mater. Interfaces* **2013,** *5,* 10098–10104. doi:10.1021/am402687j
15. Wang, D.; Liu, Y.; Yu, B.; Zhou, F.; Liu, W. *Chem. Mater.* **2009,** *21,* 1198–1206. doi:10.1021/cm802384y
16. Zhang, Z.; Wang, P. *Energy Environ. Sci.* **2012,** *5,* 6506–6512. doi:10.1039/C2EE03461A
17. Yu, C.; Yang, K.; Shu, Q.; Yu, J. C.; Cao, F.; Li, X.; Zhou, X. *Sci. China: Chem.* **2012,** *55,* 1802–1810. doi:10.1007/s11426-012-4721-8
18. Yu, C.; Yu, J. C. *Catal. Lett.* **2009,** *129,* 462–470. doi:10.1007/s10562-008-9824-7
19. Yu, C.; Fan, Q.; Xie, Y.; Chen, J.; Shu, Q.; Yu, J. C. *J. Hazard. Mater.* **2012,** *237-238,* 38–45. doi:10.1016/j.jhazmat.2012.07.072
20. Yoong, L. S.; Chong, F. K.; Dutta, B. K. *Energy* **2009,** *34,* 1652–1661. doi:10.1016/j.energy.2009.07.024
21. Peng, L.; Xie, T.; Lu, Y.; Fan, H.; Wang, D. *Phys. Chem. Chem. Phys.* **2010,** *12,* 8033–8041. doi:10.1039/c002460k
22. Yu, C.; Li, G.; Kumar, S.; Kawasaki, H.; Jin, R. *J. Phys. Chem. Lett.* **2013,** *4,* 2847–2852. doi:10.1021/jz401447w
23. Zhu, W.; Liu, X.; Liu, H.; Tong, D.; Yang, J.; Peng, J. *J. Am. Chem. Soc.* **2010,** *132,* 12619–12626. doi:10.1021/ja1025112
24. Shin, K.; Seok, S. i.; Im, S. H.; Park, J. H. *Chem. Commun.* **2010,** *46,* 2385–2387. doi:10.1039/b923022j
25. Zhang, H.; Lv, X.; Li, Y.; Wang, Y.; Li, J. *ACS Nano* **2010,** *4,* 380–386. doi:10.1021/nn901221k
26. Li, B.; Cao, H. *J. Mater. Chem.* **2011,** *21,* 3346–3349. doi:10.1039/c0jm03253k
27. Li, Q.; Guo, B.; Yu, J.; Ran, J.; Zhang, B.; Yan, H.; Gong, J. R. *J. Am. Chem. Soc.* **2011,** *133,* 10878–10884. doi:10.1021/ja2025454
28. Li, L.; Wu, G.; Yang, G.; Peng, J.; Zhao, J.; Zhu, J.-J. *Nanoscale* **2013,** *5,* 4015–4039. doi:10.1039/c3nr33849e
29. Peng, J.; Gao, W.; Gupta, B. K.; Liu, Z.; Romero-Aburto, R.; Ge, L.; Song, L.; Alemany, L. B.; Zhan, X.; Gao, G.; Vithayathil, S. A.; Kaipparettu, B. A.; Marti, A. A.; Hayashi, T.; Zhu, J.-J.; Ajayan, P. M. *Nano Lett.* **2012,** *12,* 844–849. doi:10.1021/nl2038979
30. Shen, J.; Zhu, Y.; Chen, C.; Yang, X.; Li, C. *Chem. Commun.* **2011,** *47,* 2580–2582. doi:10.1039/c0cc04812g
31. Zhu, S.; Zhang, J.; Tang, S.; Qiao, C.; Wang, L.; Wang, H.; Liu, X.; Li, B.; Li, Y.; Yu, W.; Wang, X.; Sun, H.; Yang, B. *Adv. Funct. Mater.* **2012,** *22,* 4732–4740. doi:10.1002/adfm.201201499
32. Dong, Y.; Li, G.; Zhou, N.; Wang, R.; Chi, Y.; Chen, G. *Anal. Chem.* **2012,** *84,* 8378–8382. doi:10.1021/ac301945z
33. Gupta, V.; Chaudhary, N.; Srivastava, R.; Sharma, G. D.; Bhardwaj, R.; Chand, S. *J. Am. Chem. Soc.* **2011,** *133,* 9960–9963. doi:10.1021/ja2036749
34. Li, F.; Kou, L.; Chen, W.; Wu, C.; Guo, T. *NPG Asia Mater.* **2013,** *5,* e60. doi:10.1038/am.2013.38
35. Zhuo, S.; Shao, M.; Lee, S.-T. *ACS Nano* **2012,** *6,* 1059–1064. doi:10.1021/nn2040395
36. Qu, D.; Zheng, M.; Du, P.; Zhou, Y.; Zhang, L.; Li, D.; Tan, H.; Zhao, Z.; Xie, Z.; Sun, Z. *Nanoscale* **2013,** *5,* 12272–12277. doi:10.1039/c3nr04402e
37. Yu, Y.; Ren, J.; Meng, M. *Int. J. Hydrogen Energy* **2013,** *38,* 12266–12272. doi:10.1016/j.ijhydene.2013.07.039
38. Guo, C. X.; Dong, Y.; Yang, H. B.; Li, C. M. *Adv. Energy Mater.* **2013,** *8,* 997–1003. doi:10.1002/aenm.201300171
39. Li, Y.; Zhao, Y.; Cheng, H.; Hu, Y.; Shi, G.; Dai, L.; Qu, L. *J. Am. Chem. Soc.* **2012,** *134,* 15–18. doi:10.1021/ja206030c

40. Zhu, S.; Zhang, J.; Qiao, C.; Tang, S.; Li, Y.; Yuan, W.; Li, B.; Tian, L.; Liu, F.; Hu, R.; Gao, H.; Wei, H.; Zhang, H.; Sun, H.; Yang, B. *Chem. Commun.* **2011,** *47,* 6858–6860. doi:10.1039/c1cc11122a
41. Varghese, O. K.; Paulose, M.; LaTempa, T. J.; Grimes, C. A. *Nano Lett.* **2009,** *9,* 731–737. doi:10.1021/nl803258p
42. Jin, S. H.; Kim, D. H.; Jun, G. H.; Hong, S. H.; Jeon, S. *ACS Nano* **2013,** *7,* 1239–1245. doi:10.1021/nn304675g
43. Paulose, M.; Prakasam, H. E.; Varghese, O. K.; Peng, L.; Popat, K. C.; Mor, G. K.; Desai, T. A.; Grimes, C. A. *J. Phys. Chem. C* **2007,** *111,* 14992–14997. doi:10.1021/jp075258r
44. Jiang, F.; Chen, D.; Li, R.; Wang, Y.; Zhang, G.; Li, S.; Zheng, J.; Huang, N.; Gu, Y.; Wang, C.; Shu, C. *Nanoscale* **2013,** *5,* 1137–1142. doi:10.1039/c2nr33191h

License and Terms

This is an Open Access article under the terms of the Creative Commons Attribution License (http://creativecommons.org/licenses/by/2.0), which permits unrestricted use, distribution, and reproduction in any medium, provided the original work is properly cited.

The license is subject to the *Beilstein Journal of Nanotechnology* terms and conditions: (http://www.beilstein-journals.org/bjnano)

The definitive version of this article is the electronic one which can be found at: doi:10.3762/bjnano.5.81

Beilstein Journal of Nanotechnology

Nanostructure sensitization of transition metal oxides for visible-light photocatalysis

Hongjun Chen and Lianzhou Wang*

Review

Open Access

Address:
Nanomaterials Centre, School of Chemical Engineering, The University of Queensland, St. Lucia, Brisbane, QLD, 4072, Australia

Email:
Lianzhou Wang* - l.wang@uq.edu.au

* Corresponding author

Keywords:
carbon nanostructures; nanostructure sensitization; plasmonic metal nanostructures; quantum dots; transition metal oxides; visible-light photocatalysis

Beilstein J. Nanotechnol. **2014,** *5,* 696–710.
doi:10.3762/bjnano.5.82

Received: 31 December 2013
Accepted: 21 April 2014
Published: 23 May 2014

This article is part of the Thematic Series "Photocatalysis".

Guest Editor: R. Xu

© 2014 Chen and Wang; licensee Beilstein-Institut.
License and terms: see end of document.

Abstract

To better utilize the sunlight for efficient solar energy conversion, the research on visible-light active photocatalysts has recently attracted a lot of interest. The photosensitization of transition metal oxides is a promising approach for achieving effective visible-light photocatalysis. This review article primarily discusses the recent progress in the realm of a variety of nanostructured photosensitizers such as quantum dots, plasmonic metal nanostructures, and carbon nanostructures for coupling with wide-bandgap transition metal oxides to design better visible-light active photocatalysts. The underlying mechanisms of the composite photocatalysts, e.g., the light-induced charge separation and the subsequent visible-light photocatalytic reaction processes in environmental remediation and solar fuel generation fields, are also introduced. A brief outlook on the nanostructure photosensitization is also given.

Introduction

In response to the decreasing supply of fossil fuels and the environmental problems caused by their exploitation, the search for a renewable and sustainable energy supply has been intensified in the past decades. Solar energy is clean and abundant, yet its utilization is still very low. There is a strong need for scientists to develop a sustainable and cost-effective manner for harvesting solar energy to satisfy the growing energy demand of the world with a minimal environmental impact.

Photocatalysis plays an important role for the conversion of solar energy into chemical fuel, electricity, the decomposition of organic pollutants etc. All of these photocatalytic reactions occur on the surface of semiconductors. Basically, the photocatalytic process can be mainly divided into three pathways [1-3], as shown in Figure 1. (1) Firstly, the incident light is absorbed by the semiconductor material, known as photocatalyst. If the incident light energy is larger than the bandgap of the photocatalyst, it can absorb light energy and further excite the electrons from the valence band (VB) to the conduction band (CB), leaving free holes in the VB. (2) The recombination of photogenerated electrons and holes (charge carriers) has frequently happened either on the surface or in the bulk of a semicon-

ductor accompanied with releasing photons or heat. In addition to this, there is also the possibility for photo-generated electrons and holes to migrate to the surfaces of the semiconductor. (3) Subsequently, the reduction reactions happen between the photo-generated electrons and absorbed molecules on the semiconductor surface, which play the role of electron scavengers ($A \rightarrow A^-$). The holes can generate strong oxidizing agents like hydroxyl radicals by directly reacting with surface hydroxyl groups or oxidizing adsorbed molecules ($D \rightarrow D^+$). The basic mechanisms of the photocatalytic process include these reduction and oxidation reactions as well as some secondary reactions, which forms the driving force of a number of important photocatalytic applications.

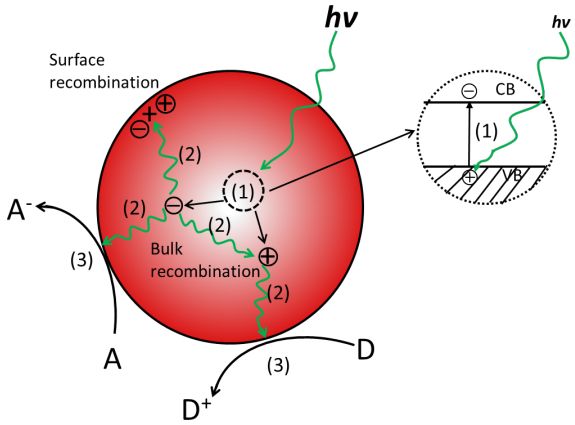

Figure 1: Schematic steps for the photocatalytic reactions occuring on the surface of a semiconductor. Adapted from [3].

Since the discovery of TiO_2 for photoelectrochemical splitting of water in 1972 by Fujishima and Honda [4], great efforts have been directed to the research of the conversion of solar energy, in the process of which the development and utilization of a variety of semiconductor photocatalysts have received significant attention. Up to now, more than 100 photocatalysts have been developed [5,6]. However, most of the photocatalysts under investigation are wide-bandgap transition metal oxides and only active under ultraviolet (UV) light. To be of practical use for photocatalysis, the photo-response of the transition metal oxides would be required to be within the visible light spectrum. Visible light accounts for around 43% of the electromagnetic radiation on the planet's surface compared to approximately 5% for UV light. Therefore, an appropriate photocatalyst should function in the visible-light region ($420\ nm < \lambda < 800\ nm$) with a band gap of less than 3 eV. An effective method used to overcome the limitation of well-developed UV-active photocatalysts is by photosensitization.

In the past two decades, the emergence of nanomaterials as new building blocks in the research area of photocatalysis has attracted increasing attention. Compared with bulk materials, nanomaterials often exhibit unusual features such as large surface areas, diverse morphologies and size-dependent physicochemical properties. Size-dependent properties include an increased absorption coefficient, increased band-gap energy, a reduced carrier-scattering rate, and higher reactive sites [7-10], which sums up to nanomaterials having superior properties in light harvesting and energy transfer efficiency. Thus, the usage of nanomaterials as new building blocks has opened a new way to utilize solar energy for the investigation of photocatalysis. There is a large array of excellent review articles covering selected aspects of the design of photocatalysts in the past years. In this review, we focus on a variety of nanostructures including quantum dots, plasmonic metal nanostructures and carbon-based nanostructures used as photosensitizers for tailoring wide-bandgap transition metal oxides toward visible light photocatalysts. A systematic overview on different nanostructured photosensitizers, light-induced charge transfer mechanisms and their potential applications is discussed in this article as well as a brief summary of the development prospects of this research topic.

Photosensitization of transition metal oxide

Photosensitization is an effective method to improve the visible-light photocatalytic ability of wide-bandgap transition metal oxides. The photosensitized transition metal oxides can realize visible-light photocatalysis by virtue of a narrow bandgap of photosensitizers, which is fundamentally different from the metal or non-metal doped ones. The photosensitizer can be an organic dye, an inorganic complex, and different nanostructures. Normally, photosensitizers have a bandgap, which is, narrower and has a higher CB minimum or lowest unoccupied molecular orbital (LUMO) in comparison with wide-bandgap transition metal oxides. Because a photosensitizer normally has a narrow bandgap, it can absorb the visible sunlight and even the infrared sunlight to generate electron–hole pairs. Then, if coupled with a transition metal oxide, the photogenerated electrons can be easily transferred from the CB minimum of the photosensitizer or LUMO to that of a transition metal oxide. Thus the efficient charge separation in the metal oxide-photosensitizer nanocomposites facilitates visible light photocatalysis which is important for the photo-degradation of organic pollutants and the splitting of water for the production of H_2 fuel.

In this section, we mainly focus on the different nanostructures like quantum dots, plasmonic metal nanostructures, and carbon-based nanostructures used as photosensitizers for transition metal oxides. Note that various organic dyes such as rhodamine B, porphyrins, and phthalocyanines have been employed as

photosensitizers [11-14] and these dyes also play an important role in the photosensitization of dye-sensitized solar cells (DSSCs) [15-17], we will not repeatedly discuss this part. In the past decade, the rapid development of nanotechnology has provided excellent opportunities for designing a broad range of photosensitized transition metal oxide systems by using different nanostructures as the photosensitizers.

Quantum dots as the photosensitizer

Quantum dots are fluorescent nanoparticles with sizes of several nm, which contain a core of hundreds to thousands of atoms of group II and VI elements (e.g., CdS, CdSe and CdTe) or group III and V elements (e.g., InAs and InP). Due to the quantum confinement effect of the charge carriers, quantum dots have a unique photoluminescence (PL). In comparison with organic dyes, quantum dots are characterized by unique optical and electronic properties such as a higher PL quantum efficiency, a wide continuous absorption, a narrower PL band, tunable luminescence depending only on their size, and higher photostability [8], which qualifies quantum dots as good candidates for the photosensitization of wide-band transition metal oxides.

CdS is a fascinating material with ideal band gap energy (E_g = 2.4 eV) for visible light applications. As early as 1987, Spanhel et al. confirmed that CdS particles can be excited and efficiently injected electrons to the CB of the attached TiO_2 particles under visible light illumination [18]. In the case of CdS photosensitized TiO_2, the energy of visible light cannot directly excite TiO_2 particle due to its wide bandgap (E_g = 3.2 eV). However, because the bandgap of CdS is much narrower, the same light source may be able to generate electron–hole pairs and excite the electrons from the VB to the CB of CdS. Because the CB of CdS is more negative than that of TiO_2, the photogenerated electrons will transfer from the CB of CdS to the CB of the adjacent TiO_2, while the photogenerated holes stay in the VB of CdS. Consequently, the charge separation is improved, and the separated electrons and holes are continually involved in the following reduction and oxidation reactions. The charges transfer scheme is shown in Figure 2. Zhang et al. have conducted direct femtosecond measurements of the electron transfer process from CdS to TiO_2 and found that this process could be completed on a time constant of 2 picoseconds, resulting in a significantly slower recombination of the charge carriers generated upon light absorption in CdS [19]. Improved charge separation, decreased electron–hole recombination and enhanced photocatalytic efficiency of such photosensitized transition metal oxides attracted increasing development of CdS–metal oxide composite systems [20-26]. For example, Yu and co-workers reported a microemulsion-mediated solvothermal method for the fabrication of nanosized CdS-sensitized TiO_2 nanocrystals [27]. The obtained photocatalysts exhibited a high efficiency for the decomposition of methylene blue under visible light irradiation, demonstrating the strong coupling and effective electron transfers between nanosized CdS and TiO_2 nanocrystal. The formation of Ti^{3+} was observed in the electron paramagnetic resonance (EPR) spectrum, which confirms an effective transfer of photogenerated electrons from the CB of CdS to the CB of TiO_2. The same group also successfully extended this method for the oxidation of nitric oxide in air under visible light irradiation [28]. The same configuration of CdS photosensitized TiO_2 was also used for the photocatalytic oxidation of ethanol vapour [29] and for the production of hydrogen from aqueous H_2S solution under visible light [30]. In addition to TiO_2 nanocrystals, 1D tubular structure of TiO_2 nanotubes and 2D layered titanate nanosheets were also used for the photosensitization. The CdS quantum dots photosensitized TiO_2 nanotubes by covalent bonding [21] or a sonication-assisted sequential chemical bath deposition approach [31] led to a more efficient separation of photogenerated electrons from CdS to TiO_2 nanotubes, and exhibited a much enhanced photocurrent generation and photocatalytic efficiency under visible-light irradiation. Kamat et al. compared the performances of CdS photosensitized ordered arrays of tubular TiO_2 architectures with a CdS photosensitized particulate structure and found a more efficient means of separating electron–hole pairs on the tubular TiO_2 architectures, leading to an improved performance of the CdS photosensitized tubular TiO_2 architectures [32]. Figure 3 outlines the electron transport in these two different architectures. Kim et al. reported a layer-by-layer self-assembly between positively charged CdS quantum dots and negatively charged exfoliated titanate nanosheets to design noble-metal free photocatalysts. The resultant composites exhibited a much higher photocatalytic H_2 production activity than pristine titanate and CdS quantum dots [33]. Such superior photocatalytic properties could be attributable to a combination of a few factors including the depression of electron–hole recombination, bandgap narrowing, and increased surface area upon hybridization.

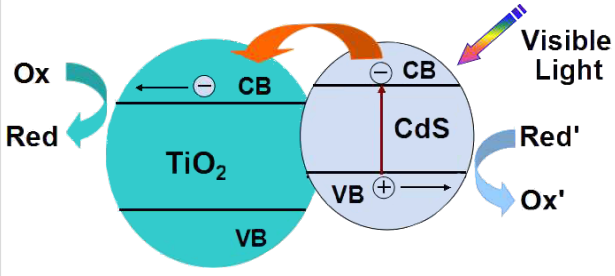

Figure 2: Schematic diagram illustrating the principle of charge transfer between CdS and TiO_2.

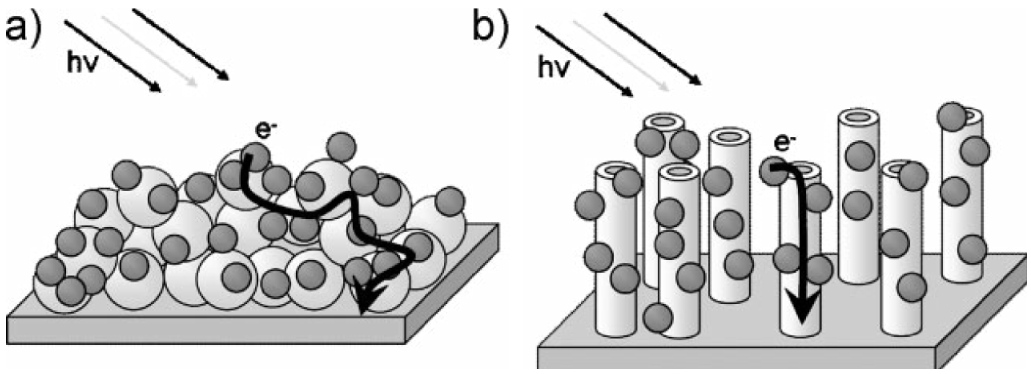

Figure 3: Photoinduced charge separation and transport in a) TiO_2 particulate film and b) TiO_2 nanotube array modified with CdS quantum dots. Reprinted from [32] copyright (2009), with permission from Wiley.

Due to the rapid development of nanotechnology, a variety of quantum dots and transition metal oxides with varied morphologies have been developed in recent years. This subsequently provides more chances for the fabrication of new classes of quantum dots photosensitized transition metal oxides. For instance, the Weller group has conducted a series of research work on the photosensitization of nanoporous titanium dioxide, zinc oxide, tin dioxide, niobium oxide, and tantalum oxide by quantum-sized cadmium sulfide, lead sulfide, silver sulfide, antimony sulfide, and bismuth sulfide. They found that the photocurrent quantum yields of these photosensitized transition metal oxides can be up to nearly 80% and open circuit voltages up to the 1 V range [24]. Ho et al. revealed that the CdSe–TiO_2 coupled system had a much higher photocatalytic activity than that of pure TiO_2 and CdSe in the degradation of 4-chlorophenol under visible light irradiation [34]. Wang et al. reported facet ZnO–CdS heterostructures and found that the hydrogen evolution rate over ZnO disk–CdS nanoparticle heterostructures is 2.8 times higher than the hydrogen evolution rate of the ZnO rod–CdS nanoparticle because photoexcited electron–hole separation is significantly enhanced by polar interfaces [35] and the greatly prolonged lifetime of photoexcited carriers [36]. We also investigated the photoelectrochemical behavior of CdS sensitized TiO_2 film with {001} facet enriched anatase nanocrystals [37]. Zhang et al. developed a double-sided CdS and CdSe quantum dot co-sensitized ZnO nanowire arrayed photoanode for photoelectrochemical hydrogen generation [38]. As shown in Figure 4, the scheme shows that the quantum dots of CdS and CdSe on both sides of ITO can be excited and transfer electrons to the ZnO nanowire array. The CB edges of CdS and CdSe are higher than that of ZnO (Figure 4b). Due to this unique configuration and the band alignment between CdS and CdSe, the co-sensitized ZnO nanowire arrayed photoanode exhibited almost the entire visible-light absorption and fast electron transfer from CdSe quantum dots to ZnO nanowires and thereby the IPCE value can reach 45% at 0 V vs Ag/AgCl, as demonstrated in Figure 4c [38]. A synergetic effect of nitrogen-doping and CdSe quantum-dot-sensitization on nanocrystalline TiO_2 was also investigated. Interestingly, a significant photoelectrochemical hydrogen generation enhancement was observed due to CdSe sensitization and N-doping that can facilitate hole transport from CdSe to TiO_2 via oxygen vacancy states mediated by N-doping [39,40]. There are also a large number of heterostructures in literature consisting of quantum dots and transition metal oxides, for instance, CdS/CdSe co-sensitized TiO_2 [41], CdTe or CdTe/CdSe quantum dots on TiO_2 nanotube arrays [42-44], CdTe quantum dot monolayer sensitized ZnO nanowire [45], CdS nanoparticle/ZnO nanowire array [46,47], CdS/ TiO_2 nanofibers heteroarchitectures [48], ZnO/CdS core/shell nanowire [49], CdS nanowires decorated with TiO_2 nanoparticles [50], and their potential applications for photoelectrochemical water splitting in order to produce hydrogen [35,38,39,41,45] and the photocatalytic reduction of CO_2 were reported [51]. In addition to the applications in photocatalysis, quantum dots are often used as photosensitizer to sensitize the mesoporous TiO_2 photoelectrode as the photoanode in quantum dots solar cells. Because quantum dots solar cells are out of the topic of this review; readers may refer to recently published reviews on this topic [52,53].

The quality of heterojunctions between quantum dots and semiconductors has an important impact on the overall photoconversion efficiency. There are mainly two methods used to modify quantum dots on the surface of semiconductor. The first method is the in situ growth method. The second method is based on the ex situ assembly of pre-synthesized quantum dots by covalent bonding, electrostatic force or the external forces such as electrophoresis. If covalent bonding is used, the length of the bifunctional linker and the surface of the transition metal oxides or quantum dots all play important roles for the photosensitized charge injection. Dibbell et al. investigated the influence of

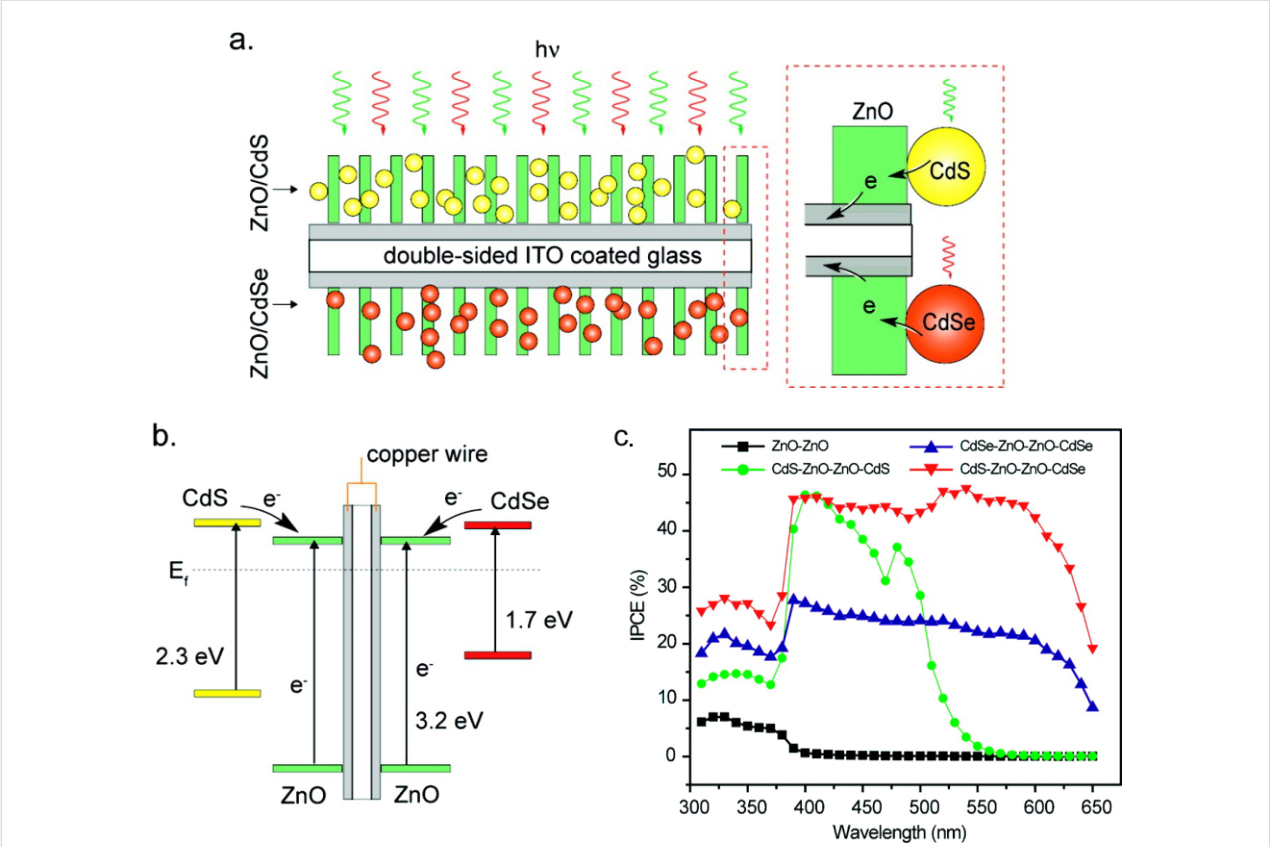

Figure 4: Schematic diagrams illustrating (a) the architecture and (b) the corresponding energy diagram of double-sided CdS–ZnO–ZnO–CdSe NW arrayed photoanode. The dashed box highlights the CdS–ZnO and CdSe–ZnO interfaces. (c) Measured IPCE spectra of double-sided NW samples collected at the incident wavelength range from 310 to 650 nm at a potential of 0 V vs Ag/AgCl. Reprinted from [38] copyright (2010), with permission from the American Chemical Society.

bifunctional linkers with different lengths between CdS quantum dots and TiO_2 nanoparticles on the electron injection from photoexcited CdS to TiO_2 [54]. They found the electron injection yield decreased with increasing chain length of the linker and interparticle separation. Parkinson et al. compared the in situ ligand exchange method and the ex situ ligand exchange method for binding CdSe quantum dots on single crystal TiO_2 surface. They revealed that the different ligand modification methods can strongly affect quantum dots adsorption and thus photosensitized charge injection [55]. Yang et al. directly compared the in situ growth method and the ex situ assembly pre-synthesized quantum dots method and found that the performance of heterojunctions by the in situ growth method exhibits a more efficient interfacial charge transfer than that of electrophoretic deposition [44]. From this comparison, it can be clearly seen that the in situ growth method can directly modify quantum dots on the surface of transition metal oxides without any linker or ligand, which is beneficial for the injection of excited charges. More importantly, the in situ growth method can load multilayer of quantum dots on the surface of transition metal oxides, which can generate many more photoexcited charges at the same time. However, the shortcoming of this method is the difficulty to control the size of the quantum dots. Due to the wide size distributions it is hard to fully utilize the size quantization effects of quantum dots. Recently, Kamat et al. highlighted a systematic evaluation of size dependent electron transfer rates in CdSe–TiO_2 semiconductor heterostructures [56]. Based on femtosecond transient absorption measurement it was found that the CB of CdSe quantum dots become more negative and the energy difference between the CB of CdSe and TiO_2 is much larger with decreasing particle size of CdSe quantum dots. Accordingly, the driving force and the electron transfer rate are significantly enhanced. There is still a need for the development of a novel method or a suitable adaptation of present deposition methods so that not only the size quantization effects of quantum dots are utilizable, but also an efficient interfacial charge transfer between quantum dots and semiconductors is improved upon.

The usage of quantum dots as a sensitizer is an effective method to extend the absorption of wide-bandgap semiconductor to visible light and even the IR region as well as dramatically

improves their visible-light photocatalytic abilities. Yet, this method also has some inherent shortcomings. One drawback is that most quantum dots are composed of heavy metals like Cd and Pb, which gives rise to environmental concerns. The other one is the photoelectrochemical stability of quantum dots. Although quantum dots combined with a wide-bandgap transition metal oxide such as ZnO and TiO_2 can overcome this stability issues to some extent, quantum dots still face a serious photocorrosion problem. For example, CdS is unstable due to serious self-oxidation by the photo-generated holes in the VB. In order to protect the quantum dots, a sacrificing chemical is normally required. For example, an aqueous solution of Na_2S and Na_2SO_3 is normally used as an electrolyte for photoelectrochemical splitting of water. In this mixture, Na_2S acts as a hole scavenger and is oxidized into S_2^{2-} to prevent the photocorrosion of quantum dots, and Na_2SO_3 reduces S_2^{2-} back to S^{2-} to ensure repeated usage of S^{2-}. An alternative way is the fabrication of the quantum dots/transition metal oxide core/shell nanostructures. Ghows et al. reported a fast and easy way for the fabrication of CdS/TiO_2 core/shell nanocrystal by microemulsion under ultrasound [57]. Co-axial arrays of CdS/TiO_2 core/shell structures were also reported to be fabricated by an anodic aluminium oxide template [58]. This type of configuration can not only protect the quantum dots from photocorrosion, but also increases the contact interface and facilitates the vectorial electron transfer.

Plasmonic metal nanostructures as the photosensitizer

Surface plasmon resonance (SPR) is the resonant photon-induced collective oscillation of valence electrons, which happens only if the frequency of photons matches the natural frequency of surface electrons oscillation on certain metallic nanostructures (e.g., Cu, Ag and Au). This radiation generates strong localized electromagnetic fields around the metallic nanostructures and leads to greatly enhanced optical absorption and scattering occurring at specific wavelengths, which depends not only on the nature of the metal, but also on the size and shape of the metallic nanostructures. For example, the plasmon resonance of silver can be tuned from UV to the visible range by reducing the size of silver particles in the nanometer range. Similarly, it is possible to shift the plasmon resonance of gold from the visible range to infrared wavelength by tuning the aspect ratio of different gold nanorods. Over the past years, a new method has emerged, which uses the strong plasmon resonance of plasmonic metal nanostructures for improving the efficiency of the photocatalytic process. Similar to the organic dyes or quantum dots, the plasmonic metal nanostructures can also be used as photosensitizer to effectively improve the visible-light response of transition metal oxides, which yields novel heterostructures of plasmonic metal photosensitized photocatalysts with a variety of applications including DSSC [59-63], photocatalytic water splitting [64,65] photoelectrochemical water splitting [66-72], photocatalytic conversion of CO_2 with H_2O to hydrocarbon fuels [73], and degradation of organic molecules [74].

In 2004, Tatsuma et al. reported that nanoporous TiO_2 films loaded with gold and silver nanoparticles exhibited anodic photocurrents in response to visible light irradiation [75]. Based on this finding, they proposed a charge transfer mechanism to explain the phenomenon. More specifically, due to the plasmon resonance effect, gold nanoparticles can be photoexcited to generate hot electrons, which are injected from the surface of the gold nanoparticles to the CB of TiO_2. Meanwhile, the compensative electrons can be transferred from a certain type of donor in the solution to the gold nanoparticles [76]. The proposed charge transfer mechanism is shown in Figure 5. The phenomenon of plasmon-enhanced photocatalysis was also successively discussed by other groups. For example, Primo et al. reported that 1 wt % gold-supported ceria nanoparticles generated oxygen from water under visible light ($\lambda > 400$ nm) more efficiently than the standard WO_3 under UV irradiation [65]. Ingram et al. employed plasmonic Ag nanocubes as building blocks to fabricate silver nanocube-N doped TiO_2 photoelectrocatalysts for PEC water splitting [67]. An investigation of the relationship between the photocurrent and light intensity by Ingram et al. revealed that N-doped TiO_2 exhibited

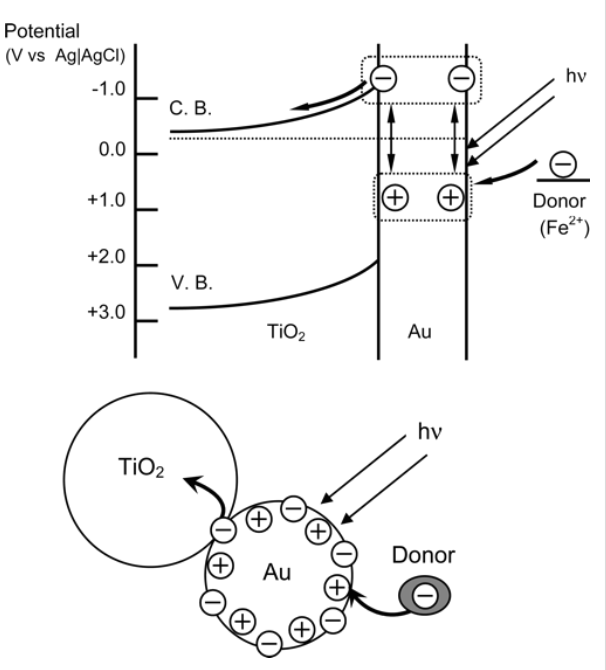

Figure 5: Proposed charge transfer mechanism for the visible-light-irradiated gold nanoparticle−TiO_2 system. Reprinted from [76] copyright (2005), with permission from American Chemical Society.

a half-order dependence and silver nanocube-N doped TiO_2 displays a first-order dependence. This indicates that the intense electric fields generated at the silver nanocubes increase the formation rate of electron–hole pairs at the nearby N-doped TiO_2 particle surface. More importantly, they also proposed a new local electric field enhancement mechanism, which is totally different from the charge transfer mechanism proposed by the Tatsuma group. Cronin and co-workers shared a viewpoint similar to that of Ingram et al. and observed enhancements of up to 66 times in the photocatalytic splitting of water in TiO_2 nanotubes with the addition of Au nanoparticles under 633 nm illumination, but a 4-fold reduction in the photocatalytic activity under UV radiation [66]. They ascribed the improvement of visible-light photocatalytic activity to the increase of the electron–hole pair generation rate by the local electric field enhancement. After a comparison of these two different mechanisms, the main difference is the origin of the photogenerated charges. The decision which mechanism takes center stage in the plasmonic enhancement traced back to the question whether there is an overlap in the absorption spectra between transition metal oxides and gold nanoparticles. Due to N-doping and N- and F-impurities generated in the anodization process, the N-doped TiO_2 nanoparticles and TiO_2 nanotubes have absorption spectra in the visible range and show an overlap with that of gold nanoparticles. Therefore, when the composite photocatalysts are illuminated under visible light, the N-doped TiO_2 nanoparticles and TiO_2 nanotubes can generate electron–hole pairs. Meanwhile, an intense local electrical field is also generated near the surface of the gold nanoparticle due to the irradiating wavelength matching the plasmon resonance frequency of gold nanoparticles, which increases the formation rate of electron–hole pairs at the surface of the TiO_2. Thus, the amount of photogenerated charges contributing to the visible-light photocatalysis is correspondingly increased. Consequently, the composite photocatalysts exhibit a much better photocatalytic performance than N-doped TiO_2 nanoparticles or TiO_2 nanotubes alone. Electromagnetic simulations based on the finite-difference time-domain method provided the theoretical support for this local electric field enhancement mechanism. In contrast to the local electric field enhancement mechanism, there is no overlap in the absorption between transition metal oxide and plasmonic metal nanostructures. Moreover, the source of the photogenerated charges is the plasmonic metal nanostructures, not the transition metal oxides.

Although two different plasmonic enhancement mechanisms are proposed, the debate is still ongoing and there are partly contradictory opinions. Therefore, many different techniques and approaches are adopted to investigate the plasmonic metal nanostructures–transition metal oxides heterostructures and unravel the mechanism behind the visible-light activity of plasmonic photocatalysts. For example, Furube et al. reported the direct evidence of plasmon-induced electron transfer from gold nanoparticles to TiO_2 by using a femtosecond transient absorption technique. They found that the electron injection from the excited gold nanoparticles to TiO_2 was complete within 50 fs and the electron injection yield reached 20–50% under 550 nm excitation [77,78]. Brückner et al. were first to use in situ EPR spectroscopy for monitoring water reduction over Au–TiO_2 photocatalysts. They observed a visible-light driven electron transfer from the Au nanoparticles to the CB of TiO_2 [79]. The results suggest that this electron transfer is a joint action by either d–sp interband transitions in the lower or SPR transitions in the higher wavelength range of the visible spectrum. Cushing et al. designed Au@SiO_2@Cu_2O sandwich core-shell nanostructures and used transient-absorption and photocatalysis action spectrum measurement to determine the underlying plasmonic energy-transfer mechanism [80]. Due to the insulating SiO_2 shell the gold core can only transfer the plasmonic energy to the Cu_2O shell by resonant energy transfer and the electron–hole pairs generated by the dipole–dipole interaction between the gold core and the Cu_2O semiconductor shell.

Plasmonic metal nanostructures have been incorporated into different transition metal oxides to enhance the solar-light harvesting and the energy-conversion efficiency for the photoelectrochemical water splitting. For example, Zhang and co-workers have investigated the influence of different sizes of gold nanoparticles on the performance of the composite Au/TiO_2 nanotube photonic crystal (NTPC) photocatalysts [72]. As described in Figure 6, a variable photocurrent density can be obtained if the TiO_2 NTPC is modified with different sizes of gold nanoparticles under visible light illumination (≥420 nm). The gold nanoparticles with a SPR peak located at 556 nm have the maximum photocurrent density and the IPCE value can reach around 8%. The authors described the good match between the plasmonic wavelength of gold nanoparticles and the photonic bandgap of photonic crystal as the main reason for Au (556)/TiO_2 NTPC to display the best photoelectrochemical performance among three different sizes of Au/TiO_2 NTPC photocatalysts. There are also other groups of nanoarchitectures such as silver nanoparticle–WO_3 [81], gold nanoparticles–Fe_2O_3 [69,82,83], gold nanoparticle–ZnO nanorods [68], gold nanorod–TiO_2 [70,71,84], gold nanoparticles–TiO_2 nanotube [66,72]. For more details, readers may refer to recent excellent reviews for basic principle and detailed effects of localized surface plasmons on transition metal oxides [85-87].

In comparison with quantum dots sensitized semiconductors the usage of plasmonic nanoparticles as photosensitizers is more stable and environmentally friendlier. The shortcoming of these plasmonic metals is their high price. This holds true for gold in

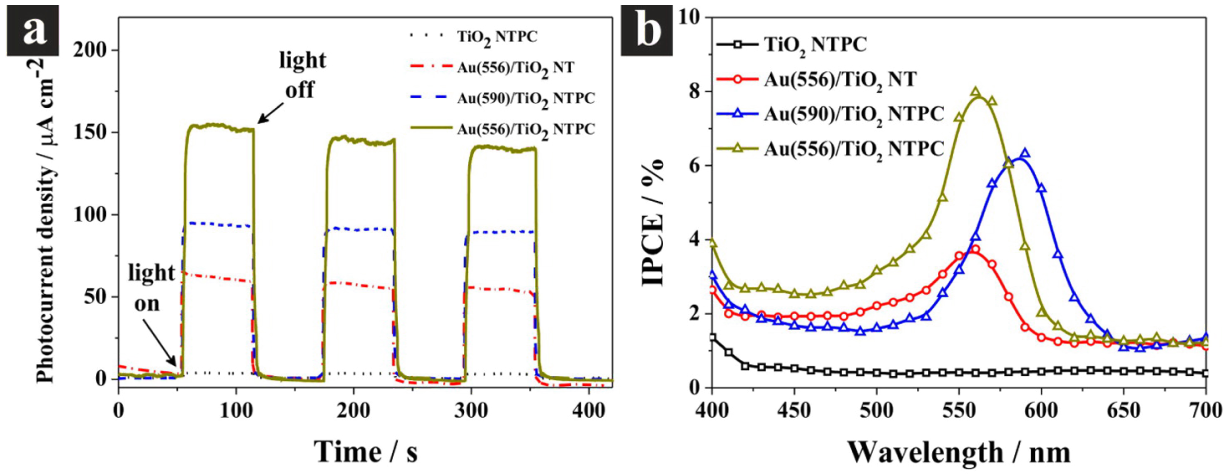

Figure 6: Photoelectrochemical properties of the TiO_2 NTPC and Au/TiO_2 NTPC and schematic diagram of SPR charge carrier transfer mechanisms. (a) Amperometric I–t curves at an applied potential of 1.23 V vs RHE under illumination of visible light with wavelength ≥420 nm and 60 s cycles of light turned on/off. (b) IPCE plots in the range of 400–700 nm at 1.23 V vs RHE. Reprinted from [72] copyright (2013), with permission from American Chemical Society.

particular. Moreover, the photoconversion efficiency of plasmonic nanoparticles photosensitized semiconductors is not as good as that of quantum dots sensitized semiconductors. Plasmon-enhanced photocatalysis is still in an early research stage and the underlying mechanism is unclear. Furthermore, there are contradictory phenomena reported in the literature. For example, Ingram et al. found that Au-N–TiO_2 has no enhancement for visible-light PEC water splitting [67], while in most other cases gold nanoparticles are described as an important photosensitizer for the production of H_2 under visible light [70-72,75,76,88]. The other disputed phenomenon is that some researchers report on the reduction of the photocurrent after the gold nanoparticles are in contact with TiO_2 nanotubes under UV illumination [66,89], while other researchers did not observe such a phenomenon [64,72]. There are also some debates about whether the hot electrons can cross over or transfer through the potential barrier of the Schottky junction at the metal–semiconductor interface [68,88].

It is noteworthy that the plasmonic nanostructures can play different roles under UV and visible light. Under UV light, the plasmonic nanostructures play the role of a co-catalyst, which may act as electron sinks to draw them away from the holes and enhance their lifetimes [64]. Under visible light, the plasmonic nanostructures enhance the solar-light harvesting and increase the visible-light energy-conversion efficiency as photosensitizer. It is well-known that the resonant wavelength and SPR intensity depend not only on the nature of the metal, but also on the size and shape of the metallic nanostructures. The control of parameters such as composition, size and shape of plasmonic nanoparticles facilitates the design of nanostructures interacting with the entire solar spectrum [85]. Therefore, it is of great interest to develop novel classes of plasmonic nanostructures photosensitized transition metal oxides with higher photoconversion efficiency. Recently, new findings have been published. For example, Tatsuma et al. found that gold clusters can also be utilized as "organic dyes" for the conversion of light to current under visible and/or near-infrared light irradiation [90-92]. These gold clusters with tens of atoms are much smaller than gold nanoparticles, which caused gold clusters to exhibit no localized SPR but a molecular orbital. For example, Au_{25} nanoclusters are characterized by molecular-like excited-state properties with well-defined absorption and emission features, which results in Au_{25} nanoclusters acting as photosensitizer and exhibiting photoinduced electron-transfer properties. This finding may pave the way for the photosensitization of semiconductors for potential applications in solar cells and photocatalysis. Another interesting phenomenon related to plasmonic metal nanoparticles is that the metal themselve may also be used as a photocatalyst for photo-oxidation or even water splitting.

Carbon nanostructure as the photosensitizer

Carbon nanostructures as one of the important building blocks has been used in many research fields due to its unique properties such as good conductivity, chemical stability and high surface area. Carbon nanotube is a particular carbon nanostructure and displays a variety of unique properties such as a high number of active sites for the adsorption of reactants, good charge carrier separation and possible visible-light excitation by bandgap modification or sensitization. Consequently, carbon nanotubes are good candidates for the enhancement of photo-

catalysis. Usually, carbon nanotubes are used as an electron sink to improve the charge carrier separation and reduce the recombinations of electron–hole pairs. This way, the photocatalytic activity of the composite carbon nanotube/transition metal oxides is effectively improved (Figure 7a) [93]. Recently, it has been found that carbon nanostructure can also be used as a sensitizer to activate wide-bandgap semiconductors under visible light. For example, Liao et al. investigated the photocatalytic ability of the composite photocatalysts including multi-walled carbon nanotubes, TiO_2 and Ni particle. They found that the rate of H_2 evolution can reach 38.1 μmol/h under visible light illumination [94]. In this process, multi-walled carbon nanotube plays the role of a photosensitizer by enhancing the visible-light activity of the composite photocatalyst. The photosensitization of carbon nanotubes was also reported for carbon nanotube–TiO_2 composite photocatalysts in the case of the photocatalytic degradation of phenol under visible light irradiation [95] (Figure 7b). In this photo-excitation process, carbon nanotubes are firstly excited by visible light and transfer electrons to the CB of a transition metal oxide for the reduction reaction to occur. Meanwhile, the positively charged carbon nanotubes extract electrons from the VB of transition metal oxide and transfer the holes to the transition metal oxide for the redox processes. Sigmund and co-workers also proposed a third mechanism as shown in Figure 7c [96], which is essentially similar to carbon-doped transition metal oxides.

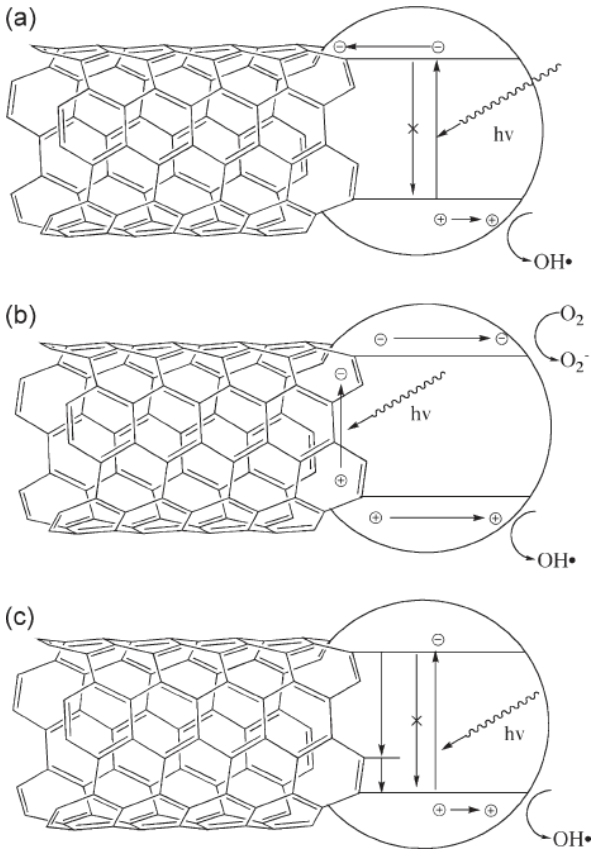

Figure 7: Proposed mechanisms for the carbon nanotube-mediated enhancement of photocatalysis. a) Carbon nanotubes act as electron sinks to inhibit the recombination of electron–hole pairs. b) Photosensitizing mechanism of carbon nanotubes based on generation of charge carriers in the carbon nanotubes. c) The carbon nanotubes act as an impurity by introducing additional energy levels within the transition metal oxide band gap. Reprinted from [96] copyright (2009), with permission from Wiley.

As a representative carbon nanostructure, graphene is a 2D network of hexagonally structured sp2-hybridized carbon atoms [97]. Compared with other carbon nanostructures, graphene exhibits some outstanding properties, such as a large specific surface area (2630 $m^2\ g^{-1}$), an exceptional conductivity (106 S cm^{-1}), a fast room temperature mobility of charge carriers (200000 $cm^2\ V^{-1}\ s^{-1}$), and an excellent optical transmittance (97.7%) [98]. Very recently, it has been reported that graphene has the function for the sensitization of semiconductors based on several experimental and theoretical researches. For instance, Du et al. used ab initio calculations to demonstrate that a graphene/titania interface in the ground electronic state forms a charge-transfer complex due to the large difference of work functions between graphene and TiO_2 [99]. Most interestingly, valence electrons may be directly excited from graphene into the CB of TiO_2 under visible light illumination, so that graphene may be used as a photosensitizer. The authors also investigated the graphene–g-C_3N_4 interface by hybrid functional DFT methods and found a band gap (around 70 meV) forming an electron–hole puddle in a g-C_3N_4-supported graphene monolayer [100]. Song and co-workers observed an enhancement of the photoconversion efficiency up to 15 times for a TiO_2 nanotube composite electrode decorated by graphene oxide (GO) in comparison with pristine TiO_2 nanotube arrays under identical measurement conditions [101]. The reduced graphene oxide (RGO) can act as a photosensitizer similar to organic dyes in the ZnS–RGO nanocomposites, which subsequently leads to efficient visible-light driven photoactivity for both the aerobic selective oxidation of alcohols and the epoxidation of alkenes under ambient conditions [102]. The similar photosensitization of graphene was also demonstrated in a $ZnWO_4$/graphene hybrid photocatalysts for the degradation of methylene blue [103], a RGO–ZnO heterojunction for the photoelectrochemical H_2 production [104], and GO–TiO_2 for the photochemical water splitting [105]. The mechanisms in these research works are very similar. As shown in Figure 8a, $ZnWO_4$ can absorb UV light to produce photogenerated electron–hole pairs, and then the holes transfer from the VB of $ZnWO_4$ to the highest occupied molecular orbital (HOMO) of graphene because the VB position of $ZnWO_4$ is lower than the HOMO of graphene. Since the CB position of $ZnWO_4$ is lower than the LUMO of graphene, the photogener-

ated electrons can only stay at the CB of $ZnWO_4$ and take part in the surface reaction to form radicals [103]. For visible light irradiation, the electrons are firstly excited from HOMO to LUMO of graphene, and then injected into the CB of $ZnWO_4$ to participate in the reduction reaction on the surface, thus producing the visible-light activity (Figure 8b) [106]. This effective separation of photogenerated electron–hole pairs can effectively reduce the probability of recombination, thus resulting in an enhanced photocatalytic activity. Apart from photosensitization, graphene also has other functionalities such as the role of an electron acceptor and transporter, a cocatalyst, and a photocatalyst in the field of hydrogen generation. Readers may refer to a recently published review for more detailed information [106].

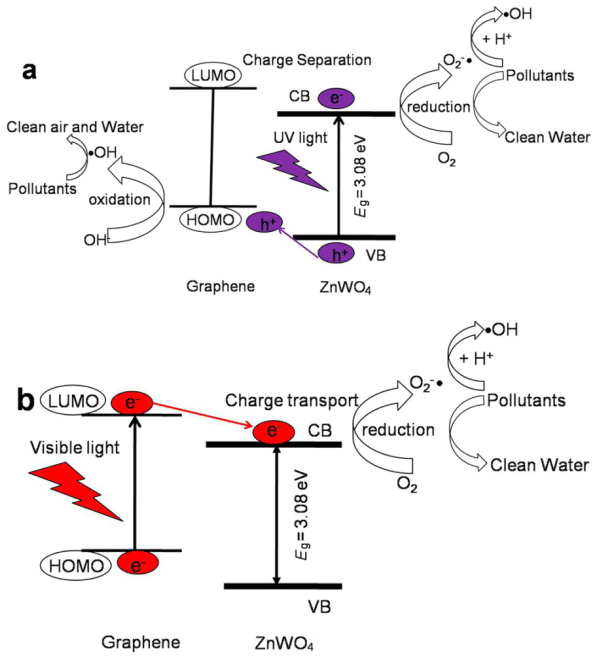

Figure 8: Schematic drawing illustrating the mechanism of charge separation and photocatalytic process over $ZnWO_4$/graphene photocatalysts under UV light (a) and visible light (b) irradiation. Reprinted from [103] copyright (2012), with permission from the American Chemical Society.

Carbon nanodots are a new class of carbon nanomaterials and consist of discrete, quasispherical nanoparticles with sizes below 10 nm [107-110]. Since they have been reported on in 2004 for the first time [111], carbon dots have gradually become an important member in the nanocarbon family due to their benign, abundant and low-cost nature. As carbonaceous quantum dots, carbon nanodots display PL behavior dependent on their size and the excitation wavelength. In addition, carbon dots are also characterized by water solubility, chemical inertness and resistance to photobleaching. Up to now, many methods [112-127] are available for the fabrication of carbon nanodots, for instance, the electrochemical method, the microwave method, the ultrasonic method, the hydrothermal method. Due to their easy fabrication methods in addition to their unique properties carbon nanodots are a versatile material candidate for bioimaging, sensors, catalysis and photovoltaic devices [107-110]. There are also some reviews covering the synthetic methods, physical and chemical properties, and potential applications of carbon nanodots [107-110], among the latter of which is their use as a photosensitizer for the visible-light photocatalysis. For example, TiO_2/carbon nanodots demonstrate an efficient photodegradation of methyl blue under visible light [112]. The visible-light photocatalytic mechanism for TiO_2/carbon nanodots is schematically shown in Figure 9. When TiO_2/carbon nanodots are illuminated by visible light, the carbon nanodots can absorb visible light ($\lambda > 520$ nm) and emit UV light ($325 < \lambda < 425$ nm) due to the PL upconversion of carbon nanodots. The UV light emitted by carbon nanodots can further excite TiO_2 to generate electron–hole pairs, which will finally lead to the production of active oxygen radicals for the degradation of the methyl blue [112]. Besides TiO_2/carbon nanodots, ZnO/carbon nanodots are also reported as superior photocatalysts for the degradation of benzene and methanol under visible light at room temperature [128]. The photocatalytic activities of ZnO/carbon nanodots are also reported to degrade aqueous solutions of rhodamine B under visible light irradiation [129]. Similarly, other carbon nanodots based wide-bandgap transition metal oxides, such as carbon nanodot–TiO_2 nanotube [130], carbon nanodot–$SrTiO_3$ film [131], carbon nanodot–TiO_2 nanoparticle [114], and carbon nanodot–ZnO nanorod arrays [132], exhibited a good performance for photoelectrochemical water splitting or photocatalytic activity in dye degradation under visible light irradiation due to the photosensitization of carbon nanodots. By virtue of PL upconversion prop-

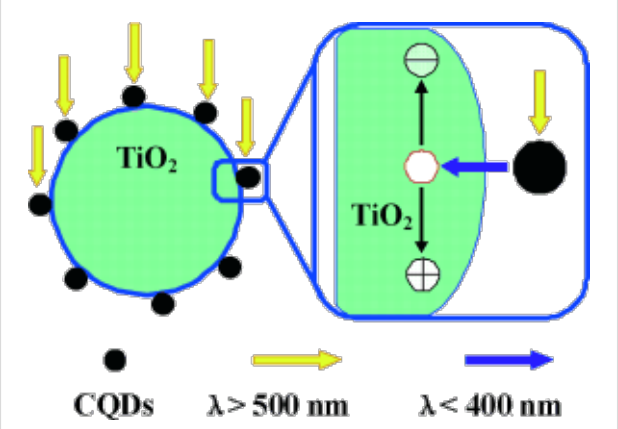

Figure 9: Photocatalytic mechanism for TiO_2–carbon nanodots under visible-light illumination. Reprinted from [112] copyright (2010), with permission from Wiley.

erties, carbon nanodots can also be used as photosensitizer to harness near-infrared light to further enhance the photocatalytic activity of some visible-light active semiconductors. Kang et al. recently reported that carbon nanodots can effectively harness the broad spectrum of sunlight to improve the photocatalytic activities of monoclinic bismuth vanadate (m-$BiVO_4$) for the photodegradation of methylene blue [133]. The carbon nanodots play a twofold role in this photocatalytic process. Firstly, carbon nanodots function as electron collectors and transporters to trap electrons and transfer electrons generated from m-$BiVO_4$ nanoparticles ($\lambda < 520$ nm), which can effectively improve the charge separation and thus the photocatalytic activity. Secondly, carbon nanodots can absorb longer wavelength light ($\lambda > 520$ nm) and then emit shorter wavelength light (300 to 530 nm) for the excitation of m-$BiVO_4$ to further generate electron–hole pairs for photocatalytic degradation. Due to the special upconversion property of carbon nanodots, the carbon nanodots–m-$BiVO_4$ nanospheres can be used as photocatalysts under the broad spectrum of sunshine. Based on a similar mechanism carbon nanodots can also be combined with Cu_2O, Ag_3PO_4 or Fe_2O_3 for the photocatalytic degradation of methyl blue, methyl orange, and toxic gases of benzene and methanol, respectively [134-136].

The merits of carbon nanostructures, and carbon nanodots in particular, such as a low cost and non-toxicity, furnishes them with superior advantages compared to other photosensitizers. More importantly, their property of feature PL upconversion can even extend the activity of carbon nanodots based photocatalysts to the infrared region. Therefore, the photosensitization of carbon nanodots is effective not only for wide-bandgap semiconductors, but also for visible-light active semiconductors, so that a broad spectrum of solar energy can be efficiently used for the photocatalysis. However, it is still required to further improve the quantum efficiency of carbon nanodots based photocatalysts.

Conclusion

In this review, recent advances of the nanostructure sensitization of transition metal oxides for visible-light photocatalysis are summarized. Nanostructure sensitization is an effective method to realize the transformation of UV-active transition metal oxides into visible-light-responsive photocatalysts. Thanks to the rapid development of nanotechnology, more methods are available for the synthesis of shape- and size-controlled nanostructures and facet-controlled transition metal oxides [137-139]. These advances provide a rich library for an improved photocatalyst design. For example, ion-exchangeable semiconductors, one type of transition metal oxide, have recently attracted more attention due to their inherent features. Firstly, the special gallery structures of ion-exchangeable semiconductors render them attractive for non-metal doping. We investigated a range of non-metal doping such as N, S, I and even S, N co-doping, in a serial of ion-exchangeable semiconductors [140-144]. It was found that homogeneous doping can be more easily realized on ion-exchangeable semiconductors than on bulk crystal semiconductors because the special structure of the interlayer galleries of ion-exchangeable semiconductors provides excellent channels for the diffusion of dopant and finally resulted in a uniform distribution of dopant over the whole semiconductor materials. The homogeneous doping leads to a significantly enhanced photocatalytic performance for ion-exchangeable semiconductors in the visible region. Secondly, ion-exchangeable layered semiconductors have spatially well-separated photocatalytic reduction and oxidation reaction sites, which can effectively decelerate the recombination of the photogenerated electron–hole pairs and further improve the photocatalytic ability [145]. The last feature is that an appreciable number of ion-exchangeable semiconductors can be exfoliated into single-layer two-dimensional (2D) nanosheets by the intercalation–exfoliation method, as shown in Figure 10. The thickness of the single-layer 2D nanosheets is less than 1 nm and has extremely high surface areas. Thus, exfoliated 2D nanosheets not only can be easily used as building blocks for the fabrication of photocatalysts with good photocatalytic ability [146], but also offer a nearly infinite surface area in aqueous solution for the photosensitizers to anchor. The hybridization of exfoliated nanosheets with nanosized photosensitizers often shows a tunable electronic structure and new physicochemical properties. All these features attribute to a promising future of nanostructure sensitization in the ion-exchangeable semiconductor family for photocatalytic applications.

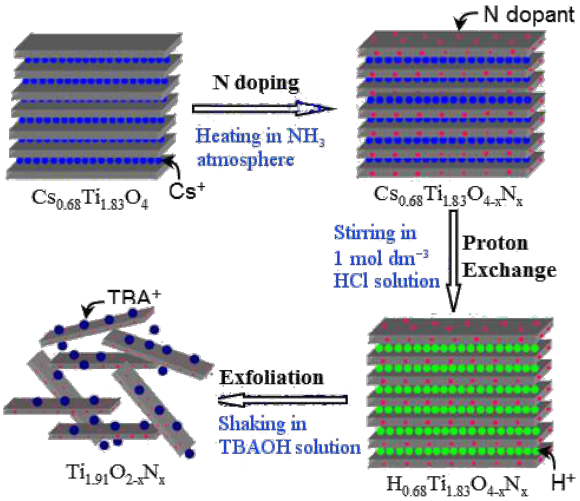

Figure 10: The schematic procedures for the preparation of nitrogen-doped $Ti_{0.91}O_2$ nanosheets. TBA^+: tetrabutylammonium ion. Reprinted from [146] copyright (2009), with permission from the Royal Society of Chemistry.

The synergistic effect of doping and sensitization is also applied to certain wide-bandgap transition metal oxides. It is found that doping with photosensitization can dramatically change the visible-light absorption and significantly enhance the photocatalytic ability. For example, Zhang and co-workers have recently reported on the synergistic effect of CdSe quantum dot sensitization and N doping of TiO_2 nanostructures for photoelectrochemical water splitting [39]. In this report, it has been found that the photocurrent density of CdSe/N-TiO_2 is much larger than either TiO_2 sensitized by CdSe quantum dots or TiO_2 doped with N. This also demonstrates the synergistic effect in the photo-excitation process. The synergistic effect also happens on composite photocatalysts containing two different types of photosensitizers. For example, in order to extend the photocatalytic activity of a semiconductor into a much longer wavelength, two different quantum dots like CdS/CdSe or CdSe/CdTe co-sensitized ZnO or TiO_2 have been reported [38,41,44]. The synergistic effects of CdSe quantum dots and carbon nanodots co-sensitized TiO_2 for the photoelectrochemcial hydrogen generation has also been explored [147]. In this case, carbon nanodots absorb near-infrared photons ($\lambda > 750$ nm) and emit visible photons through the upconversion effect to excite CdSe again. The strategy of these studies may pave the way for the design of near-infrared active photoelectrochemical systems in the future.

There are also new nanostructures with special features for the potential application in visible-light photocatalysis. For example, very recently, Heinz and co-workers found that by decreasing the thickness of MoS_2 to a monolayer [148], the indirect bandgap bulk semiconductor can change into a direct bandgap. Correspondingly, the monolayer of MoS_2 exhibits 104 times enhancement of luminescence quantum efficiency than that of bulk material. This new finding has also been verified by other research groups [149,150]. Based on this new finding, one may easily imagine that the monolayer of MoS_2 has great potential as a photosensitizer in the near future. In addition to monolayer MoS_2, the nanostructures of gold clusters and carbon nanodots are still in a stage of early development, providing numerous challenges and opportunities for future investigation.

Although visible-light photocatalysis is still in an early phase of development, the photocatalysts have played effective roles in many potential applications including solar fuel production, pollutant decomposition, and water/air purification. In the course of, we believe that a fundamental understanding of the photocatalytic process and the rational design of visible-light photocatalysts with a high conversion efficiency may lead to an important role of nanostructure photosensitization in visible-light photocatalysis for efficient solar energy conversion.

Acknowledgements

The Australian Research Council is acknowledged for its financial support by means of the Discovery and Future Fellowship project, and Dr. H. Chen thanks the University of Queensland for a UQ Postdoctoral Fellowship and a UQ Early Career Researcher grant support.

References

1. Hoffmann, M. R.; Martin, S. T.; Choi, W.; Bahnemann, D. W. *Chem. Rev.* **1995,** *95,* 69–96. doi:10.1021/cr00033a004
2. Mills, A.; Le Hunte, S. *J. Photochem. Photobiol., A: Chem.* **1997,** *108,* 1–35. doi:10.1016/S1010-6030(97)00118-4
3. Zong, X.; Wang, L. *J. Photochem. Photobiol., C: Photochem. Rev.* **2014,** *18,* 32–49. doi:10.1016/j.jphotochemrev.2013.10.001
4. Fujishima, A.; Honda, H. *Nature* **1972,** *238,* 37–38. doi:10.1038/238037a0
5. Kudo, A.; Miseki, Y. *Chem. Soc. Rev.* **2009,** *38,* 253–278. doi:10.1039/b800489g
6. Osterloh, F. E. *Chem. Mater.* **2008,** *20,* 35–54. doi:10.1021/cm7024203
7. Chen, X.; Mao, S. S. *Chem. Rev.* **2007,** *107,* 2891–2959. doi:10.1021/cr0500535
8. Nozik, A. J.; Beard, M. C.; Luther, J. M.; Law, M.; Ellingson, R. J.; Johnson, J. C. *Chem. Rev.* **2010,** *110,* 6873–6890. doi:10.1021/cr900289f
9. Burda, C.; Chen, X.; Narayanan, R.; El-Sayed, M. A. *Chem. Rev.* **2005,** *105,* 1025–1102. doi:10.1021/cr030063a
10. Eder, D. *Chem. Rev.* **2010,** *110,* 1348–1385. doi:10.1021/cr800433k
11. Kalyanasundaram, K.; Grätzel, M. *Coord. Chem. Rev.* **1998,** *177,* 347–414. doi:10.1016/S0010-8545(98)00189-1
12. Argazzi, R.; Murakami Iha, N. Y.; Zabri, H.; Odobel, F.; Bignozzi, C. A. *Coord. Chem. Rev.* **2004,** *248,* 1299–1316. doi:10.1016/j.ccr.2004.03.026
13. Jaeger, C. D.; Fan, F.-R. F.; Bard, A. J. *J. Am. Chem. Soc.* **1980,** *102,* 2592–2598. doi:10.1021/ja00528a012
14. Giraudeau, A.; Fan, F.-R. F.; Bard, A. J. *J. Am. Chem. Soc.* **1980,** *102,* 5137–5142. doi:10.1021/ja00536a001
15. Stipkala, J. M.; Castellano, F. N.; Heimer, T. A.; Kelly, C. A.; Livi, K. J. T.; Meyer, G. J. *Chem. Mater.* **1997,** *9,* 2341–2353. doi:10.1021/cm9703177
16. Kalyanasundaram, K.; Grätzel, M. *Coord. Chem. Rev.* **1986,** *69,* 57–125. doi:10.1016/0010-8545(86)85009-3
17. Memming, R. *Prog. Surf. Sci.* **1984,** *17,* 7–73. doi:10.1016/0079-6816(84)90012-1
18. Spanhel, L.; Weller, H.; Henglein, A. *J. Am. Chem. Soc.* **1987,** *109,* 6632–6635. doi:10.1021/ja00256a012
19. Evans, J. E.; Springer, K. W.; Zhang, J. Z. *J. Chem. Phys.* **1994,** *101,* 6222–6225. doi:10.1063/1.468376
20. Sun, W.-T.; Yu, Y.; Pan, H.-Y.; Gao, X.-F.; Chen, Q.; Peng, L.-M. *J. Am. Chem. Soc.* **2008,** *130,* 1124–1125. doi:10.1021/ja0777741
21. Kim, J. C.; Choi, J.; Lee, Y. B.; Hong, J. H.; Lee, J. I.; Yang, J. W.; Lee, W. I.; Hur, N. H. *Chem. Commun.* **2006,** 5024–5026. doi:10.1039/b612572g
22. Kiyonaga, T.; Akita, T.; Tada, H. *Chem. Commun.* **2009,** 2011–2013. doi:10.1039/b818825d
23. Park, H.; Choi, W.; Hoffmann, M. R. *J. Mater. Chem.* **2008,** *18,* 2379–2385. doi:10.1039/b718759a

24. Vogel, R.; Hoyer, P.; Weller, H. *J. Phys. Chem.* **1994,** *98,* 3183–3188. doi:10.1021/j100063a022
25. Peter, L. M.; Riley, D. J.; Tullb, E. J.; Wijayantha, K. G. U. *Chem. Commun.* **2002,** 1030–1031. doi:10.1039/b201661c
26. Chen, Y.; Wang, L.; Lu, G. (M.); Yao, X.; Guo, L. *J. Mater. Chem.* **2011,** *21,* 5134–5141. doi:10.1039/c0jm03945d
27. Yu, J. C.; Wu, L.; Lin, J.; Li, P.; Li, Q. *Chem. Commun.* **2003,** 1552–1553. doi:10.1039/b302418k
28. Wu, L.; Yu, J. C.; Fu, X. *J. Mol. Catal. A: Chem.* **2006,** *244,* 25–32. doi:10.1016/j.molcata.2005.08.047
29. Kozlova, E. A.; Kozhevnikova, N. S.; Cherepanova, S. V.; Lyubina, T. P.; Gerasimov, E. Yu.; Kaichev, V. V.; Vorontsov, A. V.; Tsybulya, S. V.; Rempel, A. A.; Parmon, V. N. *J. Mol. Catal. A: Chem.* **2012,** *250,* 103–109. doi:10.1016/j.jphotochem.2012.09.014
30. Jang, J. S.; Li, W.; Oh, S. H.; Lee, J. S. *Chem. Phys. Lett.* **2006,** *425,* 278–282. doi:10.1016/j.cplett.2006.05.031
31. Xie, Y.; Ali, G.; Yoo, S. H.; Cho, S. O. *ACS Appl. Mater. Interfaces* **2010,** *2,* 2910–2914. doi:10.1021/am100605a
32. Baker, D. R.; Kamat, P. V. *Adv. Funct. Mater.* **2009,** *19,* 805–811. doi:10.1002/adfm.200801173
33. Kim, H. N.; Kim, T. W.; Kim, I. Y.; Hwang, S.-J. *Adv. Funct. Mater.* **2011,** *21,* 3111–3118. doi:10.1002/adfm.201100453
34. Ho, W.; Yu, J. C. *J. Mol. Catal. A: Chem.* **2006,** *247,* 268–274. doi:10.1016/j.molcata.2005.11.057
35. Wang, X.; Yin, L.; Liu, G.; Wang, L.; Saito, R.; Lu, G. Q. (M.); Cheng, H.-M. *Energy Environ. Sci.* **2011,** *4,* 3976–3979. doi:10.1039/c0ee00723d
36. Wang, X.; Liu, G.; Chen, Z.-G.; Li, F.; Wang, L.; Lu, G. Q.; Cheng, H.-M. *Chem. Commun.* **2009,** 3452–3454. doi:10.1039/b904668b
37. Wang, X.; Liu, G.; Wang, L.; Pan, J.; Lu, G. Q. (M.); Cheng, H.-M. *J. Mater. Chem.* **2011,** *21,* 869–873. doi:10.1039/c0jm02694h
38. Wang, G.; Yang, X.; Qian, F.; Zhang, J.; Li, Y. *Nano Lett.* **2010,** *10,* 1088–1092. doi:10.1021/nl100250z
39. Hensel, J.; Wang, G.; Li, Y.; Zhang, J. Z. *Nano Lett.* **2010,** *10,* 478–483. doi:10.1021/nl903217w
40. López-Luke, T.; Wolcott, A.; Xu, L.-p.; Chen, S.; Wen, Z.; Li, J.; De La Rosa, E.; Zhang, J. Z. *J. Phys. Chem. C* **2008,** *112,* 1282–1292. doi:10.1021/jp077345p
41. Lee, Y.-L.; Chi, C.-F.; Liau, S.-Y. *Chem. Mater.* **2010,** *22,* 922–927. doi:10.1021/cm901762h
42. Gao, X.-F.; Li, H.-B.; Sun, W.-T.; Chen, Q.; Tang, F.-Q.; Peng, L.-M. *J. Phys. Chem. C* **2009,** *113,* 7531–7535. doi:10.1021/jp810727n
43. Seabold, J. A.; Shankar, K.; Wilke, R. H. T.; Paulose, M.; Varghese, O. K.; Grimes, C. A.; Choi, K.-S. *Chem. Mater.* **2008,** *20,* 5266–5273. doi:10.1021/cm8010666
44. Yang, H.; Fan, W.; Vaneski, A.; Susha, A. S.; Teoh, W. Y.; Rogach, A. L. *Adv. Funct. Mater.* **2012,** *22,* 2821–2829. doi:10.1002/adfm.201103074
45. Chen, H. M.; Chen, C. K.; Chang, Y.-C.; Tsai, C.-W.; Liu, R.-S.; Hu, S.-F.; Chang, W.-S.; Chen, K.-H. *Angew. Chem., Int. Ed.* **2010,** *49,* 5966–5969. doi:10.1002/anie.201001827
46. Tak, Y.; Kim, H.; Lee, D.; Yong, K. *Chem. Commun.* **2008,** 4585–4587. doi:10.1039/b810388g
47. Tak, Y.; Hong, S. J.; Lee, J. S.; Yong, K. *Cryst. Growth Des.* **2009,** *9,* 2627–2632. doi:10.1021/cg801076b
48. Su, C.; Shao, C.; Liu, Y. *J. Colloid Interface Sci.* **2011,** *359,* 220–227. doi:10.1016/j.jcis.2011.03.044
49. Tak, Y.; Hong, S. J.; Lee, J. S.; Yong, K. *J. Mater. Chem.* **2009,** *19,* 5945–5951. doi:10.1039/b904993b
50. Jang, J. S.; Kim, H. G.; Joshi, U. A.; Jang, J. W.; Lee, J. S. *Int. J. Hydrogen Energy* **2008,** *33,* 5975–5980. doi:10.1016/j.ijhydene.2008.07.105
51. Wang, C.; Thompson, R. L.; Baltrus, J.; Matranga, C. *J. Phys. Chem. Lett.* **2010,** *1,* 48–53. doi:10.1021/jz9000032
52. Kamat, P. V. *J. Phys. Chem. C* **2007,** *111,* 2834–2860. doi:10.1021/jp066952u
53. Kamat, P. V. *J. Phys. Chem. C* **2008,** *112,* 18737–18753. doi:10.1021/jp806791s
54. Dibbell, R. S.; Watson, D. F. *J. Phys. Chem. C* **2009,** *113,* 3139–3149. doi:10.1021/jp809269m
55. Sambur, J. B.; Riha, S. C.; Choi, D.; Parkinson, B. A. *Langmuir* **2010,** *26,* 4839–4847. doi:10.1021/la903618x
56. Robel, I.; Kuno, M.; Kamat, P. V. *J. Am. Chem. Soc.* **2007,** *129,* 4136–4137. doi:10.1021/ja070099a
57. Ghows, N.; Entezari, M. H. *Ultrason. Sonochem.* **2011,** *18,* 629–634. doi:10.1016/j.ultsonch.2010.08.003
58. Hsua, M.-C.; Leu, I.-C.; Sun, Y.-M.; Hon, M.-H. *J. Cryst. Growth* **2005,** *285,* 642–648. doi:10.1016/j.jcrysgro.2005.08.060
59. Qi, J.; Dang, X.; Hammond, P. T.; Belcher, A. M. *ACS Nano* **2011,** *5,* 7108–7116. doi:10.1021/nn201808g
60. Du, J.; Qi, J.; Wang, D.; Tang, Z. *Energy Environ. Sci.* **2012,** *5,* 6914–6918. doi:10.1039/c2ee21264a
61. Choi, H.; Chen, W. T.; Kamat, P. V. *ACS Nano* **2012,** *6,* 4418–4427. doi:10.1021/nn301137r
62. Li, Y.; Wang, H.; Feng, Q.; Zhou, G.; Wang, Z.-S. *Energy Environ. Sci.* **2013,** *6,* 2156–2165. doi:10.1039/c3ee23971c
63. Brown, M. D.; Suteewong, T.; Kumar, R. S. S.; D'Innocenzo, V.; Petrozza, A.; Lee, M. M.; Wiesner, U.; Snaith, H. J. *Nano Lett.* **2011,** *11,* 438–445. doi:10.1021/nl1031106
64. Silva, C. G.; Juárez, R.; Marino, T.; Molinari, R.; García, H. *J. Am. Chem. Soc.* **2011,** *133,* 595–602. doi:10.1021/ja1086358
65. Primo, A.; Marino, T.; Corma, A.; Molinari, R.; García, H. *J. Am. Chem. Soc.* **2011,** *133,* 6930–6933. doi:10.1021/ja2011498
66. Liu, Z.; Hou, W.; Pavaskar, P.; Aykol, M.; Cronin, S. B. *Nano Lett.* **2011,** *11,* 1111–1116. doi:10.1021/nl104005n
67. Ingram, D. B.; Linic, S. *J. Am. Chem. Soc.* **2011,** *133,* 5202–5205. doi:10.1021/ja200086g
68. Chen, H. M.; Chen, C. K.; Chen, C.-J.; Cheng, L.-C.; Wu, P. C.; Cheng, B. H.; Ho, Y. Z.; Tseng, M. L.; Hsu, Y.-Y.; Chan, T.-S.; Lee, J.-F.; Liu, R.-S.; Tsai, D. P. *ACS Nano* **2012,** *6,* 7362–7372. doi:10.1021/nn3024877
69. Thimsen, E.; Le Formal, F.; Grätzel, M.; Warren, S. C. *Nano Lett.* **2011,** *11,* 35–43. doi:10.1021/nl1022354
70. Pu, Y.-C.; Wang, G.; Chang, K.-D.; Ling, Y.; Lin, Y.-K.; Fitzmorris, B. C.; Liu, C.-M.; Lu, X.; Tong, Y.; Zhang, J. Z.; Hsu, Y.-J.; Li, Y. *Nano Lett.* **2013,** *13,* 3817–3823. doi:10.1021/nl4018385
71. Mubeen, S.; Lee, J.; Singh, N.; Krämer, S.; Stucky, G. D.; Moskovits, M. *Nat. Nanotechnol.* **2013,** *8,* 247–251. doi:10.1038/nnano.2013.18
72. Zhang, Z.; Zhang, L.; Hedhili, M.; Zhang, H.; Wang, P. *Nano Lett.* **2013,** *13,* 14–20. doi:10.1021/nl3029202
73. Hou, W.; Hung, W. H.; Pavaskar, P.; Goeppert, A.; Aykol, M.; Cronin, S. B. *ACS Catal.* **2011,** *1,* 929–936. doi:10.1021/cs2001434
74. Yu, J.; Dai, G.; Huang, B. *J. Phys. Chem. C* **2009,** *113,* 16394–16401. doi:10.1021/jp905247j
75. Tian, Y.; Tatsuma, T. *Chem. Commun.* **2004,** 1810–1811. doi:10.1039/b405061d
76. Tian, Y.; Tatsuma, T. *J. Am. Chem. Soc.* **2005,** *127,* 7632–7637. doi:10.1021/ja042192u

77. Furube, A.; Du, L.; Hara, K.; Katoh, R.; Tachiya, M. *J. Am. Chem. Soc.* **2007,** *129,* 14852–14853. doi:10.1021/ja076134v
78. Du, L.; Furube, A.; Hara, K.; Katoh, R.; Tachiya, M. *J. Photochem. Photobiol., C: Photochem. Rev.* **2013,** *15,* 21–30. doi:10.1016/j.jphotochemrev.2012.11.001
79. Priebe, J. B.; Karnahl, M.; Junge, H.; Beller, M.; Hollmann, D.; Brückner, A. *Angew. Chem., Int. Ed.* **2013,** *52,* 11420–11424. doi:10.1002/anie.201306504
80. Cushing, S. K.; Li, J.; Meng, F.; Senty, T. R.; Suri, S.; Zhi, M.; Li, M.; Bristow, A. D.; Wu, N. *J. Am. Chem. Soc.* **2012,** *134,* 15033–15041. doi:10.1021/ja305603t
81. Solarska, R.; Królikowska, A.; Augustyński, J. *Angew. Chem., Int. Ed.* **2010,** *49,* 7980–7983. doi:10.1002/anie.201002173
82. Gao, H.; Liu, C.; Jeong, H. E.; Yang, P. *ACS Nano* **2012,** *6,* 234–240. doi:10.1021/nn203457a
83. Thomann, I.; Pinaud, B. A.; Chen, Z.; Clemens, B. M.; Jaramillo, T. F.; Brongersma, M. L. *Nano Lett.* **2011,** *11,* 3440–3446. doi:10.1021/nl201908s
84. Lee, J.; Mubeen, S.; Ji, X.; Stucky, G. D.; Moskovits, M. *Nano Lett.* **2012,** *12,* 5014–5019. doi:10.1021/nl302796f
85. Linic, S.; Christopher, P.; Ingram, D. B. *Nat. Mater.* **2011,** *10,* 911–921. doi:10.1038/nmat3151
86. Warren, S. C.; Thimsen, E. *Energy Environ. Sci.* **2012,** *5,* 5133–5146. doi:10.1039/C1EE02875H
87. Hou, W.; Cronin, S. B. *Adv. Funct. Mater.* **2013,** *23,* 1612–1619. doi:10.1002/adfm.201202148
88. Mubeen, S.; Hernandez-Sosa, G.; Moses, D.; Lee, J.; Moskovits, M. *Nano Lett.* **2011,** *11,* 5548–5552. doi:10.1021/nl203457v
89. Zhang, N.; Liu, S.; Fu, X.; Xu, Y.-J. *J. Phys. Chem. C* **2011,** *115,* 9136–9145. doi:10.1021/jp2009989
90. Sakai, N.; Tatsuma, T. *Adv. Mater.* **2010,** *22,* 3185–3188. doi:10.1002/adma.200904317
91. Kogo, A.; Sakai, N.; Tatsuma, T. *Nanoscale* **2012,** *4,* 4217–4221. doi:10.1039/c2nr30480e
92. Chen, Y.-S.; Choi, H.; Kamat, P. V. *J. Am. Chem. Soc.* **2013,** *135,* 8822–8825. doi:10.1021/ja403807f
93. Yao, Y.; Li, G.; Ciston, S.; Lueptow, R. M.; Gray, K. A. *Environ. Sci. Technol.* **2008,** *42,* 4952–4957. doi:10.1021/es800191n
94. Ou, Y.; Lin, J.; Fang, S.; Liao, D. *Chem. Phys. Lett.* **2006,** *429,* 199–203. doi:10.1016/j.cplett.2006.08.024
95. Wang, W.; Serp, P.; Kalck, P.; Faria, J. L. *J. Mol. Catal. A: Chem.* **2005,** *235,* 194–199. doi:10.1016/j.molcata.2005.02.027
96. Woan, K.; Pyrgiotakis, G.; Sigmund, W. *Adv. Mater.* **2009,** *21,* 2233–2239. doi:10.1002/adma.200802738
97. Novoselov, K. S.; Geim, A. K.; Morozov, S. V.; Jiang, D.; Zhang, Y.; Dubonos, S. V.; Grigorieva, I. V.; Firsov, A. A. *Science* **2004,** *306,* 666–669. doi:10.1126/science.1102896
98. Geim, A. K.; Novoselov, K. S. *Nat. Mater.* **2007,** *6,* 183–191. doi:10.1038/nmat1849
99. Du, A.; Ng, Y. H.; Bell, N. J.; Zhu, Z.; Amal, R.; Smith, S. C. *J. Phys. Chem. Lett.* **2011,** *2,* 894–899. doi:10.1021/jz2002698
100. Du, A.; Sanvito, S.; Li, Z.; Wang, D.; Jiao, Y.; Liao, T.; Sun, Q.; Ng, Y.; Zhu, Z.; Amal, R.; Smith, S. C. *J. Am. Chem. Soc.* **2012,** *134,* 4393–4397. doi:10.1021/ja211637p
101. Song, P.; Zhang, X.; Sun, M.; Cui, X.; Lin, Y. *Nanoscale* **2012,** *4,* 1800–1804. doi:10.1039/c2nr11938b
102. Zhang, Y.; Zhang, N.; Tang, Z.-R.; Xu, Y.-J. *ACS Nano* **2012,** *6,* 9777–9789. doi:10.1021/nn304154s
103. Bai, X.; Wang, L.; Zhu, Y. *ACS Catal.* **2012,** *2,* 2769–2778. doi:10.1021/cs3005852
104. Lin, Y.-G.; Lin, C.-K.; Miller, J. T.; Hsu, Y.-K.; Chen, Y.-C.; Chen, L.-C.; Chen, K.-H. *RSC Adv.* **2012,** *2,* 11258–11262. doi:10.1039/c2ra21988c
105. Zeng, P.; Zhang, Q.; Zhang, X.; Peng, T. *J. Alloys Compd.* **2012,** *516,* 85–90. doi:10.1016/j.jallcom.2011.11.140
106. Xie, G.; Zhang, K.; Guo, B.; Liu, Q.; Fang, L.; Gong, J. R. *Adv. Mater.* **2013,** *25,* 3820–3839. doi:10.1002/adma.201301207
107. Baker, S. N.; Baker, G. A. *Angew. Chem., Int. Ed.* **2010,** *49,* 6726–6744. doi:10.1002/anie.200906623
108. Shen, J.; Zhu, Y.; Yang, X.; Li, C. *Chem. Commun.* **2012,** *48,* 3686–3699. doi:10.1039/c2cc00110a
109. Li, H.; Kang, Z.; Liu, Y.; Lee, S.-T. *J. Mater. Chem.* **2012,** *22,* 24230–24253. doi:10.1039/c2jm34690g
110. Zhang, Z.; Zhang, J.; Chen, N.; Qu, L. *Energy Environ. Sci.* **2012,** *5,* 8869–8890. doi:10.1039/c2ee22982j
111. Xu, X.; Ray, R.; Gu, Y.; Ploehn, H. J.; Gearheart, L.; Raker, K.; Scrivens, W. A. *J. Am. Chem. Soc.* **2004,** *126,* 12736–12737. doi:10.1021/ja040082h
112. Li, H.; He, X.; Kang, Z.; Huang, H.; Liu, Y.; Liu, J.; Lian, S.; Tsang, C. H. A.; Yang, X.; Lee, S. T. *Angew. Chem., Int. Ed.* **2010,** *49,* 4430–4434. doi:10.1002/anie.200906154
113. Zhao, Q.-L.; Zhang, Z.-L.; Huang, B.-H.; Peng, J.; Zhang, M.; Pang, D.-W. *Chem. Commun.* **2008,** 5116–5118. doi:10.1039/b812420e
114. Ming, H.; Ma, Z.; Liu, Y.; Pan, K.; Yu, H.; Wang, F.; Kang, Z. *Dalton Trans.* **2012,** *41,* 9526–9531. doi:10.1039/c2dt30985h
115. Zhu, H.; Wang, X.; Li, Y.; Wang, Z.; Fan, Y.; Yang, X. *Chem. Commun.* **2009,** 5118–5120. doi:10.1039/b907612c
116. Li, L.-L.; Ji, J.; Fei, R.; Wang, C.-Z.; Lu, Q.; Zhang, J.-R.; Jiang, L.-P.; Zhu, J.-J. *Adv. Funct. Mater.* **2012,** *22,* 2971–2979. doi:10.1002/adfm.201200166
117. Li, H.; He, X.; Liu, Y.; Huang, H.; Lian, S.; Lee, S.-T.; Kang, Z. *Carbon* **2011,** *49,* 605–609. doi:10.1016/j.carbon.2010.10.004
118. Pan, D.; Zhang, J.; Li, Z.; Wu, M. *Adv. Mater.* **2010,** *22,* 734–738. doi:10.1002/adma.200902825
119. Hea, X.; Li, H.; Liu, Y.; Huang, H.; Kang, Z.; Lee, S.-T. *Colloids Surf., B* **2011,** *87,* 326–332. doi:10.1016/j.colsurfb.2011.05.036
120. Wang, F.; Kreiter, M.; He, B.; Pang, S.; Liu, C.-y. *Chem. Commun.* **2010,** *46,* 3309–3311. doi:10.1039/c002206c
121. Wang, F.; Pang, S.; Wang, L.; Li, Q.; Kreiter, M.; Liu, C.-Y. *Chem. Mater.* **2010,** *22,* 4528–4530. doi:10.1021/cm101350u
122. Qiao, Z.-A.; Wang, Y.; Gao, Y.; Li, H.; Dai, T.; Liu, Y.; Huo, Q. *Chem. Commun.* **2010,** *46,* 8812–8814. doi:10.1039/c0cc02724c
123. Shen, J.; Zhu, Y.; Chen, C.; Yang, X.; Li, C. *Chem. Commun.* **2011,** *47,* 2580–2582. doi:10.1039/c0cc04812g
124. Fang, Y.; Guo, S.; Li, D.; Zhu, C.; Ren, W.; Dong, S.; Wang, E. *ACS Nano* **2012,** *6,* 400–409. doi:10.1021/nn2046373
125. Liu, H.; Ye, T.; Mao, C. *Angew. Chem., Int. Ed.* **2007,** *46,* 6473–6475. doi:10.1002/anie.200701271
126. Hu, S.-L.; Niu, K.-Y.; Sun, J.; Yang, J.; Zhao, N.-Q.; Du, X.-W. *J. Mater. Chem.* **2009,** *19,* 484–488. doi:10.1039/b812943f
127. Ray, S. C.; Saha, A.; Jana, N. R.; Sarkar, R. *J. Phys. Chem. C* **2009,** *113,* 18546–18551. doi:10.1021/jp905912n
128. Yu, H.; Zhang, H.; Li, H.; Huang, H.; Liu, Y.; Ming, H.; Kang, Z. *New J. Chem.* **2012,** *36,* 1031–1035. doi:10.1039/c2nj20959d
129. Lian, S.; Huang, H.; Zhang, J.; Kang, Z.; Liu, Y. *Solid State Commun.* **2013,** *155,* 53–56. doi:10.1016/j.ssc.2012.11.003
130. Zhang, X.; Wang, F.; Huang, H.; Li, H.; Han, X.; Liu, Y.; Kang, Z. *Nanoscale* **2013,** *5,* 2274–2278. doi:10.1039/c3nr34142a

131. Wang, F.; Liu, Y.; Ma, Z.; Li, H.; Kang, Z.; Shen, M. *New J. Chem.* **2013,** *37,* 290–294. doi:10.1039/c2nj40988g
132. Guo, C. X.; Dong, Y.; Yang, H. B.; Li, C. M. *Adv. Energy Mater.* **2013,** *3,* 997–1003. doi:10.1002/aenm.201300171
133. Tang, D.; Zhang, H.; Huang, H.; Liu, R.; Han, Y.; Liu, Y.; Tong, C.; Kang, Z. *Dalton Trans.* **2013,** *42,* 6285–6289. doi:10.1039/c3dt50567g
134. Li, H.; Liu, R.; Liu, Y.; Huang, H.; Yu, H.; Ming, H.; Lian, S.; Lee, S.-T.; Kang, Z. *J. Mater. Chem.* **2012,** *22,* 17470–17475. doi:10.1039/c2jm32827e
135. Zhang, H.; Huang, H.; Ming, H.; Li, H.; Zhang, L.; Liu, Y.; Kang, Z. *J. Mater. Chem.* **2012,** *22,* 10501–10506. doi:10.1039/c2jm30703k
136. Zhang, H.; Ming, H.; Lian, S.; Huang, H.; Li, H.; Zhang, L.; Liu, Y.; Kang, Z.; Lee, S.-T. *Dalton Trans.* **2011,** *40,* 10822–10825. doi:10.1039/c1dt11147g
137. Yang, H. G.; Sun, C. H.; Qiao, S. Z.; Zou, J.; Liu, G.; Smith, S. C.; Cheng, H. M.; Lu, G. Q. *Nature* **2008,** *453,* 638–641. doi:10.1038/nature06964
138. Yang, H. G.; Liu, G.; Qiao, S. Z.; Sun, C. H.; Jin, Y. G.; Smith, S. C.; Zou, J.; Cheng, H. M.; Lu, G. Q. (M.). *J. Am. Chem. Soc.* **2009,** *131,* 4078–4083. doi:10.1021/ja808790p
139. Wu, X.; Chen, Z.; Lu, G. Q. (M.); Wang, L. *Adv. Funct. Mater.* **2011,** *21,* 4167–4172. doi:10.1002/adfm.201100828
140. Liu, G.; Wang, L.; Sun, C.; Yan, X.; Wang, X.; Chen, Z.; Smith, S. C.; Cheng, H.-M.; Lu, G. Q. *Chem. Mater.* **2009,** *21,* 1266–1274. doi:10.1021/cm802986r
141. Liu, G.; Sun, C.; Wang, L.; Smith, S. C.; Lu, G. Q. (M.); Cheng, H.-M. *J. Mater. Chem.* **2011,** *21,* 14672–14679. doi:10.1039/c1jm11295c
142. Zong, X.; Sun, C.; Chen, Z.; Mukherji, A.; Wu, H.; Zou, J.; Smith, S. C.; Lu, G. Q.; Wang, L. *Chem. Commun.* **2011,** *47,* 6293–6295. doi:10.1039/c0cc05440b
143. Mukherji, A.; Marschall, R.; Tanksale, A.; Sun, C.; Smith, S. C.; Lu, G. Q.; Wang, L. *Adv. Funct. Mater.* **2011,** *21,* 126–132. doi:10.1002/adfm.201000591
144. Marschall, R.; Mukherji, A.; Tanksale, A.; Sun, C.; Smith, S. C.; Wang, L.; Lu, G. Q. (M.). *J. Mater. Chem.* **2011,** *21,* 8871–8879. doi:10.1039/c0jm02549f
145. Matsumoto, Y.; Ida, S.; Inoue, T. *J. Phys. Chem. C* **2008,** *112,* 11614–11616. doi:10.1021/jp804625r
146. Liu, G.; Wang, L.; Sun, C.; Chen, Z.; Yan, X.; Cheng, L.; Cheng, H.-M.; Lu, G. Q. (M.). *Chem. Commun.* **2009,** 1383–1385. doi:10.1039/b820483g
147. Zhang, X.; Huang, H.; Liu, J.; Liu, Y.; Kang, Z. *J. Mater. Chem. A* **2013,** *1,* 11529–11533. doi:10.1039/c3ta12568h
148. Mak, K. F.; Lee, C.; Hone, J.; Shan, J.; Heinz, T. F. *Phys. Rev. Lett.* **2010,** *105,* 136805. doi:10.1103/PhysRevLett.105.136805
149. Splendiani, A.; Sun, L.; Zhang, Y.; Li, T.; Kim, J.; Chim, C.-Y.; Galli, G.; Wang, F. *Nano Lett.* **2010,** *10,* 1271–1275. doi:10.1021/nl903868w
150. Eda, G.; Yamaguchi, H.; Voiry, D.; Fujita, T.; Chen, M.; Chhowalla, M. *Nano Lett.* **2011,** *11,* 5111–5116. doi:10.1021/nl201874w

License and Terms

This is an Open Access article under the terms of the Creative Commons Attribution License (http://creativecommons.org/licenses/by/2.0), which permits unrestricted use, distribution, and reproduction in any medium, provided the original work is properly cited.

The license is subject to the *Beilstein Journal of Nanotechnology* terms and conditions: (http://www.beilstein-journals.org/bjnano)

The definitive version of this article is the electronic one which can be found at: doi:10.3762/bjnano.5.82

Beilstein Journal of Nanotechnology

Visible light photooxidative performance of a high-nuclearity molecular bismuth vanadium oxide cluster

Johannes Tucher and Carsten Streb*§

Full Research Paper

Open Access

Address:
Ulm University, Institute of Inorganic Chemistry I, Albert-Einstein-Allee 11, 89081 Ulm, Germany

Email:
Carsten Streb* - carsten.streb@uni-ulm.de

* Corresponding author
§ web: http://www.strebgroup.net

Keywords:
photocatalysis; photooxidation; polyoxometalate; self-assembly; vanadium oxide

Beilstein J. Nanotechnol. **2014,** *5,* 711–716.
doi:10.3762/bjnano.5.83

Received: 18 December 2013
Accepted: 01 May 2014
Published: 26 May 2014

This article is part of the Thematic Series "Photocatalysis".

Guest Editor: R. Xu

© 2014 Tucher and Streb; licensee Beilstein-Institut.
License and terms: see end of document.

Abstract

The visible light photooxidative performance of a new high-nuclearity molecular bismuth vanadium oxide cluster, $H_3[\{Bi(dmso)_3\}_4V_{13}O_{40}]$, is reported. Photocatalytic activity studies show faster reaction kinetics under anaerobic conditions, suggesting an oxygen-dependent quenching of the photoexcited cluster species. Further mechanistic analysis shows that the reaction proceeds via the intermediate formation of hydroxyl radicals which act as oxidant. Trapping experiments using ethanol as a hydroxyl radical scavenger show significantly decreased photocatalytic substrate oxidation in the presence of EtOH. Photocatalytic performance analyses using monochromatic visible light irradiation show that the quantum efficiency Φ for indigo photooxidation is strongly dependent on the irradiation wavelength, with higher quantum efficiencies being observed at shorter wavelengths (Φ_{395nm} ca. 15%). Recycling tests show that the compound can be employed as homogeneous photooxidation catalyst multiple times without loss of catalytic activity. High turnover numbers (TON ca. 1200) and turnover frequencies up to TOF ca. 3.44 min^{-1} are observed, illustrating the practical applicability of the cluster species.

Introduction

The bottom-up self-assembly of molecular photocatalysts is a well-established method which gives access to materials for which light absorption, catalytic activity and selectivity can be tuned by structural and chemical modifications [1-6]. Prime examples for this approach are molecular metal oxides, so-called polyoxometalates (POMs) [7,8]. POMs are anionic metal oxide clusters formed primarily from early transition metals, mainly vanadium, molybdenum and tungsten [8]. The cluster assembly proceeds in solution by oligo-condensation reactions between reactive fragments, often by using templates to control the final cluster architecture [9,10]. POMs have attracted wide interest from researchers working in chemistry, biology, catalysis, molecular electronics and materials science [8,11-13]. In particular, POMs have been employed as photoox-

idation catalysts for the oxidation of a wide range of organic substrates such as alcohols, olefins and others [1-3,14]. However, as POMs often only absorb light in the UV range, little is known about the visible-light photocatalytic activity of POMs [5,15]. One means of addressing this challenge is to tune the cluster structure and reactivity by incorporation of a reactive metal site into the cluster shell [15-19]. Using this approach, materials for energy conversion and storage [20,21], homogeneous and heterogeneous catalysis [1,14], biomedical applications [22-24] and nanostructured functional materials [17,25,26] have been developed.

We have recently started systematic studies into the tuning of (photo-)chemical properties of polyoxometalates by selective cluster functionalization with a range of s-block [27,28], p-block [29], d-block [30,31] and f-block [32] metals. Using this approach, we were able to demonstrate that molybdate clusters can be functionalized with single vanadium centres so as to increase their visible-light photoactivity for selective oxidations of alcohols to aldehydes [5,6,31]. Further, we have recently shown that chiral, visible-light driven photooxidation catalysts are accessible in cerium-functionalized vanadate clusters [32]. In previous work with direct relevance to this report, we showed that POM chemistry can be inspired by solid-state photocatalysts when the first molecular analogue of bismuth vanadate ($BiVO_4$) photocatalysts was obtained [33-36]. Bismuth vanadate is one of the best-known solid-state visible light photocatalysts and is employed in photochemical and photoelectrochemical visible-light-driven water splitting systems [37-41].

At the start of our studies, no molecular bismuth vanadium oxides were known in the literature. We thus developed a synthetic approach to bismuth vanadate clusters based on a recently-established fragmentation-and-reaggregation strategy, see Supporting Information File 1. The route gives general access to metal-functionalized, anion-templated vanadium oxide clusters [5,27-32,42]. Here, this approach was successfully employed and gave the cluster species $H_3[\{Bi(dmso)_3\}_4V_{13}O_{40}]$ × ca. 4 DMSO (= **1** × ca. 4 DMSO). **1** is formed spontaneously by reaction of $Bi(NO_3)_3{\cdot}5H_2O$ and $(n\text{-}Bu_4N)_3[H_3V_{10}O_{28}]$ in dimethyl sulfoxide (DMSO) and it was shown that the cluster features both acidic and visible-light photocatalytic activity [29]. To date, to the best of our knowledge, **1** is the only reported example of a molecular bismuth vanadium oxide cluster. Briefly, single-crystal X-ray diffraction showed that the cluster is based on a central *ortho*-vanadate template (VO_4^{3-}). Around this template, four so-called $\{V_3\}$ triads ($\{V_3O_{13}\}$) are assembled so that each oxygen atom of the VO_4^{3-} template is linked centrally to one triad. This leads to the formation of a $[(VO_4)V_{12}O_{36}]^{15-}$ anion which is the first example of a purely vanadate-based ε-Keggin anion [29,43-45]: As the vanadate anion has a high, destabilizing negative charge (15−), it has previously only been proposed as a transient species with short lifetime using ^{51}V NMR spectroscopy [46]. In the present case, the anion is electrostatically stabilized by four bismuth(III) ions which coordinate to binding pockets formed on the cluster surface, see Scheme 1.

Initial photocatalytic studies using the photooxidation of the dye patent blue V as a test reaction showed high activity (quantum efficiency $\Phi > 7\%$, TOF ca. 5 min^{-1}) and high stability under turnover conditions (TON > 1200) under irradiation with monochromatic visible light (LED light source, $\lambda = 470$ nm) [29].

In the present study, we are focusing on the photooxidative performance of the cluster at various wavelengths in the visible region to evaluate cluster application for sunlight-driven oxidation reactions. Further, initial mechanistic catalysis studies are discussed where reactive intermediates and effects of oxygen in the reaction mixture are illustrated.

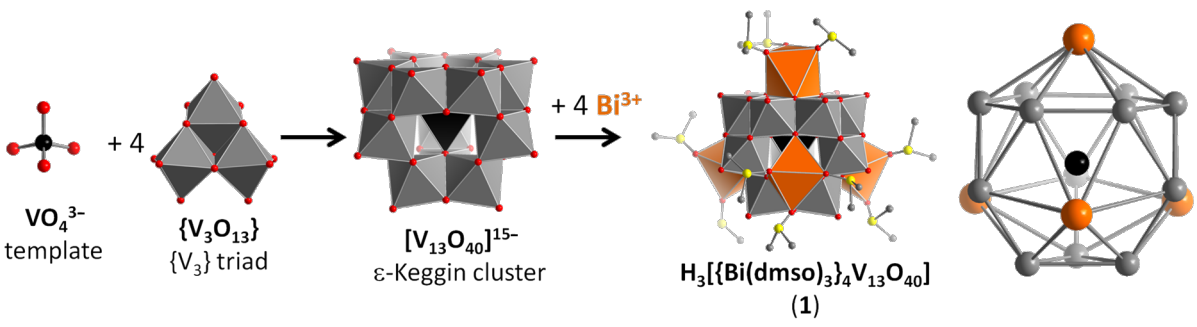

Scheme 1: Self-assembly of the $H_3[\{Bi(dmso)_3\}_4V_{13}O_{40}]$ cluster **1**. An *ortho*-vanadate (VO_4^{3-}) template allows the assembly of four $\{V_3\}$ triads into an ε-Keggin anion ($[V_{13}O_{40}]^{15-}$). Electrostatic stabilization of the ε-Keggin anion by four Bi(III) centres gives the final, stable cluster $H_3[\{Bi(dmso)_3\}_4V_{13}O_{40}]$ (**1**). The metal-only framework of **1** is illustrated on the right. Colour scheme: V (template): black, V (cluster): grey, O: red; Bi: orange, S: yellow; C: dark grey.

Results and Discussion

Photochemical characterization of the bismuth vanadate cluster 1

UV–vis spectroscopy of **1** shows that the cluster features a prominent ligand to metal charge-transfer (LMCT) absorption band centred at λ = 335 nm with tailing of the absorption band up to λ ≈ 560 nm, making the cluster attractive for visible light absorption. When compared with a prototype pure vanadium oxide cluster such as $[H_3V_{10}O_{28}]^{3-}$, the increase in extinction coefficient and the higher visible light absorption are obvious, see Figure 1.

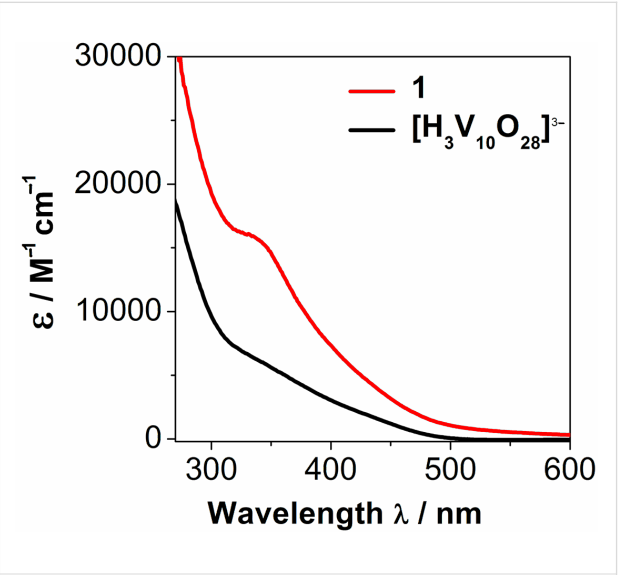

Figure 1: UV–vis spectroscopic data for the bismuth vanadium oxide cluster $H_3[\{Bi(dmso)_3\}_4V_{13}O_{40}]$ (**1**, red line). The compound features a near-visible LMCT absorption band with ε_{335} = 15940 M^{-1} cm^{-1}. In contrast, the pure vanadium oxide cluster $[H_3V_{10}O_{28}]^{3-}$ features significantly reduced visible-light absorption (black line).

Photooxidative decomposition of the model pollutant dye indigo

Compound **1** was tested as a homogeneous, visible-light driven photooxidation catalyst for the oxidative degradation of the model pollutant dye indigo (hereafter: Ind). To this end, aliquots of cluster **1** and the dye were mixed in *N*,*N*-dimethylformamide (DMF) solution (typical molar ratio [Ind]:[1] = 5:1). The solutions were subsequently irradiated with monochromatic visible light with wavelengths between 395 nm and 505 nm in order to study the photooxidative performance of the cluster.

Standard photooxidative analyses were performed with an irradiation wavelength of λ = 430 nm in DMF. In these screening reactions it was found that **1** performs as an effective visible-light driven photooxidant for the degradation of indigo, see Figure 2.

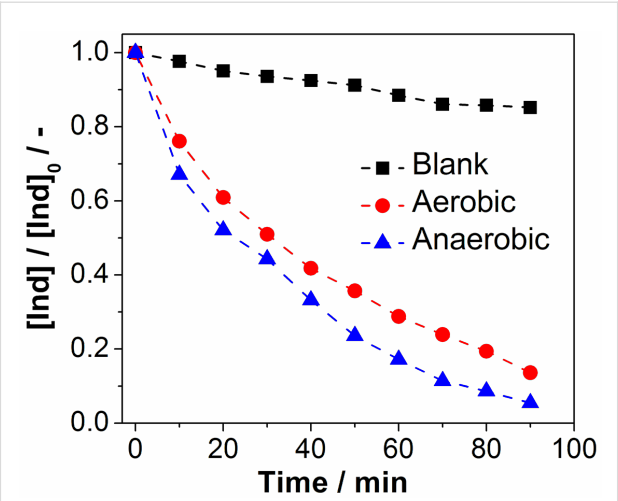

Figure 2: Photooxidative performance of **1** under anaerobic (blue triangles) and aerobic (red circles) conditions in the homogeneous photooxidation of indigo (Ind). Solvent: DMF, light source: monochromatic LED (λ = 430 nm, $P_{nominal}$ = 3 W), [1] = 1.0 μM, $[Ind]_0$ = 5.0 μM).

Photooxidative activity of 1

In detail, it was found that dye degradation under visible light irradiation (here: λ = 430 nm) is significantly enhanced by the presence of photocatalyst **1**. After $t_{irradiation}$ = 80 min and under anaerobic conditions, virtually full dye degradation in the presence of **1** is observed ($[Ind]/[Ind]_0$ < 3%), see Figure 2. In the absence of any photocatalyst, the dye concentration after an identical irradiation time is $[Ind]/[Ind]_0$ ca. 85%, illustrating the visible-light photooxidative activity of **1**. Initial spectroscopic and gas chromatographic analyses suggest that dye degradation is only partial and no full mineralization leading to the formation of CO or CO_2 was observed.

Aerobic vs anaerobic photocatalytic activity of 1

When comparing the photooxidative performance of **1** in the presence and absence of oxygen, it was found that under anaerobic conditions (solvent degassed with argon for 10 min prior to the experiment), enhanced reaction rates are observed. To quantify the different observed kinetics, observed pseudo-first order rate constants k_{obs} were determined for the photooxidation. Comparison of the rate constants clearly demonstrates that anaerobic conditions lead to an approximately 20% increase in reaction rate, suggesting that molecular oxygen interferes with the photooxidation and acts as a quencher for the photoexcited cluster **1** [31,47], see Table 1. Our current hypothesis is that $^3O_2$ acts as a triplet radical quencher that interacts with the reactive triplet state of the photoexcited cluster molecule by energy and/or electron transfer, resulting in an overall reduced photoreactivity of **1** under aerobic conditions [48]. This hypothesis is currently being investigated using TD-DFT and transient absorption spectroscopy methods.

Identification of hydroxyl radicals as intermediates

To gain further insight into the reaction mechanism involved in the photooxidation of indigo by **1**, homogeneous dye degradation was performed in the presence of ethanol in the reaction mixture ([EtOH]:[1] = 50:1). Ethanol is a well-known hydroxyl radical scavenger [49], and the test was performed to demonstrate that hydroxyl radicals are involved as intermediate oxidizing species formed upon irradiation of **1** (see Supporting Information File 1 for proposed mechanism) [5]. If a hydroxyl radical mechanism was present, a significant drop in indigo photooxidation activity would be expected in the presence of EtOH. This behaviour was indeed observed: both under aerobic and anaerobic conditions, significant decrease of reactivity was observed. Quantitative analysis using the observed pseudo-first order rate constant k_{obs} gave a decrease in rate constant of ca. 32% (anaerobic) and ca. 44% (aerobic), respectively, see Table 1 and Figure 3. These significant changes are most likely due to an effective scavenging of hydroxyl radical intermediates by ethanol.

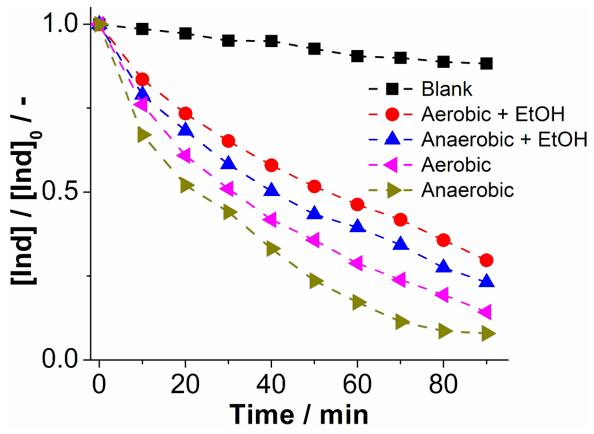

Figure 3: Photooxidative performance of **1** depending on the presence of EtOH under aerobic and anaerobic conditions for the homogeneous photooxidation of indigo (Ind). Solvent: DMF (aerobic/anaerobic), light source: monochromatic LED (λ = 430 nm, $P_{nominal}$ = 3 W), [EtOH]:[1] = 50:1.

Wavelength-dependent quantum efficiency of 1

In order to gain insight into the wavelength-dependent photoactivity of **1** and to identify the most promising wavelength regions in the visible range, wavelength-dependent quantum efficiency studies for the indigo photooxidation by **1** were performed [50]. As shown in Figure 4, at short wavelengths (λ < 400 nm, quantum efficiencies Φ ca. 15% are observed; in the region between λ = 400–450 nm, quantum efficiencies drop to Φ ca. 12–6%. At wavelengths λ > 450 nm, low quantum efficiencies Φ < 3% are observed, see Figure 4. The data suggest that in the 400–450 nm region, compound **1** might be employed as a homogeneous polyoxometalate photocatalyst with promising efficiencies for this compound class [5].

Table 1: Kinetic parameters for the photooxidation of indigo by compound **1** under aerobic/anaerobic conditions in the presence and absence of EtOH as hydroxyl radical scavenger.

Reaction[a]	k_{obs}/h^{-1}	Standard deviation σ/h^{-1}
aerobic	1.41	0.13
anaerobic	1.68	0.20
aerobic + EtOH	0.79	0.15
anaerobic + EtOH	1.14	0.16
blank reference	0.30	0.12

[a]Conditions: Homogeneous reaction, solvent: DMF, irradiation with monochromatic LED light source, λ = 430 nm; [Ind]$_0$ = 5.0 μM, [1] = 1.0 μM, [EtOH] = 50 μM.

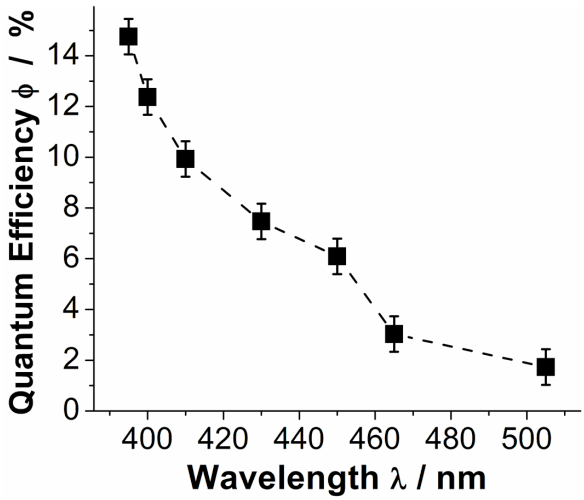

Figure 4: Quantum effiencies Φ for the homogeneous photooxidation of indigo by **1** in the visible range between λ = 395–505 nm. Solvent: DMF (aerobic), molar ratio [Ind]$_0$:[1] = 1:1. light source: monochromatic high-power LED, quantum efficiencies were determined using a custom-built setup [49].

Recyclability of 1

To demonstrate the long-term stability and recyclability of **1**, three consecutive photooxidative indigo decomposition runs were performed using the same catalyst sample. In the test, a DMF solution containing indigo and **1** ([Ind]$_0$:[1] = 5:1) was irradiated under standard conditions (λ = 430 nm) until complete dye decomposition was observed UV–vis spectroscopically (run 1). Using the same sample, the initial indigo concentration was restored by addition of a concentrated indigo stock solution and the photooxidation was repeated to complete indigo degradation (run 2). In run 3, the initial indigo concentration was tripled to demonstrate the photooxidative capacity of the cluster and full dye degradation was observed upon irradi-

ation, see Figure 5. The experimental series demonstrates that the cluster can be employed multiple times and catalyst recycling under photooxidative conditions is indeed possible.

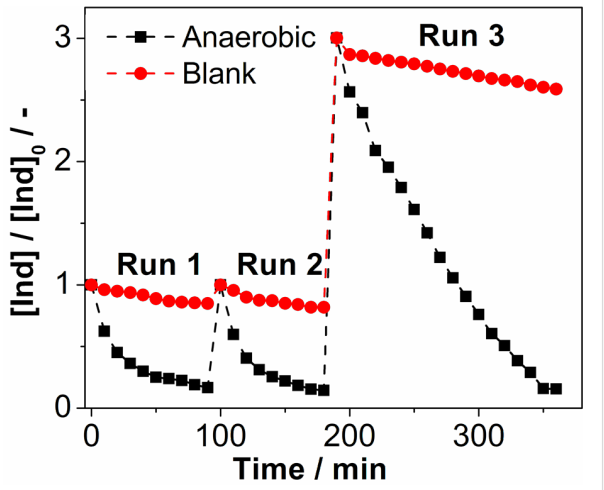

Figure 5: Recyclability of **1** as a homogeneous indigo photooxidation catalyst under anaerobic conditions. Run 1 and run 2 were performed at $[Ind]_0$:[1] = 5:1, in run 3, the $[Ind]_0$:[1] ratio was increased to 15:1. Solvent: DMF (anaerobic), light source: monochromatic LED (λ = 430 nm, $P_{nominal}$ = 3 W).

Stability of **1** under irradiation

To understand the long-term stability of **1**, long-irradiation runs with high substrate molar ratios up to [Ind]:[1] ca. 1200 were performed. These experiments showed that the cluster compound is capable of photooxidatively decomposing large amounts of the dye, thereby illustrating the chemical robustness of the bismuth vanadium oxide framework. Comparative studies under aerobic and anaerobic conditions showed that the cluster can reach similar turnover numbers (TONs) of ca. 1200, however, higher turnover frequencies for anaerobic conditions ($TOF_{anaerobic} \approx 3.44\ min^{-1}$) were found compared with aerobic conditions ($TOF_{aerobic} \approx 3.01\ min^{-1}$). The findings confirm that under long-term irradiation, the original observation of higher catalytic activity for **1** under anaerobic conditions still holds (see Supporting Information File 1).

Conclusion

In summary we report the visible-light photocatalytic activity of the first molecular bismuth vanadium oxide cluster, by using the homogeneous photooxidative degradation of the model pollutant indigo as a test reaction. Wavelength-dependent photocatalytic activity is reported and high quantum efficiencies of ca. 15% are observed at the UV–vis border. Practical quantum efficiencies >5% are found up to wavelengths of λ = 450 nm. Recycling studies show that the cluster can be used multiple times without significant loss of activity. Further, initial mechanistic studies show increased cluster reactivity in the absence of oxygen which might act as a quencher for the photoexcited cluster. In addition, we provide initial experimental evidence that the photooxidative mechanism proceeds via the intermediate formation of hydroxyl radicals. Cluster stability with high turnover numbers (ca. 1200) has been demonstrated. Future work will focus on the applications of the cluster for the selective photooxidation of organic substrates (alcohols, olefins). Primary focus will be product selectivity, quantum efficiency as well as long-term catalytic performance.

Experimental

For experimental, analytical and photocatalytic details, see Supporting Information File 1.

Supporting Information

Supporting Information File 1

Detailed synthetic, analytic and photocatalytic data.
[http://www.beilstein-journals.org/bjnano/content/supplementary/2190-4286-5-83-S1.pdf]

Acknowledgements

Financial support by Ulm University, and the DFG Graduate School GRK1626 (University of Regensburg) is gratefully acknowledged. C.S. thanks the Fonds der Chemischen Industrie (FCI) for a Liebig-Fellowship.

References

1. Hill, C. L. Polyoxymetalates: Reactivity. In *Comprehensive Coordination Chemistry II;* McCleverty, J. A.; Meyer, T. J., Eds.; Elsevier Ltd., 2003; Vol. 4, pp 679–759. doi:10.1016/B0-08-043748-6/03036-X
2. Hill, C. L.; Prosser-McCartha, C. M. Photocatalytic and photoredox properties of polyoxometalate systems. In *Photosensitization and Photocatalysis using inorganic and organometallic compounds;* Graetzel, M.; Kalyanasundaram, K., Eds.; Kluwer Academic Publishers: Dordrecht, 1993; pp 307–326. doi:10.1007/978-94-017-2626-9_10
3. Papaconstantinou, E. *Chem. Soc. Rev.* **1989,** *18,* 1–31. doi:10.1039/cs9891800001
4. Whitesides, G. M.; Mathias, J. P.; Seto, C. T. *Science* **1991,** *254,* 1312–1319. doi:10.1126/science.1962191
5. Streb, C. *Dalton Trans.* **2012,** *41,* 1651–1659. doi:10.1039/c1dt11220a
6. Streb, C.; Kastner, K.; Tucher, J. Polyoxometalates in Photocatalysis. In *Chemical Photocatalysis;* König, B., Ed.; De Gruyter: Berlin, 2013; pp 247–258.
7. Long, D.-L.; Burkholder, E.; Cronin, L. *Chem. Soc. Rev.* **2007,** *36,* 105–121. doi:10.1039/b502666k
8. Pope, M. T. *Heteropoly and isopoly oxometalates;* Springer-Verlag: Heidelberg, 1983.
9. Pope, M. T.; Müller, A. *Angew. Chem., Int. Ed. Engl.* **1991,** *30,* 34–48. doi:10.1002/anie.199100341

10. Pope, M. T. *Nature* **1992,** *355,* 27. doi:10.1038/355027a0
11. Kortz, U.; Liu, T., guest Eds. Polyoxometalates (Cluster Issue). *Eur. J. Inorg. Chem.* **2013,** 1556–1967.
12. Cronin, L.; Müller, A., guest Eds. *Chem. Soc. Rev.* **2012,** *41,* 7333–7634. doi:10.1039/c2cs90087d
13. Hill, C. L., guest Ed. *Chem. Rev.* **1998,** *98,* 1–2. doi:10.1021/cr960395y
14. Hill, C. L., guest Ed. *J. Mol. Catal. A* **2007,** *262,* 2–6. doi:10.1016/j.molcata.2006.08.042
15. Argitis, P.; Papaconstantinou, E. *Inorg. Chem.* **1986,** *25,* 4386–4389. doi:10.1021/ic00244a021
16. Geletii, Y. V.; Botar, B.; Kögerler, P.; Hillesheim, D. A.; Musaev, D. G.; Hill, C. L. *Angew. Chem., Int. Ed.* **2008,** *47,* 3896–3899. doi:10.1002/anie.200705652
17. Long, D.-L.; Tsunashima, R.; Cronin, L. *Angew. Chem., Int. Ed.* **2010,** *49,* 1736–1758. doi:10.1002/anie.200902483
18. Muradov, N.; T-Raissi, A. *J. Sol. Energy Eng.* **2006,** *128,* 326–330. doi:10.1115/1.2212442
19. Gao, G.; Li, F.; Xu, L.; Liu, X.; Yang, Y. *J. Am. Chem. Soc.* **2008,** *130,* 10838–10839. doi:10.1021/ja801560t
20. Lv, H.; Geletii, Y. V.; Zhao, C.; Vickers, J. W.; Zhu, G.; Luo, Z.; Song, J.; Lian, T.; Musaev, D. G.; Hill, C. L. *Chem. Soc. Rev.* **2012,** *41,* 7572–7589. doi:10.1039/c2cs35292c
21. Sartorel, A.; Bonchio, M.; Campagna, S.; Scandola, F. *Chem. Soc. Rev.* **2013,** *42,* 2262–2280. doi:10.1039/c2cs35287g
22. Hasenknopf, B. *Front. Biosci., Landmark Ed.* **2005,** *10,* 275–287.
23. Aureliano, M.; Fraqueza, G.; Ohlin, C. A. *Dalton Trans.* **2013,** *42,* 11770–11777. doi:10.1039/c3dt50462j
24. Judd, D. A.; Nettles, J. H.; Nevins, N.; Snyder, J. P.; Liotta, D. C.; Tang, J.; Ermolieff, J.; Schinazi, R. F.; Hill, C. L. *J. Am. Chem. Soc.* **2001,** *123,* 886–897. doi:10.1021/ja001809e
25. Kurth, D. G. *Sci. Technol. Adv. Mater.* **2008,** *9,* No. 014103.
26. Streb, C.; Tsunashima, R.; MacLaren, D. A.; McGlone, T.; Akutagawa, T.; Nakamura, T.; Scandurra, A.; Pignataro, B.; Gadegaard, N.; Cronin, L. *Angew. Chem., Int. Ed.* **2009,** *48,* 6490–6493. doi:10.1002/anie.200901650
27. Kastner, K.; Puscher, B.; Streb, C. *Chem. Commun.* **2013,** *49,* 140–142. doi:10.1039/c2cc36638j
28. Kastner, K.; Streb, C. *CrystEngComm* **2013,** *15,* 4948–4955. doi:10.1039/c3ce40536b
29. Tucher, J.; Nye, L. C.; Ivanovic-Burmazovic, I.; Notarnicola, A.; Streb, C. *Chem.–Eur. J.* **2012,** *18,* 10949–10953. doi:10.1002/chem.201200404
30. Forster, J.; Rösner, B.; Fink, R. H.; Nye, L. C.; Ivanovic-Burmazovic, I.; Kastner, K.; Tucher, J.; Streb, C. *Chem. Sci.* **2013,** *4,* 418–424. doi:10.1039/c2sc20942j
31. Tucher, J.; Wu, Y.; Nye, L. C.; Ivanovic-Burmazovic, I.; Khusniyarov, M. M.; Streb, C. *Dalton Trans.* **2012,** *41,* 9938–9943. doi:10.1039/c2dt30304c
32. Seliverstov, A.; Streb, C. *Chem. Commun.* **2014,** *50,* 1827–1829. doi:10.1039/c3cc48834a
33. Li, G.; Zhang, D.; Yu, J. C. *Chem. Mater.* **2008,** *20,* 3983–3992. doi:10.1021/cm800236z
34. Kudo, A.; Omori, K.; Kato, H. *J. Am. Chem. Soc.* **1999,** *121,* 11459–11467. doi:10.1021/ja992541y
35. Jia, Q.; Iwashina, K.; Kudo, A. *Proc. Natl. Acad. Sci. U. S. A.* **2012,** *109,* 11564–11569. doi:10.1073/pnas.1204623109
36. Li, R.; Zhang, F.; Wang, D.; Yang, J.; Li, M.; Zhu, J.; Zhou, X.; Han, H.; Li, C. *Nat. Commun.* **2013,** *4,* No. 1432. doi:10.1038/ncomms2401
37. Saito, R.; Miseki, Y.; Sayama, K. *Chem. Commun.* **2012,** *48,* 3833–3835. doi:10.1039/c2cc30713h
38. Seabold, J. A.; Choi, K.-S. *J. Am. Chem. Soc.* **2012,** *134,* 2186–2192. doi:10.1021/ja209001d
39. Zhong, D. K.; Choi, S.; Gamelin, D. R. *J. Am. Chem. Soc.* **2011,** *133,* 18370–18377. doi:10.1021/ja207348x
40. Kudo, A. *J. Ceram. Soc. Jpn.* **2001,** *109,* S81–S88. doi:10.2109/jcersj.109.1270_S81
41. Abdi, F. F.; Han, L.; Smets, A. H. M.; Zeman, M.; Dam, B.; van de Krol, R. *Nat. Commun.* **2013,** *4,* No. 2195. doi:10.1038/ncomms3195
42. Forster, J.; Rösner, B.; Khusniyarov, M. M.; Streb, C. *Chem. Commun.* **2011,** *47,* 3114–3116. doi:10.1039/c0cc05536k
43. Yamase, T.; Makino, H.; Naruke, H.; San José Wéry, A. M. *Chem. Lett.* **2000,** *29,* 1350–1351. doi:10.1246/cl.2000.1350
44. Dolbecq, A.; Mialane, P.; Lisnard, L.; Marrot, J.; Sécheresse, F. *Chem.–Eur. J.* **2003,** *9,* 2914–2920. doi:10.1002/chem.200204670
45. Dolbecq, A.; Mellot-Draznieks, C.; Mialane, P.; Marrot, R.; Férey, G.; Sécheresse, F. *Eur. J. Inorg. Chem.* **2005,** 3009–3018. doi:10.1002/ejic.200500230
46. Pettersson, L.; Andersson, I.; Howarth, O. W. *Inorg. Chem.* **1992,** *31,* 4032–4033. doi:10.1021/ic00046a003
47. Tanielian, C.; Schweitzer, C.; Seghrouchni, R.; Esch, M.; Mechin, R. *Photochem. Photobiol. Sci.* **2003,** *2,* 297–305. doi:10.1039/b210786b
48. Grewer, C.; Brauer, H.-D. *J. Phys. Chem.* **1994,** *98,* 4230–4235. doi:10.1021/j100067a006
49. Billany, M. R.; Khatib, K.; Gordon, M.; Sugden, J. K. *Int. J. Pharm.* **1996,** *137,* 143–147. doi:10.1016/0378-5173(96)04246-9
50. Megerle, U.; Lechner, R.; König, B.; Riedle, E. *Photochem. Photobiol. Sci.* **2010,** *9,* 1400–1406. doi:10.1039/c0pp00195c

License and Terms

This is an Open Access article under the terms of the Creative Commons Attribution License (http://creativecommons.org/licenses/by/2.0), which permits unrestricted use, distribution, and reproduction in any medium, provided the original work is properly cited.

The license is subject to the *Beilstein Journal of Nanotechnology* terms and conditions: (http://www.beilstein-journals.org/bjnano)

The definitive version of this article is the electronic one which can be found at: doi:10.3762/bjnano.5.83

Beilstein Journal of Nanotechnology

Biomolecule-assisted synthesis of carbon nitride and sulfur-doped carbon nitride heterojunction nanosheets: An efficient heterojunction photocatalyst for photoelectrochemical applications

Hua Bing Tao, Hong Bin Yang*, Jiazang Chen, Jianwei Miao and Bin Liu*

Full Research Paper

Open Access

Address:
School of Chemical and Biomedical Engineering, Nanyang Technological University, 62 Nanyang Drive, Singapore 637459, Singapore

Email:
Hong Bin Yang* - hbyang@ntu.edu.sg; Bin Liu* - liubin@ntu.edu.sg

* Corresponding author

Keywords:
graphitic carbon nitride (g-C_3N_4); heterojunction; photoelectrochemical; photocatalysis; sulfur doping

Beilstein J. Nanotechnol. **2014,** *5,* 770–777.
doi:10.3762/bjnano.5.89

Received: 27 January 2014
Accepted: 09 May 2014
Published: 03 June 2014

This article is part of the Thematic Series "Photocatalysis".

Guest Editor: R. Xu

© 2014 Tao et al; licensee Beilstein-Institut.
License and terms: see end of document.

Abstract

A biomolecule-assisted pyrolysis method has been developed to synthesize sulfur-doped graphitic carbon nitride (CNS) nanosheets. During the synthesis, sulfur could be introduced as a dopant into the lattice of carbon nitride (CN). Sulfur doping changed the texture as well as relative band positions of CN. By growing CN on preformed sulfur-doped CN nanosheets, composite CN/CNS heterojunction nanosheets were constructed, which significantly enhanced the photoelectrochemical performance as compared with various control counterparts including CN, CNS and physically mixed CN and CNS (CN+CNS). The enhanced photoelectrochemical performance of CN/CNS heterojunction nanosheets could be ascribed to the efficient separation of photoexcited charge carriers across the heterojunction interface. The strategy of designing and preparing CN/CNS heterojunction photocatalysts in this work can open up new directions for the construction of all CN-based heterojunction photocatalysts.

Introduction

Over the past few years, graphitic carbon nitride (CN) has attracted significant research attention in visible-light-driven photocatalysis because of its unique physical and chemical properties including chemical and thermal stability, physical abundance, as well as suitable bandgap energy and band position [1-4]. The polymeric nature of CN could facilitate the tuning of the physical and chemical properties by simply changing the CN precursors, by varying the pyrolysis conditions and by doping with foreign atoms [5-8]. However, the photocatalytic performance of CN is still limited because of the fast charge recombination [6,8-10]. How to efficiently separate photogenerated charge carriers in CN becomes a critical factor

in further improving the photocatalytic performance. The construction of heterojunctions is a simple and effective way to enhance charge carrier separation, in which the build-in electric field across the junction could drive electrons and holes moving towards different parts of the photocatalyst, and thus improving the lifetime of charge carriers [11]. Numerous CN-based heterojunctions have been constructed by coupling CN with various types of photocatalysts, e.g., oxides and chalcogenides, which have shown improved photocatalytic performances [12-18]. However, the formation of interfacial defects at the CN/photocatalyst heterojunction arising from lattice mismatches would trap photogenerated electrons or holes, which reduces the benefits of build-in electric field created from the heterojunction. A smooth transition from one crystal phase to the other in a heterojunction could minimize the formation of interfacial defects, thus benefiting the interfacial charge transfer [19]. The formation of a smooth crystal transition would be expected at the interface of an all CN-based heterojunction. However, it is still challenging to synthesize a composite CN photocatalyst which is solely based on CN with different band structures [20].

Herein, we employ a biomolecule-assisted (L-cysteine) pyrolysis method to synthesize sulfur-doped carbon nitride (CNS) nanosheets, which can serve as the framework to grow CN to form an all CN-based heterojunction composite. The formation of CN/CNS heterojunctions significantly improves the photoelectrochemical performance, which is attributed to the efficient separation of photoexcited charge carriers across the heterojunction interface. The strategy of designing and preparing CN/CNS heterojunction photocatalysts in this work can open up new directions for the construction of all CN-based heterojunction photocatalysts.

Results and Discussion

Figure 1a and Figure 1b show the FESEM images of as-prepared CN and CNS. CN is composed of large micrometer-sized particles, whereas CNS consists of small pieces of thin nanosheets, which are loosely connected with each other. Transmission electron microscopy gives a deeper insight into the crystal structure and morphology. As shown in Figure 1c and Figure 1d, in stark contrast with CN, CNS nanosheets are much smaller and thinner with worm-like nanopores dispersed on the surface of the nanosheets, owing predominantly to the drastic decomposition/delamination of CNS at high temperature. X-ray photoelectron spectroscopy (XPS) measurements were performed to study the chemical states of CN and CNS. As shown in the survey spectra in Figure 1e, CN has the typical C1s and N1s signals, which evidence the successful formation of CN through thermal decomposition and polymerization of the amine precursor. Besides C1s and N1s signals, an additional S2p signal is observed in CNS. The atomic concentration of sulfur in CNS is determined to be about 0.36 atom %. The high-resolution S2p spectrum of CNS deconvolutes into two peaks centered at 163.5 and 168.2 eV, which could be ascribed to S–$(C)_3$ (tertiary sulfur) and C–S(O)–C (secondary sulfur), respectively, providing a compelling evidence of sulfur doping (sulfur is introduced into CN through substituting lattice nitrogen with sulfur on both tertiary and secondary nitrogen sites) [21]. The higher intensity for the peak centered at 163.5 eV than for that at 168.2 eV suggests that the replacement of the secondary nitrogen with sulfur in CN is more favorable.

The effects of sulfur doping on the optical and energy band structure were investigated by UV–vis absorption and Mott–Schottky measurements. Figure 2a shows the UV–vis diffuse reflectance spectra of CN and CNS. Both CN and CNS feature a semiconductor-like absorption. The abrupt absorption onset for CN and CNS at ca. 450 nm is due to the photoexcitation of electrons from the valence band to the conduction band. The tail absorption in the long wavelength region for CNS could be attributed to the interband transition induced by defects through sulfur doping. The bandgap energy (E_g) estimated from the $(\alpha h\nu)^2$ versus $h\nu$ plots are 2.79 and 2.82 eV for CN and CNS, respectively. Mott–Schottky measurements were conducted to estimate the relative conduction band position. From the intersects of the Mott–Schottky plots, the flatband potential and thus the conduction band edge of CN and CNS are estimated to be about −1.22 and −1.01 eV vs Ag/AgCl, respectively. Together with the bandgap energy obtained from optical absorption measurements, the valence band position for CN and CNS are estimated to be about 1.57 and 1.81 eV vs Ag/AgCl.

Based on the above analysis, it is clear that CN can form a type-II heterojunction upon CNS with band offsets of 0.24 eV (1.57 eV/1.81 eV vs Ag/AgCl) and 0.21 eV (−1.22 eV/−1.01 eV vs Ag/AgCl) at the valence and conduction band, respectively (Figure 3a). This type-II band alignment means that once CN and CNS are electronically coupled, a well-matched band structure for charge separation will be formed. In this case, the photogenerated electrons are transferred from CN to CNS, while the photogenerated holes are transferred from CNS to CN, leading to an improved charge separation. To test our hypothesis, we designed a strategy to construct CN/CNS heterostructures. In our method, we firstly grow CNS nanosheets by using a biomolecule-assisted pyrolysis method, followed by growing CN on preformed CNS nanosheets to form a well-mixed CN/CNS heterostructure.

Figure 4a shows the FESEM image of a CN/CNS composite heterostructure. In comparison with CNS (Figure 1b), the framework of CNS was well preserved after CN growth, while

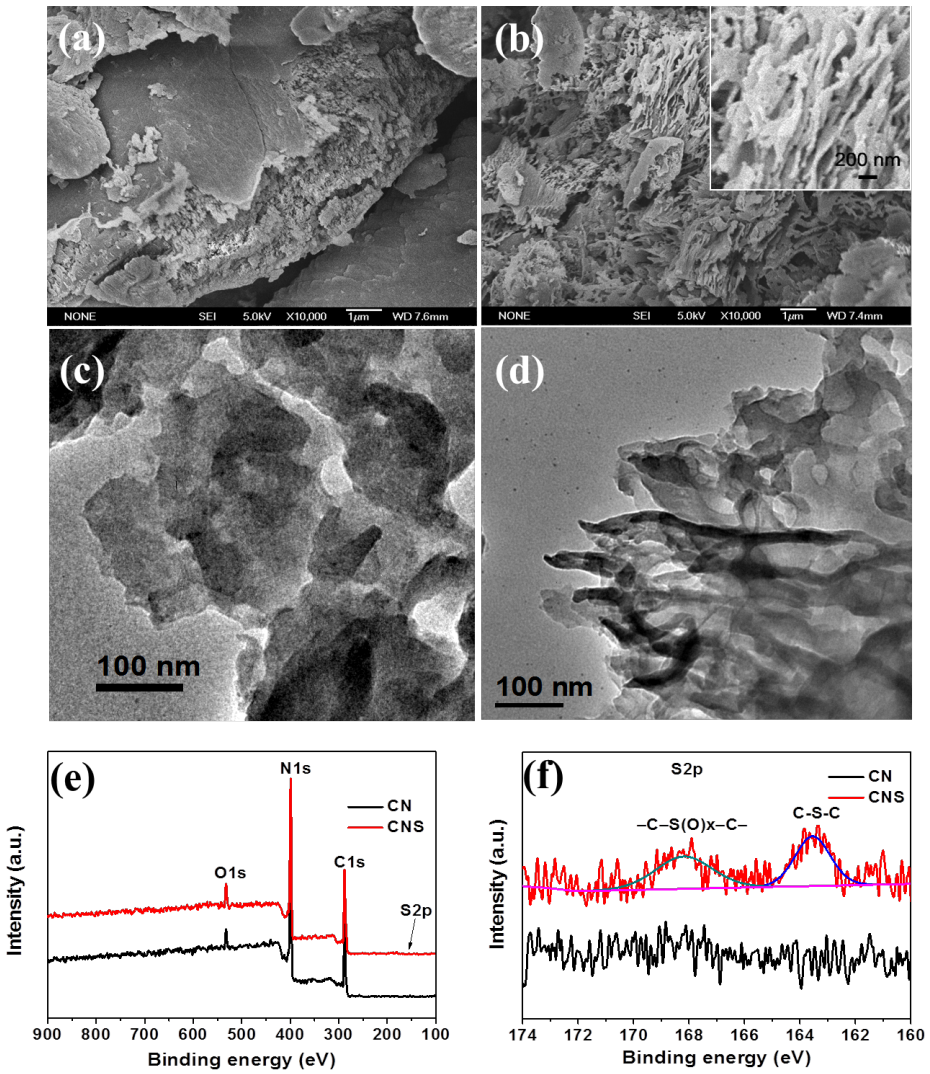

Figure 1: FESEM and TEM images of (a,c) CN, and (b,d) CNS samples. The inset of (b) is an enlarged FESEM image of the CNS sample. (e,f) Survey XPS spectra and high-resolution S2p XPS spectra of CN and CNS samples.

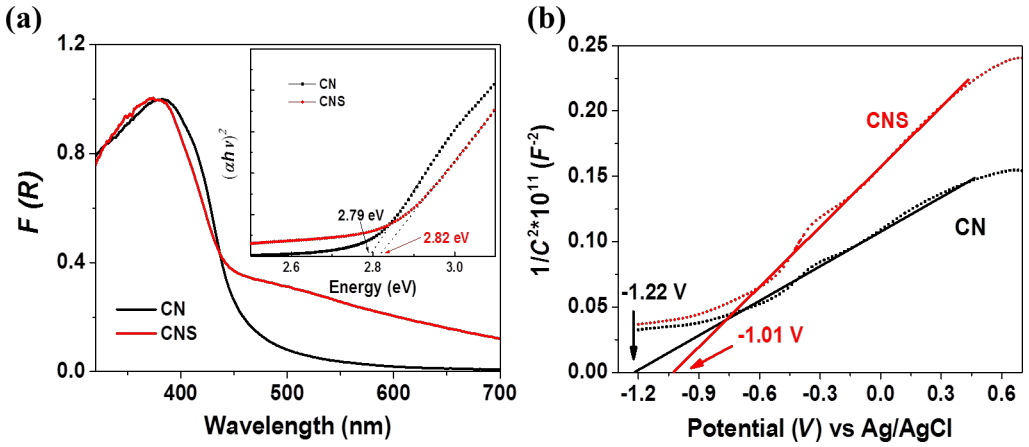

Figure 2: (a) Optical absorption spectra of CN and CNS. Inset shows the Tauc plots for bandgap determination, (b) Mott–Schottky plots for CN and CNS.

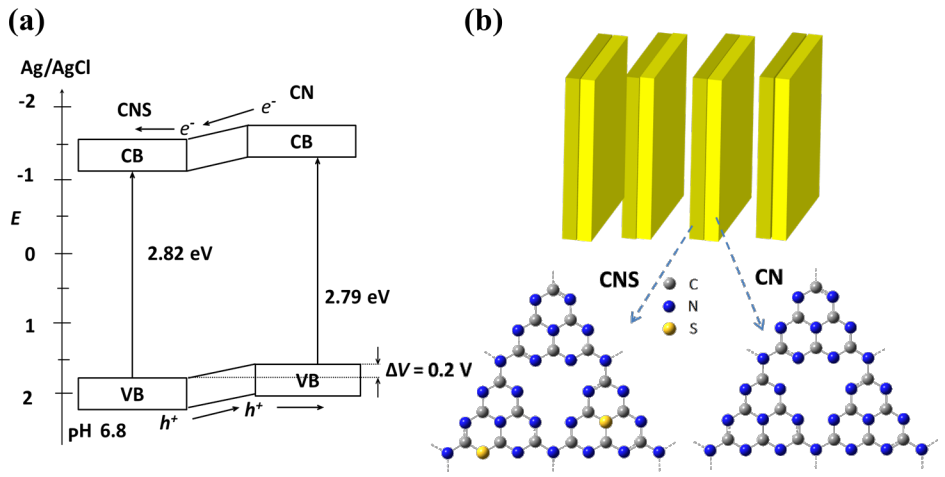

Figure 3: Schematic illustration of (a) electron–hole separation at the CN/CNS heterojunction interface, (b) the structure of CN/CNS heterojunction.

the thickness of nanosheets increased from ca. 30 nm for CNS to ca. 50 nm for CN/CNS composite. Figure 4b shows the XRD patterns of CN, CNS and the CN/CNS heterojunction composite. Two diffraction peaks are clearly visible in all XRD patterns. The peak centered at 13° could be indexed to the (100) plane of CN, corresponding to the in-plane structural packing motif of tristriazine unit. The peak was slightly shifted towards a higher diffraction angle when sulfur was introduced into the CN lattice. The calculated hole-to-hole distances in the nitride pores of CN and CNS are 0.691 and 0.660 nm, respectively. The other peak at 27.5° could be assigned to the interlayer stacking of aromatic units, which is also noted as (002) plane. Analogous to the (100) peak, the (002) peak shifted from 27.2° in CN to 27.7° in CNS, indicating a reduction of the inter-plane distance after sulfur doping. The calculated interlayer distances of CN and CNS are 0.327 and 0.322 nm, respectively. The (002) peak of CN/CNS becomes wider than that of CN and CNS. A further analysis shows that the peak of CN/CNS can be

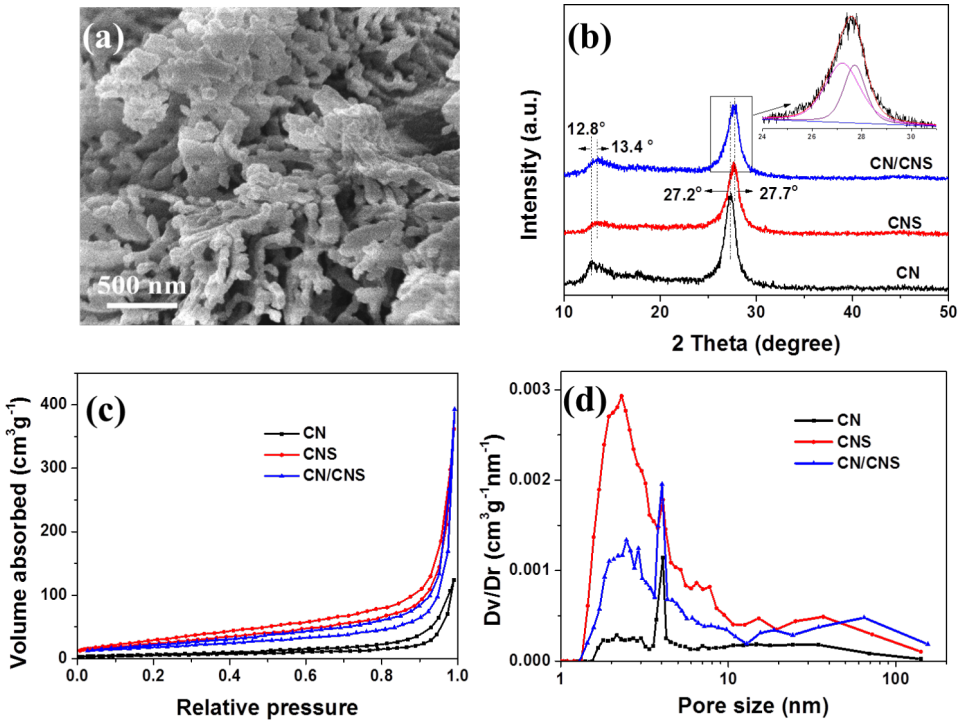

Figure 4: (a) FESEM image of CN/CNS heterostructure, (b) XRD and (c) nitrogen adsorption–desorption isotherms and (d) pore size distribution (insert) of CN, CNS and CN/CNS heterostructure.

split into two peaks at 27.2° and 27.7°, corresponding to the (002) peaks of CN and CNS, respectively. The composite peak of CN/CNS indicates that CN/CNS is a hybrid of CN and CNS, confirming the formation of a CN/CNS heterostructure. Nitrogen adsorption–desorption analysis in Figure 4c confirmed the significant change of the CN texture after sulfur doping. The specific surface area for CN and CNS are 21 and 118 $cm^2 \cdot mg^{-1}$, respectively. The surface area of the CN/CNS heterostructure (about 56 $cm^2 \cdot mg^{-1}$) is reduced to about half of that of CNS due to increased thickness of nanosheets. Figure 4d presents the pore size distribution of CN, CNS and the CN/CNS heterostructure. It is clear that sulfur doping significantly increases the pore volume of micro- (smaller than 10 nm) and meso- (larger than 100 nm) pores, which could favor the photocatalytic performance [22].

Figure 5 shows the TEM image of CN/CNS heterostructure. As shown in Figure 5a, a layered structure made up of a dark region and a dim region can be clearly distinguished. The dark and dim region can be ascribed to dense CN and CNS nanosheets, respectively, based on the high-resolution TEM (HRTEM) analysis as shown in Figure 5b. Furthermore, it can be observed that the dense CN layer intimately connects with the CNS nanosheet to form a heterostructure. The HRTEM image of CN/CNS as shown in Figure 5b clearly distinguishes the phases of CN (the dark region) and CNS (the dim region). The lattice spacing for the dark region and the dim region are 0.328 nm and 0.322 nm respectively, which are consistent with the XRD results. The HRTEM image gives solid evidence towards the formation of heterojunction in CN/CNS.

Figure 6a shows the photoluminescence (PL) spectra of CN, CNS and a CN/CNS heterostructure. In comparison with CN and CNS, a substantial reduction in PL intensity was observed for the hybrid CN/CNS heterostructure, suggesting an efficient charge carrier separation at the CN/CNS interface. Linear sweep photovoltammetry measurements were performed to study the photoelectrochemical performances of CN, CNS and the CN/CNS heterostructure. As shown in Figure 6b, photocurrent densities of the samples increase with forward bias voltage, indicating a typical n-type semiconductor behavior. Among all samples, the CN/CNS heterostructure demonstrates the highest photocurrent as compared with the other counterparts including CN, CNS and physically mixed CN and CNS over the entire potential profile. It is worth noting that the dark current densities of the photoelectrodes follow the order of CN/CNS heterostructure > CNS > CN, indicating the best charge transport properties of CN/CNS photoelectrode, which can be attributed to the large contact area between the CN/CNS photoelectrode and the electrolyte as well as an appropriate band alignment of the CN/CNS interface. It has been well-established that photocurrent is generated because of the diffusion of photogenerated electrons to the back contact and the simultaneous consumption of photogenerated holes by the hole acceptor in the electrolyte. As such, the superior photocurrent of CN/CNS heterostructure indicates the more efficient charge carrier separation and longer lifetime of the free charge carriers. A control experiment using physically mixed CN and CNS (1:1 in mass, named as CN+CNS) as photoelectrode was preformed (UV–vis and *J*–*V* curves are shown in Figure S1a and Figure S1b, respectively). Although the absorption of physically mixed CN and CNS is nearly the same as that of the CN/CNS heterojunction sample, the photocurrent of CN+CNS is much lower, implying that the enhanced photoresponse of heterojunction sample comes from better separation of photogenerated electrons and holes instead of improved photon absorption. The mechanism

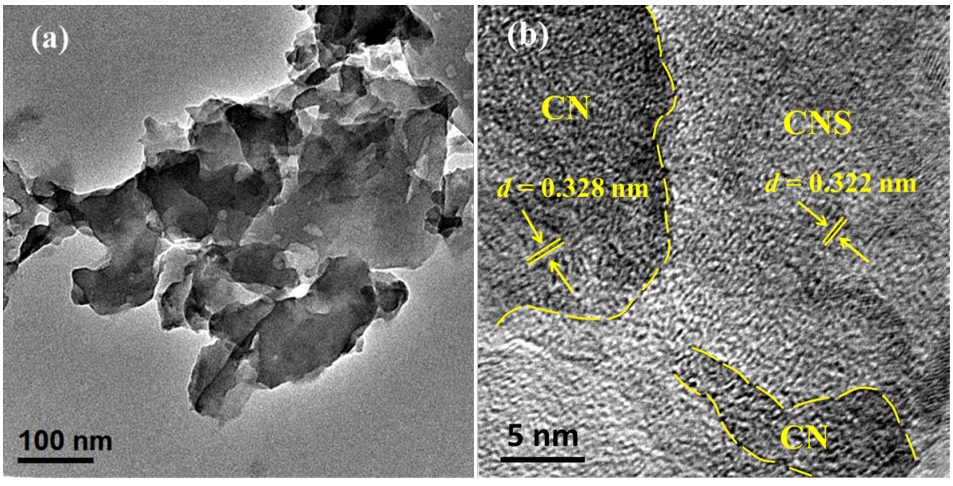

Figure 5: TEM (a) and HRTEM (b) images of a CN/CNS heterostructure.

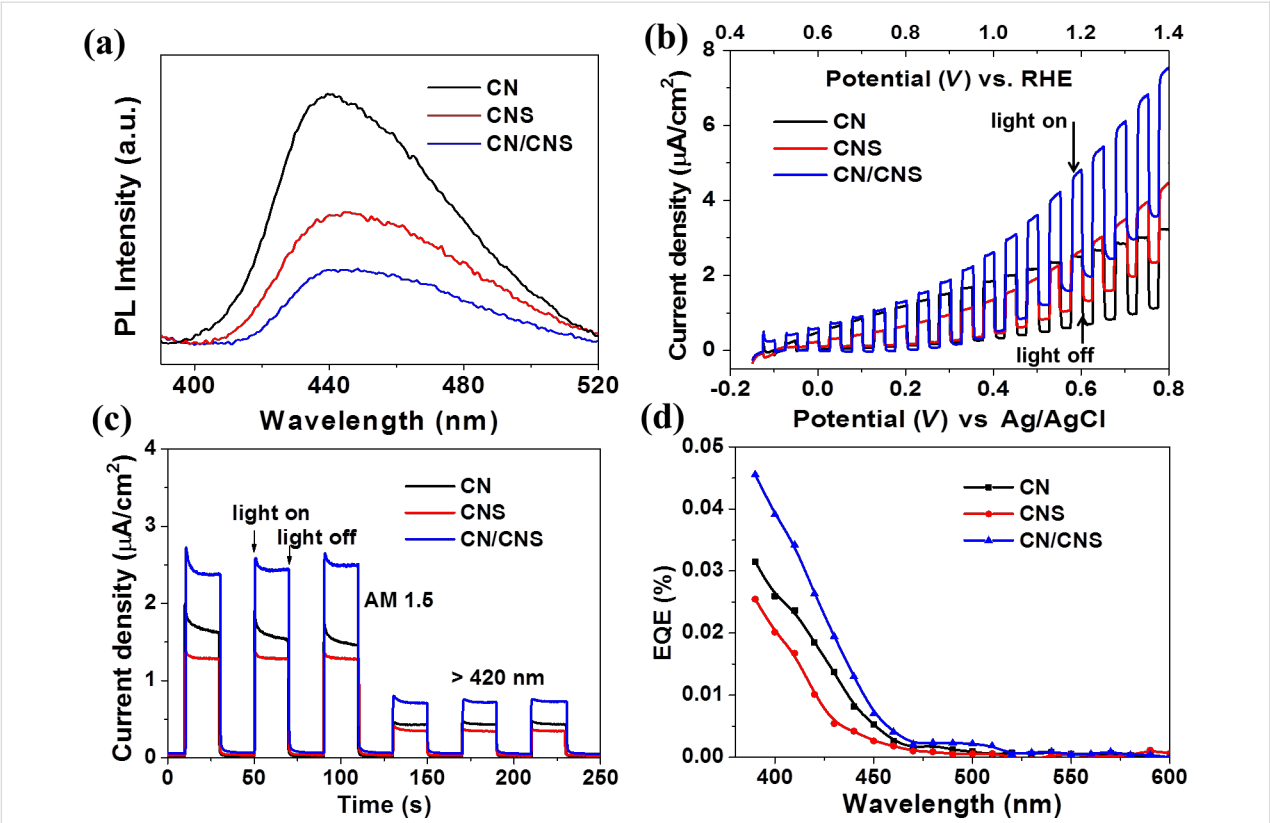

Figure 6: (a) Photoluminescence of CN, CNS and CN/CNS in aqueous solution. (b) Current density–voltage (*J*–*V*) curves for CN, CNS and CN/CNS electrodes under simulated sunlight (AM 1.5, 100 mW/cm^2). All experiments were performed in 0.2 M Na_2SO_4 aqueous solution at a scan rate of 10 mV/s. (c) Current density–time (*J*–*t*) curves for CN, CNS and CN/CNS electrodes with 0.4 V bias vs Ag/AgCl under simulated sunlight (AM 1.5, 100 mW/cm^2) and visible light (λ > 420 nm). (d) External quantum efficiency (EQE) of CN, CNS and CN/CNS photoelectrodes.

for photocurrent enhancement was further studied by measuring the photoresponse under different light source and the EQE spectra. Figure 6c exhibits the photoresponse of CN, CNS and CN/CNS under different light sources. It can be observed that the photocurrent can be reproducibly produced under AM 1.5G simulated sunlight or visible light (λ > 420 nm) with the same trend following the order of CN/CNS heterostructure > CN > CNS. The low photocurrent density might be due to the poor contact among CN particles and FTO substrate. Figure 6d shows the external quantum efficiency (EQE) of CN, CNS and the CN/CNS heterostructure, which matches well with the corresponding photocurrent density. It is worth mentioning that the shape of the three EQE curves are similar with the same cut off at nearly 470 nm, indicating that the enhanced photocurrent of CN/CNS heterostructure mainly comes from improved charge separation at the CN/CNS heterojunction interface.

Conclusion

In conclusion, we have developed a biomolecule-assisted pyrolysis method to synthesize sulfur doped carbon nitride nanosheets (CNS), which offers an effective way to modify the texture and energy band positions of carbon nitride (CN). By growing CN on preformed sulfur-doped CN nanosheets, composite CN/CNS heterojunction nanosheets were constructed, which exhibited a significantly enhanced photoelectrochemical performance as compared with various control counterparts including CN, CNS and physically mixed CN and CNS (CN+CNS). The enhanced photoelectrochemical performance of CN/CNS heterojunction nanosheets could be ascribed to the efficient separation of photoexcited charge carriers across the heterojunction interface. Our approach offers a facile way to construct an all carbon nitride based heterojunction photocatalyst.

Experimental

Materials preparation

Graphitic carbon nitride (CN) was prepared according to a reported pyrolysis method [23]. Typically, 2 g of melamine powder was put into an alumina crucible covered with a piece of titanium sheet, then heated at a heating rate of 2.3 °C/min to 550 °C in a tube furnace and maintained at this temperature for 4 h under flowing argon. To synthesize sulfur-doped carbon nitride (CNS), 222 mg of L-cysteine was blended with 2 g of melamine in an agate mortar, wherein L-cysteine acts as the

sulfur source for sulfur doping. During the pyrolysis process, the –SH functional group in L-cysteine reacts with the amine group in melamine to substitute the N atoms and to form the S–C bond. Following, this mixture was heated to 550 °C at a heating rate of 2.3 °C/min and maintained at this temperature for 2 h. The CN/CNS heterojunction was prepared through thermal condensation of melamine on preformed CNS nanosheets. Specifically, 1 g of melamine and 1 g of preformed CNS nanosheets were mixed together and underwent the same pyrolysis process as that for the preparation of CN. Physical mixtures of CN and CNS (1:1 mass ratio) were also prepared as reference.

Characterization

The morphology of the samples was examined by using field emission scanning electron microscopy (FESEM, JEOL, JSM6701F) and transmission electron microscopy (TEM, JEOL 3010). The chemical bonding information was studied with X-ray photoelectron spectroscopy (Kratos AXIS Ultra spectrometer) with a monochromatized Al Kα X-ray source (1486.71 eV). The Brunauer–Emmett–Teller (BET) surface area of sample was obtained on a nitrogen adsorption apparatus (Autosorb-6B, Quantachrome Instruments) with all samples degassed at 150 °C for 16 h prior to the measurement. The UV–vis diffuse reflectance spectra (DRS) were obtained on a UV–vis spectrometer (ShimadzuUV2450) using $BaSO_4$ as reference. The powder X-ray diffraction (XRD) patterns were obtained on a Bruker D2 diffractometer (Bruker AXS, $\lambda = 0.15418$ nm). The chemical states and percentage of sulfur were measured by using X-ray photoelectron spectroscopy (XPS) on a VG Escalab 220i XL and the binding energies were calibrated by using the C 1s peak at 285.0 eV. The photoluminescence (PL) spectra were recorded using an LP920-KS instrument from Edinburgh Instruments, equipped with a photomultiplier tube.

Photoelectrochemical measurements

The photoelectrochemical properties of as-prepared samples were measured by using an electrochemical workstation (CHI 760E, CH Instrument Inc., USA) in a standard three-electrode setup with a Pt plate as the counter electrode and an Ag/AgCl as the reference electrode. In all cases, 0.2 M Na_2SO_4 aqueous solution (pH 6.8) was used as the electrolyte. Prior to each measurement, the electrolyte was deaerated by continuously purging nitrogen for 30 min. The working electrode was prepared as the following: briefly, 10 mg of as-prepared sample was suspended in 1 mL of isopropyl alcohol (IPA). Then, 50 μL of the colloidal suspension (10 mg/mL) was dropcasted onto precleaned fluorine-doped tin oxide (FTO) substrate with a fixed area of 1 cm^2. After coating, the film was dried at 70 °C in ambient atmosphere, followed by annealing at 350 °C for 1 h under argon to improve physical and electrical contact. The light source used for photoelectrochemical measurement was a 300 W xenon lamp (Newport, Oriel, 91160) equipped with an AM 1.5G filter (Newport, 81094) and a UV-filter (Newport, FSQ-GG420) (cut off: 420 nm). Prior to each measurement, the light intensity was determined by a calibrated silicon photodiode. The external quantum efficiency (EQE) was measured under +0.4 V external bias (three-electrode) condition. The monochromatic light was supplied by a xenon lamp (300 W, Oriel) illuminating through a monochromator (Newport) with a bandwidth of 5 nm.

Supporting Information

Supporting Information File 1

Additional experimental data.
[http://www.beilstein-journals.org/bjnano/content/supplementary/2190-4286-5-89-S1.pdf]

Acknowledgements

The authors acknowledge Nanyang Technological University and the Singapore–Berkeley Research Initiative for Sustainable Energy (SinBeRISE) for the financial support.

References

1. Wang, X.; Maeda, K.; Chen, X.; Takanabe, K.; Domen, K.; Hou, Y.; Fu, X.; Antonietti, M. *J. Am. Chem. Soc.* **2009,** *131,* 1680–1681. doi:10.1021/ja809307s
2. Wang, X.; Maeda, K.; Thomas, A.; Takanabe, K.; Xin, G.; Carlsson, J. M.; Domen, K.; Antonietti, M. *Nat. Mater.* **2009,** *8,* 76–80. doi:10.1038/nmat2317
3. Wang, X.; Chen, X.; Thomas, A.; Fu, X.; Antonietti, M. *Adv. Mater.* **2009,** *21,* 1609–1612. doi:10.1002/adma.200802627
4. Zhang, J.; Chen, X.; Takanabe, K.; Maeda, K.; Domen, K.; Epping, J. D.; Fu, X.; Antonietti, M.; Wang, X. *Angew. Chem., Int. Ed.* **2010,** *49,* 441–444. doi:10.1002/anie.200903886
5. Zhang, J.; Sun, J.; Maeda, K.; Domen, K.; Liu, P.; Antonietti, M.; Fu, X.; Wang, X. *Energy Environ. Sci.* **2011,** *4,* 675–678. doi:10.1039/c0ee00418a
6. Wang, Y.; Wang, X.; Antonietti, M. *Angew. Chem., Int. Ed.* **2012,** *51,* 68–89. doi:10.1002/anie.201101182
7. Wang, Y.; Li, H.; Yao, J.; Wang, X.; Antonietti, M. *Chem. Sci.* **2011,** *2,* 446–450. doi:10.1039/c0sc00475h
8. Dong, F.; Zhao, Z.; Xiong, T.; Ni, Z.; Zhang, W.; Sun, Y.; Ho, W.-K. *ACS Appl. Mater. Interfaces* **2013,** *5,* 11392–11401. doi:10.1021/am403653a
9. Wang, X.; Blechert, S.; Antonietti, M. *ACS Catal.* **2012,** *2,* 1596–1606. doi:10.1021/cs300240x
10. Zheng, Y.; Liu, J.; Liang, J.; Jaroniec, M.; Qiao, S. Z. *Energy Environ. Sci.* **2012,** *5,* 6717–6731. doi:10.1039/c2ee03479d
11. Marschall, R. *Adv. Funct. Mater.* **2014,** *24,* 2421–2440. doi:10.1002/adfm.201303214
12. Xiang, Q.; Yu, J.; Jaroniec, M. *J. Phys. Chem. C* **2011,** *115,* 7355–7363. doi:10.1021/jp200953k

13. Yan, S. C.; Lv, S. B.; Li, Z. S.; Zou, Z. G. *Dalton Trans.* **2010,** *39,* 1488–1491. doi:10.1039/b914110c
14. Sun, J.-X.; Yuan, Y.-P.; Qiu, L.-G.; Jiang, X.; Xie, A.-J.; Shen, Y.-H.; Zhu, J.-F. *Dalton Trans.* **2012,** *41,* 6756–6763. doi:10.1039/c2dt12474b
15. Sun, L.; Qi, Y.; Jia, C.-J.; Jin, Z.; Fan, W. *Nanoscale* **2014,** *6,* 2649–2659. doi:10.1039/C3NR06104C
16. Wang, Y.; Bai, X.; Pan, C.; He, J.; Zhu, Y. *J. Mater. Chem.* **2012,** *22,* 11568–11573. doi:10.1039/c2jm16873a
17. Fu, J.; Chang, B.; Tian, Y.; Xi, F.; Dong, X. *J. Mater. Chem. A* **2013,** *1,* 3083–3090. doi:10.1039/c2ta00672c
18. Zhang, J.; Wang, Y.; Jin, J.; Zhang, J.; Lin, Z.; Huang, F.; Yu, J. *ACS Appl. Mater. Interfaces* **2013,** *5,* 10317–10324. doi:10.1021/am403327g
19. Liu, B.; Khare, A.; Aydil, E. S. *ACS Appl. Mater. Interfaces* **2011,** *3,* 4444–4450. doi:10.1021/am201123u
20. Zhang, J.; Zhang, M.; Sun, R.-Q.; Wang, X. *Angew. Chem., Int. Ed.* **2012,** *51,* 10145–10149. doi:10.1002/anie.201205333
21. Liu, G.; Niu, P.; Sun, C.; Smith, S. C.; Chen, Z.; Lu, G. Q.; Cheng, H.-M. *J. Am. Chem. Soc.* **2010,** *132,* 11642–11648. doi:10.1021/ja103798k
22. Liu, B.; Zeng, H. C. *Chem. Mater.* **2008,** *20,* 2711–2718. doi:10.1021/cm800040k
23. Yan, S. C.; Li, Z. S.; Zou, Z. G. *Langmuir* **2009,** *25,* 10397–10401. doi:10.1021/la900923z

License and Terms

This is an Open Access article under the terms of the Creative Commons Attribution License (http://creativecommons.org/licenses/by/2.0), which permits unrestricted use, distribution, and reproduction in any medium, provided the original work is properly cited.

The license is subject to the *Beilstein Journal of Nanotechnology* terms and conditions: (http://www.beilstein-journals.org/bjnano)

The definitive version of this article is the electronic one which can be found at: doi:10.3762/bjnano.5.89

Beilstein Journal of Nanotechnology

Enhancement of photocatalytic H_2 evolution of eosin Y-sensitized reduced graphene oxide through a simple photoreaction

Weiying Zhang, Yuexiang Li*, Shaoqin Peng and Xiang Cai

Full Research Paper

Open Access

Address:
Department of Chemistry, Nanchang University, Nanchang 330031, China

Email:
Yuexiang Li* - liyx@ncu.edu.cn

* Corresponding author

Keywords:
eosin Y sensitization; graphene oxide; H_2 evolution; photocatalysis; photoreduction; sp^2 conjugated domains

Beilstein J. Nanotechnol. **2014,** *5,* 801–811.
doi:10.3762/bjnano.5.92

Received: 29 December 2013
Accepted: 05 May 2014
Published: 06 June 2014

This article is part of the Thematic Series "Photocatalysis".

Guest Editor: R. Xu

© 2014 Zhang et al; licensee Beilstein-Institut.
License and terms: see end of document.

Abstract

A graphene oxide (GO) solution was irradiated by a Xenon lamp to form reduced graphene oxide (RGO). After irradiation, the epoxy, the carbonyl and the hydroxy groups are gradually removed from GO, resulting in an increase of sp^2 π-conjugated domains and defect carbons with holes for the formed RGO. The RGO conductivity increases due to the restoration of sp^2 π-conjugated domains. The photocatalytic activity of EY-RGO/Pt for hydrogen evolution was investigated with eosin Y (EY) as a sensitizer of the RGO and Pt as a co-catalyst. When the irradiation time is increased from 0 to 24 h the activity rises, and then reaches a plateau. Under optimum conditions (pH 10.0, 5.0×10^{-4} mol L^{-1} EY, 10 μg mL^{-1} RGO), the maximal apparent quantum yield (AQY) of EY-RGO24/Pt for hydrogen evolution rises up to 12.9% under visible light irradiation ($\lambda \geq 420$ nm), and 23.4% under monochromatic light irradiation at 520 nm. Fluorescence spectra and transient absorption decay spectra of the EY-sensitized RGO confirm that the electron transfer ability of RGO increases with increasing irradiation time. The adsorption quantity of EY on the surface of RGO enhances, too. The two factors ultimately result in an enhancement of the photocatalytic hydrogen evolution over EY-RGO/Pt with increasing irradiation time. A possible mechanism is discussed.

Introduction

Hydrogen is an efficient and green energy carrier. Photocatalytic water splitting into hydrogen by means of solar energy and semiconductor photocatalysts is a environmentally friendly way to produce storable energy [1-4]. In order to enhance the activity of photocatalysts for hydrogen evolution, various graphene-based composite photocatalysts, such as graphene/TiO_2 composite and graphene/ZnO composite, have recently been reported [5-8]. Kim et al. [8] have reported that two graphene/TiO_2 composites, a nanographene shell on a TiO_2 core and TiO_2 nanoparticles on a graphene sheet, exhibit a

higher photocatalytic H_2 evolution than TiO_2 under UV irradiation. This can be attributed to an efficient electron transfer from TiO_2 to graphene [9,10]. Interestingly, single reduced graphene oxide itself (RGO) shows a higher activity as a semiconductor under UV irradiation [11,12]. Yeh et al. [12] reported that RGO sheets with in situ photoreduced platinum displayed a high activity for hydrogen evolution from an aqueous methanol solution. However, the RGO exhibits a very low photocatalytic activity under visible light irradiation.

Eosin Y (EY), a xanthene dye, is a very good sensitizer [13-18]. EY has been used to sensitize various matrixes such as TiO_2 [13], $Na_2Ti_2O_4(OH)_2$ nanotubes [14], g-C_3N_4 [15], and α-$[AlSiW_{11}(H_2O)O_{39}]^{5-}$ [18], and the sensitized photocatalysts are characterized by a high activity for H_2 evolution under visible light irradiation. Recently, to improve the photocatalytic activity for hydrogen evolution in the visible light region, EY has been employed to sensitize RGO, and the sensitized photocatalyst displays an increased photoactivity for hydrogen evolution [19-21]. Mou et al. [19] found that the photocatalytic activity of EY-RGO for hydrogen evolution was superior to that of EY-GO. However, the activity of the former was still very low. Min and Lu [20] demonstrated a successful example of enhancing H_2 evolution activity by using RGO as an efficient electron relay between the photoexcited EY and the loaded Pt co-catalyst, which shows an AQY of 4.15% under visible light irradiation. In these works, RGO was obtained by a chemical reduction of GO with hydrazine or sodium borohydride as a reductant.

Graphene, an atom-thick two-dimensional (2D) sheet of sp^2-hybrized carbon, has received tremendous research interests based on its extraordinary electronic, thermal, optical and excellent electron transport properties [21,22]. Graphene can be easily obtained by reducing graphene oxide (GO), which is a cheap and scalable preparation method [23-26]. The GO contains not only hydroxy and epoxy groups in the 2D sheet, but also carbonyl and carboxyl groups at the edges of the sheet [27,28]. The oxygen-containing groups in the sheet break the sp^2 π-conjugation, leading to the formation of oxidized aliphatic six-membered rings with sp^3-hybridization in the GO layer. As a result, the conductivity of GO decreases greatly compared with that of graphene. Amongst various methods for the reduction of GO to form RGO, photoreaction (photoreduction) is "green" without any toxic chemical reagents. Moreover, it is easy to control the degree of reduction by applying different UV irradiation times [29-32]. The RGO prepared by UV irradiation is of high dispersion, can be stored for a long time without getting aggregated, and exists in the quasi homogeneous form [33,34].

In this work, we prepared RGO starting from an aqueous GO solution by controlling UV irradiation time. The RGO solution and its powder were denoted as RGO*x* and RGO*x*-p, respectively, where *x* (in hours) represents the particular UV irradiation time. The photocatalytic activity of EY-sensitized RGO*x* was investigated by using Pt as a co-catalyst and trimethylamine (TMA) as a sacrificial electron donor. To the best of our knowledge, studies on the effect of irradiation time on the performance of RGO*x* for the dye sensitized H_2 generation have not been reported so far. The sensitization activity for hydrogen evolution under visible light illumination is much higher than that of EY-RGO/Pt produced by chemical reduction methods in the literature [19,20]. A possible mechanism is discussed.

Results and Discussion

The effect of irradiation time on the performance of RGO*x*

Figure 1 shows UV–vis spectra of GO and RGO*x* solution. The peak at 232 nm is due to the C=C bond in an aromatic ring [35], whereas the broad shoulder peak at 291 nm can be assigned to C=O [36]. The absorption over 291 nm is expected to be caused by the conjugated fused ring plane [37]. An increase of the irradiation time from 0 to 24 h entails an increase of the absorption strength of the RGO*x* solution over 291 nm and a red-shift of the absorption. The absorption of RGO36 is close to that of RGO24, indicating that the deoxygenation reaction takes place slowly at that stage [38]. This can be attributed to an enhancement of π-conjugated sp^2 domains (restoration of sp^2 π-conjugated network) by the removal of oxygen-containing groups whose carbon atoms are sp^3 hybridized, and a decrease of sp^3 domains (see Mechanism section, Scheme 1). The inset of Figure 1 shows a picture of GO and RGO24. The GO disper-

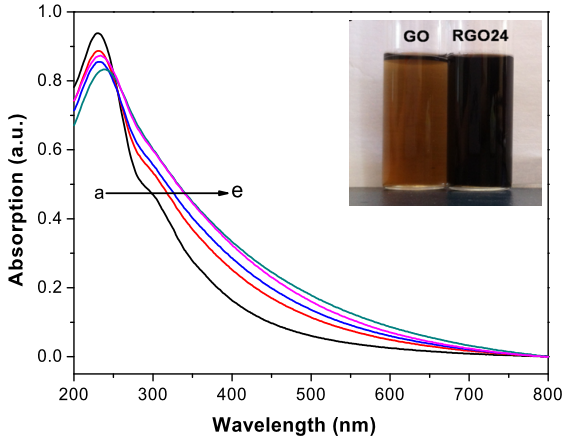

Figure 1: UV–vis spectra of (a) GO, (b) RGO4, (c) RGO12, (d) RGO24, and (e) RGO36 solution (20 μg mL^{-1}). The inset is an image of GO and RGO24.

sion is yellow–brown and semitransparent, gradually changes to dark brown after irradiation (not shown here), and finally turns black and opaque after 24 h of irradiation. This indicates an increase of the degree of sp^2 conjugation by a regeneration of the sp^2 π-conjugated network [35].

Figure 2A displays ATR-IR spectra of GO-p, RGO4-p and RGO24-p. The peak intensity at 1626 cm^{-1}, which can be assigned to C=C [39], increases with irradiation time, whereas the epoxy C–O peak at 993 cm^{-1} [12] disappears after irradiation of 24 h. These suggest that epoxy C–O–C has been reduced to produce sp^2 carbons [40]. Figure 2B shows XPS spectra of C1s for GO-p, RGO4-p and RGO24-p. The deconvoluted peaks centered in a binding energy range of 284.8–285.0 eV and 287–287.2 eV are attributed to C–C, C=C, and C–H bonds, and C–O bonds (C–O–C and C–OH), respectively [30]. The deconvoluted peaks at binding energy of 287.8 eV and 289.0 eV belongs to C=O and O=C–OH respectively [41]. The peak intensities of epoxy C–O–C and C=O decrease with increasing irradiation time, which suggests that most of epoxy C–O–C and C=O are removed to produce sp^2 domains [40]. Clearly, the peak intensities of C–C, C=C, and C–H bonds increase. As shown in Table 1, the O/C atomic ratio decreases from 0.33 in the GO sample to 0.26 after 24 h of photoreaction. This further indicates the restoration of the sp^2 π-conjugated network for RGO after the photoreaction. Due to restoration of the sp^2 π-conjugated network in RGO*x*, its conductivity is expected to increase [42]. To verify this enhancement, the electrochemical impedance spectroscopy (EIS) of GO, RGO4 and RGO24 were measured. Figure 2C shows the Nyquist diagrams for GO, RGO4 and RGO24. The semicircles correspond to the charge transfer resistance (R_{CT}) [43] and become smaller and smaller after irradiation. This suggests that their conductivity order is RGO24 > RGO4 > GO, which is due to the increase of the aromatic ring plane, more specifically, the increase of sp^2 π-conjugated domains [44].

The interaction between EY and GO/RGO*x*

The chemical structure of EY is shown in Figure 3. The benzoate ring is perpendicular to the xanthenes moiety. The main interaction between EY and graphene is through π–π stacking [19-21] of the xanthene moiety (the fused ring) of EY with sp^2 π-conjugated domains of graphene.

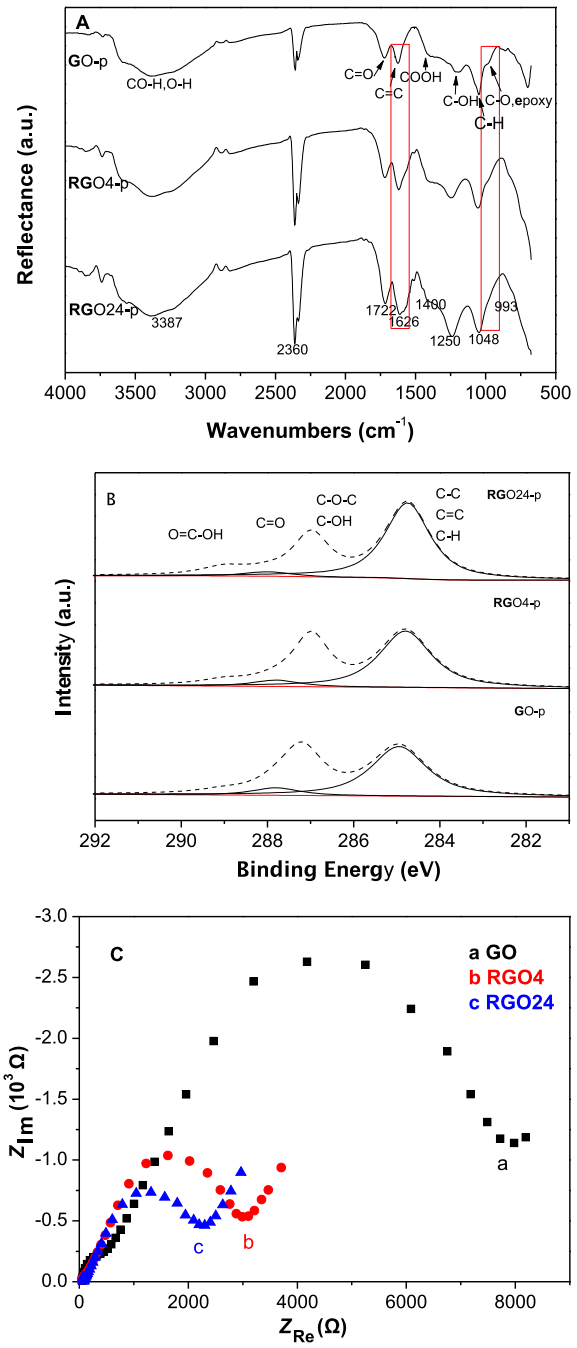

Figure 2: (A) ATR-IR spectra of GO-p, RGO4-p and RGO24-p, (B) XPS spectra of C1s for GO-p, RGO4-p and RGO24-p, and (C) Nyquist diagrams of GO, RGO4 and RGO24.

Table 1: Peak area ratios of oxygen-containing bonds to CC bonds and O/C ratio obtained from Figure 2B.

sample	A_{C-O}/A_{CC}	$A_{C=O}/A_{CC}$	A_{OCOH}/A_{CC}	O/C
GO	0.69	0.13	0.05	0.33
RGO4	0.59	0.10	0.07	0.30
RGO24	0.42	0.06	0.08	0.26

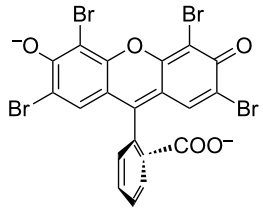

Figure 3: Chemical structure of EY.

Table 2 lists the amount of adsorbed EY on the surface of RGO*x*. Before the irradiation, the adsorption amount of EY on the GO surface is 11.7 μmol g^{-1}. After irradiation of GO for 4, 12 and 24 h, the adsorption amount increases to 15.0, 32.7 and 74.3 μmol g^{-1}, respectively. This is because the sp^2 domains of RGO*x* increase with the reaction time (see Mechanism section, Scheme 1). As a result, the π–π stacking interaction between EY and RGO becomes stronger.

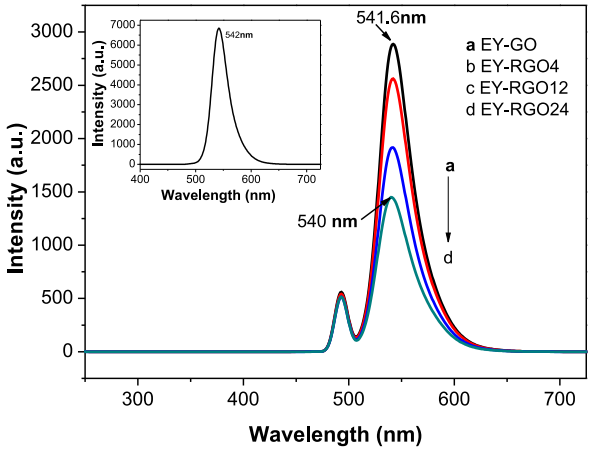

Figure 4: Fluorescence spectra of EY-RGO*x* in TMA solution. The inset shows the fluorescence spectrum of EY in TMA solution. Conditions: 30 μg mL^{-1} GO or RGO*x*; 1.0 × 10^{-5} mol L^{-1} EY; 7.7 × 10^{-2} mol L^{-1} TMA.

To further confirm the interaction between EY and GO/RGO*x*, the fluorescence spectra of the mixture of EY and GO or RGO*x* were measured, as shown in Figure 4. The inset of Figure 4 displays a strong fluorescence peak of EY (about 6.8 × 10^3 a.u.) at 542 nm. This can be attributed to the large visible light absorption by its conjugated xanthenes structure and the strong recombination of photo-excited electron–hole pairs. When GO is added to the EY solution, the fluorescence intensity of EY at 541.6 nm sharply declines to about 2.8 × 10^3 a.u. The addition of RGO24 results in a great fluorescence quenching of EY (Figure 4d,), the emission peak intensity decreases to about 1.4 × 10^3 a.u., and the fluorescence peak shifts from 541.6 to 540.0 nm. This is because the number of sp^2 π-conjugated domains (larger adsorption amount for EY) and the conductivity of RGO*x* increase with longer irradiation times, thereby enhancing the ability for a photo-induced electron transfer from the excited dye molecules to RGO*x*. The slight blue shift suggests that an intermolecular π-π stacking interaction between RGO24 and EY is stronger than the interaction between GO and EY [20].

To further confirm the increased ability to transfer electrons between RGO*x* and EY, transient absorption decay spectra of $^3EY^*$ at 580 nm in EY-RGO*x* and EY-GO systems were measured on a laser flash photolysis spectrometer (Figure 5). It is well-known that EY molecules are excited to the singlet excited state ($^1EY^*$) which is of short-life, and then produce long-lived triplet excited states ($^3EY^*$) by inter-system crossing [45,46]. $^3EY^*$ has an absorption peak below 580 nm [47]. In the absence of GO or RGO*x*, the lifetime of $^3EY^*$ is 103.5 μs, while in the presence of GO, the lifetime of $^3EY^*$ is reduced to 93.5 μs. The addition of RGO4 and RGO24 yields a declined lifetime of $^3EY^*$ to 89.4 and 79.6 μs, respectively. This result confirms that RGO*x* can transfer the electron of $^3EY^*$ more effectively than GO [16]. The ability to transfer electrons in decreasing order is RGO24 > RGO4 > GO, which is in accordance with the result of the fluorescence spectra.

Photocatalytic H_2 evolution

Figure 6 shows the photocatalytic H_2 evolution of EY-sensitized GO and RGO*x* under visible light irradiation. The amount of H_2 evolution increases with an increase of the irradiation time from 0 to 24 h, and then keeps almost unchanged. In the absence of GO or RGO*x*, the photocatalytic activity of the EY–Pt system is 21.5 μmol, whereas in the absence of EY, no hydrogen is produced from the RGO24/Pt system. This suggests that the visible light activity is comes from the EY sensitization. When GO is added to the EY solution, the photocatalytic

Table 2: Adsorbed amount of EY on the surface of GO or RGOx.

sample	GO	RGO4	RGO12	RGO24
amount of adsorbed EY (μmol g^{-1})	11.7	15.0	32. 7	74.3

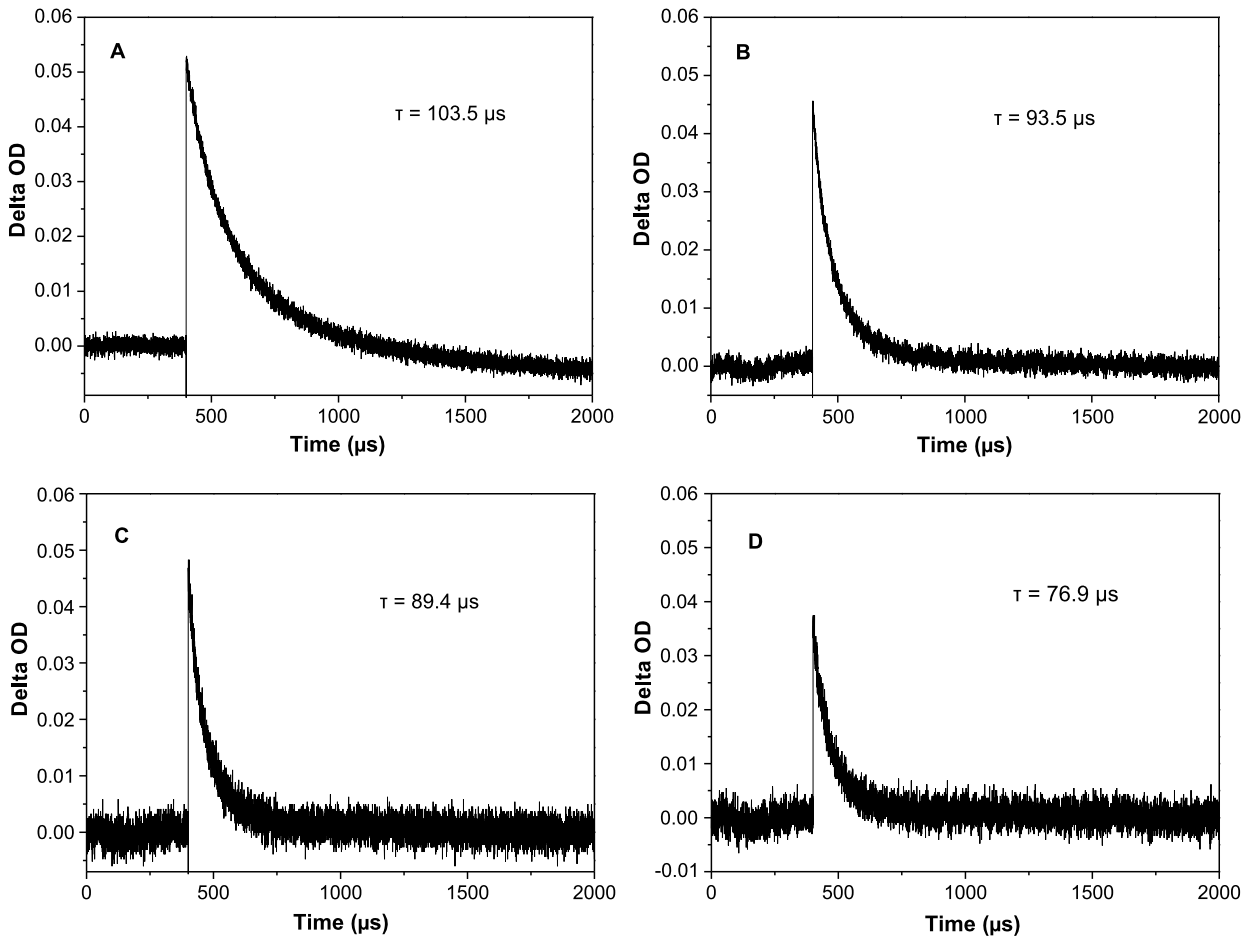

Figure 5: Transient absorption decay of $^3EY^*$ followed at 580 nm for (A) EY, (B) EY−GO, (C) EY−RGO4, and (D) EY−RGO24 under pulse irradiation of 532 nm. Conditions: 30 μg mL^{-1} GO or RGO*x*; 2.0 × 10^{-5} mol L^{-1} EY.

activity is 50.1 μmol. When RGO24 is added, the H_2 evolution reaches 156.8 μmol. The activity increases by a factor of 3.1 compared to the activity of EY-GO/Pt. This result can be attributed to an enhancement of the adsorption quantity of EY on the surface of RGO*x* and the increased electron transfer ability (Table 2 and Figures 2,4,5). However, further irradiation of GO does not lead significant changes of the photocatalytic activity. This may be attributed to a slow increase of the sp^2 domains of RGO*x* after an irradiation time of over 24 h.

We also investigated the effects of the pH value, EY and RGO24 concentration on the photocatalytic activity for hydrogen evolution over EY-RGO24/Pt. Figure 7A shows that the pH value has a remarkable effect on the photocatalytic activity in the presence of TMA as a sacrificial donor. The hydrogen evolution of EY-RGO24/Pt increases with a rise of the pH from 7.0 to 10.0, and then decreases starting at 11.9 (nature pH). When the pH value of the TMA solution is 7.0, no

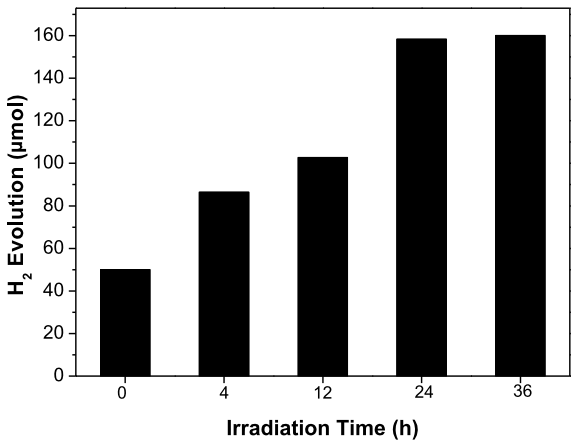

Figure 6: Photocatalytic H_2 evolution of EY sensitized GO and RGO*x*. Conditions: 30 μg mL^{-1} GO or RGO*x*; 1.45 × 10^{-4} mol L^{-1} EY; 4.6 × 10^{-6} mol L^{-1} H_2PtCl_6; 7.7 × 10^{-2} mol L^{-1} TMA, pH 11.9; irradiation 2 h.

hydrogen evolution is observed, because TMA ($pK_b = 4.22$) is completely protonated and $TMAH^+$ cannot act as an effective electron donor [48]. With the pH value increasing, more and more TMA species exists in its molecular form. Thus, the activity increases with the pH value and reaches a maximal value at pH 10.0. However, over pH 10.0, the activity decreases. This is caused by the increasing negativity of the redox potential of H^+/H_2, which is disadvantageous for an efficient generation of hydrogen [49].

Figure 7B displays the effect of the concentration of EY on the photocatalytic activity. The activity increases with increasing concentrations of EY. The maximal activity is at 5.0×10^{-4} mol L^{-1} and then decreases with higher concentrations. When the concentration of EY is 2.0×10^{-5} mol L^{-1}, the amount of generated hydrogen in 2 h is very low, only 0.7 μmol. This may be due to the deceleration of the light absorption of EY by RGO24, which results in the formation of few photo-excited electrons at low concentrations of dye. When the EY concentration increases to 5.0×10^{-4} mol L^{-1}, more and more EY molecules adsorb at RGO24, which can effectively absorb photons and transfer photo-induced electrons into the sp^2 domains of RGO24 for hydrogen evolution. Nevertheless, with a further increase of the concentration of EY, more and more free EY molecules are in solution. These free dye molecules cannot effectively transfer their photo-excited electrons to RGO. Moreover, excess EY in solution may not only screen the light absorption of EY-RGO but also produce self-quenching, which greatly decreases the utilization efficiency of the incident light [20,50]. Thus, the photocatalytic activity decreases at 1.0×10^{-3} mol L^{-1} EY.

Figure 7C shows the influence of the concentration of RGO24 on the activity of hydrogen evolution. The activity enhances with an increase of the RGO24 concentration and then declines. The optimal concentration of RGO24 is 10 μg mL^{-1}, and the corresponding activity for hydrogen evolution is 290 μmol. Its calculated AQY reaches 12.9%, which is much higher than the reported AQY of EY-sensitized RGO obtained by sodium borohydride reduction [20]. The activity decreases notably at higher RGO24 concentrations, which is ascribed to a strong visible light absorption of RGO24 (Figure 1), which shields the absorption of EY.

The wavelength dependence of the photocatalytic H_2 evolution of EY-RGO24/Pt was investigated. Figure 8 displays the AQY for EY-RGO24/Pt as a function of the incident light wavelength. AQY increases with increasing wavelength, the highest AQY is 23.4% at 520 nm, and then it decreases. This corresponds with the absorption wavelength of EY in TMA solution (inset of Figure 8).

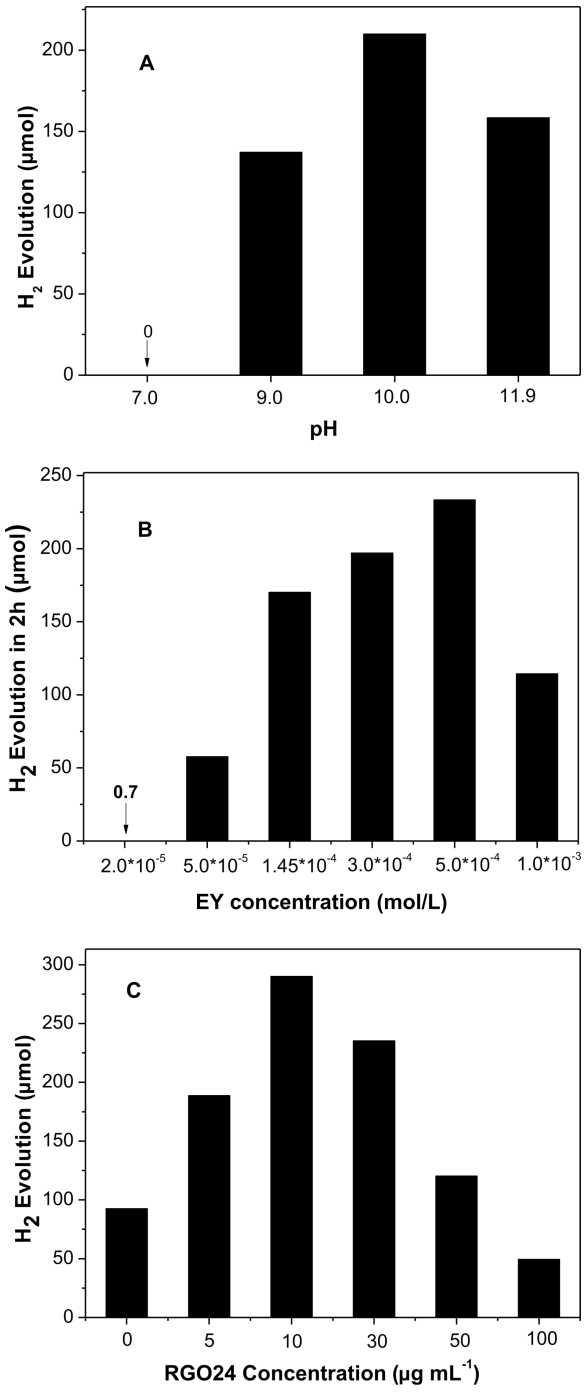

Figure 7: (A) The effect of the pH value on the photocatalytic activity of EY-RGO24/Pt. Conditions: 30 μg mL^{-1} RGO24; 1.45×10^{-4} mol L^{-1} EY; 4.6×10^{-6} mol L^{-1} H_2PtCl_6; 7.7×10^{-2} mol L^{-1} TMA; irradiation 2 h. (B) The effect of the EY concentration on the photocatalytic H_2 evolution over EY-RGO24/Pt. Conditions: 30 μg mL^{-1} RGO24; 4.6×10^{-6} mol L^{-1} H_2PtCl_6; 7.7×10^{-2} mol L^{-1} TMA, pH 10.0; irradiation 2 h. (C) The effect of the RGO24 concentration on the photocatalytic H_2 evolution over EY-RGO24/Pt. Conditions: 5.0×10^{-4} mol L^{-1} EY; 4.6×10^{-6} mol L^{-1} H_2PtCl_6; 7.7×10^{-2} mol L^{-1} TMA, pH 10.0; irradiation 2 h.

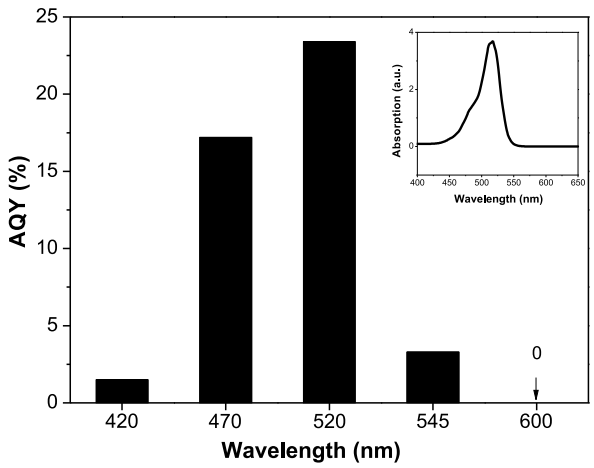

Figure 8: AQY of the EY-RGO24/Pt photocatalyst plotted as a function of the wavelength of the incident light. Conditions: 10 μg mL^{-1} RGO24; 5.0 × 10^{-4} mol L^{-1} EY; 4.6 × 10^{-6} mol L^{-1} H_2PtCl_6; 7.7 × 10^{-2} mol L^{-1} TMA, pH 10.0; irradiation 2 h. The inset is the UV–vis absorption spectrum of EY in TMA solution.

Mechanism

When GO is irradiated by UV light, holes h^+ (in HOMO) and electrons e^- (in LUMO) are produced in its π-conjugated domains due to π–π* band excitation [35]. These holes (h^+) and electrons (e^-) react with the oxygen-containing groups of GO sheets, e.g., the epoxy groups. The reactions can be expressed as follows [51]:

$$\mathrm{C-O-C\ (GO)} + 2\mathrm{H^+} + 2\mathrm{e^-} \rightarrow \mathrm{C-C\ (defect\ carbon)} + \mathrm{H_2O} \quad (1)$$

$$\mathrm{C-O-C\ (GO)} + \mathrm{H_2O} + 2\mathrm{h^+} \rightarrow \mathrm{C\ (defect\ carbon)} + \mathrm{CO_2} + 2\mathrm{H^+} \quad (2)$$

Similarly, photoreactions of the hydroxy group of the GO can be described by the following reactions:

$$\mathrm{C-OH} + \mathrm{H_2O} + 3\mathrm{h^+} \rightarrow \mathrm{CO_2} + 3\mathrm{H^+} \quad (3)$$

$$\mathrm{C-OH} + \mathrm{H^+} + \mathrm{e^-} \rightarrow \mathrm{C\ (defect\ carbon)} + \mathrm{H_2O} \quad (4)$$

For the C=O and O=C–OH groups of GO, similar reactions take place to form defect carbon atoms. In our irradiation system for GO, due to the presence of O_2 (see Experimental section), the solved O_2 would trap the electrons:

$$\mathrm{O_2} + \mathrm{e^-} \rightarrow \mathrm{O_2^-} \quad (5)$$

The formed O_2^- is a strong oxidant which can also oxidize the oxygen-containing groups to form CO_2 and defect carbon atoms. However, at a later stage of the reaction, the oxidation action decreases, as more and more O_2 is consumed in the closed reaction system.

The formed defect carbons (radicals) are active, and are expected to react to form C=C. As shown in Scheme 1, π-conjugated domains extend, which is consistent with the results shown in Figure 1 and Figure 2. At the same time , many holes in RGO*x* sheets occur caused by the oxidation of the holes and O_2^- produced by the UV excitation. Figure 9A and Figure 9B show the morphology change of GO before and after the photoreaction. Before the irradiation, GO are complete sheets except for a few wrinkles. After the irradiation, many small holes occur in the RGO24 sheet (Figure 9B), which is consistent with the model shown in Scheme 1. The model is similar to the one reported in [51].

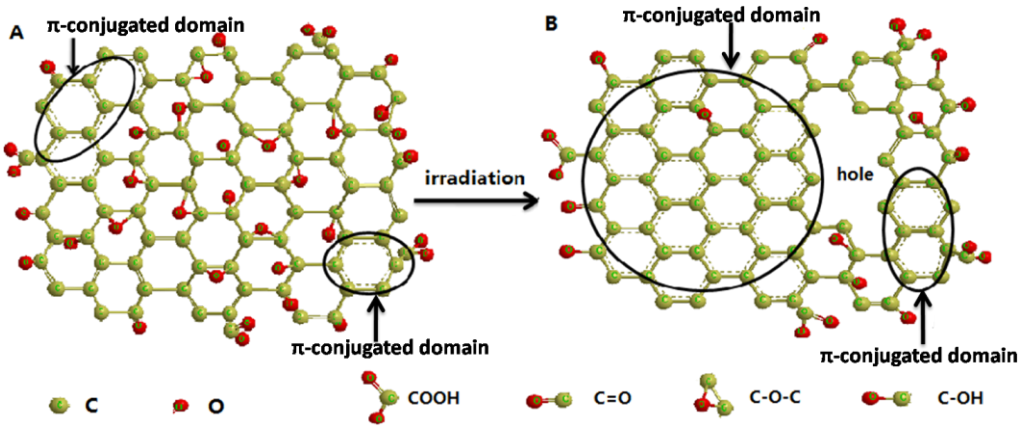

Scheme 1: Schematic diagram of the reduction of GO by irradiation.

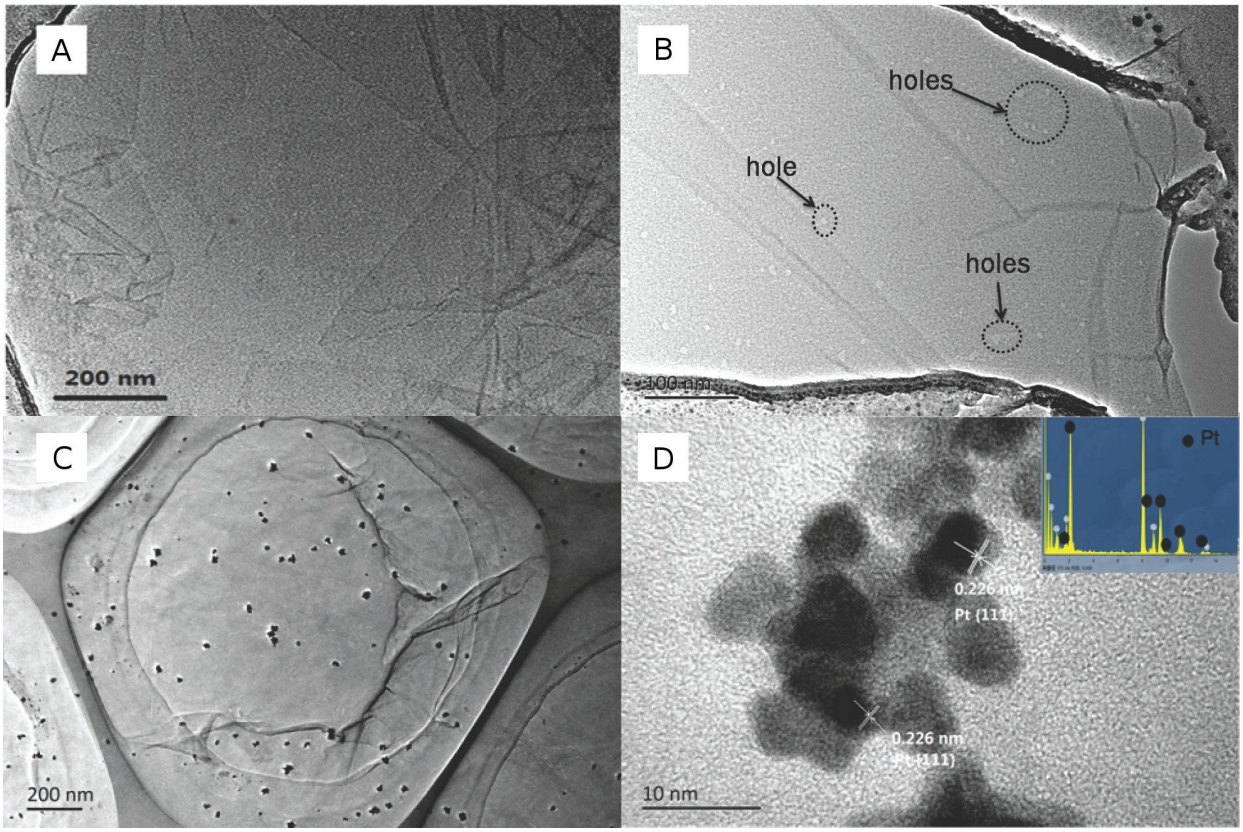

Figure 9: TEM images of GO (A), RGO24 (B), RGO24 with deposited Pt (C), and HRTEM image of deposited Pt (D). The inset of Figure 9D is the EDS spectrum.

The ferromagnetic properties [51] of RGO obtained by a photoreaction and its paramagnetic resonance (EPR) spectra [38] indicate that there are some radicals or defect carbons at the zigzag hole edges of the RGO. The defect carbons or radicals are stable due to larger π-conjugated domains, which are expected to exist for a long time at room temperature [38,52].

When EY adsorbed at RGO*x* absorbs the visible light, the excited EY^* forms by transferring its HOMO electron to the LUMO. The formed EY^* injects its electron into the RGO*x* to produce EY^+. The electron can be transferred to the radicals or defect carbons of RGO*x* via the π-conjugated domains (higher conductivity) to form $RGOx^-$ ions. Then, EY^+ is transformed into EY by the electron donor TMA. These processes can be described by the following reactions.

$$EY + h\nu \rightarrow EY^* \quad (6)$$

$$EY^* + RGOx \rightarrow RGOx^- + EY^+ \quad (7)$$

$$EY^+ + TMA \rightarrow EY + TMA_{OX} \quad (8)$$

The formed $RGOx^-$ can reduce $PtCl_6^{2-}$ at the zigzag edges of the RGO*x*.

$$PtCl_6^{2-} + 4RGOx^- \rightarrow Pt + RGOx + 6Cl^- \quad (9)$$

Figure 9C shows the Pt nanoparticles deposited on the surface of RGO24 by an in situ photoreduction of H_2PtCl_6 with EY sensitization. It clearly displays the uniform Pt aggregated nanograins with a diameter of 24–30 nm. High-resolution TEM (Figure 9D) shows that the Pt nanograins consists of small Pt nanoparticles with a diameter of about 5 nm. The lattice spacing of 0.226 nm could be indexed to the {111} planes of Pt. After the Pt deposition, the electron from the excited EY can transfer to the radicals or defect carbons to form $RGOx^-$ ions, which would be trapped by the deposited Pt to reduce water into H_2.

$$2RGOx^- + 2H_2O \rightarrow 2RGOx + H_2 + 2OH^- \text{ on Pt} \quad (10)$$

The possible mechanism for the photocatalytic H_2 evolution in a EY-RGO*x*/Pt system is described by Scheme 2.

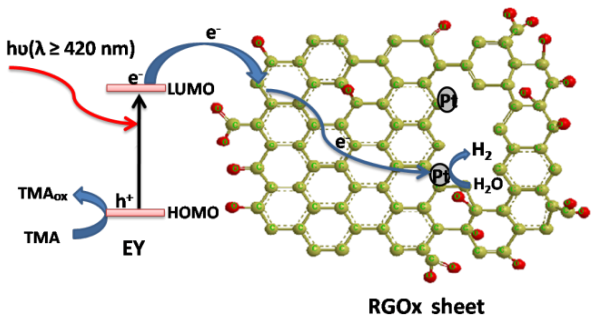

Scheme 2: Proposed mechanism for the photocatalytic hydrogen evolution of a EY-RGO*x*/Pt system under visible light irradiation.

Conclusion

In summary, RGO*x* was prepared by a simple photoreaction through controlling irradiation time. After the irradiation, the epoxy, carbonyl and hydroxy groups of GO are gradually removed, sp^2 π-conjugated domains increase, and the formed RGO sheets have holes. The conductivity of RGO*x* and the adsorption amount of EY on the surface of RGO*x* increase with the irradiation time. The two factors lead to the enhancement of the photocatalytic hydrogen evolution over EY-RGO/Pt with increasing irradiation time. The maximal apparent quantum yield of EY-RGO24/Pt for hydrogen evolution is up to 12.9% under visible light irradiation (λ ≥ 420 nm), and 23.4% under monochromatic light irradiation at 520 nm.

Experimental

Preparation of GO

All the reagents were of analytical grade except EY (bioreagent) and were used without further purification. Graphite oxide was synthesized from natural flake graphite powder (Sinopharm Chemical Reagent Co. Ltd) by the modified Hummers method [53,54]. In a typical method, natural graphite (2 g), $NaNO_3$ (1 g), and H_2SO_4 (46 mL) were mixed in an ice bath, then $KMnO_4$ (6 g) was slowly added to this mixture, and was stirred continuously for 30 min. Then the resulting mixture was heated to a temperature of 35 °C and was stirred for 2 h. 90 mL of distilled water was added slowly to the mixture for 20 min. Then the mixture was rapidly heated to 98 °C and kept stirring for 15 min. 144 mL of distilled water and 20 mL of H_2O_2 were added to the mixture. After the reaction, the obtained yellow-brown dispersion of graphite oxide was washed with 5% HCl and water until pH 5 and dried in an oven at 60 °C. 0.5 g of graphite oxide powder was added into 1 L of distilled water, and the dispersion was treated with ultrasound (KQ-800KDB, KunShan Ultrasonic Instrument Co. Ltd) for 2 h until the solution became clear to obtain a graphene oxide (GO) solution.

Photoreaction of GO

100 mL of GO solution (0.5 mg mL^{-1}) in a sealed Pyrex flask with a flat window was irradiated with a Xenon lamp (XQ350, ShangHai LanSheng Electronics Co. Ltd.). The headspace of the flask is air. The irradiation time was 4, 12, 24 and 36 h, respectively. The obtained reduced graphene oxide solution is denoted as RGO*x*, where *x* represents the reaction time in hours. In order to characterize the performance of RGO*x*, its powder (denoted as RGO*x*-p) was obtained by centrifuging at 12000 rpm for 30 min and drying at 120 °C.

Characterization methods

An X-ray photoelectron spectrometer (XPS) was used to analyze GO and RGO*x* on an ESCALAB250xi equipped with a Mg Kα X-ray source. The C1s peak set at 284.8 eV was used as an internal reference for the absolute binding energy. Attenuated total reflection infrared (ATR-IR) spectra were recorded on a FTIR Nicolet 5700 spectrometer equipped with a ZnSe crystal horizontal ATR unit. UV–vis absorption spectra were measured on a Hitachi U-3310 spectrophotometer with distilled water for reference. The fluorescence spectra were measured on a Hitachi F-7000 fluorescence spectrophotometer. The transmission electron microscopy (TEM) and high-resolution TEM (HRTEM) images were taken on a JEOL JEM-2010 (TEM) equipped with an energy dispersive spectrometer (EDS).

Electrochemical impedance spectroscopy (EIS) was measured on an IVIUMSTAT electrochemical workstation (Netherlands). The electrochemical experiments were performed in a 3-compartment cell with a glassy carbon electrode (diameter 2 mm) as the working electrode, a platinum wire as the counter electrode, and an Ag/AgCl electrode as the reference electrode. The electrolyte was a solution of 0.1 M phosphate buffer solution (PBS, pH 7), 0.1 M KCl, 10 mM $K_3Fe(CN)_6$ and 10 mM $K_4Fe(CN)_6$.

Adsorption amounts of EY on GO and RGO*x* were measured as follows: 6 mL of GO or RGO*x* solution (0.5 mg mL^{-1}) and 0.5 mL of 1 mM EY were added into trimethylamine (TMA) solution (93.5 mL, 7.7×10^{-2} mol L^{-1}). The mixture was stirred for 5 h at room temperature in the dark, and then centrifuged at 12000 rpm for 45 min to remove RGO*x* or GO with EY. The EY concentration of the supernatant was measured on the spectrophotometer. The adsorption amount of EY onto RGO*x* was calculated based on the concentration difference (ΔC) before and after the mixing.

Transient absorption decay measurements for $^3EY^*$ were performed on a LP-920 laser flash photolysis spectrometer (Edinburgh). The excitation pulses were obtained from the unfocused second harmonic (532 nm) output of a Nd:YAG laser

(Brilliant b), the probe light was provided by a Xenon short arc lamp (450 W). The measured aqueous solution was prepared as follows: 6 mL of GO or RGO*x* solution (0.5 mg mL^{-1}), 0.2 mL of 10 mM EY and distilled water were added to keep the volume 100 mL, and then the mixtures were stirred for 30 min at room temperature. The dispersion was transferred to a cuvette with a cover, and then aerated for 20 min with nitrogen gas before measurements.

Photocatalytic H_2 evolution

Photocatalytic H_2 evolution activity was evaluated in a similar manner as described in [18]. The photocatalytic reaction was carried out in a 190 mL Pyrex cell with a side flat window at room temperature (an efficient irradiation area of ca. 16.9 cm^2). A high pressure Hg lamp (400 W) was used as the light source, equipped with a cutoff filter ($\lambda \geq 420$ nm) to remove radiation below 420 nm. The IR fraction of the beam was removed by means of a cool water filter to ensure an illumination with visible light only. In a typical photocatalytic experiment, 6 mL of GO or RGO*x* solution (0.5 mg mL^{-1}), 1.45 mL of 10 mM EY solution, and 0.24 mL of 1.93 mM H_2PtCl_6 aqueous solution were added to 92.3 mL of TMA solution. Before irradiation, the suspension of the catalyst was bubbled with N_2 for 30 min to completely remove oxygen. Sampling was operated intermittently through the septum during experiments. The amount of photocatalytic hydrogen evolution for 2 h of irradiation was determined on a gas chromatograph (TCD, 13X molecular sieve column, N_2 as gas carrier).

The average photon flux of the incident light determined on an FGH-1 Ray virtual radiation actinometer (light spectrum: 400–700 nm) was 363 μmol m^{-2} s^{-1}. The apparent quantum yield (AQY) was calculated according to the following equation.

$$\text{AQY}\ [\%] = 2 \times \frac{\text{mol of hydrogen evolved}}{\text{mol of incident photons}} \times 100$$

The quantum yields under monochromatic light irradiation were also measured by using various monochromatic LED lamps (UVEC-4, Shenzhen LAMPLIC Science Co.Ltd, China) as light sources. The apparent quantum yields were based on the amount of produced hydrogen for 2 h irradiation by using various LED lamps. All other reaction conditions except the light resources were identical to the conditions of the photocatalytic reaction.

Acknowledgements

This work was supported by the National Nature Science Foundation of China (No.20763006) and the National Basic Research Program of China (2009CB220003).

References

1. Zhang, W.; Wang, Y. B.; Wang, Z.; Zhong, Z. Y.; Xu, R. *Chem. Commun.* **2010,** *46,* 7631–7633. doi:10.1039/c0cc01562h
2. Wei, L.; Chen, Y. J.; Zhao, J. L.; Li, Z. H. *Beilstein J. Nanotechnol.* **2013,** *4,* 949–955. doi:10.3762/bjnano.4.107
3. Yao, W. F.; Huang, C. P.; Muradov, N.; T-Raissi, A. *Int. J. Hydrogen Energy* **2011,** *36,* 4710–4715. doi:10.1016/j.ijhydene.2010.12.124
4. Kozlova, E. A.; Vorontsov, A. V. *Int. J. Hydrogen Energy* **2010,** *35,* 7337–7343. doi:10.1016/j.ijhydene.2010.04.122
5. Pan, X.; Zhao, Y.; Liu, S.; Korzeniewski, C. L.; Wang, S.; Fan, Z. Y. *ACS Appl. Mater. Interfaces* **2012,** *4,* 3944–3950. doi:10.1021/am300772t
6. Liang, Y. Y.; Wang, H. L.; Sanchez Casalongue, H.; Chen, Z.; Dai, H. J. *Nano Res.* **2010,** *3,* 701–705. doi:10.1007/s12274-010-0033-5
7. Bai, X. J.; Wang, L.; Zong, R. L.; Lv, Y.; Sun, Y.; Zhu, Y. F. *Langmuir* **2013,** *29,* 3097–3105. doi:10.1021/la4001768
8. Kim, H.-i.; Moon, G.-h.; Monllor-Satoca, D.; Park, Y.; Choi, W. Y. *J. Phys. Chem. C* **2012,** *116,* 1535–1543. doi:10.1021/jp209035e
9. Wan, X.; Long, G.; Huang, L.; Chen, Y. *Adv. Mater.* **2011,** *23,* 5342–5358. doi:10.1002/adma.201102735
10. Xiang, Q. J.; Yu, J. G.; Jaroniec, M. *Chem. Soc. Rev.* **2012,** *41,* 782–796. doi:10.1039/c1cs15172j
11. Yoo, E. J.; Okata, T.; Akita, T.; Kohyama, M.; Nakamura, J.; Honma, I. *Nano Lett.* **2009,** *9,* 2255–2259. doi:10.1021/nl900397t
12. Yeh, T.-F.; Syu, J.-M.; Cheng, C.; Chang, T.-H.; Teng, H. S. *Adv. Funct. Mater.* **2010,** *20,* 2255–2262. doi:10.1002/adfm.201000274
13. Li, Y. X.; Guo, M. M.; Peng, S. Q.; Lu, G. X.; Li, S. B. *Int. J. Hydrogen Energy* **2009,** *34,* 5629–5636. doi:10.1016/j.ijhydene.2009.05.100
14. Li, Q. Y.; Lu, G. X. *J. Mol. Catal. A: Chem.* **2006,** *266,* 75–79. doi:10.1016/j.molcata.2006.10.047
15. Xu, J. Y.; Li, Y. X.; Peng, S. Q.; Lu, G. X.; Li, S. B. *Phys. Chem. Chem. Phys.* **2013,** *15,* 7657–7665. doi:10.1039/c3cp44687e
16. Liu, X.; Li, Y. X.; Peng, S. Q.; Lu, G. X.; Li, S. B. *Photochem. Photobiol. Sci.* **2013,** *12,* 1903–1910. doi:10.1039/c3pp50167a
17. Li, Q. Y.; Jin, Z. L.; Peng, Z. G.; Li, Y. X.; Li, S. B.; Lu, G. X. *J. Phys. Chem. C* **2007,** *111,* 8237–8241. doi:10.1021/jp068703b
18. Liu, X.; Li, Y. X.; Peng, S. Q.; Lu, G. X.; Li, S. B. *Int. J. Hydrogen Energy* **2012,** *37,* 12150–12157. doi:10.1016/j.ijhydene.2012.06.028
19. Mou, Z. G.; Dong, Y. P.; Li, S. J.; Du, Y.; Wang, X.; Yang, P.; Wang, S. *Int. J. Hydrogen Energy* **2011,** *36,* 8885–8893. doi:10.1016/j.ijhydene.2011.05.003
20. Min, S. X.; Lu, G. X. *J. Phys. Chem. C* **2011,** *115,* 13938–13945. doi:10.1021/jp203750z
21. Min, S. X.; Lu, G. X. *Int. J. Hydrogen Energy* **2013,** *38,* 2106–2116. doi:10.1016/j.ijhydene.2012.11.124
22. Geim, A. K. *Science* **2009,** *324,* 1530–1534. doi:10.1126/science.1158877
23. Zhang, Y.; Tan, Y. W.; Stormer, H. L.; Kim, P. *Nature* **2005,** *438,* 201–204. doi:10.1038/nature04235
24. Stoller, M. D.; Park, S.; Zhu, Y.; An, J.; Ruoff, R. S. *Nano Lett.* **2008,** *8,* 3498–3502. doi:10.1021/nl802558y
25. Allen, M. J.; Tung, V. C.; Kaner, R. B. *Chem. Rev.* **2010,** *110,* 132–145. doi:10.1021/cr900070d

26. Balandin, A. A.; Ghosh, S.; Bao, W.; Calizo, I.; Teweldebrhan, D.; Miao, F.; Lau, C. N. *Nano Lett.* **2008,** *8,* 902–907. doi:10.1021/nl0731872
27. Xu, L. Q.; Wang, L.; Zhang, B.; Lim, C. H.; Chen, Y.; Neoh, K.-G.; Kang, E. T.; Fu, G. D. *Polymer* **2011,** *52,* 2376–2383. doi:10.1016/j.polymer.2011.03.054
28. Ganguly, A.; Sharma, S.; Papakonstantinou, P.; Hamilton, J. *J. Phys. Chem. C* **2011,** *115,* 17009–17019. doi:10.1021/jp203741y
29. Williams, G.; Seger, B.; Kamat, P. V. *ACS Nano* **2008,** *7,* 1487–1491. doi:10.1021/nn800251f
30. Li, H. L.; Pang, S. P.; Feng, X. L.; Bubeck, C. *Chem. Commun.* **2010,** *46,* 6243–6245. doi:10.1039/c0cc01098g
31. Zhang, H. H.; Liu, Q.; Feng, K.; Chen, B.; Tung, C.-H.; Wu, L. Z. *Langmuir* **2012,** *28,* 8224–8229. doi:10.1021/la301429g
32. Liu, R. J.; Li, S. W.; Yu, X. L.; Zhang, G. J.; Zhi, L. J. *J. Mater. Chem.* **2012,** *22,* 3319–3322. doi:10.1039/c2jm15875b
33. Xiang, Q. J.; Yu, J. G.; Jaroniec, M. *J. Phys. Chem. C* **2011,** *115,* 7355–7363. doi:10.1021/jp200953k
34. Tung, V. C.; Allen, M. J.; Yang, Y.; Kaner, R. B. *Nat. Nanotechnol.* **2009,** *4,* 25–29. doi:10.1038/nnano.2008.329
35. Li, D.; Müller, M. B.; Gilje, S.; Kaner, R. B.; Wallace, G. G. *Nat. Nanotechnol.* **2008,** *3,* 101–105. doi:10.1038/nnano.2007.451
36. Skoog, D. A.; Haller, F. J.; Niemann, T. A. *Principles of Instrumental Analysis;* Hartcourt Brace & Company: Philadelphia, 1998.
37. Karousis, N.; Economopous, S. P.; Sarantopoulou, E.; Tagmatarchis, N. *Carbon* **2010,** *48,* 854–860. doi:10.1016/j.carbon.2009.10.039
38. Hou, X. L.; Li, J. L.; Drew, S. C.; Tang, B.; Sun, L.; Wang, X. G. *J. Phys. Chem. C* **2013,** *117,* 6788–6793. doi:10.1021/jp311727t
39. Li, J. F.; Lin, H.; Li, J. B. *Carbon* **2011,** *49,* 3024–3030. doi:10.1016/j.carbon.2011.03.022
40. Matsumoto, Y.; Koinuma, M.; Kim, S. Y.; Watanabe, Y.; Taniguchi, T.; Hatakeyama, K.; Tateishi, H.; Ida, S. *ACS Appl. Mater. Interfaces* **2010,** *12,* 3461–3466. doi:10.1021/am100900q
41. Stankovich, S.; Dikin, D. A.; Piner, R. D.; Kohlhaas, K. A.; Kleinhammes, A.; Jia, Y. Y.; Wu, Y.; Nguyen, S. B.; Ruoff, R. S. *Carbon* **2007,** *45,* 1558–1565. doi:10.1016/j.carbon.2007.02.034
42. Akhavan, O.; Abdolahad, M.; Esfandiar, A.; Mohatashamifar, M. *J. Phys. Chem. C* **2010,** *114,* 12955–12959. doi:10.1021/jp103472c
43. Casero, E.; Parra-Alfambra, A. M.; Petit-Domínguez, M. D.; Pariente, F.; Lorenzo, E.; Alonso, C. *Electrochem. Commun.* **2012,** *20,* 63–66. doi:10.1016/j.elecom.2012.04.002
44. Guo, S.; Dong, S. *Chem. Soc. Rev.* **2011,** *40,* 2644–2672. doi:10.1039/c0cs00079e
45. Shimidzu, T.; Iyoda, T.; Koide, Y. *J. Am. Chem. Soc.* **1985,** *107,* 35–41. doi:10.1021/ja00287a007
46. Moser, J.; Graetzel, M. *J. Am. Chem. Soc.* **1984,** *106,* 6557–6564. doi:10.1021/ja00334a017
47. Fisher, G. J.; Lewis, C.; Madill, D. *Photochem. Photobiol.* **1976,** *24,* 223–228. doi:10.1111/j.1751-1097.1976.tb06815.x
48. Lee, J.; Choi, W. Y. *Environ. Sci. Technol.* **2004,** *38,* 4026–4033. doi:10.1021/es034954b
49. Lazarides, T.; McCormick, T.; Du, P. W.; Luo, G. G.; Lindley, B.; Eisenberg, R. *J. Am. Chem. Soc.* **2009,** *131,* 9192–9194. doi:10.1021/ja903044n
50. Fu, N.; Lu, G. X. *Chem. Commun.* **2009,** 3591–3593. doi:10.1039/b906073a
51. Matsumoto, Y.; Koinuma, M.; Ida, S.; Hayami, S.; Taniguchi, T.; Hatakeyama, K.; Tateishi, H.; Watanabe, Y.; Amano, S. *J. Phys. Chem. C* **2011,** *115,* 19280–19286. doi:10.1021/jp206348s
52. Radovic, L. R.; Silva-Villalobos, A. F.; Silva-Tapia, A. B.; Vallejos-Burgos, F. *Carbon* **2011,** *49,* 3471–3487. doi:10.1016/j.carbon.2011.04.046
53. Hummers, W. S., Jr..; Offeman, R. E. *J. Am. Chem. Soc.* **1958,** *80,* 1339. doi:10.1021/ja01539a017
54. Kovtyukhova, N.; Ollivier, P.; Martin, B. R.; Mallouk, T. E.; Chizhik, S. A.; Buzaneva, E. V.; Gorchinskiy, A. D. *Chem. Mater.* **1999,** *11,* 771–778. doi:10.1021/cm981085u

License and Terms

This is an Open Access article under the terms of the Creative Commons Attribution License (http://creativecommons.org/licenses/by/2.0), which permits unrestricted use, distribution, and reproduction in any medium, provided the original work is properly cited.

The license is subject to the *Beilstein Journal of Nanotechnology* terms and conditions: (http://www.beilstein-journals.org/bjnano)

The definitive version of this article is the electronic one which can be found at: doi:10.3762/bjnano.5.92

Beilstein Journal of Nanotechnology

Optical modeling-assisted characterization of dye-sensitized solar cells using TiO_2 nanotube arrays as photoanodes

Jung-Ho Yun*[1], Il Ku Kim[2], Yun Hau Ng*[3], Lianzhou Wang[1] and Rose Amal[3]

Full Research Paper

Open Access

Address:
[1]Nanomaterials Centre, School of Chemical Engineering, University of Queensland, St Lucia QLD 4072, Australia, [2]School of Mathematics and Physics, University of Queensland, St Lucia QLD 4072, Australia, and [3]School of Chemical Engineering, University of New South Wales, Kensington NSW 2052, Australia

Email:
Jung-Ho Yun* - j.yun1@uq.edu.au;
Yun Hau Ng* - yh.ng@unsw.edu.au

* Corresponding author

Keywords:
charge generation; dye-sensitized solar cells; generalized transfer matrix method; optical process; photocatalysis; TiO_2 nanotubes

Beilstein J. Nanotechnol. **2014,** *5,* 895–902.
doi:10.3762/bjnano.5.102

Received: 20 January 2014
Accepted: 27 May 2014
Published: 24 June 2014

This article is part of the Thematic Series "Photocatalysis".

Guest Editor: R. Xu

© 2014 Yun et al; licensee Beilstein-Institut.
License and terms: see end of document.

Abstract

Photovoltaic characteristics of dye-sensitized solar cells (DSSCs) using TiO_2 nanotube (TNT) arrays as photoanodes were investigated. The TNT arrays were 3.3, 11.5, and 20.6 μm long with the pore diameters of 50, 78.6, and 98.7 nm, respectively. The longest TNT array of 20.6 μm in length showed enhanced photovoltaic performances of 3.87% with significantly increased photocurrent density of 8.26 $mA{\cdot}cm^{-2}$. This improvement is attributed to the increased amount of the adsorbed dyes and the improved electron transport property with an increase in TNT length. The initial charge generation rate was improved from 4×10^{21} $s^{-1}{\cdot}cm^{-3}$ to 7×10^{21} $s^{-1}{\cdot}cm^{-3}$ in DSSCs based on optical modelling analysis. The modelling analysis of optical processes inside TNT-based DSSCs using generalized transfer matrix method (GTMM) revealed that the amount of dye and TNT lengths were critical factors influencing the performance of DSSCs, which is consistent with the experimental results.

Introduction

Owing to its chemical durability, non-toxicity, and abundance, TiO_2 has attracted great attention as a good photoelectrode material in dye-sensitized solar cells (DSSCs) [1,2]. In particular, the light harvesting capacity and dye loading, which are the important parameters affecting the amount of photogenerated electron charges for DSSCs performance, can be controlled by the structure and morphology of TiO_2. For instance, roughness-increased surface-structured TiO_2 photoelectrode layers, composed of sub-micrometer sized particulate, 2D-structured, or 1D-structured TiO_2, can improve the light harvesting efficiency by promoting light scattering [3-5]. In addition, the electron transport or recombination rate could be influenced by physical properties such as porosity, morphology, crystallinity, and uniformity of the TiO_2 structure [6-9]. TiO_2 photoelectrode

candidate materials with different structures and morphologies such as mesoporous TiO_2, nanorods, nanotubes, nanosheets and hollow spheres have, therefore, been investigated to improve the performance of DSSCs by using various synthetic and modification methods [4-6,10,11].

Compared to the conventional DSSCs, which employ mesoporous TiO_2 nanoparticles, vertically well-ordered TNT-based DSSCs presented an enhanced electron transport by efficiently reducing the recombination possibility of photogenerated charge carriers through minimizing the trapping sites that normally exist in the grain boundaries of randomly oriented TiO_2 particulate films [12]. Consequently, this enhanced charge transport led to an improvement in the efficiency of light energy conversion. According to Zhu et al., as considering the charge collection efficiency between TiO_2 nanoparticle-based and TNT-based DSSCs with comparable TiO_2 thickness, the TNT-based DSSCs showed a 25 % higher charge collection efficiency than the TiO_2 nanoparticle-based DSSCs. An outstanding optical effect induced by the well-ordered 1D-structure of the TNT array contributed to the improvement of the photovoltaic performance as well [5]. The light that penetrates into the open channels of the TNT array is scattered into deeper sites of the nanotubes, generating larger volume of excited electrons, thus enhancing the light harvesting efficiency in DSSCs [5,13]. Likewise, one of the strategies to improve the photovoltaic performance of the DSSCs is to increase the light harvest by tuning the optical processes in the devices. The optical processes in the solar cells include electric field intensity, charge generation rate, absorption and reflectance at all the interfaces formed between structural layers and electrodes in the devices [14,15]. These optical processes inside the devices can be modeled trough physical and optical parameters of the layers. In this work, the optical modeling study will provide critical insight for the experimental design by understanding the internal optical processes and parameters within the structure. Despite the promising optical properties of TNT arrays, the optical modeling of TNT-based DSSCs has rarely been studied. Thus the experimental work of TNT-based DSSCs coupled with optical modeling will be a good platform to understand the photovoltaic performance of the solar cells. The optical modeling result will provide the important information in assigning major contributing factors in the improvement of DSSC performance.

In this work, we present a comprehensive study on the ruthenium-based N719 dye-sensitized solar cells using TNT photoanodes through experimental work coupled with optical modeling analysis. The photovoltaic performances and electron transport properties of the fabricated DSSCs with different thickness of the TNT photoanodes are investigated. The simplified standard structures under the experimental condition are simulated by using a generalized transfer matrix method (GTMM) [15,16]. The comparison of the experimental results with the optical modeling results presents how charge generation and charge transport are associated with the unique morphological property of 1D-TNT photoanodes when enhancing the photovoltaic performance.

Results and Discussion

TNT-based N719 dye-sensitized solar cells

Prior to fabricating DSSCs, the anodization condition for TNT arrays as photoelectrodes was determined. The lengths of TNT arrays employed in the DSSCs fabrication were 3.3, 11.5, and 20.6 μm with different pore diameters of 50, 78.6, and 98.7 nm, respectively. In Figure 1, TNT-based DSSCs are operated by harvesting light illuminated from a back side passing through Pt-deposited FTO glass, and subsequently the penetrated light is absorbed by dye-sensitized well-ordered TNT arrays.

In Figure 2, the photocurrent density–voltage curves for the TNT-based N719 DSSCs are shown depending on 3.3, 11.5, and 20.6 μm long TNT arrays as photoelectrodes. The DSSC with 3.3 μm long TNT arrays shows a short-circuit density (J_{sc}) of 1.32 mA·cm^{-2}, an open-circuit voltage (V_{oc}) of 0.76 V, and a fill factor (FF) of 0.65, with a solar energy conversion effi-

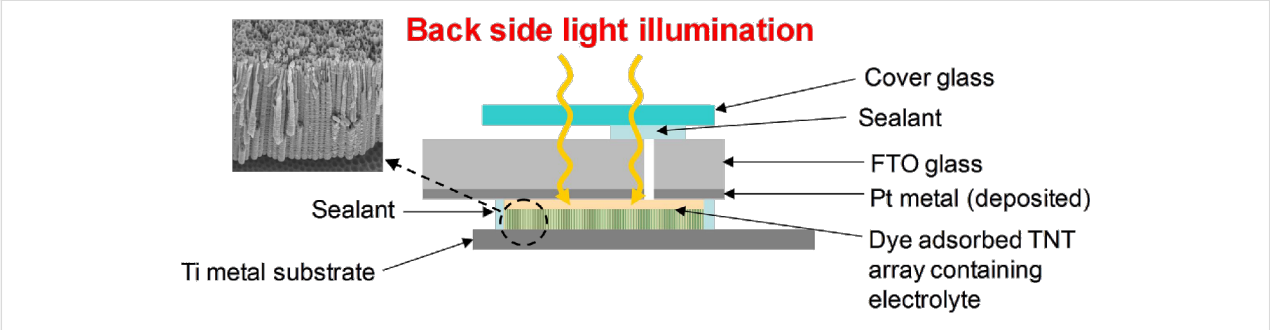

Figure 1: Schematic diagram of TNT-based DSSCs under back side light illumination (Inset SEM image indicates well-ordered TNT arrays prepared by anodization).

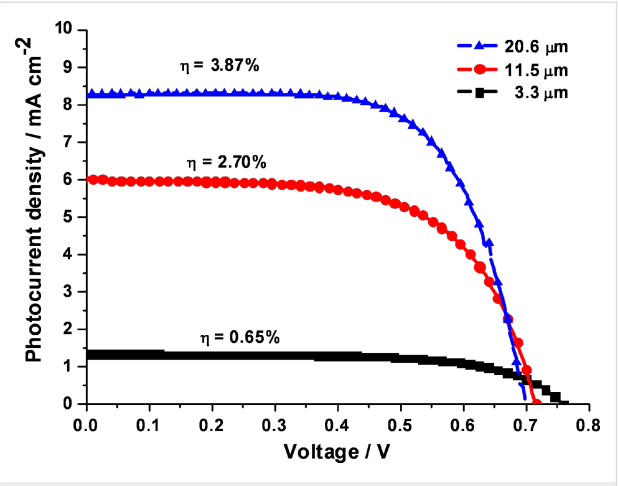

Figure 2: Photocurrent–voltage characteristics of N719-DSSCs fabricated by using 3.3 μm, 11.5 μm, and 20.6 μm TNT arrays under an AM 1.5 solar simulator (100 mW·cm^{-2}).

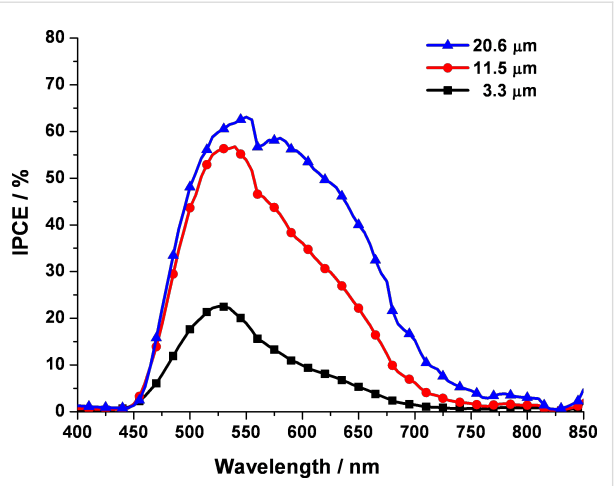

Figure 3: IPCE spectrum of the N719-DSSCs fabricated by using 3.3 μm, 11.5 μm, and 20.6 μm TNT arrays.

ciency of 0.65%. Meanwhile, 11.5 and 20.6 μm long TNT array-based DSSCs exhibited increases in J_{sc} to 6.02 mA·cm^{-2} (FF = 0.62) and 8.26 mA·cm^{-2} (FF = 0.67), respectively, whereas their V_{oc} values were reduced to 0.72 and 0.70 V, respectively. Consequently, in comparison with the photovoltaic performances of the 3.3 μm long TNT-based DSSC, these photovoltaic performances led to enhanced solar energy conversion efficiencies of 2.7% for the 11.5 μm long TNT array-based DSSC and 3.87% for the 20.6 μm long TNT array-based DSSC. Considering the results in Figure 2 and Table 1, the improved J_{sc} with the increase in the lengths of TNT arrays can be attributed to a larger surface area available for the adsorption of larger amounts of dye (Table 1), thus leading to the large amount of photogenerated electrons. Meanwhile, the decreased V_{oc} with the increase in the tube lengths can be explained by the electron dilution effect. The intensity of the penetrated light gradually decreases with an increase in the thickness of an electrode. Therefore, as the tube length increases, the excessive electron density becomes lower, resulting in a lower V_{oc}. The higher series resistance of a longer tube length also influences the reduction of photovoltage [17-19].

As seen in Figure 3, under the short-circuit condition, the incident photon-to-current conversion efficiency (IPCE) measurement was performed on the samples characterized in Figure 2. As the primary IPCE peak of N719-dye sensitized devices is usually observed at a wavelength of approximately 530–550 nm, the IPCE value of the 3.3 μm long TNT array was around 23% in this wavelength range. The increase in tube lengths to 11.5 and 20.6 μm led to the enhancement of the IPCE values to 57% and 63%, respectively. Below 500 nm the IPCE values were rapidly decreasing due to the reduced light absorption by the reflection effect of the electrolyte layer and the Pt deposited FTO glass in the counter electrode through back side illumination [20]. The steady increase in IPCE with longer tube lengths is attributed to the increase in J_{sc} by the increased amount of dyes adsorbed on the longer TNT arrays, followed by a further increase in the overall energy conversion efficiency. In principle, the IPCE depends on the light harvesting efficiency (LHE), the efficiency of electron injection from the photoexcited dye into the TiO_2 conduction band (η_{inj}), and the efficiency of charge collection at contacts (η_{cc}) (Equation 1).

$$\text{IPCE} = \text{LHE} \times \eta_{inj} \times \eta_{cc} \quad (1)$$

Herein, the LHE is determined by the amount of adsorbed dye, which is proportional to the tube length, and the light scattering effect that depends on film thickness and morphology [5,21,22].

Table 1: Photovoltaic performances of N719-DSSCs using different TNT arrays under an AM 1.5 solar simulator.

TNT length (μm)	V_{oc} (V)	J_{sc} (mA·cm^{-2})	FF	efficiency η (%)	dye loading (μM·cm^{-2})	pore volume (× 10^{-5} cm^3)
3.3	0.76	1.32	0.65	0.65	20	5.94
11.5	0.72	6.02	0.62	2.70	38	12.36
20.6	0.70	8.26	0.67	3.87	59	28.24

Zhu et al. studied the differences of LHE between TNT-based DSSCs and TiO_2 nanoparticle-based DSSCs. With comparable dye coverage and redox electrolyte composition on the different TiO_2 electrodes, the TNT-based DSSCs showed an enhanced LHE value, which was ascribed to enhanced channeled light scattering in the TNT array with respect to that in the TiO_2 nanoparticulate film [5]. Taking these results into account, the TNT morphology is beneficial to enhance the photovoltaic performances in the DSSCs by facilitating light scattering effects while enabling the manipulation of the tube length to accommodate for larger amounts of dye.

For the understanding and characterization of the fundamental photovoltaic parameters of the DSSCs, electrochemical impedance spectroscopy (EIS) offers valuable information. Figure 4 shows the Bode phase plots and the Nyquist plots obtained from electron transfer at the TiO_2 and electrolyte interface under a solar simulator of AM 1.5. Figure 4a shows the negative shift of the frequencies of the main peaks with an increase in the lengths of TNT arrays. The peak frequencies were 16.7, 7.68, and 3.94 Hz with 3.3, 11.5, and 20.6 µm long TNT-based DSSCs, respectively. These peak frequencies in the Bode plot and the large semicircles in the Nyquist plot seen in Figure 4b are derived from the charge transfer reaction at the dye-sensitized TNT and electrolyte interface, whereas the smaller semicircle of the two semicircles in the Nyquist plots is attributed to the redox reaction at the electrolyte and counter electrode interface. In the meantime, the series resistance values of the DSSCs using 3.3, 11.5, and 20.6 µm long TNT arrays were 5.48, 5.86, and 6.51 Ω, respectively, indicating the series resistance obtained from EIS analysis is closely related to the thickness of the TiO_2 films. It is clear that the series resistance increases with the increase in the length of the TNT arrays. This is confirmed by the result that the low V_{oc} value observed for the DSSC, which uses the long TNT array, shown in Figure 2, was due to the high series resistance. From the EIS results, furthermore, the electron lifetime of the 20.6 µm long TNT-based DSSCs with a lower peak frequency was longer than those of DSSCs using shorter TNT arrays (3.3 and 11.5 µm in length) with relatively high peak frequencies (Equation 2). The elongation of electron lifetime in the longer TNT arrays can be attributed to an increase in the electron retention time, accompanied by an increase in electron diffusion length from Equation 3.

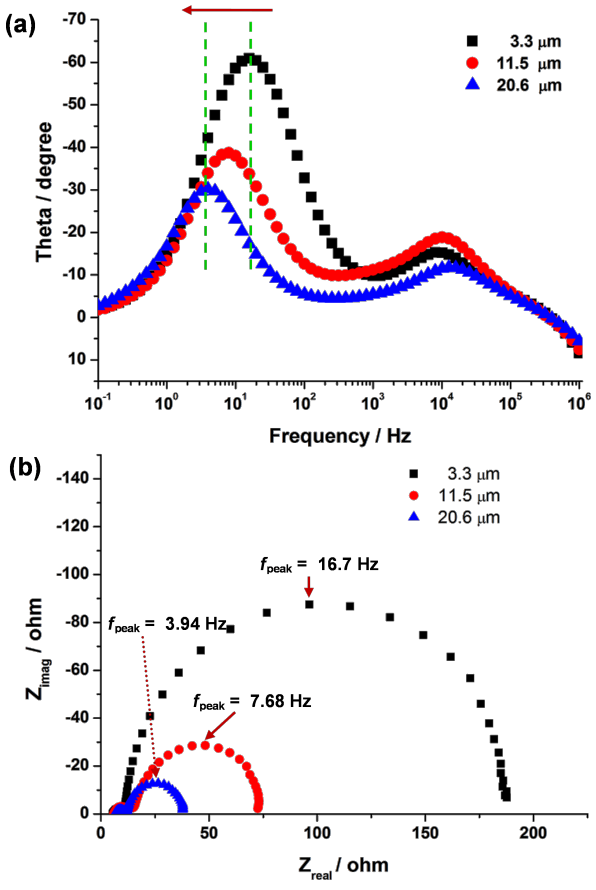

Figure 4: Experimental impedances of the N719-DSSCs fabricated using 3.3 µm, 11.5 µm, and 20.6 µm TNT arrays. (a) Bode phase plots and (b) Nyquist plots.

$$\tau = f_{\text{peak}}^{-1} \tag{2}$$

$$L = \left(D \cdot \tau\right)^{1/2} \tag{3}$$

where τ, f_{peak}, L, and D represent the electron lifetime in TiO_2, the peak frequency of a large semicircle in Figure 4a, the electron diffusion length, and the diffusion coefficient, respectively.

Optical modeling of TNT-based dye-sensitized solar cells

The generalized transfer matrix method (GTMM) has been applied to calculate and analyze the interference effect by multilayers in solar cells [15]. The optical modeling using GTMM provides reliable information about the spatial distribution of the electric field intensity and the internal light absorption efficiency of the solar cells with mixed coherent and incoherent multi-layers [16]. The electric field intensity and charge generation rate as a function of the thickness of multi-layers and light fraction intensity were calculated based on Equations 4–6 according to Burkhard et al. [15]. For this, the only needed term of the optical constants is the imaginary part, k.

$$k = \lambda\alpha/4\pi \tag{4}$$

where λ is the wavelength of light and α the absorption coefficient. α is related to the optical density and the transmitted intensity by,

$$\alpha = \left(\text{optical density}\right) \ln\left(10\right)/x \quad (5)$$

$$I/I_0 = e^{-ax} \quad (6)$$

where I/I_0 is the fraction of light that remains after passing through the film and x is the layer thickness.

Figure 5 shows the calculated electric field intensity of the DSSCs with different TNT lengths by using GTMM. The electric field formed between active layers of solar cells triggers the charge separation of electron and hole generated in the solar cell system. The electric field intensity in Figure 5a shows the behavior of charge separation occurring at an interface between multi-layers as a function of the position in the device. The position in the device refers to the distance from the first layer (Pt layer) illuminated by light. Herein, for the modeling analysis, the configuration of DSSCs was simplified to three main layers: Pt layer, dye-sensitized TNT layer, and Ti foil, which are in the order of light contact under back-side light illumination. Figure 5b shows the electric field intensity of DSSCs when 3.3 μm, 11.5 μm, and 20.6 μm long TNT arrays are applied as a photoanode. The illuminating light has a wavelength of 550 nm, which is a primary light absorption peak of N719 dye, corresponding to the IPCE result in Figure 3. Under the same illumination of 550 nm wavelength, the magnitude of the electric field intensity increased with the increase in the lengths of the TNT. The magnitude of the dye/TNT active region in DSSCs using 20.6 μm long TNT arrays was the largest as seen in the blue-colored integrated area of Figure 5b, where the DSSCs with 20.6 μm long TNT arrays is expected to have the best light absorption efficiency at the wavelength of 550 nm. In addition, the valid layer thickness governed by the electric field intensity in DSSCs is a function of the TNT lengths: they were 30, 90 and 110 nm for 3.3, 11.5 and 20.5 μm long TNT arrays, respectively, as determined by the onset points of the position in device. Considering the fact that the employed TNT arrays are on the micrometer-scale, the valid layer thickness at the nanometer-scale indicates the active layer in the DSSCs is mainly controlled by the adsorbed dye on the TNT array. The valid layer thickness is likely to be the imaginary thickness of the adsorbed dye layer in terms of optical modeling although the adsorbed dye is usually considered as a volume. Therefore, with the longer TNT array, the larger magnitude of the electric field intensity and the thicker electric field-valid layer contribute to the higher light harvesting with an enhanced charge separation. This is well matched with the J_{sc} and IPCE results and this explanation is supported by the modeled results which will be discussed later.

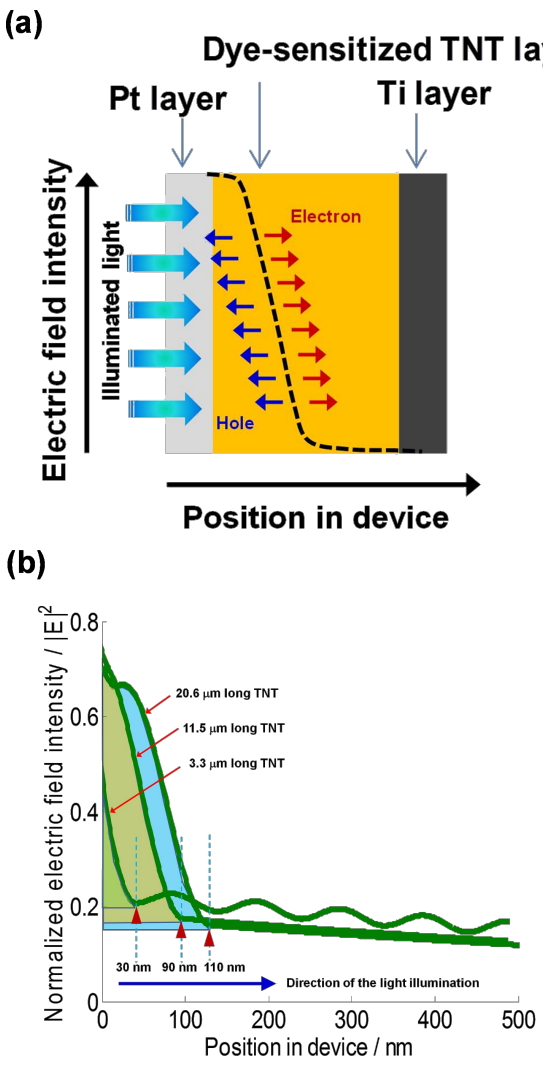

Figure 5: (a) A schematic diagram of charge separation driven by the electric field intensity as a function of layer thickness and (b) Electric field intensity of DSSCs with different TNT lengths calculated by using GTMM. (The onset values, 30 nm, 90 nm, and 110 nm, are electric field-valid layer thickness. That is the distance from the Pt layer.)

Figure 6 shows the light intensity fraction of absorption and reflectance of the TNT-based DSSCs by using GTMM with 3.3 μm, 11.5 μm, and 20.6 μm long TNT arrays. As indicated in Figure 6a, the rate of reflection of light is higher than the rate of absorption of the dye, which indicates that incident light is lost by reflection. This clearly supports that the IPCE value of DSSCs with the 3.3 μm long TNT array was lower at all incident wavelengths than those of longer TNT-employed DSSCs (Figure 3). Additionally, the fluctuating light fraction intensity result of 3.3 μm long TNT-DSSCs presents the active layer consisting of dye and TNT array did not absorb the penetrating

light effectively, confirmed by the experimental result of the lowest J_{sc} (1.32 mA·cm^{-2}). In contrast, with longer TNT lengths of 11.5 µm and 20.6 µm, the reflectance and absorbance shows significantly reversed changes (Figure 6b and Figure 6c). As the light is illuminated into DSSCs using 11.5 µm and 20.6 µm long TNT arrays, the reflectance dramatically decreases and the absorption significantly increases, while the magnitude of light fraction intensity of the 20.6 µm long TNT array is slightly higher than that of the 11.5 µm long TNT array. These light fraction intensity results reflect the charge generation rate with different TNT lengths in Figure 7.

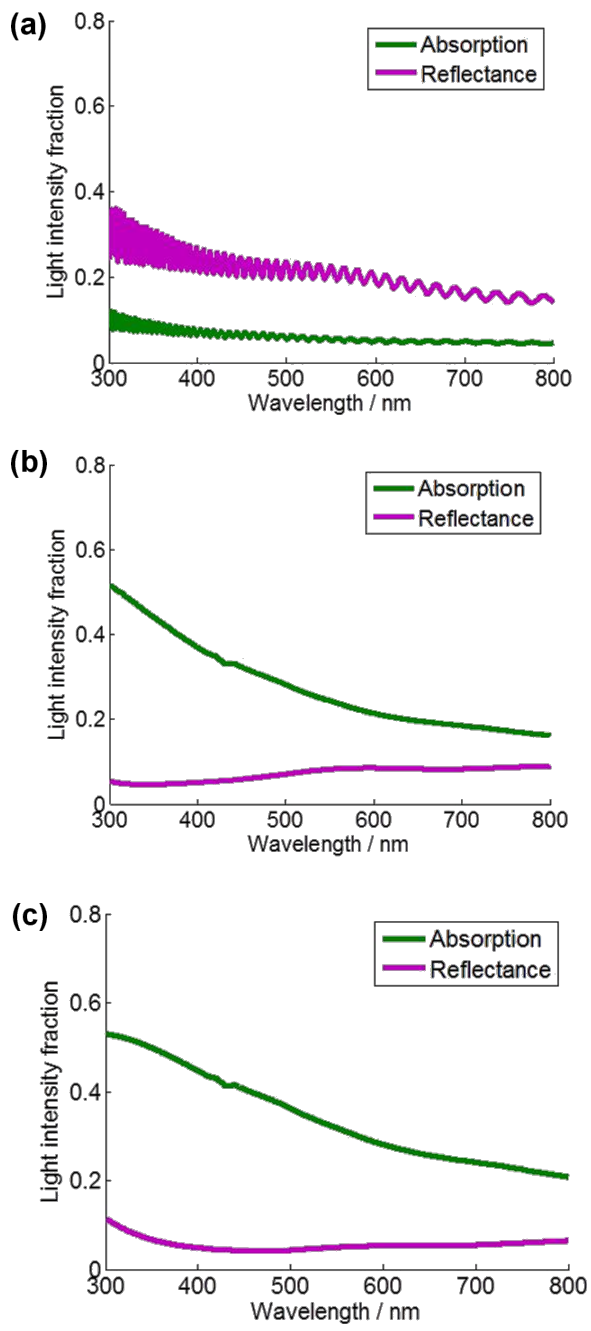

Figure 6: Calculated absorption and reflectance of the DSSCs with different TNT lengths by using GTMM: (a) 3.3 µm long TNT array, (b) 11.5 µm long TNT array, and (c) 20.6 µm long TNT array.

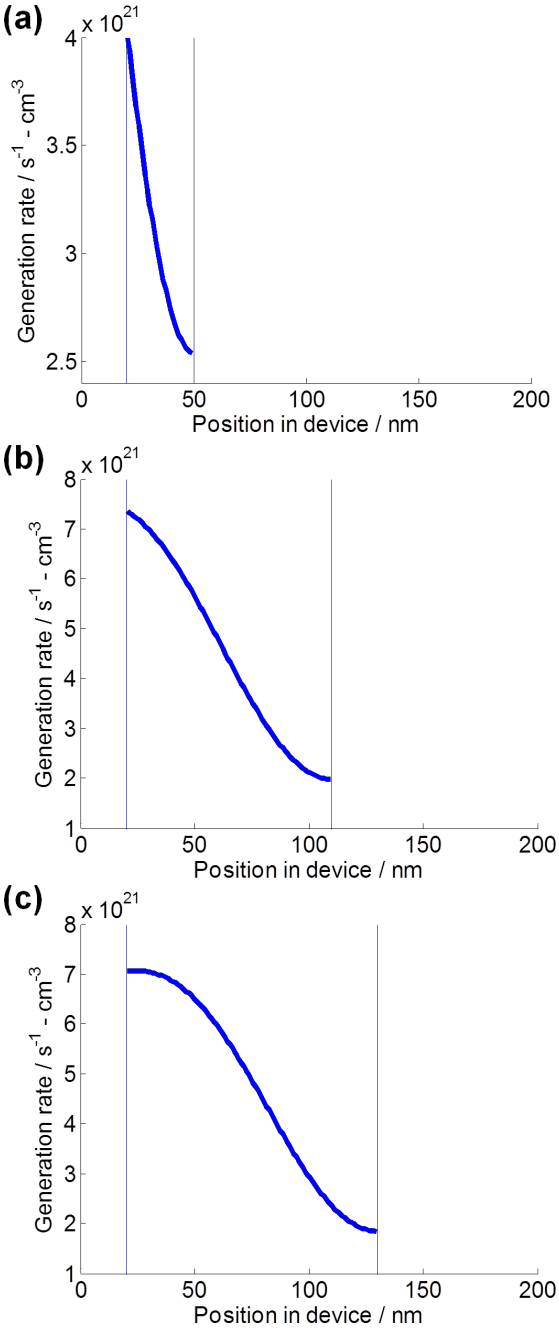

Figure 7: Calculated charge generation rate of the DSSCs with different TNT lengths using GTMM under 1 sun condition (100 mW·cm^{-2}). Charge generation rate for DSSCs with (a) 30 nm thick electric field-valid layer of a 3.3 µm long TNT array, (b) 90 nm thick electric field-valid layer of a 11.5 µm long TNT array, and (c) 110 nm thick electric field-valid layer of a 20.6 µm long TNT array.

While the major contribution of GTMM is to understand the electric field intensity distribution, it can also be applied for calculating the amount of generated charges in the photo-active layer [23]. In all cases, charge generation is mostly in the dye-sensitized active layer. In Figure 7, the charge generation rate is calculated in the range of the electric field-valid layer thicknesses obtained from Figure 5b. There is an initially high rate of charge generation which gradually decreases. This is due to an increase in recombination and a decrease in light absorption with an increase in thickness of layer. With an increase of the electric field-valid layer thickness from 30 nm to 110 nm (Figure 5b), the initial rate of charge generation of 4×10^{21} $s^{-1} \cdot cm^{-3}$ is boosted up to 7×10^{21} $s^{-1} \cdot cm^{-3}$. While the initial charge generation rates of DSSCs using 11.5 μm long TNT arrays and 20.6 μm long TNT arrays are comparable, their slopes in Figure 7b and Figure 7c show different patterns. In Figure 7c, the generated charge is retained up to 50 nm of position in the device before it drops. In contrast, Figure 7b shows that the generated charge rate rapidly decreases within the range of the electric field-valid layer of 90 nm. Therefore, compared to J_{sc} (6.02 $mA \cdot cm^{-2}$) of DSSCs using 11.5 μm long TNT arrays, the higher J_{sc} (8.26 $mA \cdot cm^{-2}$) of DSSCs using 20.6 μm long TNT arrays was attributed to relatively high charge generation rate [24]. By comparing the calculated charge generation rates with experimental data such as IPCE and EIS, the enhancement of photovoltaic performance with higher J_{sc} is achieved from the improvement of charge generation rate facilitated by light harvest, charge separation and electron lifetime.

Conclusion

DSSCs using 1D-TNT photoanodes have been comprehensively studied by optical modeling-assisted characterization. The photovoltaic performance of DSSCs with longer TNT lengths was significantly enhanced through an increase in J_{sc}. The amount of dye and IPCE analysis confirmed the increase in J_{sc} was due to the increased light harvest rate, supported by the charge generation rate calculated from optical modeling using GTMM. The increase in J_{sc} was also due to the excellent charge transport property of 1D-TNT structured photoanodes accompanying effective electron–hole charge separation and longer electron lifetime, which were confirmed by EIS analysis and the simulated electric field intensity. Therefore, our characterization approach employing optical modeling contributes to a deeper understanding of the improved light harvesting and charge transport properties observed in the solar cell devices using 1D-TNT photoanodes.

Experimental

Fabrication of TNT-based DSSCs

Under the anodization conditions of 60 V with ethylene glycol containing 0.5 wt % NaF and 5 wt % water, TNT arrays (6×6 mm^2) with different lengths and pores were obtained by various anodizing durations of 1, 5, and 15 h [25]. The TNT arrays were immersed in 0.04 M of $TiCl_4$ at 70 °C for 30 min followed by rinsing with water. The $TiCl_4$ treated TNT was calcined at 450 °C for 3 h and reheated to 450 °C for 30 min if not immediately used. For N719-DSSCs, the TNT array was soaked in 0.3 mM N719 (*cis*-diisothiocyanato-bis(2,2′-bipyridyl-4,4′-dicarboxylato)ruthenium(II) bis(tetrabutylammonium)) dye solution in anhydrous acetonitrile for 18 h. N719 compound was purchased from Sigma-Aldrich. A sandwich-type DSSC was assembled using the dye-sensitized TNT array onto the Ti foil (20×20 mm^2) as a photoelectrode and platinum-deposited fluorine-doped tin oxide (FTO) glass (20×15 mm^2, Asahi, $R_s \leq 8$ $\Omega \cdot sq^{-1}$) as a counter electrode separated by a sealant (Surlyn 60 μm thickness, Solaronix). The electrolyte was a mixture of 0.1 M LiI, 0.6 M 1, 2-dimethyl-3-propylimidazolium iodide (DMPII), 0.03 M I_2 and 0.5 M *t*-butylpyridine (*t*-BP) in acetonitrile. The electrolyte was injected to the cell through a hole (diameter 1 mm) drilled through the counter electrode with the aid of a vacuum. The fabricated active area in the single cell was 0.16 cm^2 (4×4 mm^2).

Characterization of TNT-based DSSCs

The photovoltaic performances of the DSSCs were measured using a Keithley 2400 source measure unit under a calibrated AM 1.5 solar simulator (Oriel) at 100 $mW \cdot cm^{-2}$ light intensity. Incident photon-to-current conversion efficiency (IPCE) spectra of the devices were measured under a Xe-lamp (Newport 66902) equipped with a monochromator (Newport 74125). The light illumination was concentrated onto a spot smaller than the cell area. The short-circuit current response of the devices was measured in 5 nm steps using a Keithley 2400 source measure unit. The amount of adsorbed dye concentration was determined by measuring the absorbance of dye solution desorbed from the surface of the TNT array in basic solution. In order to desorb dyes, N719 dye-adsorbed TNT arrays were immersed in a 0.1 M NaOH in water for about 40 min. The absorbance measurement was performed using UV–vis spectrophotometer (Cary 300, Varian). The electrochemical impedance spectroscopy (EIS) measurements were performed by illuminating the DSSCs with a AM 1.5 solar simulator calibrated at 100 $mW \cdot cm^{-2}$ at open-circuit conditions between 0.1 Hz and 100 kHz with an AC amplitude of ± 10 mV using a Gamry Reference 600 instrument.

Transfer matrix method analysis for TNT-based DSSCs

For transfer matrix method analysis for TNT-based DSSCs, the ellipsometry measurement system was used to get the optical constants such as refractive index (n) and extinction

coefficient (k). Prior to the ellipsometry measurement, the individual layers inside the DSSCs were prepared on a cleaned Si wafer of 2.5 × 2.5 cm^2. The Si wafer was sequentially cleaned in acetone, isopropyl alcohol and milli-Q water with 5 min sonication, respectively. The N719 dye and Pt layers were deposited on the Si wafer using spin coating under the condition of 2000 rpm for 60 s. For the TNT arrays, TNT arrays with three different lengths (3.3 μm, 11.5 μm, and 20.6 μm) were transplanted from Ti foil substrate to the Si wafer with 0.04 M $TiCl_4$ solution and then calcined at 450 °C for 3 h. The Ti foil was cut to 2.5 × 2.5 cm^2. Optical constants were obtained by using a VUV-VASE ellipsometer system (J. A. Woollam Co., Inc.). The transfer matrix program and procedure were adopted from the literature [15,16].

Acknowledgements

This work has been supported by the Australian Research Council Discovery Project (DP110101638). This work was performed in part at the QLD node of the Australian National Fabrication Facility, a company established under the National Collaborative Research Infrastructure Strategy to provide nano- and micro-fabrication facilities for Australia's researchers. In addition, this work is partially based on the Ph.D. thesis of J.–H. Yun from the University of New South Wales.

References

1. Fujishima, A.; Honda, K. *Nature* **1972,** *238,* 37–38. doi:10.1038/238037a0
2. Li, J.; Zhang, J. Z. *Coord. Chem. Rev.* **2009,** *253,* 3015–3041. doi:10.1016/j.ccr.2009.07.017
3. Koo, H.-J.; Park, J.; Yoo, B.; Yoo, K.; Kim, K.; Park, N.-G. *Inorg. Chim. Acta* **2008,** *361,* 677–683. doi:10.1016/j.ica.2007.05.017
4. Wu, X.; Chen, Z.; Lu, G. Q.; Wang, L. *Adv. Funct. Mater.* **2011,** *21,* 4167–4172. doi:10.1002/adfm.201100828
5. Zhu, K.; Neale, N. R.; Miedaner, A.; Frank, A. J. *Nano Lett.* **2007,** *7,* 69–74. doi:10.1021/nl062000o
6. Barbé, C. J.; Arendse, F.; Comte, P.; Jirousek, M.; Lenzmann, F.; Shklover, V.; Grätzel, M. *J. Am. Ceram. Soc.* **1997,** *80,* 3157–3171. doi:10.1111/j.1151-2916.1997.tb03245.x
7. Ghicov, A.; Albu, S. P.; Hahn, R.; Kim, D.; Stergiopoulos, T.; Kunze, J.; Schiller, C.-A.; Falaras, P.; Schmuki, P. *Chem.–Asian J.* **2009,** *4,* 520–525. doi:10.1002/asia.200800441
8. Tsekouras, G.; Miyashita, M.; Kho, Y. K.; Teoh, W. Y.; Mozer, A. J.; Amal, R.; Mori, S.; Wallace, G. G. *IEEE J. Sel. Top. Quantum Electron.* **2010,** *16,* 1641–1648. doi:10.1109/JSTQE.2010.2049734
9. Zukalová, M.; Zukal, A.; Kavan, L.; Nazeeruddin, M. K.; Liska, P.; Grätzel, M. *Nano Lett.* **2005,** *5,* 1789–1792. doi:10.1021/nl051401l
10. Kang, S. H.; Choi, S. H.; Kang, M. S.; Kim, J. Y.; Kim, H. S.; Hyeon, T.; Sung, Y. E. *Adv. Mater.* **2008,** *20,* 54–58. doi:10.1002/adma.200701819
11. Park, J. H.; Jung, S. Y.; Kim, R.; Park, N.-G.; Kim, J.; Lee, S.-S. *J. Power Sources* **2009,** *194,* 574–579. doi:10.1016/j.jpowsour.2009.03.075
12. Mor, G. K.; Shankar, K.; Paulose, M.; Varghese, O. K.; Grimes, C. A. *Nano Lett.* **2006,** *6,* 215–218. doi:10.1021/nl052099j
13. Paulose, M.; Shankar, K.; Varghese, O. K.; Mor, G. K.; Hardin, B.; Grimes, C. A. *Nanotechnology* **2006,** *17,* 1446–1448. doi:10.1088/0957-4484/17/5/046
14. Topič, M.; Čampa, A.; Filipič, M.; Berginc, M.; Krašovec, U. O.; Smole, F. *Curr. Appl. Phys.* **2010,** *10,* S425–S430. doi:10.1016/j.cap.2010.02.042
15. Burkhard, G. F.; Hoke, E. T.; McGehee, M. D. *Adv. Mater.* **2010,** *22,* 3293–3297. doi:10.1002/adma.201000883
16. Jung, S.; Kim, K.-Y.; Lee, Y.-I.; Youn, J.-H.; Moon, H.-T.; Jang, J.; Kim, J. *Jpn. J. Appl. Phys.* **2011,** *50,* 122301. doi:10.7567/JJAP.50.122301
17. Gómez, R.; Salvador, P. *Sol. Energy Mater. Sol. Cells* **2005,** *88,* 377–388. doi:10.1016/j.solmat.2004.11.008
18. Ni, M.; Leung, M. K. H.; Leung, D. Y. C. *Can. J. Chem. Eng.* **2008,** *86,* 35–42. doi:10.1002/cjce.20015
19. Nazeeruddin, M. K.; Kay, A.; Rodicio, I.; Humphry-Baker, R.; Mueller, E.; Liska, P.; Vlachopoulos, N.; Graetzel, M. *J. Am. Chem. Soc.* **1993,** *115,* 6382–6390. doi:10.1021/ja00067a063
20. Halme, J.; Boschloo, G.; Hagfeldt, A.; Lund, P. *J. Phys. Chem. C* **2008,** *112,* 5623–5637. doi:10.1021/jp711245f
21. Frank, A. J.; Kopidakis, N.; v. d. Lagemaat, J. *Coord. Chem. Rev.* **2004,** *248,* 1165–1179. doi:10.1016/j.ccr.2004.03.015
22. Hore, S.; Vetter, C.; Kern, R.; Smit, H.; Hinsch, A. *Sol. Energy Mater. Sol. Cells* **2006,** *90,* 1176–1188. doi:10.1016/j.solmat.2005.07.002
23. Hägglund, C.; Zäch, M.; Kasemo, B. *Appl. Phys. Lett.* **2008,** *92,* 013113. doi:10.1063/1.2830817
24. Mihailetchi, V. D.; Koster, L. J. A.; Hummelen, J. C.; Blom, P. W. M. *Phys. Rev. Lett.* **2004,** *93,* 216601. doi:10.1103/PhysRevLett.93.216601
25. Yun, J.-H.; Ng, Y. H.; Ye, C.; Mozer, A. J.; Gordon, G. G.; Amal, R. *ACS Appl. Mater. Interfaces* **2011,** *3,* 1585–1593. doi:10.1021/am200147b

License and Terms

This is an Open Access article under the terms of the Creative Commons Attribution License (http://creativecommons.org/licenses/by/2.0), which permits unrestricted use, distribution, and reproduction in any medium, provided the original work is properly cited.

The license is subject to the *Beilstein Journal of Nanotechnology* terms and conditions: (http://www.beilstein-journals.org/bjnano)

The definitive version of this article is the electronic one which can be found at: doi:10.3762/bjnano.5.102

BEILSTEIN JOURNAL OF NANOTECHNOLOGY

Functionalized nanostructures for enhanced photocatalytic performance under solar light

Liejin Guo*, Dengwei Jing*, Maochang Liu, Yubin Chen, Shaohua Shen, Jinwen Shi and Kai Zhang

Review

Open Access

Address:
International Research Center for Renewable Energy & State Key Laboratory of Multiphase Flow in Power Engineering, Xi'an Jiaotong University Xi'an 710049, China

Email:
Liejin Guo* - lj-guo@mail.xjtu.edu.cn;
Dengwei Jing* - dwjing@mail.xjtu.edu.cn

* Corresponding author

Keywords:
functionalized nanostructures; hydrogen; photocatalysis; photocatalytic; solar light

Beilstein J. Nanotechnol. **2014,** *5,* 994–1004.
doi:10.3762/bjnano.5.113

Received: 20 February 2014
Accepted: 02 June 2014
Published: 09 July 2014

This article is part of the Thematic Series "Photocatalysis".

Guest Editor: R. Xu

© 2014 Guo et al; licensee Beilstein-Institut.
License and terms: see end of document.

Abstract

Photocatalytic hydrogen production from water has been considered to be one of the most promising solar-to-hydrogen conversion technologies. In the last decade, various functionalized nanostructures were designed to address the primary requirements for an efficient photocatalytic generation of hydrogen by using solar energy: visible-light activity, chemical stability, appropriate band-edge characteristics, and potential for low-cost fabrication. Our aim is to present a short review of our recent attempts that center on the above requirements. We begin with a brief introduction of photocatalysts coupling two or more semiconductors, followed by a further discussion of the heterostructures with improved matching of both band structures and crystal lattices. We then elaborate on the heterostructure design of the targeted materials from macroscopic regulation of compositions and phases, to the more precise control at the nanoscale, i.e., materials with the same compositions but different phases with certain band alignment. We conclude this review with perspectives on nanostructure design that might direct future research of this technology.

Review

Introduction

The increasing energy demand as well as the serious environmental contamination caused by the usage of fossil fuels give rise to the necessity to develop clean alternative fuels. Hydrogen, as a pollution-free and storable energy fuel, is a promising substitute of fossil fuels. Nowadays hydrogen is mainly manufactured from hydrocarbons such as fossil fuels, which limits its wide utilization. Therefore, the ability to economically and efficiently harvest hydrogen from renewable energies is central to advances in many areas and should be the fundamental research issue [1-4]. Photocatalytic hydrogen production from water by

using solar energy is one of the most acceptable routes for this aim, since only abundant water and solar energy are needed for hydrogen production in the process. If the economic viability for industrial application is successfully satisfied, it will ultimately solve the energy and environmental problems [5,6].

Since the first report by Fujishima and Honda in 1972 [7], hydrogen production from water over semiconducting powders or films by using solar energy has been extensively studied. Thermodynamically, the reaction of producing hydrogen and oxygen from water splitting has a standard Gibbs free energy (ΔG) of 237 kJ/mol and is therefore an uphill reaction. Energy input is therefore indispensible for this reaction to proceed. In principle, the photocatalytic reaction over semiconductors is triggered by the direct absorption of a photon by the band gap of semiconductor materials (Figure 1). Upon photon excitation, the photogenerated charges move to the surface of semiconductor particles where photocatalytic reactions occur. Consequently, the efficiency of photocatalytic water splitting is closely affected by the band structure of the semiconductors [8].

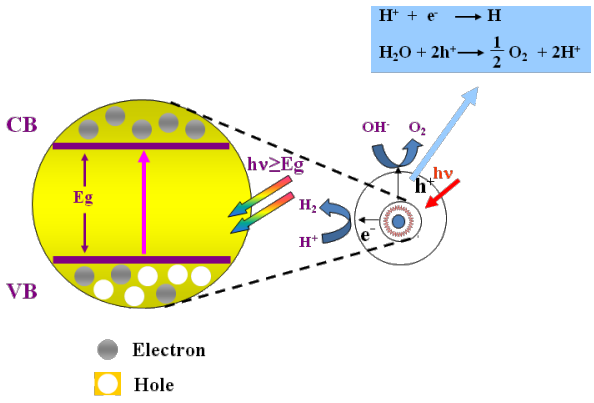

Figure 1: Basic principle for overall water splitting over semiconductor photocatalysts. Reprinted with permission from [6]. Copyright (2010) Elsevier.

The band gap of semiconductor photocatalysts must be larger than the potential of water electrolysis to meet the energetic requirement for overall water splitting (1.23 eV, corresponding to an absorption threshold of 1000 nm). In particular, the bottom level of the conduction band (CB) must be more negative than the reduction potential of water, while the top level of the valance band (VB) should be more positive than the oxidation potential of water. In order to utilize the abundant visible light from the sun, the band gap of photocatalysts has to be less than 3.0 eV (corresponding to an absorption threshold larger than 420 nm). Efficient utilization of these huge amounts of "low energy" photons is crucial to the realization of commercial solar photocatalytic hydrogen production. To this end, band engineering is necessary to design semiconductor photocatalysts with satisfactory hydrogen production efficiency. In addition, the photocatalytic efficiency also depends on the fate of photogenerated hole–electron pairs. To improve the quantum efficiency (QE) of a photocatalytic process, two sequential steps, (1) the efficient separation and transfer of the photogenerated charge carriers to the target surface reaction sites within their life time to avoid their recombination in the form of heat dissipation, and (2) the rapid implementation of reduction and oxidation reactions by those excited charges, should be promoted.

Among the various approaches, nanostructure design with well-tailored band alignment provides a powerful means to the improvement of the photocatalytic activity. In the process of our study, we have also paid special attention on the nanoscale control of the material morphology and construction of functionalized nanostructures to promote charge separation and prolong the lifetime of the photoexcited charge carriers. Our discussion is principally organized around this topic, which constructs the main theme of this review.

Strategies for the development of various functionalized nanostructures

Nanosized functionalized morphology

As mentioned above, absorption of photons with energy equal or higher than the band gap of the semiconductor could lead to photogenerated electrons (e^-) and holes (h^+) within conduction and valence bands, respectively. Generally, the photocatalytic reaction often occurs at the semiconductor surface. So the ability to accelerate the migration of photogenerated charges from the interior of the semiconductor to its surface avoiding their bulk recombination enables substantial improvement of photocatalytic efficiency. In this regard, semiconductors with nanosized functionalized morphology could be a beneficial choice. Since the first reports on mesoporous silica MCM-41 [9], inorganic oxides with controlled porosity have been extensively investigated. It is known that mesoporous photocatalysts usually exhibit high specific surface areas that can provide more surface reactive sites. The nanoscale channel walls of mesoporous photocatalysts can also facilitate the migration of photogenerated charges from bulk to surface [10]. It has been reported that porous semiconductor photocatalysts, such as TiO_2 [11], Nb_2O_5 [12] and Ta_2O_5 [10], displayed much better photocatalytic properties than their bulk counterparts. Meanwhile, when semiconductor nanocrystals are dispersed in the mesoporous substrate, greatly enhanced photocatalytic properties can also be achieved. For example, dispersing TiO_2 nanoclusters in MCM-41 [13] and MCM-48 [14] resulted in much higher photocatalytic activities than that of bulk TiO_2 under UV light irradiation. Our work was carried out on Ni modified mesoporous TiO_2 photocatalysts [15]. It was found

that Ni ions were highly dispersed in the framework of mesoporous TiO_2 resulting in enhanced hydrogen production in methanol aqueous solution compared to Ni-doped particulate TiO_2. The photocatalytic activity was found to have a close relationship with the doping amount of Ni ions and the highest activity was obtained when the amount of Ni doping was 1%. Here, the enhanced photocatalytic activity was attributed to doped Ni^{2+} ions which served as shallow trapping sites, preferentially trapping photoexcited holes. The assumption of the role of Ni^{2+} as shallow trapping sites could be rationalized by considering that the energy level of Ni^{2+} is located very close to the valence band edge of TiO_2 [16]. After trapping a hole, Ni^{2+} will be oxidized to Ni^{3+}. However, due to the instability of Ni^{3+}, it will quickly return to Ni^{2+} again. The shallow trapping can therefore separate the arrival of photogenerated charges at the surface, so the recombination at the channel surface of mesopores could be greatly reduced. However, when the doping concentration is higher than the optimal level, or for too large particles, the exited hole can be trapped more than once, and recombine with the electron excited by another photon. An optimal dopant concentration is therefore crucial. In another example, we also synthesized Fe-doped mesoporous Ta_2O_5 that showed an enhanced activity compared to the bulk counterpart [17].

It should be pointed out that TiO_2 can only respond to UV light, even metal ion doping can hardly enhance its visible light activity. Sensitization with dyes or nanocrystals is one possible approach to extend the light absorption of TiO_2. Sreethawong et al. found that eosin Y-sensitized mesoporous-assembled Pt/TiO_2 nanocrystal photocatalysts exhibited enhanced photocatalytic hydrogen production under visible light irradiation [18]. Lee et al. also reported that CdS and CdSe nanocrystals dispersed on the internal surface of mesoporous TiO_2 films could lead to the promoted photocatalytic hydrogen production under visible light [19]. We have also investigated the visible-light-driven photocatalytic performance over a nanosized WS_2-sensitized mesoporous TiO_2 photocatalyst [20]. Compared to bulk TiO_2 without mesopores, more WS_2 can be loaded in the mesoporous TiO_2. Moreover, the mesoporous channels can prevent the light-induced detachment of WS_2 nanoparticles from the substrate during the photocatalytic reaction. These factors resulted in much higher activity and better stability, as schematically illustrated in Figure 2. Here the elevation of the conduction band of nanosized WS_2 due to quantum confinement effect is considered to be crucial. As the recombination of photogenerated charges within TiO_2 could be neglected, the rate-determining step for photocatalytic reaction is the electron transfer from TiO_2 to H^+ in the solution. Therefore, deposition of Pt as cocatalyst is indispensable for an efficient hydrogen evolution.

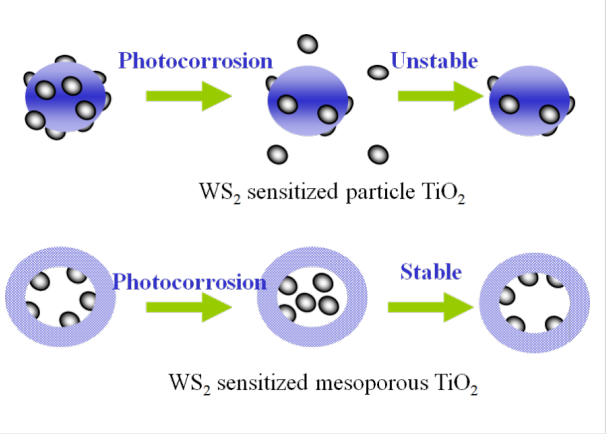

Figure 2: Illustration of mesoporous wall on the anti-photocorrosion of sulfide photocatalyst.

Generally, MCM-41 is not photo-reactive. But it can be activated by coupling with a semiconductor or doping a transitional metal. Figure 3 shows the proposed charge separation mechanism within a representative transitional metal-containing molecular sieve photocatalyst [21]. In principle, after excitation by visible light, photogenerated electrons are transferred from CdS to the Ti-MCM-41 substrate to conduct a reduction reaction. The holes, on the contrary, remain at the CdS to let oxidation reactions occur. We also investigated the effect taken by transitional metal doping such as Cr or/and Ti incorporation in MCM-41. Active visible light absorption sites could be generated in MCM-41 due to transitional metal doping. It was found that the highly dispersed Cr ions within MCM 41 could be easily excited by visible light irradiation due to the electron transfer from O^{2-} to Cr^{6+}. Such excited states are active for charge transfer and thus showed a relatively high photocatalytic activity. Accordingly, the unique arrangement of the localized charges in the ordered mesoporous structure leads to a significantly prolonged life time of electron–hole pairs compared to traditional metal ion doped semiconductors.

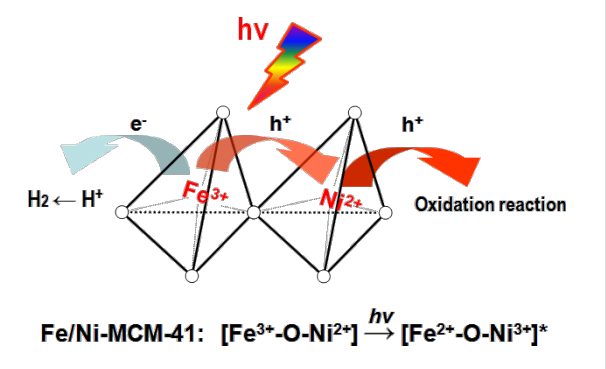

Figure 3: Proposed mechanism for charge transfer in Fe/Ni co-doped MCM-41. Reprinted with permission from [21]. Copyright (2014) Elsevier.

As was found, Cr-Ti-MCM-41 showed much higher activity than Cr-MCM-41 with similar amount of Cr doping for two kinds of MCM-41 material. Due to the presence of Ti, the photocatalytic mechanism of Cr-Ti-MCM-41 is quite different from that of Cr-MCM-41. For the former material, the Cr–O–Ti interaction should be responsible [22]. In this case, a second metal element introduced as a donor can closely link to the first metal element by forming an oxo bridge, which is supposed to be robust chromophore induced by metal-to-metal charge-transfer (MMCT).

Nanosized functionalized surface

A noble-metal cocatalyst, such as Pt, is usually indispensable for many photocatalysts to achieve high photocatalytic activities for hydrogen production. It was recently reported that the valance state of platinum plays an important role in the hydrogen production efficiency, and oxidized platinum was demonstrated to be more efficient than metallic platinum as cocatalyst for hydrogen production [23,24]. Taking into account the cost of the designed photocatalyst for commercial purposes, the development of noble-metal free cocatalysts is still valued. Alternative cocatalysts such as MoS_2 have been reported to be effective to enhance photocatalytic H_2 evolution on CdS [25]. Low-cost WC was also used as efficient cocatalyst on CdS because of its low overpotential for hydrogen production and proper physicochemical properties [26]. The Xu group has studied the effect of NiS working as a cocatalyst. A simple hydrothermal method was used to synthesize NiS/CdS photocatalysts, which have a remarkably high QE of 51.3% at 420 nm in lactic acid sacrificial solution [27]. Co-loading of both reduction and oxidation cocatalysts on the semiconductor was also suggested to be able to enhance the photocatalytic hydrogen production [28].

Here, it is assumed that the photocatalytic activity could be significantly improved if the cocatalysts were loaded especially on a nanosized functionalized surface. We reported the design and preparation of a highly efficient $Cd_{0.5}Zn_{0.5}S$ photocatalyst decorated with nanosized NiS surface heterojunctions. The hydrogen evolution rate over this photocatalyst could reach 1.4 mmol/h, with a QE of 33.9%. This efficiency is much higher than that of many photocatalysts containing noble metals. As shown in Figure 4, in the hybrid photocatalyst, the NiS nanoparticles can serve as electron trapping sites and extract photogenerated electrons from $Cd_{0.5}Zn_{0.5}S$ substrate, which finally leads to spatially separated photoreduction and oxidation reactions. NiS plays a similar role as a noble metal, which can provide active sites for proton reduction, and thus efficiently enhance the overall photocatalytic activity. Our work demonstrates that efficient and low cost photocatalytic hydrogen production can be achieved through the substitution of noble metal cocatalyst with a properly engineered surface heterojunction [29].

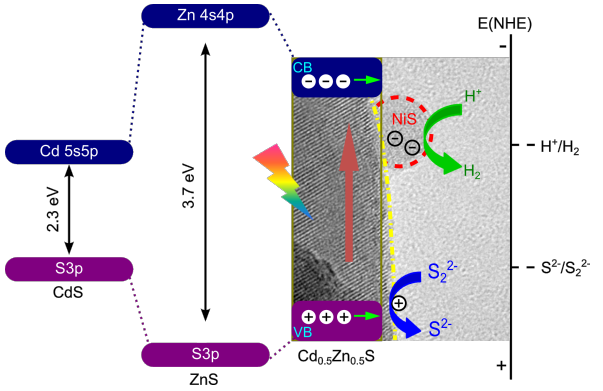

Figure 4: Proposed photocatalytic charge separation process over the band-structure controlled NiS/$Cd_{0.5}Zn_{0.5}S$ photocatalyst. Reprinted from with permission from [29]. Copyright (2010) Elsevier.

In addition to the screening for a noble-metal free cocatalyst, we have also tried to modify the surface of the photocatalyst, aiming to form functionalized surface nanostructures. A highly active and stable CdS photocatalyst was obtained by a two-step thermal sulfuration method. Nanostep structures formed at the surface of the CdS photocatalyst, leading to a significantly improved photocatalytic activity compared to CdS prepared by traditional approaches [30]. The enrichment of Pt around nanostep regions revealed the preferred migration of photoexcited electrons there and the reduction H_2PtCl_6 precursor to metallic Pt. Similar nanosteps were also reported by Kudo for another metal sulfide photocatalyst [31]. Although the mechanism for the formation of nanostep structures could be different, the important role of the nanostep surface for the enhancement of photocatalytic performance was also shown.

The surface architecture of composite photocatalysts can significantly affect the photocatalytic process. For example, Jang and co-workers reported that bulky CdS decorated with TiO_2 nanoparticles was much more active than bulky TiO_2 decorated with CdS nanoparticles [32]. We have prepared CdS/titanate nanotubes (CdS/TNTs) photocatalysts with a unique morphology by a simple one-step hydrothermal method [33]. As schematically illustrated in Figure 5, the CdS nanoparticle was intimately enwrapped by the TNTs, resulting in a remarkably enhanced charge separation efficiency and thereby photocatalytic hydrogen production activity. The similar enwrapped structure can also be achieved for $Cd_{0.5}Zn_{0.5}S$/TNTs nanocomposites [34]. The QE at 420 nm over the nanocomposites reached 38.1% without loading any cocatalyst. Meanwhile, except for the greatly reduced toxicity by using Zn^{2+} instead of Cd^{2+} (Cd content, 4.0 wt %), $Cd_{0.5}Zn_{0.5}S$/TNTs also showed a

good stability for hydrogen production. These factors are significantly beneficial for their further application in the field of solar energy conversion.

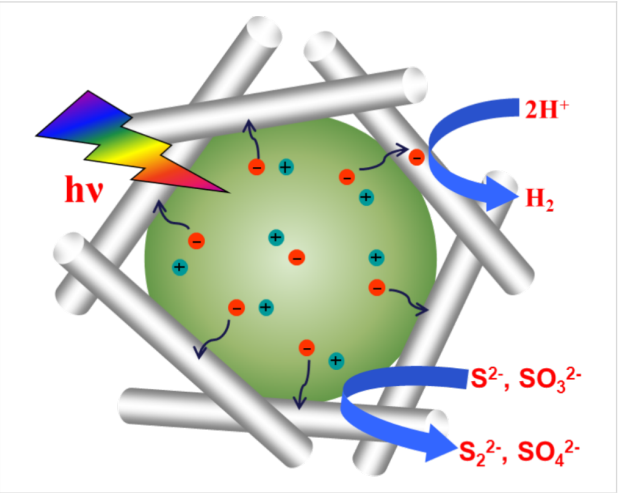

Figure 5: CdS nanoparticle enwrapped by the surrounding TNTs showed a significant enhancement of charge separation and therefore a high activity. Reproduced with permission from [33]. Copyright (2011) The Royal Society of Chemistry.

Crystal facets engineering

As we know, the surface of a given semiconductor nanocrystal usually consists of certain crystal facets that occupy specific coordination numbers and atom ratios, leading to a deviation of their band structure from their bulk counterpart. Consequently, some crystal facets have shown higher activity than other facets for many photocatalyst during a certain photocatalytic reaction [35-37]. Jang et al. found that ZnO nanoplates with a preferential exposure of Zn(0001) faces showed high photocatalytic activity [38]. Wang et al. constructed ZnO–CdS heterostructures by employing ZnO rods enclosed with well-developed {1100} and {0001} facets to promote photocatalytic hydrogen evolution [39]. Pan et al. found that {001}, {101} and {010} facets of anatase TiO_2 had different photocatalytic activities. However, when partially terminated with fluorine, the three facets had similar photocatalytic activity in H_2 evolution [40]. Engineering the morphology of semiconductors to preferably expose active facets is therefore a promising approach, yet a big challenge to date. Selecting Cu_2WS_4 as model photocatalyst, we obtained interesting decahedral morphologies by a one-step hydrothermal method. The hydrothermal method avoids the using of toxic H_2S gas and simplifies the catalyst preparation process. Owing to the oriented growth and the presence of a large percentage of active (001) crystal planes, the photocatalyst showed high visible-light activity. The highest activity was obtained over the Cu_2WS_4 decahedrons that were hydrothermally prepared at 200 °C for 72 h, with an QE at 425 nm for photocatalytic hydrogen production of 11% [41].

Regarding the stability, oxide photocatalysts would be better than sulfide and nitride photocatalysts [42]. Regrettably, oxide semiconductors frequently possess either low conduction band positions or wide band gaps, which seriously impair their suitability as photocatalysts for hydrogen production [43]. Among the very few visible-light-responsive photocatalysts, cuprous oxide (Cu_2O) deserves our special attention. Cu_2O is a p-type oxide semiconductor with a direct band gap of 2.0 eV. Theoretically, its light-to-hydrogen conversion efficiency can reach 18% [44]. We have thus devoted to the fabrication of Cu_2O nanocrystals with controlled shape to improve its photocatalytic activity for hydrogen production. As shown in Figure 6, multifaceted Cu_2O with controlled crystal facets exposure has been prepared through a facile one-step method. It was revealed that photogenerated electrons preferred to accumulate on high-indexed facets, while photogenerated holes tended to migrate to {100} facets, leading to an efficient spatial charge separation and thereby enhanced photocatalytic hydrogen production from reforming of glucose over the Cu_2O polyhedron [45]. The origin of the charge separation on different crystal facets of TiO_2 has been already theoretically calculated [40]. A slight band offset was observed in both valance and conduction band between two different facets, driving the charge transfer from one facet to another. Our research indicated that a controlled fabrication of different crystal facets with separated functions, such as separated oxidation and reduction sites is one of the effective approaches to the enhancement of the activity of the existing semiconductors.

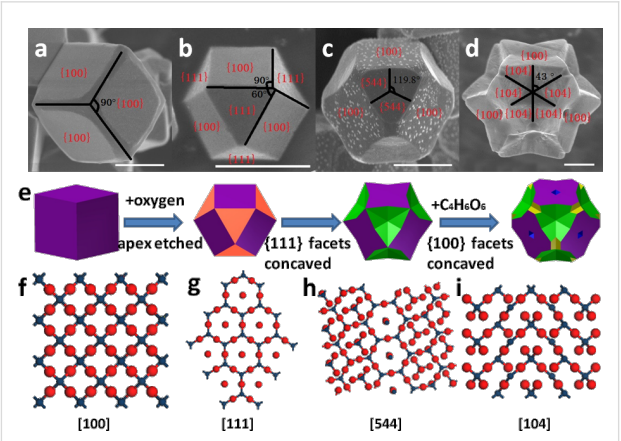

Figure 6: Morphological evolution of Cu_2O prepared with different reaction times, (a) 30 min, (b) 60 min, (c) 90 min and (d) 120 min, all scale bars are 1 μm. Reprinted with permission from [45]. Copyright (2014) The Royal Society of Chemistry.

Perovskite ABO_3 is another group of metal oxide materials deserving in-depth exploring. Most of metal elements can be stably located in ABO_3 structures, and functionalized multicomponent ABO_3 materials can thus be prepared by partial substitu-

tion of cations in A and B sites [46-48]. In this approach, we have successfully synthesized hexagonal single-crystal nanosheet-based $NaSbO_3$ and $AgSbO_3$ hierarchical cuboidal microclusters with exposed {001} facets via a facile and surfactant-free hydrothermal reaction. The light absorption, charge separation and surface reaction were simultaneously optimized through the unique structure assembled from nanosheets, leading to the greatly enhanced photocatalytic activity [49]. Micro- or nanoscale surface-structuring can increase the degree of horizontal light distribution via light scattering. Otherwise, the trapped photons would be lost by direct reflection from a flat surface [50]. As shown in Figure 7, enhanced light absorption arising from multiple light reflections in the nanosheet-based hierarchical structure could be achieved over $NaSbO_3$ and $AgSbO_3$ photocatalysts. Meanwhile, the single-crystal nature can reduce the crystal defects leading to more efficient charge separation. The larger surface area provides more active sites for photocatalytic reaction. The exposed {001} facets as the reactive surfaces can accelerate the redox reactions. Therefore, nanosheet-based $AgSbO_3$ photocatalysts showed a 1.8 times higher initial O_2 evolution rate than $AgSbO_3$ photocatalysts without the hierarchical structure under visible-light irradiation.

Besides facet control, microstructure refinements of the crystal facets, such as distortion of the lattice and configuration of certain crystal facets, can also promote the charge separation and facilitate charge transfer. For example, we have investigated the effects of synthesis conditions on the structure and the photocatalytic property of $ZnIn_2S_4$ [51-53]. It was discovered that the distance of $d(001)$ $ZnIn_2S_4$ could be adjusted by controlling preparation condition. The enlarged $d(001)$ spacing led to distorted $[ZnS_4]$ and $[InS_4]$ tetrahedrons within the $ZnIn_2S_4$ crystal lattice, which in turn, generated an electrostatic field induced by a change of the dipole moments of the lattice. Such a built-in electrostatic field is obviously favorable for an efficient charge separation and hence leads to enhanced photocatalytic activity.

Combined control of band structure and morphology

In principle, a semiconductor photocatalyst should meet at least two requirements to achieve high visible-light photocatalytic activity. A high conduction band is necessary to ensure enough potential for proton reduction. It should also have a narrow band gap in order to utilize incident light to the largest extent. $Cd_{1-x}Zn_xS$, as the solid solution of CdS and ZnS, has received lots of attention in recent years, owing to the tunable band structure and excellent photocatalytic properties for hydrogen production under visible light without needing noble metal cocatalysts [54]. However, the band gap of $Cd_{1-x}Zn_xS$ is not narrow enough for an efficient utilization of visible light. As reported by Kudo et al, a donor level above the valence band of ZnS could be formed when it is doped with Ni^{2+}, which is responsible for the visible light response of Ni-doped ZnS [55]. It inspired us to further tune the band structure of $Cd_{1-x}Zn_xS$ solid solution by Ni doping. Ni^{2+}-doped $Cd_{1-x}Zn_xS$ microspheres were prepared in our work. Here, the doped Ni^{2+} is expected to form a donor level above the valence band of $Cd_{1-x}Zn_xS$ and increase its visible light absorption. At the same time, its high conduction band can be still maintained. The enhanced photocatalytic activity was thus achieved [56]. Moreover, $Cd_{1-x}Zn_xS$ could be also modified by doping with alkali metals. We have also successfully synthesized Sr and Ba doped $Cd_{1-x}Zn_xS$ solid solution photocatalysts with improved activity [57,58]. The underlying role of the doping ions might be quite different. However, the band structure of the solid solution was similarly affected.

Mesoporous zirconium–titanium mixed phosphates (ZTP) is also a photocatalyst of interest as they not only show both cation- and anion-exchange capacity, but also can split pure

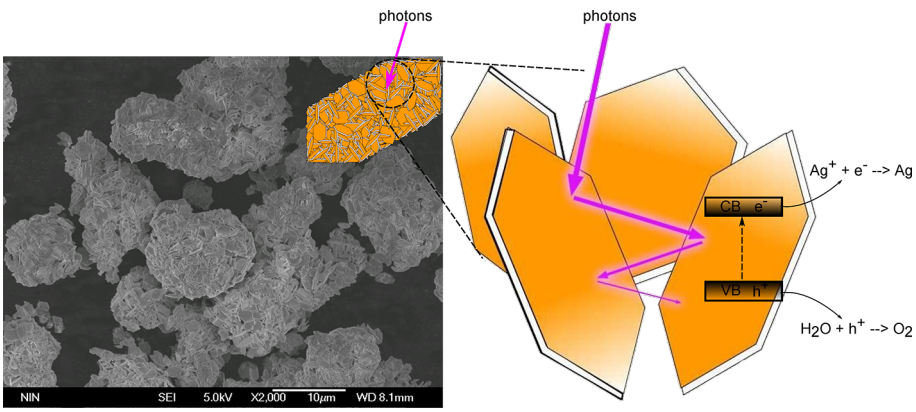

Figure 7: Enhanced light absorption ascribed to multiple light reflections in the nanosheet-based hierarchical structure.

water for hydrogen production under UV light irradiation [59]. These properties make ZTP an ideal candidate after coupling with CdS to form visible-light composite photocatalysts. In addition, due to the adjustable Zr to Ti ratio, the optical properties of this material can be readily tuned. Employing ZTP as substrate and functional constituent, a novel CdS/mesoporous ZTP composite photocatalyst was successfully synthesized via the two-step thermal sulfuration method. We have found that the prepared composite photocatalyst displayed superior activity compared to that prepared by direct sulfuration at room or high temperatures. As shown in Figure 8, the conduction band of ZTP could be continuously controlled by regulating the Zr/Ti ratio. At the optimal Ti to Zr ratio of 3, the energy difference between conduction bands of CdS and ZTP could ensure a large driving force for fluent electron transfer from CdS to ZTP, while the electron localized on the ZTP substrate is still sufficiently active for hydrogen evolution. Combination of CdS with band adjustable mesoporous ZTP could thus inherit the advantage of ZTP in terms of both morphology and band structure. The QE of this composite photocatalyst at 420 nm was determined to be 27.2% [60].

In addition, we also prepared flower like Ni-doped $ZnIn_2S_4$ with plenty of curved nanosheets using hydrothermal method, as shown in Figure 9. It was found that there existed an optimal Ni doping concentration, i.e., 0.3 wt %, for the highest hydrogen production efficiency. Only Ni ions occupying crystal lattice sites of $ZnIn_2S_4$ were found to be active. A higher Ni doping is not effective due to the limited solubility of Ni in the lattice of $ZnIn_2S_4$ and could be detrimental owing to the coverage of surface reaction sites. The existence of thin nanoscale sheets is regarded to be important for its increased activity. Ni^{2+} ions were also expected to be shallow trapping sites, which could enhance the charge separation [61]. Similar combined control of band structure and morphology were also carried out by other groups. Kudo and co-workers prepared layered $AGa_2In_3S_8$ (A = Cu or Ag) by a solid state method for photocatalytic hydrogen production. Both $CuGa_2In_3S_8$ (1.91 eV) and $AgGa_2In_3S_8$ (2.27 eV) showed a quite high photocatalytic activity [62]. Chen and co-workers synthesized hierarchical ZnS–In_2S_3–CuS nanospheres with a nanoporous structure. A high QE of 22.6% at 420 nm is achieved without loading cocatalysts due to their high crystallinity, high surface area and unique microstructure [63].

As the crystal size of the semiconductor is close to the exciton Bohr radius, its bandgap can be enlarged with a reduced crystal size due to the quantum confinement effect. Therefore, we have synthesized Co_3O_4 quantum dots (3–4 nm) via a facile reverse micelle method for the first time. Co_3O_4 has been widely employed as a photocatalyst for oxygen production due to its nontoxicity, low cost and narrow band gap (2.1 eV). However,

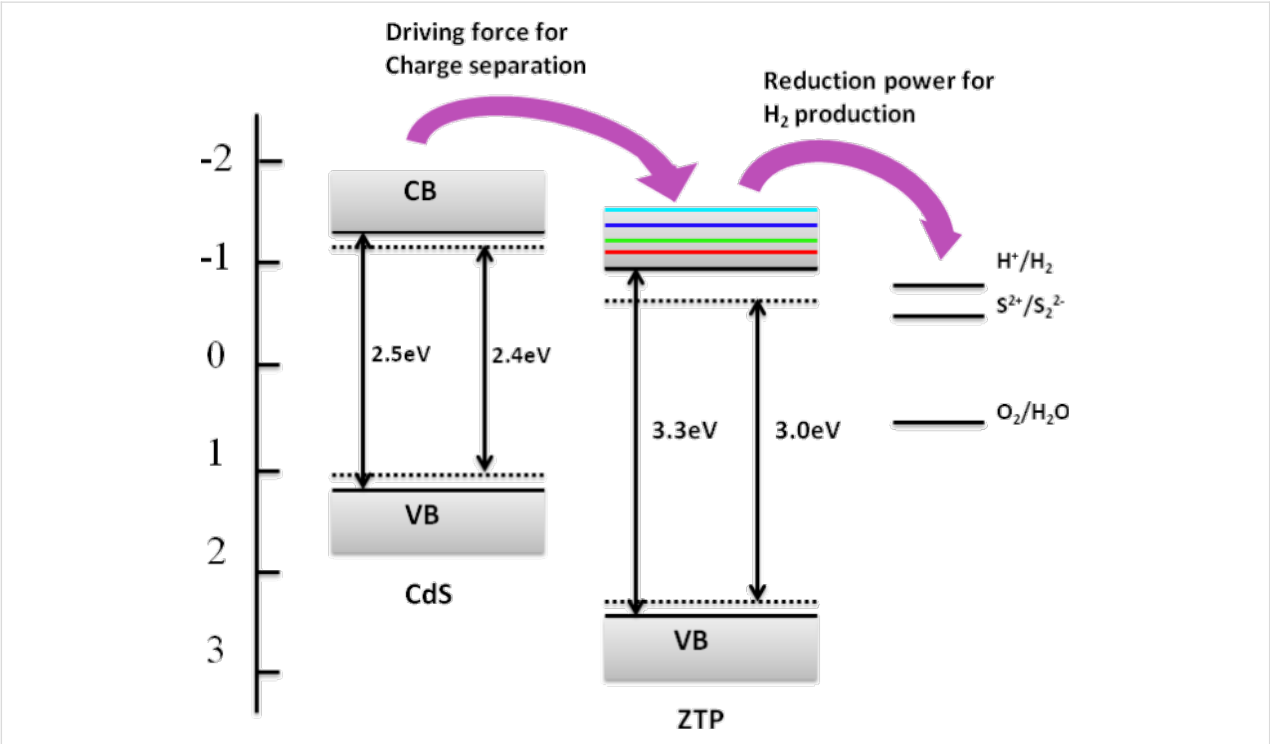

Figure 8: Schematic illustration for the charge separation in CdS/mesoporous ZTP. Reprinted with permission from [60]. Copyright (2007) The American Chemical Society.

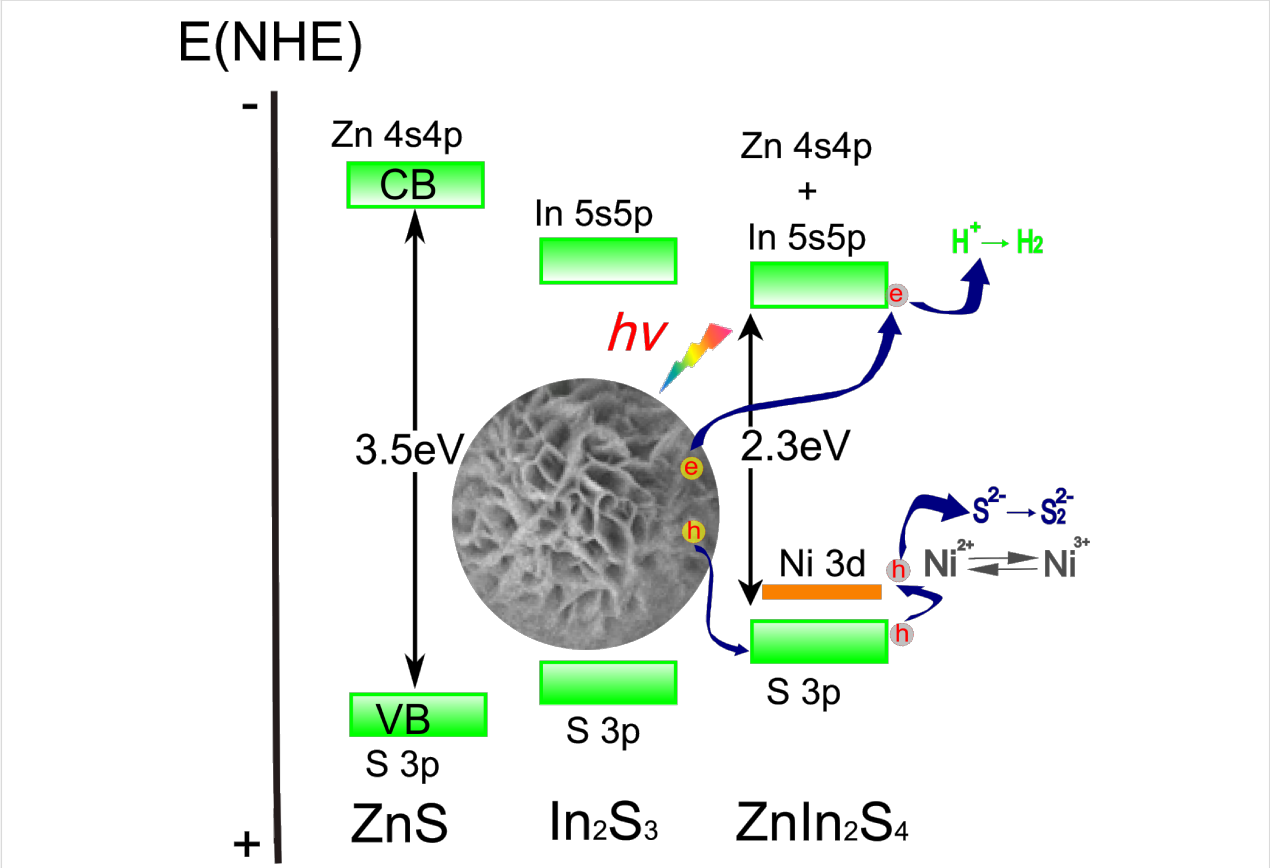

Figure 9: Photocatalytic mechanism over Ni-doped $ZnIn_2S_4$ with plenty of curved nanosheets. Reprinted with permission from [61]. Copyright (2010), Springer.

photocatalytic hydrogen production could not be achieved, because the conduction band edge of bulk Co_3O_4 is not negative enough to reduce H^+. Compared with bulk Co_3O_4, Co_3O_4 quantum dots have a wider bandgap. Valence-band XPS spectra showed that the valance band maxima (VBM) of Co_3O_4 quantum dots and bulk Co_3O_4 are almost at the same position, implying that the enlarged bandgap of Co_3O_4 quantum dots was mainly ascribed to the conduction band minimum (CBM) upshift. Due to the negative shift of the conduction band, Co_3O_4 quantum dots can split pure water into O_2 and H_2 stoichiometrically under visible light irradiation without any cocatalyst. This is the first report to date of Co_3O_4 photocatalysts capable of splitting pure water, which provides a new route to the development of nanosized photocatalysts for water splitting [64].

From single heterojunction to long range ordered homojunction

Semiconductor heterostructures can be engineered to combine functionalities that result from the bulk properties of their constituent phases with properties that are directly related to the electronic and atomic character of their interfaces [65]. The concept has been proven in photovoltaic cells and optoelectronic devices, where junction-type semiconductors show greatly improved efficiency compared with junction-free semiconductors [66]. Depending on the band gaps and the electronic affinity of semiconductors, semiconductor heterostructures can be divided into three different cases: type-I, type-II and type-III band alignment [67]. In a type-II band alignment, the band offsets in the conduction and valance bands go in the same direction, resulting in a band bending at the interface between two semiconductors. Such band bending consequently induces a built-in field, which drives the vectorial migration of the photogenerated charges at the interface, leading to a spatial separation of e^- and h^+ on different sides of the heterojunction. Most type-II heterojunctions have been obtained from two different semiconductors [68,69]. Matching of two semiconductor materials with both their band positions and crystal lattices is the key challenge of this strategy. Most recently, successful efforts have been made to fabricate heterojunctions of different phases of the same material. Bao and co-workers prepared CdS photocatalysts with different phases for photocatalytic hydrogen production [70]. Interestingly, a higher photocatalytic activity is observed from the composite of hexagonal and cubic CdS as compared to single hexagonal or cubic

CdS. However, the relation of electronic interaction between different phases with the photocatalytic activities was not discussed in their study [70]. Li and co-workers have demonstrated the greatly enhanced photocatalytic overall water splitting over an α–β phase junction of Ga_2O_3 [71]. The improved photocatalytic activity results from the efficient charge separation and transfer across the α–β phase junctions of the Ga_2O_3 particles.

We have found that spherical twin-containing noble-metal-free $Cd_{0.5}Zn_{0.5}S$ is a superb photocatalyst for hydrogen production, showing a QE of 43% at 425 nm [72]. However, the low density of twin planes and the insufficient control of the crystal shape in these catalysts inspired us to further improve their photocatalytic efficiency by fabricating more effective junctions. Recently, we reported a twinned $Cd_{0.5}Zn_{0.5}S$ anisotropic nanocrystal with controllable aspect ratios and a high percentage of long-range ordered twin planes. As shown in Figure 10, the densely distributed rotational twin planes are found to be parallel to each other and perpendicular to the <111> direction. More interestingly, zinc-blende (ZB) and wurtzite (WZ) segments alternatively occur along the <111> direction of the designed material, resulting in its unique optical and electrical properties. It was also shown that type-II staggered band alignment between WZ and ZB segments resulted in an immense number of homojunctions in a specific dimension. Unlike the well-known heterojunctions, no foreign-atom doping or combination was required for the formation of these junctions, resulting in the homogeneity of the materials themselves and thereby enabling us to engineer the necessary semiconductor band structures

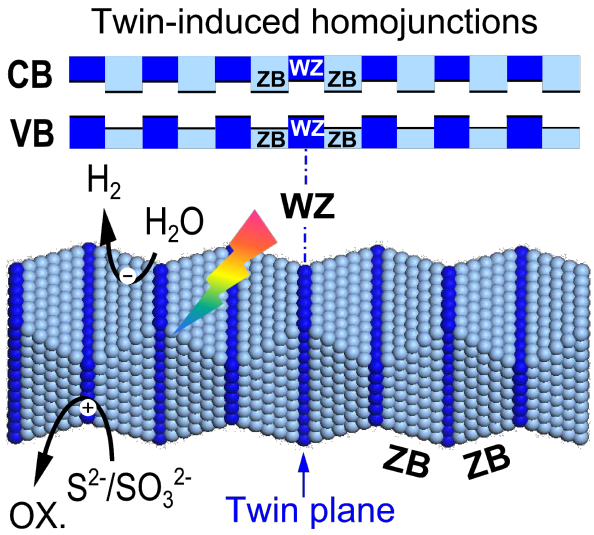

Figure 10: Illustration of twin-induced 1D long range ordered homojunctions over $Cd_{0.5}Zn_{0.5}S$ with alternative zinc-blende (ZB) and wurtzite (WZ) segments.

more exactly. Notably, it was possible to raise the QE for the photocatalytic hydrogen formation to 62% because of the improved efficiency in charge separation [73]. These dense homojunctions are clearly superior to the single homojunction formed by introduction of a thin p-type layer on n-type α-Fe_2O_3 and creating a built-in field as reported in [74]. We suggest that our results have the potential to lead to a new general method for the synthesis of new, highly active photocatalysts by the application of our method to other semiconducting materials.

Conclusion

With the rapid development of creative nanomaterials for new energy applications [75], the nanostructures have also been found essential for achieving high efficient photocatalysts and cocatalysts. The heart of the study is the nanostructure design from functionalized nanosized morphology and surfaces of relatively larger scale to the precise tuning of crystal facets and junctions in much smaller scale. In the process of our study, we firstly attempted the simple combination of two or more semiconductors both physically and chemically. Parallel to this advancement, nanosized functionalized morphology and surfaces are employed in these hetero-combinations to obtain enhanced charge generation and separation. We then elaborate on the combined control of band structure and morphology to reveal the synergistic effects by coupling two or three kinds of modifications in one semiconductor. In this case, enhanced matching of two components in one hybrid photocatalyst, in terms of morphologic contact, band structure and crystal lattices could be achieved. Especially, various heterostructure architectures with combined functionality of the constituent phases are suggested to be promising to address the primary requirements for an efficient photocatalytic generation of hydrogen by using solar energy: visible-light activity, chemical stability, appropriate band-edge characteristics, and potential for low-cost fabrication. Finally, we highlight the heterostructure design at a precise nanoscale control, such as materials of same composition but different phases and/or from heterojunction to homojunction engineering. As has been demonstrated by our twinned $Cd_{0.5}Zn_{0.5}S$, an ordered homojunction is much effective than a disordered one. Co-existence of two phases in same semiconducting material in an ordered way, preferably with type-II band alignment, is therefore recommended to be the most desired nanostructures enabling photo-chemistry or -electricity conversion. How to construct such nanostructures in a low-cost and time-efficient way is the challenge ahead.

Acknowledgements

The authors gratefully acknowledge the financial support from the National Natural Science Foundation of China (No. 51236007, 21276206 and 51121092) and National Basic Research Program of China (No. 2009CB220000).

References

1. Chen, X. B.; Shen, S. H.; Guo, L. J.; Mao, S. S. *Chem. Rev.* **2010,** *110,* 6503–6570. doi:10.1021/cr1001645
2. Maeda, K.; Teramura, K.; Lu, D.; Takata, T.; Saito, N.; Inoue, Y.; Domen, K. *Nature* **2006,** *440,* 295. doi:10.1038/440295a
3. Kudo, A.; Miseki, Y. *Chem. Soc. Rev.* **2009,** *38,* 253–278. doi:10.1039/b800489g
4. Jing, D. W.; Yao, S.; Cheng, P.; Liu, M.; Shi, J. W.; Zhao, L.; Yan, W.; Guo, L. J. *AIChE J.* **2012,** *58,* 3593–3596. doi:10.1002/aic.13833
5. Jing, D. W.; Liu, H.; Zhang, X. H.; Zhao, L.; Guo, L. J. *Energy Convers. Manage.* **2009,** *50,* 2919–2926. doi:10.1016/j.enconman.2009.07.012
6. Jing, D. W.; Guo, L. J.; Zhao, L.; Zhang, X. M.; Liu, H.; Li, M. T.; Shen, S. H.; Liu, G. J.; Hu, X. W.; Zhang, X. H.; Zhang, K.; Ma, L. J.; Guo, P. H. *Int. J. Hydrogen Energy* **2010,** *35,* 7087–7097. doi:10.1016/j.ijhydene.2010.01.030
7. Fujishima, A.; Honda, K. *Nature* **1972,** *238,* 37–38. doi:10.1038/238037a0
8. Van Gerven, T.; Mul, G.; Moulijn, J.; Stankiewicz, A. *Chem. Eng. Process.* **2007,** *46,* 781–789. doi:10.1016/j.cep.2007.05.012
9. Kresge, C. T.; Leonowicz, M. E.; Roth, W. J.; Vartuli, J. C.; Beck, J. S. *Nature* **1992,** *359,* 710–712. doi:10.1038/359710a0
10. Takahara, Y.; Konde, J.; Takata, N. T.; Lu, D.; Domen, K. *Chem. Mater.* **2001,** *13,* 1194–1199. doi:10.1021/cm000572i
11. Jitputti, J.; Pavasupree, S.; Suzuki, Y.; Yoshikawa, S. *J. Solid State Chem.* **2007,** *180,* 1743–1749. doi:10.1016/j.jssc.2007.03.018
12. Chen, X.; Yu, T.; Fan, X.; Zhang, H.; Li, Z.; Ye, J.; Zou, Z. *Appl. Surf. Sci.* **2007,** *253,* 8500–8506. doi:10.1016/j.apsusc.2007.04.035
13. Liu, S.-H.; Huang, Y.-J.; Lin, K.-S.; Hsiao, M.-C. *Energy Sources* **2003,** *25,* 591–596. doi:10.1080/00908310390195651
14. Zhao, D.; Budhi, S.; Rodriguez, A.; Koodali, R. T. *Int. J. Hydrogen Energy* **2010,** *35,* 5276–5283. doi:10.1016/j.ijhydene.2010.03.087
15. Jing, D. W.; Zhang, Y. J.; Guo, L. J. *Chem. Phys. Lett.* **2005,** *415,* 74–78. doi:10.1016/j.cplett.2005.08.080
16. Nishikawa, T.; Nakajima, T.; Shinohara, Y. *J. Mol. Struct.* **2001,** *545,* 67–74. doi:10.1016/S0166-1280(01)00394-3
17. Jing, D. W.; Guo, L. J. *J. Phys. Chem. Solids* **2007,** *68,* 2363–2369. doi:10.1016/j.jpcs.2007.07.045
18. Sreethawong, T.; Junbua, C.; Chavadej, S. *J. Power Sources* **2009,** *190,* 513–524. doi:10.1016/j.jpowsour.2009.01.054
19. Lee, Y.; Chi, C.; Liau, S. *Chem. Mater.* **2010,** *22,* 922–927. doi:10.1021/cm901762h
20. Jing, D. W.; Guo, L. J. *Catal. Commun.* **2007,** *8,* 795–799. doi:10.1016/j.catcom.2006.09.009
21. Shen, S. H.; Chen, J.; Koodali, R. T.; Hu, Y. F.; Xiao, Q. F.; Zhou, J. G.; Wang, X. X.; Guo, L. J. *Appl. Catal., B* **2014,** *150–151,* 138–146. doi:10.1016/j.apcatb.2013.12.014
22. Shen, S. H.; Guo, L. J. *Catal. Today* **2007,** *129,* 414–420. doi:10.1016/j.cattod.2006.08.070
23. Li, Y. H.; Xing, J.; Chen, Z. J.; Li, Z.; Tian, F.; Zheng, L. R.; Wang, H. F.; Hu, P.; Zhao, H. J.; Yang, H. G. *Nat. Commun.* **2013,** *4,* 2500. doi:10.1038/ncomms3500
24. Xing, J.; Jiang, H. B.; Chen, J. F.; Li, Y. H.; Wu, L.; Yang, S.; Zheng, L. R.; Wang, H. F.; Hu, P.; Zhao, H. J.; Yang, H. G. *J. Mater. Chem. A* **2013,** *1,* 15258–15264. doi:10.1039/c3ta13167j
25. Zong, X.; Yan, H.; Wu, G.; Ma, G.; Wen, F.; Wang, L.; Li, C. *J. Am. Chem. Soc.* **2008,** *130,* 7176–7177. doi:10.1021/ja8007825
26. Jang, J. S.; Ham, D. J.; Lakshminarasimhan, N.; Choi, W.; Lee, J. S. *Appl. Catal., A* **2008,** *346,* 149–154. doi:10.1016/j.apcata.2008.05.020
27. Zhang, W.; Wang, Y. B.; Wang, Z.; Zhong, Z. Y.; Xu, R. *Chem. Commun.* **2010,** *46,* 7631–7633. doi:10.1039/c0cc01562h
28. Yang, J. H.; Wang, D. E.; Han, H. X.; Li, C. *Acc. Chem. Res.* **2013,** *46,* 1900–1909. doi:10.1021/ar300227e
29. Li, N. X.; Zhou, B. Y.; Guo, P. H.; Zhou, J. C.; Jing, D. W. *Int. J. Hydrogen Energy* **2013,** *38,* 11268–11277. doi:10.1016/j.ijhydene.2013.06.067
30. Jing, D. W.; Guo, L. J. *J. Phys. Chem. B* **2006,** *110,* 11139–11145. doi:10.1021/jp060905k
31. Tsuji, I.; Kato, H.; Kobayashi, H.; Kudo, A. *J. Am. Chem. Soc.* **2004,** *126,* 13406–13413. doi:10.1021/ja048296m
32. Jang, J. S.; Li, W.; Oh, S. H.; Lee, J. S. *Chem. Phys. Lett.* **2006,** *425,* 278–282. doi:10.1016/j.cplett.2006.05.031
33. Chen, Y. B.; Wang, L. Z.; Lu, G. Q.; Yao, X. D.; Guo, L. J. *J. Mater. Chem.* **2011,** *21,* 5134–5141. doi:10.1039/c0jm03945d
34. Chen, Y. B.; Guo, L. J. *J. Mater. Chem.* **2012,** *22,* 7507–7514. doi:10.1039/c2jm16797b
35. Yang, H. G.; Sun, C. H.; Qiao, S. Z.; Zou, J.; Liu, G.; Smith, S. C.; Cheng, H. M.; Lu, G. Q. *Nature* **2008,** *453,* 638–641. doi:10.1038/nature06964
36. Li, R.; Zhang, F.; Wang, D.; Yang, J.; Li, M.; Zhu, J.; Zhou, X.; Han, H.; Li, C. *Nat. Commun.* **2013,** *4,* 1432. doi:10.1038/ncomms2401
37. Martin, D. J.; Umezawa, N.; Chen, X. W.; Ye, J. H.; Tang, J. W. *Energy Environ. Sci.* **2013,** *6,* 3380–3386. doi:10.1039/c3ee42260g
38. Jang, E. S.; Won, J. H.; Hwang, S. J.; Choy, J. H. *Adv. Mater.* **2006,** *18,* 3309–3312. doi:10.1002/adma.200601455
39. Wang, X. W.; Liu, G.; Chen, Z. G.; Li, F.; Wang, L. Z.; Lu, G. Q.; Cheng, H. M. *Chem. Commun.* **2009,** 3452. doi:10.1039/b904668b
40. Pan, J.; Liu, G.; Lu, G. Q.; Cheng, H. M. *Angew. Chem., Int. Ed.* **2011,** *50,* 2133–2137. doi:10.1002/anie.201006057
41. Jing, D. W.; Liu, M. C.; Chen, Q. Y.; Guo, L. J. *Int. J. Hydrogen Energy* **2010,** *35,* 8521–8527. doi:10.1016/j.ijhydene.2010.04.170
42. Huang, G.; Shi, R.; Zhu, Y. *J. Mol. Catal. A* **2011,** *348,* 100–105. doi:10.1016/j.molcata.2011.08.013
43. Luo, F.; Wu, D.; Gao, L.; Lian, S.; Wang, E.; Kang, Z.; Lan, Y.; Xu, L. *J. Cryst. Growth* **2005,** *285,* 534–540. doi:10.1016/j.jcrysgro.2005.09.032
44. Paracchino, A.; Laporte, V.; Sivula, K.; Grätzel, M.; Thimsen, E. *Nat. Mater.* **2011,** *10,* 456–461. doi:10.1038/nmat3017
45. Zhang, L. Z.; Shi, J. W.; Liu, M. C.; Jing, D. W.; Guo, L. J. *Chem. Commun.* **2014,** *50,* 192–194. doi:10.1039/c3cc46423g
46. Shi, J. W.; Guo, L. J. *Prog. Nat. Sci. Mater. Int.* **2012,** *22,* 592–615. doi:10.1016/j.pnsc.2012.12.002
47. Shi, J. W.; Ye, J.; Ma, L.; Ouyang, S.; Jing, D.; Guo, L. J. *Chem.–Eur. J.* **2012,** *18,* 7543–7551. doi:10.1002/chem.201102807
48. Shi, J. W.; Ye, J. H.; Zhou, Z. H.; Li, M. T.; Guo, L. J. *Chem.–Eur. J.* **2011,** *17,* 7858–7867. doi:10.1002/chem.201003755
49. Shi, J. W.; Ye, J. H.; Li, Q. Y.; Zhou, Z. H.; Tong, H.; Xi, G. C.; Guo, L. J. *Chem.–Eur. J.* **2012,** *18,* 3157–3162. doi:10.1002/chem.201102214
50. Osterloh, F. E. *Chem. Soc. Rev.* **2013,** *42,* 2294–2320. doi:10.1039/c2cs35266d
51. Shen, S. H.; Zhao, L.; Guo, L. J. *J. Phys. Chem. Solids* **2008,** *69,* 2426–2432. doi:10.1016/j.jpcs.2008.04.035
52. Shen, S. H.; Zhao, L.; Guo, L. J. *Int. J. Hydrogen Energy* **2008,** *33,* 4501–4510. doi:10.1016/j.ijhydene.2008.05.043

53. Shen, S. H.; Zhao, L.; Guo, L. J. *Mater. Res. Bull.* **2009,** *44,* 100–105. doi:10.1016/j.materresbull.2008.03.027
54. Zhang, K.; Guo, L. J. *Catal. Sci. Technol.* **2013,** *3,* 1672–1690. doi:10.1039/c3cy00018d
55. Kudo, A.; Kato, H.; Tsuji, I. *Chem. Lett.* **2004,** *33,* 1534–1539. doi:10.1246/cl.2004.1534
56. Zhang, X. H.; Jing, D. W.; Liu, M. C.; Guo, L. J. *Catal. Commun.* **2008,** *9,* 1720–1724. doi:10.1016/j.catcom.2008.01.032
57. Zhang, K.; Jing, D. W.; Chen, Q.; Guo, L. J. *Int. J. Hydrogen Energy* **2010,** *35,* 2048–2057. doi:10.1016/j.ijhydene.2009.12.143
58. Zhang, K.; Zhou, Z. H.; Guo, L. J. *Int. J. Hydrogen Energy* **2011,** *36,* 9469–9478. doi:10.1016/j.ijhydene.2011.05.058
59. Kapoor, M. P.; Inagaki, S.; Yoshida, H. *J. Phys. Chem. B* **2005,** *109,* 9231–9238. doi:10.1021/jp045012b
60. Jing, D. W.; Guo, L. J. *J. Phys. Chem. C* **2007,** *111,* 13437–13441. doi:10.1021/jp071700u
61. Jing, D. W.; Liu, M. C.; Guo, L. J. *Catal. Lett.* **2010,** *140,* 167–171. doi:10.1007/s10562-010-0442-9
62. Kaga, H.; Saito, K.; Kudo, A. *Chem. Commun.* **2010,** *46,* 3779–3781. doi:10.1039/b927362j
63. Li, Y. X.; Chen, G.; Wang, Q.; Wang, X.; Zhou, A. K.; Shen, Z. Y. *Adv. Funct. Mater.* **2010,** *20,* 3390–3398. doi:10.1002/adfm.201000604
64. Zhang, N.; Shi, J. W.; Mao, S. S.; Guo, L. J. *Chem. Commun.* **2014,** *50,* 2002–2004. doi:10.1039/c3cc48026g
65. Kronawitter, C. X.; Vayssieres, L.; Shen, S. H.; Guo, L. J.; Wheeler, D. A.; Zhang, J. Z.; Antoun, B. R.; Mao, S. S. *Energy Environ. Sci.* **2011,** *4,* 3889–3899. doi:10.1039/c1ee02186a
66. Jang, J. S.; Kim, H. G.; Lee, J. S. *Catal. Today* **2012,** *185,* 270–277. doi:10.1016/j.cattod.2011.07.008
67. Wang, Y. J.; Wang, Q. S.; Zhan, X. Y.; Wang, F. M.; Safdar, M.; He, J. *Nanoscale* **2013,** *5,* 8326–8339. doi:10.1039/c3nr01577g
68. McDaniel, H.; Heil, P. E.; Tsai, C. L.; Kim, K. K.; Shim, M. *ACS Nano* **2011,** *5,* 7677–7683. doi:10.1021/nn2029988
69. Guo, P. H.; Jiang, J. G.; Shen, S. H.; Guo, L. J. *Int. J. Hydrogen Energy* **2013,** *38,* 13097–13103. doi:10.1016/j.ijhydene.2013.01.184
70. Bao, N.; Shen, L.; Takata, T.; Domen, K.; Gupta, A.; Yanagisawa, K.; Grimes, C. A. *J. Phys. Chem. C* **2007,** *111,* 17527–17534. doi:10.1021/jp076566s
71. Wang, X.; Xu, Q.; Li, M. R.; Shen, S.; Wang, X. L.; Wang, Y. C.; Feng, Z. C.; Shi, J. Y.; Han, H. X.; Li, C. *Angew. Chem., Int. Ed.* **2012,** *51,* 13089–13092. doi:10.1002/anie.201207554
72. Liu, M.; Wang, L.; Lu, G.; Yao, X.; Guo, L. *Energy Environ. Sci.* **2011,** *4,* 1372–1378. doi:10.1039/c0ee00604a
73. Liu, M. C.; Jing, D. W.; Zhou, Z. H.; Guo, L. J. *Nat. Commun.* **2013,** *4,* 2278. doi:10.1038/ncomms3278
74. Lin, Y. J.; Xu, Y.; Mayer, M. T.; Simpson, Z. I.; McMahon, G.; Zhou, S.; Wang, D. *J. Am. Chem. Soc.* **2012,** *134,* 5508–5511. doi:10.1021/ja300319g
75. Mao, S. S.; Chen, X. *Int. J. Energy Res.* **2007,** *31,* 619–636. doi:10.1002/er.1283

License and Terms

This is an Open Access article under the terms of the Creative Commons Attribution License (http://creativecommons.org/licenses/by/2.0), which permits unrestricted use, distribution, and reproduction in any medium, provided the original work is properly cited.

The license is subject to the *Beilstein Journal of Nanotechnology* terms and conditions: (http://www.beilstein-journals.org/bjnano)

The definitive version of this article is the electronic one which can be found at: doi:10.3762/bjnano.5.113

BEILSTEIN JOURNAL OF NANOTECHNOLOGY

Characterization and photocatalytic study of tantalum oxide nanoparticles prepared by the hydrolysis of tantalum oxo-ethoxide $Ta_8(\mu_3\text{-}O)_2(\mu\text{-}O)_8(\mu\text{-}OEt)_6(OEt)_{14}$

Subia Ambreen[1], N D Pandey[1], Peter Mayer[2] and Ashutosh Pandey[*1]

Full Research Paper

Open Access

Address:
[1]Department of Chemistry, Motilal Nehru National Institute of Technology, Allahabad, 211004, India and [2]Department Chemie und Biochemie, Universität München, Butenandtstraße 5–13, 81377 München, Germany

Email:
Ashutosh Pandey[*] - apandey70@yahoo.com

* Corresponding author

Keywords:
bandgap; tantalum-oxo-ethoxide; Tauc plot; tantalum pentoxide (Ta_2O_5)

Beilstein J. Nanotechnol. **2014,** *5,* 1082–1090.
doi:10.3762/bjnano.5.121

Received: 07 January 2014
Accepted: 25 June 2014
Published: 18 July 2014

This article is part of the Thematic Series "Photocatalysis".

Guest Editor: R. Xu

© 2014 Ambreen et al; licensee Beilstein-Institut.
License and terms: see end of document.

Abstract

$Ta_8(\mu_3\text{-}O)_2(\mu\text{-}O)_8(\mu\text{-}OEt)_6(OEt)_{14}$ (**1**) was obtained by the controlled hydrolysis of tantalum ethoxide $Ta(OEt)_5$ in the presence of ammonia. Compound **1** is considered as the intermediate building block in the sol–gel polymerization of $Ta(OEt)_5$. Further hydrolysis of compound **1** yielded nanoparticles of Ta_2O_5, which were characterized by various techniques such as TGA-DTA-DSC, UV–vis DRS, XRD, SEM, TEM, particle size analyzer (DLS) and the Brunauer–Emmett–Teller (BET) method. The band gap of the particles was calculated by using the Tauc plot. The photocatalytic activity of Ta_2O_5 nanoparticles was tested by the degradation of the organic dye rhodamine B.

Introduction

Metal alkoxides, being excellent precursors in the sol–gel process for preparation of metal oxides have attained huge attention of researchers. Several attempts have been made in order to modify the highly moisture sensitive metal alkoxides into less sensitive species [1-4] as precursors for metal oxides with new and better properties. However, due to the fast kinetics of the hydrolysis and condensation reactions in the sol–gel route, relatively little information is available concerning the progressive structural evolution in the transition metal oxide system in general. But sometimes new species, metal oxo-alkoxides [5-9], are obtained which have been known to be the direct molecular precursors for oxide phases in sol–gel technology. These oxo-species being treated as intermediates between the metal alkoxides and the metal oxides are very

significant as they clearly indicate the route for the formation of oxides through hydrolysis. It is suggested that the hydrolysis of a metal alkoxide starts with the formation of a hydroxo derivative, which then forms the oxo derivative in a condensation step (Equation 1 and Equation 2).

$$M(OR)_x + H_2O \rightarrow M(OH)(OR)_{x-1} + ROH \quad (1)$$

$$M(OH)(OR)_{x-1} + M(OR)_x \rightarrow M_2O(OR)_{2x-2} + ROH \quad (2)$$

The investigation of the hydrolysis of titanium alkoxides showed that the reactions were very fast. Therefore the initial hydroxo compounds were not isolated [10]. Similar results were obtained for alkoxides of zirconium [11], tin(IV) [12], and uranium(V) [12]. Condensation can also occur even before hydrolysis via ether elimination between alkoxy groups leading to the formation of oxo bridges. The smaller size of μ-oxo ligands coupled with the tendency of metal centers for coordination expansion, favors the condensation via ether elimination.

Oxo-alkoxides, being less reactive toward hydrolysis and condensation, are more stable than the corresponding alkoxides. They are generally observed for large and electropositive metals. Oxo-alkoxides are normally made of edge sharing MO_6 octahedra. Usually the physical properties of metal oxo-alkoxides are decided by the degree of hydrolysis and the nature of the alkyl group. There is a tendency for lower volatility and solubility with higher degrees of hydrolysis and, therefore, oligomerization. Amongst the transition metal oxides, Ta_2O_5 has attracted growing interest due to its distinct properties such as large ion diffusion coefficient and high electrochromic reversibility, high dielectric constant, high refractive index, high chemical stability, large band gap [13-15] and photocatalytic activity for overall water decomposition and organic pollutant degradation [16-21].

The present work deals with the study of the controlled hydrolysis of tantalum ethoxide in the presence of ammonia and to prepare tantalum pentaoxide nanoparticles. In this process the stable intermediate tantalum oxo-ethoxide with composition $Ta_8(\mu_3\text{-}O)_2(\mu\text{-}O)_8(\mu\text{-}OEt)_6(OEt)_{14}$ (**1**) was isolated. When **1** was subjected to further hydrolysis it yielded nanoparticles of tantalum oxide after calcination at 750 °C for four hours. The photocatalytic activity of Ta_2O_5 nanoparticles was studied over the degradation of organic dye rhodamine B (RhB).

Results and Discussion

Tantalum penta-ethoxide was dissolved in toluene and with the aim to examine the effect of hydrolysis in basic medium, wet ammonia gas was purged into it with continuous stirring. After 1 h at pH 8.0, a white solid was formed which was separated, re-dissolved in toluene and kept at low temperature for crystallization to give compound **1** as white shiny crystals in two days. The formation of tantalum oxo-alkoxide can be described as a result of following reactions (Equation 3 and Equation 4).

$$4Ta(OEt)_5 + 10H_2O \rightarrow Ta_4(OEt)_{10}(OH)_{10} + 10EtOH \quad (3)$$

$$2Ta_4(OEt)_{10}(OH)_{10} \rightarrow Ta_8(OEt)_{20}O_{10} + 10H_2O \quad (4)$$

^{1}H NMR of compound **1** shows many sets for ethoxy groups suggesting the presence of different types of ethoxy groups such as cis pairs of terminal OEt ligands, single terminal OEt ligands and μ-OEt groups.

Crystal structure

Compound **1** was found in the monoclinic space group $P21/n$ with $Z = 2$. The molecular structure (Figure 1) consists of a centrosymmetric unit of formula $Ta_8(\mu_3\text{-}O)_2(\mu\text{-}O)_8(\mu\text{-}OEt)_6(OEt)_{14}$ (**1**). Each molecule has two $Ta_3(\mu_3\text{-}O)\text{-}(\mu\text{-}OEt)_3(OEt)_5$ units linked with two $Ta(\mu\text{-}O)_4(OEt)_2$ moieties by four μ-oxo ligands. All of the tantalum atoms display distorted octahedral configurations. Six tantalum atoms are bonded to cis pairs of terminal ethoxy ligands and the other two are bonded to single ethoxy ligands. The terminal ligands are in trans position to the μ_3- and μ-oxo atoms. The ethoxy groups are of two types. Out of the twenty ethoxy groups, fourteen are terminal while six (O8, O9, O12 and O8*, O9*, O12*) bridge the tantalum atoms. The tantalum atoms have two environments. Four tantalum atoms are coordinated to two terminal ethoxy, two bridging ethoxy, one μ-O and one μ_3-O ligands while two tantalum atoms

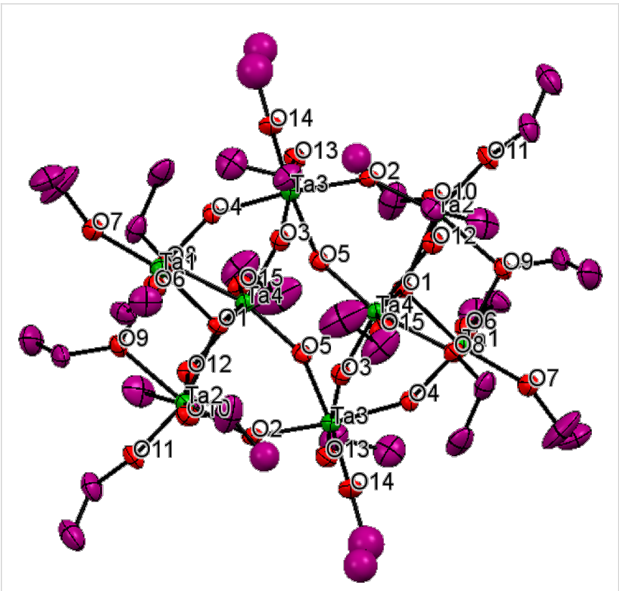

Figure 1: ORTEP representation of the molecular structure of **1** in the crystal (hydrogen atoms are omitted for clarity).

are coordinated with two terminal ethoxy and four μ-O groups. The TaO_6 octahedra are distorted, resulting in O–Ta–O angles, which differ from those for a regular octahedron. Some bond lengths and bond angles are presented in Table 1 and Table 2 respectively. Ta–O bond lengths for the terminal ethoxy ligands are shorter (av. 1.897 Å) than the bridging ethoxy ligands (av. 2.153 Å). The μ-oxo bridges are shorter than the μ_3-O bond lengths (approx. 2.0585 Å). The μ_3-oxo atom, O1 is ligated in pyramidal manner to three tantalum atoms with an average bond angle of 108.87°. The bond dimensional data are in accordance with previously reported values [5,9]. Full crystallographic details have been deposited to the Cambridge Crystallographic Data Centre. Copies of the data can be obtained free of charge on request from the CCDC, 12 Union Road, Cambridge CB2 1EZ, UK; fax: (+44) 1223-336-033; or e-mail: deposit@ccdc.cam.ac.uk or http://www.ccdc.cam.ac.uk/conts/retrieving.html quoting the deposition number CCDC 951412 for **1**.

Table 1: Selected bond lengths.

bond	length	bond	length
O1–Ta1	2.0629(1)	O7–Ta1	1.8711
O1–Ta2	2.0345(1)	O8–Ta1	2.1061(1)
O1–Ta4	2.0719(1)	O8–Ta4	2.1556(1)
O2–Ta2	1.8577	O9–Ta1	2.1533(1)
O2–Ta3	1.9928	O9–Ta2	2.1319(1)
O3–Ta3	2.0039(1)	O10–Ta2	1.8928
O3–Ta4	1.8544(1)	O11–Ta2	1.8669
O4–Ta3	2.0167(1)	O12–Ta2	2.1149(1)
O4–Ta1	1.8411	O12–Ta4	2.1725(1)
O5–Ta3	2.0238(1)	O13–Ta3	1.9083
O5–Ta4	1.8455	O14–Ta3	1.8783(1)
O6–Ta1	1.8927(1)	O15–Ta4	1.8671

Table 2: Selected bond angles.

bond	angle	bond	angle
Ta1–O1–Ta2	110.85	O9–Ta2–O11	89.83
Ta1–O1–Ta4	107.48	O9–Ta2–O12	87.09
Ta2–O1–Ta4	108.28	O10–Ta2–O11	100.04
Ta2–O2–Ta3	144.86	O10–Ta2–O12	167.96
Ta3–O3–Ta4	145.34	O11–Ta2–O12	91.4
Ta3–O4–Ta1	144.33	O2–Ta3–O3	90.31
Ta3–O5–Ta4	144.09	O2–Ta3–O4	173.29
Ta1–O8–Ta4	102.94	O2–Ta3–O5	85.31
Ta1–O9–Ta2	103.87	O2–Ta3–O13	96.48
Ta2–O12–Ta4	101.83	O2–Ta3–O14	89.15
O1–Ta1–O6	99.79	O3–Ta3–O4	83.84
O1–Ta1–O7	154.81	O3–Ta3–O5	84.94
O1–Ta1–O8	72.52	O3–Ta3–O13	168.36
O1–Ta1–O9	71.58	O3–Ta3–O14	95.05
O1–Ta1–O4	92.52	O4–Ta3–O5	90.89
O6–Ta1–O7	97.78	O4–Ta3–O13	88.77
O6–Ta1–O8	170.71	O4–Ta3–O14	94.62
O6–Ta1–O9	87.55	O5–Ta3–O13	86.2
O6–Ta1–O4	95.44	O5–Ta3–O14	174.46
O7–Ta1–O8	88.03	O13–Ta3–O14	94.49
O7–Ta1–O9	91.35	O3–Ta4–O15	101.71
O7–Ta1–O4	103.66	O3–Ta4–O1	91.83
O8–Ta1–O9	85.07	O3–Ta4–O5	101.59
O8–Ta1–O4	90.18	O3–Ta4–O8	88.23
O9–Ta1–O4	164.11	O3–Ta4–O12	161.79
O1–Ta2–O2	93.37	O15–Ta4–O1	157.42
O1–Ta2–O9	72.57	O15–Ta4–O5	101.66
O1–Ta2–O10	94.28	O15–Ta4–O8	90.91
O1–Ta2–O11	157.16	O15–Ta4–O12	91.7
O1–Ta2–O12	73.68	O1–Ta4–O5	93.07
O2–Ta2–O9	165.72	O1–Ta4–O8	71.34
O2–Ta2–O10	94.45	O1–Ta4–O12	71.76
O2–Ta2–O11	103.07	O5–Ta4–O8	161.98
O2–Ta2–O12	86.52	O5–Ta4–O12	87.48
O9–Ta2–O10	89.2	O8–Ta4–O12	79.2

Upon further subjecting to hydrolysis (pH 9.0), compound **1** initially gave a homogeneous gel which was heated to 80 °C before annealing at 750 °C to obtain Ta_2O_5 nanoparticles. The morphology and composition of Ta_2O_5 nanoparticles are greatly influenced by the pH value [22]. The agglomeration of nanoparticles is enhanced at low pH due to the fast rate of hydrolysis and acidic surface of Ta_2O_5 while at the pH values above 10, instead of Ta_2O_5, tantalate salts are formed [22].

Particle size and distribution of Ta_2O_5 nanoparticles

In order to study the size and distribution of the nanoparticles XRD, SEM, TEM and DLS measurements were carried out. Figure 2 shows the XRD patterns of calcined Ta_2O_5 nanoparticles. The peaks at 2θ values of 23.06, 28.62, 37.02, 46.94, 50.54, 55.72, 58.84, 64.18, and 71.30° revealed the Ta_2O_5 phase with an orthorhombic structure. The average crystallite size calculated from Scherrer formula was found to be 28 nm.

To reveal the morphology SEM image of the calcined Ta_2O_5 nanoparticles is shown in Figure 3. Evidently, Ta_2O_5 nanoparticles are irregularly shaped, agglomerated and exhibit a moderately uniform size distribution. The size distribution of the Ta_2O_5 nanoparticles was studied by DLS (Figure 4) in chloroform dispersion. Trioctylphosphine oxide (TOPO) was used as the surfactant for dispersing the nanoparticles in chloroform. It was found that the nanoparticles are almost uniformly distributed. TOPO is reported to fragment bigger nanoparticles or agglomerates into smaller ones. TOPO molecules attach to the metal oxide particle surface in such a manner that their

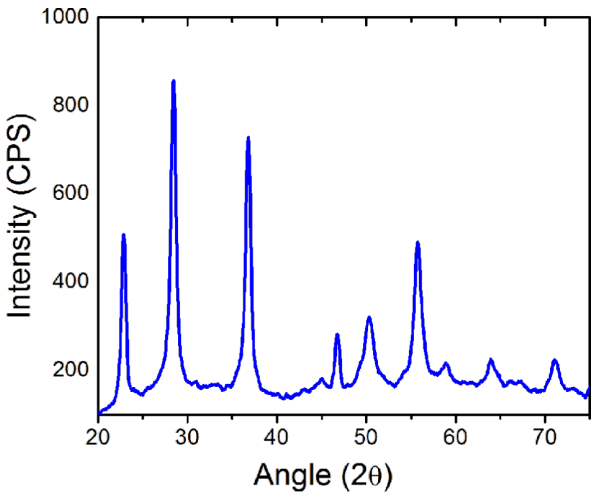

Figure 2: XRD pattern of Ta_2O_5 nanoparticles calcined at 750 °C for 4 h.

hydrophobic surfaces point toward the solvent and render colloidal stability and uniformity of the particles in organic solvents [23]. The TOPO coated particles suspended in chloroform were precipitated by adding excess methanol followed by centrifuging at 2000 rpm and re-dispersed in chloroform. A TEM image of the so obtained particles is shown in Figure 5.

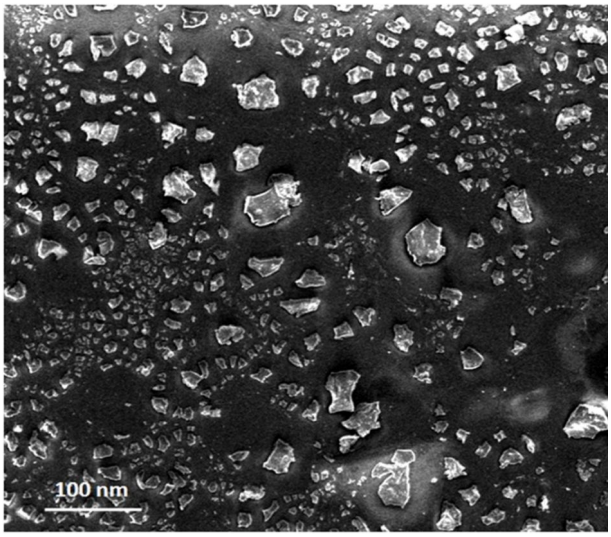

Figure 3: SEM image of Ta_2O_5 nanoparticles calcined at 750 °C for 4 h.

Thermal analysis of the prepared Ta_2O_5 nanoparticles

Thermogravimetry, differential thermal analysis and differential scanning calorimetry (TG/DTA/DSC) with a heating rate of 10 °C/min in a static air atmosphere were used to study the thermal stability of the as-prepared (dried) photocatalyst with

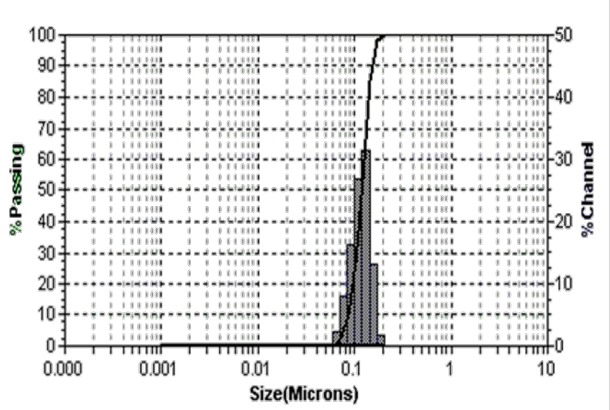

Figure 4: Size and distribution of TOPO-coated Ta_2O_5 nanoparticles in chloroform dispersion.

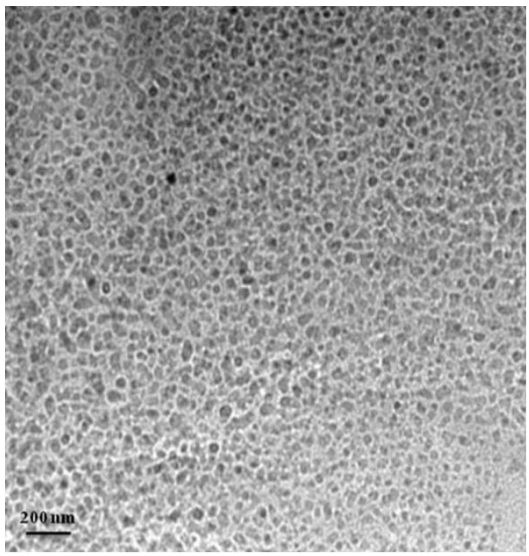

Figure 5: TEM image of the TOPO-coated Ta_2O_5 nanoparticles. The scale bar corresponds to 200 nm.

α-Al_2O_3 as the reference. Figure 6 shows the TG/DTA/DSC curves obtained from the dried gel of Ta_2O_5. The TGA graph shows a weight loss up to a temperature of 200 °C that is essentially attributed to dehydration. The decomposition of organic substances at 200–400 °C is caused by the decomposition of organic species inside the mesopores of the sample. Further the weight loss in the temperature range of 400–650 °C is due to a phase transition. An exothermic peak centered at 386.7 °C in the DTA curve supports the statements above. The observation is also supported by the DSC graph.

Band-gap determination of the Ta_2O_5 nanoparticles

The band gap energy (E_g) is a key feature of semiconductors that determines their applications in optoelectronics. The

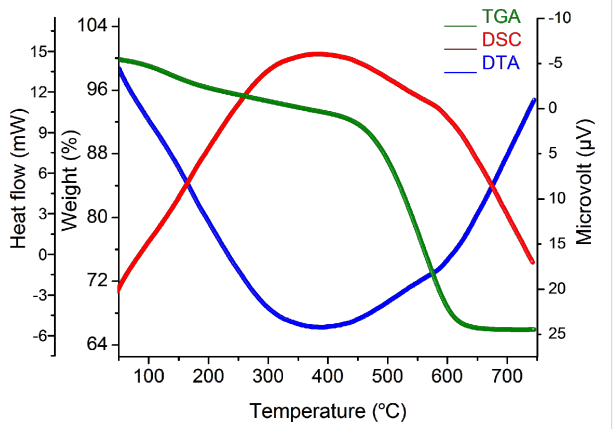

Figure 6: Thermogravimetry (TGA), differential thermal analysis (DTA) and differential scanning calorimetry (DSC) of the as-synthesized Ta_2O_5 nanoparticles.

nanoparticles were pressed into thick pellets and subject to diffuse reflectance measurement, which was done with a UV–vis spectrophotometer, attached with integrating sphere to spatially integrate the radiant flux. The pellets were placed at the entrance port of the integrating sphere. The absorption spectrum of Ta_2O_5 nanoparticles is shown in Figure 7. The reflectance data was converted to the absorption coefficient $F(R')$ values according to the Kubelka–Munk remission function [24-26] (Equation 5),

$$F\left(R'\right)=\left(1-R'\right)^2/2R=\alpha/S \tag{5}$$

where α is the absorption coefficient (cm^{-1}) and S is the dispersion factor. The absorption coefficient α is related to the incident photon energy by Equation 6:

$$\alpha = A\left(E-E_g\right)^n \tag{6}$$

A is a constant for the given material, E is the photon energy, E_g is the band gap energy and n is a constant of different values, 1/2, 3/2, 2 and 3, depending on the type of electronic transition, i.e., permitted/prohibited-direct or indirect transition. The band gap is calculated from a Tauc plot [27-30]. The band gap of the Ta_2O_5 nanoparticles as calculated from the extrapolation of the linear portion of the plot in the $\alpha h\nu^{1/2}$ vs $h\nu$ graph to the abscissa (Figure 8) was found to be 3.9 eV.

Brunauer–Emmett–Teller (BET) analysis

The BET surface area of the calcined Ta_2O_5 nanoparticles was found to be 38.35 m^2/g. The total volume of pores with diameter less than 32 Å at P/P_0 = 0.400214547 was estimated to be 0.022 cm^3/g (Figure 9 and Figure 10).

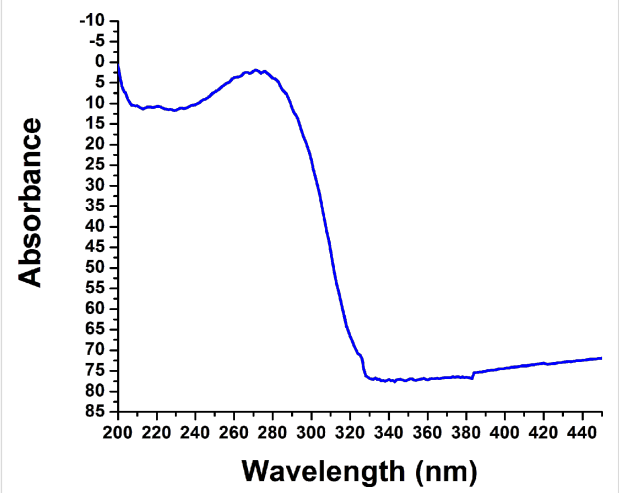

Figure 7: Solid state diffuse reflectance UV–vis spectra of Ta_2O_5 nanoparticles.

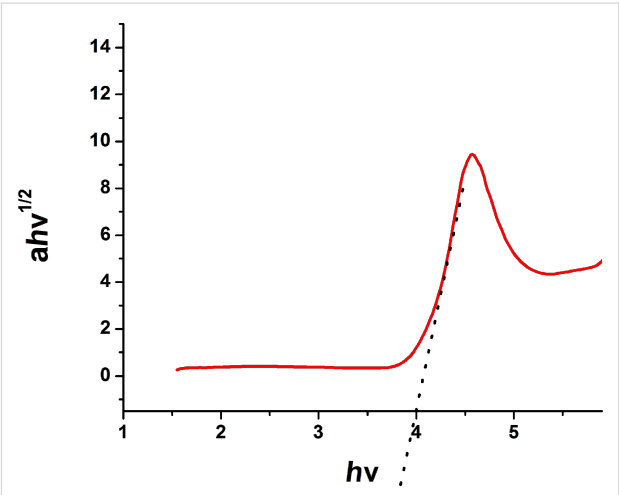

Figure 8: Calculation of band gap of Ta_2O_5 nanoparticles by Tauc plot.

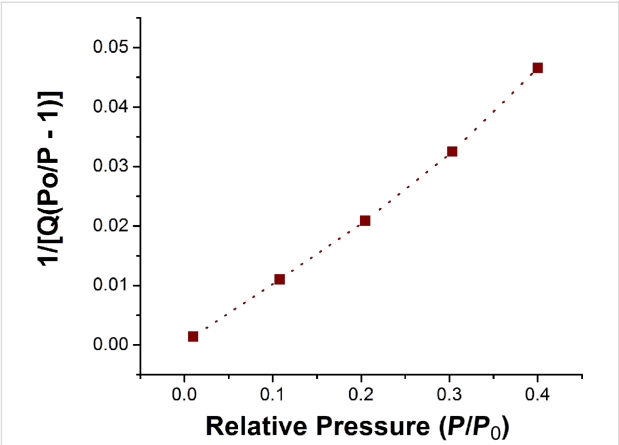

Figure 9: BET surface area plot of the calcined Ta_2O_5 nanoparticles.

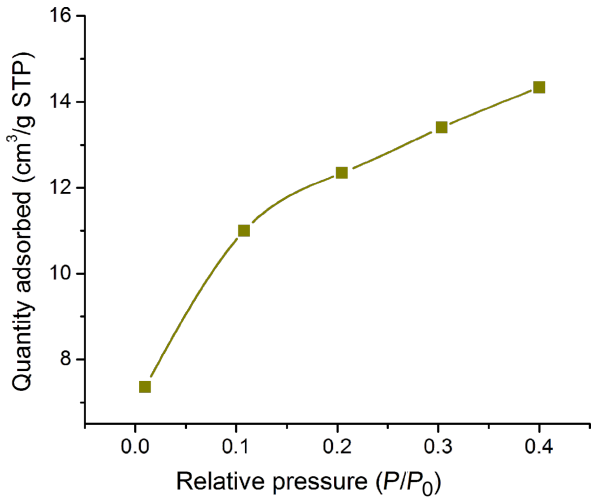

Figure 10: Degradation of rhodamine B by UV irradiation at 0.8 mg/mL catalyst loading.

Photocatalytic experiments

The photocatalytic activity was evaluated by the degradation of rhodamine B (RhB) under UV radiation for different amounts of Ta_2O_5. In each experiment Ta_2O_5 was added to 50 mL water and sonicated, followed by addition of RhB and exposure to UV light (λ = 365 nm) irradiation at room temperature. To attain an adsorption–desorption equilibrium, the dispersion was stirred in the dark for 45 min. Just before the irradiation an aliquot of 3.0 mL was taken and centrifuged. The supernatant was taken for recording the absorption spectrum at the initial concentration. After every 15 min, an aliquot of 3.0 mL was taken and the concentration of RhB was measured through the intensity of absorption (Figure 11).

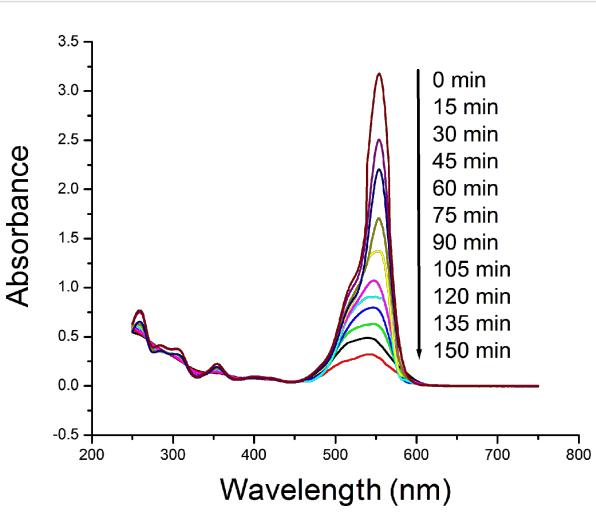

Figure 11: Effect of the concentration of Ta_2O_5 nanoparticles on the rate of degradation of rhodamine B.

Effect of catalyst concentration on the rate of degradation of rhodamine B

Figure 12 shows the degradation of dye for different of the catalyst loadings. It is clear that the optimum (89%) degradation of the dye was achieved (after 150 minutes) when 0.8 mg/mL of the photocatalyst was used in the experiment. However, when the used amounts of photocatalyst were 0.2 mg/mL, 0.5 mg/mL and 1.1 mg/mL, the degradation of dye occurred up to 55%, 68% and 74%, respectively. The amount of the photocatalyst was changed in each experiment while keeping the other factors invariable to study the optimum degradation of dye with respect to the amount of Ta_2O_5. By increasing the amount of Ta_2O_5 from 0.2 mg/mL to 0.8 mg/mL, the photocatalytic degradation rate was enhanced due to increase in the active sites accessible for the reaction on the surface of the catalyst. However, when the amount of catalyst was increased further, the rate of dye degradation was found to be lower. This may be due to the scattering of light from surface of the catalyst leading to the reduction in light penetration through the solution, which in turn reduces the rate of formation of radicals. Also, it may be assumed that the activated molecules get deactivated due to the collisions with the ground state molecules and thus reduce the degradation [31].

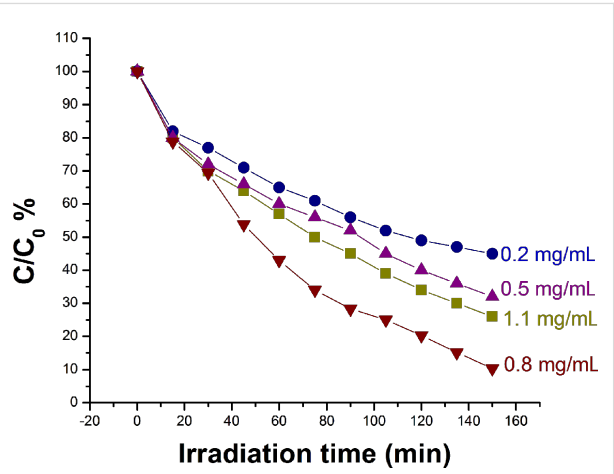

Figure 12: Effect of dye concentration on photocatalytic degradation.

Effect of dye concentration on the rate of degradation of rhodamine B

To study the effect of initial dye concentration on the photocatalytic degradation different amounts of rhodamine B were taken while keeping other factors constant. It was observed that on increasing the amount of dye from 2.5 ppm to 12.5 ppm the rate of degradation of the dye increases but a further increase of the dye concentration decreases the degradation rate (Figure 13). With the increase in dye concentration the number of dye molecules available for excitation and intersystem crossing

increases, which ultimately increases the rate of degradation. However, when the concentration of the dye was increased beyond a certain limit the excess of the dye serves as a filter for the light and also it does not allow the photons to reach the catalyst surface due to the reduced path length and, hence, retards the rate of degradation.

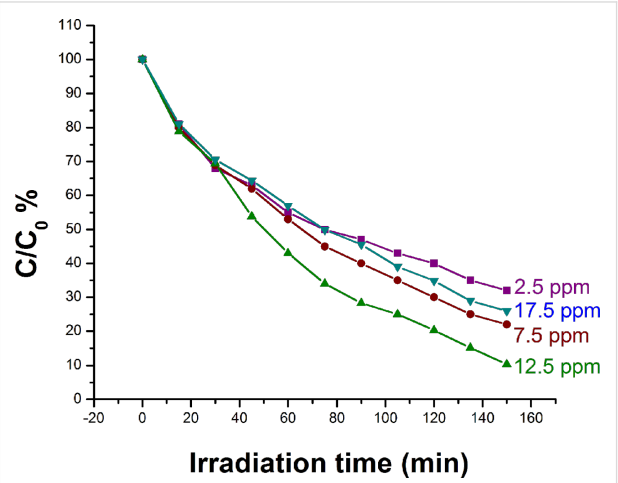

Figure 13: Effect of dye concentration on photocatalytic degradation.

Effect of the pH value on the rate of degradation of rhodamine B

Figure 14 shows the effect of the pH value on the rate of degradation of rhodamine B. The pH value was adjusted by using dilute solutions of HNO_3 and NaOH. Degradation of the dye was studied at pH 4, 7 and 10. It was observed that the rate of degradation of rhodamine B increases with the increase in pH from 4 to 7. It appears that, when more hydroxy ions (OH^-) are available, they combine with the holes (h^+) of the semiconductor resulting in the production of hydroxyl radicals. These radicals are responsible for the degradation of dye by oxidative process. However, a further increase of the pH value provides excess OH^- ions that get absorbed on the catalyst surface and obstruct the approach of the dye molecule to the catalyst surface and slow down the rate of degradation of rhodamine B (Figure 14). Moreover, the metal oxide particles agglomerate at acidic pH and hence the surface available for dye absorbance as well as the photon absorption is reduced.

Effect of calcination temperature

As-synthesized Ta_2O_5 powder was calcined in at 650 °C, 700 °C, 750 °C, and 800 °C. It was observed that Ta_2O_5 particles calcined at 750 °C possess best degradation efficiency (Figure 15). This may be due to increase in crystallinity and surface area with more active sites for photodegradation process when temperature is increased from 650 °C to 750 °C. A further increase in calcination temperature leads to bigger particles due

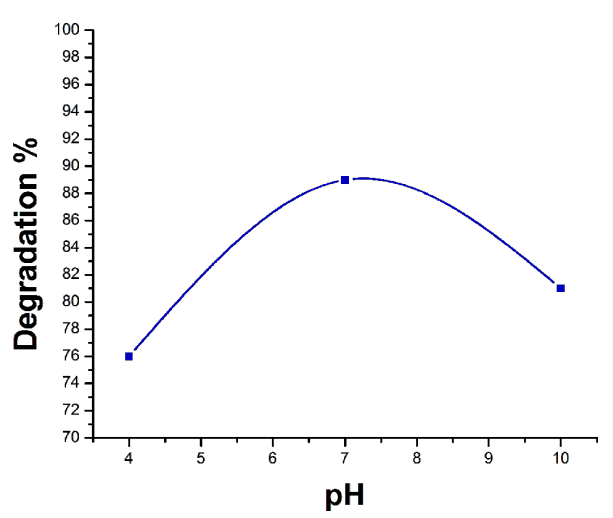

Figure 14: Effect of the pH value on the rate of degradation of rhodamine B.

to agglomeration at higher temperature, which ultimately reduces the rate of degradation of rhodamine B [32]. At higher temperature the catalyst is deactivated due to sintering processes that result in a low surface area and smaller number of active sites [33].

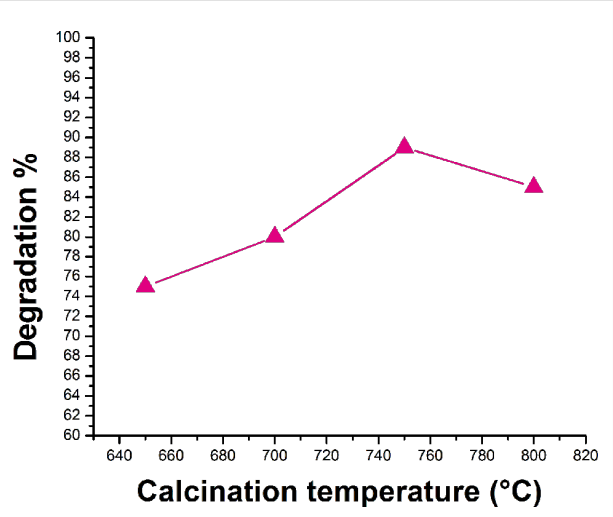

Figure 15: Effect of the calcination temperature on the rate of degradation of rhodamine B.

Conclusion

In summary, herein we report the formation of the tantalum oxo-ethoxide compound $Ta_8(\mu_3\text{-}O)_2(\mu\text{-}O)_8(\mu\text{-}OEt)_6(OEt)_{14}$ (**1**) through a sol–gel route in which hydrous ammonia gas was passed into a solution of tantalum ethoxide in toluene. Ta_2O_5 powder was obtained when a complete hydrolysis of **1** was allowed. After calcination the Ta_2O_5 nanoparticles were

employed for the degradation of the common organic dye rhodamine B. The rate of degradation of the dye highly depends on the various parameters such as amount of the catalyst, dye concentration, pH and calcination temperature.

Experimental

All the reactions before the catalyst preparation were carried out under anhydrous conditions by using Schlenk/vacuum line techniques. Tantalum ethoxide was purchased from Sigma-Aldrich. Ethanol was dried by standard procedure prior to use. Ammonia gas was first dried by passing through the columns of silica gel, fused calcium chloride and aluminum isopropoxide, then it was passed into the distilled water through a tube with a diameter of 7 mm. ^{1}H NMR spectra were recorded in C_6D_6 on a Bruker Biospin ARX spectrometer with TMS as internal reference. TGA/DTA/DSC was recorded by using a Diamond TG/DTAN instrument. X-ray diffraction patterns were recorded on SEIFERT XRD 3003 PTS Diffractometer System, using Cu Kα radiation. SEM images was obtained on an EVO MA 15 Zeiss at 15 kV. DLS measurements were carried out on a Nanotrac particle analyser. The surface area was calculated by applying the Brunauer–Emmett–Teller (BET) method to N_2 adsorption measurements on a Micromeritics ASAP 2020 instrument. TEM pictures were taken on a transmission electron microscope JEOL JEM-1011.

Preparation of **1**: Tantalum ethoxide (100 mg) was dissolved in dry toluene (20 mL). Ammonia gas (passed through 20 mL distilled water at a rate of 30 bubbles/minute) was bubbled into the solution at ambient temperature. After 1 h, a white solid precipitated. The solid was separated, re-dissolved in toluene and kept at −30 °C for crystallization to yield compound **1** in 45% yield (35 mg). ^{1}H NMR (25 °C) δ 1.33 (t, CH_3), 1.41 (t, CH_3), 1.49 (t, CH_3), 1.58 (t, CH_3), 1.62 (t, CH_3), 4.45 (q, CH_2), 4.59 (q, CH_2), 4.70 (q, CH_2), 4.90–5.00, 5.19 (q, CH_2), 5.23 (q, CH_2).

Preparation of Ta_2O_5 nanoparticles: Compound **1** was dissolved in toluene and ammonia gas was blown into it for 6 h to get a homogeneous gel. After treating the gel at 80 °C for 3h, a white solid powder was separated out, which was insoluble in any organic solvent. The powder was washed with water and ethanol and dried at 100 °C for 2 h. It was calcined at 750 °C for 4 h to develop crystallinity.

Photocatalytic activity measurements: Typical amounts (0.2 mg/mL, 0.5 mg/mL, 0.8 mg/mL and 1.1 mg/mL) of Ta_2O_5 nanoparticles as photocatalysts were taken in 50 mL of distilled water and sonicated for 5 min. Then 12.5 ppm of rhodamine B was added to it. To attain an adsorption–desorption equilibrium between the dye molecules and the catalyst surface, the solution was stirred for about 45 min in dark prior to irradiation. Before exposing to the UV radiation (λ = 365 nm), a 3 mL aliquot was taken, centrifuged and recorded as the zero time concentration of the dye. This process was repeated after every 15 min of exposure to UV light for recording the absorption of the remaining dye.

Supporting Information

Supporting Information File 1

CIF data of compound **1**.
[http://www.beilstein-journals.org/bjnano/content/supplementary/2190-4286-5-121-S1.res]

Acknowledgements

Subia Ambreen (SA) acknowledges University Grant Commission-Maulana Azad National Fellowship (UGC-MANF) for financial support. SA acknowledges useful discussions about the photocatalytic process with Mr. Shiv K. Pandey, MNNIT, Allahabad. Authors are grateful to Dr. Tamal Ghosh, Department of Chemistry, MNNIT, Allahabad, for providing UV–vis absorption facilities to perform the photocatalytic experiment. Authors also acknowledge the Department of Physics, MNNIT, Allahabad, for DRS and CIR-MNNIT, Allahabad, for the SEM facility.

References

1. Hubert-Pfalzgraf, L. G. *Inorg. Chem. Commun.* **2003,** *6,* 102–120. doi:10.1016/S1387-7003(02)00664-0
2. Pollard, K. D.; Puddephatt, R. J. *Chem. Mater.* **1999,** *11,* 1069–1074. doi:10.1021/cm981047a
3. Bradley, D. C. *Chem. Rev.* **1989,** *89,* 1317–1322. doi:10.1021/cr00096a004
4. Ambreen, S.; Gupta, K.; Singh, S.; Gupta, D. K.; Daniele, S.; Pandey, N. D.; Pandey, A. *Transition Met. Chem.* **2013,** *38,* 835–841. doi:10.1007/s11243-013-9756-y
5. Yanovsky, A. I.; Turova, N. Y.; Korolev, A. V.; Chebukov, D. E.; Pisarevsky, A. P.; Struchkova, Yu. T. *Russ. Chem. Bull.* **1996,** *45,* 115–121. doi:10.1007/BF01433743
6. Bradley, D. C.; Gaze, R.; Wardlaw, W. *J. Chem. Soc.* **1957,** 469–478. doi:10.1039/jr9570000469
7. Day, V. W.; Eberspacher, T. A.; Klemperer, W. G.; Park, C. W.; Rosenberg, F. S. *J. Am. Chem. Soc.* **1991,** *113,* 8190–8192. doi:10.1021/ja00021a068
8. Schmid, R.; Mosset, A.; Galy, J. *J. Chem. Soc., Dalton Trans.* **1991,** 1999–2005. doi:10.1039/DT9910001999
9. Abrahams, I.; Bradley, D. C.; Chudzynska, H.; Motevalli, M.; O'Shaughnessy, P. *J. Chem. Soc., Dalton Trans.* **2000,** 2685–2691. doi:10.1039/B001797N
10. Bradley, D. C.; Gaze, R.; Wardlaw, W. *J. Chem. Soc.* **1955,** 721–726. doi:10.1039/jr9550000721
11. Bradley, D. C.; Carter, D. G. *Can. J. Chem.* **1961,** *39,* 1434–1443. doi:10.1139/v61-183

12. Bradley, D. C.; Holloway, H. *Can. J. Chem.* **1962,** *40,* 1176–1182. doi:10.1139/v62-179
13. Nashed, R.; Hassan, W. M. I.; Ismail, Y.; Allam, N. K. *Phys. Chem. Chem. Phys.* **2013,** *15,* 1352–1357. doi:10.1039/c2cp43492j
14. Ezhilvalavan, S.; Tseng, T. Y. *J. Mater. Sci.: Mater. Electron.* **1999,** *10,* 9–31. doi:10.1023/A:1008970922635
15. Sayama, K.; Arakawa, H. *J. Photochem. Photobiol., A: Chem.* **1994,** *77,* 243–247. doi:10.1016/1010-6030(94)80049-9
16. Zou, Z.; Ye, J.; Sayama, K.; Arakawa, H. *Nature* **2001,** *414,* 625–627. doi:10.1038/414625a
17. Takahara, Y.; Kondo, J. N.; Takata, T.; Lu, D.; Domen, K. *Chem. Mater.* **2001,** *13,* 1194–1199. doi:10.1021/cm000572i
18. Kominami, H.; Miyakawa, M.; Murakami, S.; Yasuda, T.; Kohno, M.; Onoue, S.; Kera, Y.; Ohtani, B. *Phys. Chem. Chem. Phys.* **2001,** *3,* 2697–2703. doi:10.1039/b101313k
19. Murase, T.; Irie, H.; Hashimoto, K. *J. Phys. Chem. B* **2004,** *108,* 15803–15807. doi:10.1021/jp047874i
20. Yang, X.; Xu, L.; Yu, X.; Li, W.; Li, K.; Huo, M.; Guo, Y. *Colloids Surf., A* **2008,** *320,* 61–67. doi:10.1016/j.colsurfa.2008.01.019
21. Sreethawong, T.; Ngamsinlapasathian, S.; Suzuki, Y.; Yoshikawa, S. *J. Mol. Catal. A: Chem.* **2005,** *235,* 1–11. doi:10.1016/j.molcata.2005.03.021
22. Gömpel, D.; Tahir, M. N.; Panthöfer, M.; Mugnaioli, E.; Brandscheid, R.; Kolb, U.; Tremel, W. *J. Mater. Chem. A* **2014,** *2,* 8033–8040. doi:10.1039/C4TA00183D
23. Pandey, A.; Roy, M. K.; Pandey, A.; Zanella, M.; Sperling, R. A.; Parak, W. J.; Samaddar, A. B.; Verma, H. C. *IEEE Trans. NanoBiosci.* **2009,** *8,* 43–50. doi:10.1109/TNB.2009.2017316
24. Malčić, V. D.; Mikočević, Z. B.; Itrić, K. *Tech. Gaz. - Univ. Osijek* **2011,** *18,* 117–124.
25. Yang, L.; Kruse, B.; Miklavcic, S. J. *J. Opt. Soc. Am. A* **2004,** *21,* 1942–1952. doi:10.1364/JOSAA.21.001942
26. Licht, S.; Khaselev, O.; Ramakrishnan, P. A.; Soga, T.; Umeno, M. *J. Phys. Chem. B* **1998,** *102,* 2546–2554. doi:10.1021/jp9800564
27. Tauc, J.; Grigorovici, R.; Vancu, A. *Phys. Status Solidi* **1966,** *15,* 627–637. doi:10.1002/pssb.19660150224
28. Sánchez-Vergara, M. E.; Alonso-Huitron, J. C.; Rodriquez-Gómez, A.; Reider-Burstin, J. N. *Molecules* **2012,** *17,* 10000–10013. doi:10.3390/molecules170910000
29. Murphy, A. B. *Sol. Energy Mater. Sol. Cells* **2007,** *91,* 1326–1337. doi:10.1016/j.solmat.2007.05.005
30. Yakuphanoglu, F.; Ilican, S.; Caglar, M.; Caglar, Y. *J. Optoelectron. Adv. Mater.* **2007,** *9,* 2180–2185.
31. Byrappa, K.; Subramani, A. K.; Ananda, S.; Rai, K. M. L.; Dinesh, R.; Yoshimura, M. *Bull. Mater. Sci.* **2006,** *29,* 433–438. doi:10.1007/BF02914073
32. Zhu, Y.; Yu, F.; Man, Y.; Tian, Q.; He, Y.; Wu, N. *J. Solid State Chem.* **2005,** *178,* 224–229. doi:10.1016/j.jssc.2004.11.015
33. Sehested, J. *J. Catal.* **2003,** *217,* 417–426. doi:10.1016/S0021-9517(03)00075-7

License and Terms

This is an Open Access article under the terms of the Creative Commons Attribution License (http://creativecommons.org/licenses/by/2.0), which permits unrestricted use, distribution, and reproduction in any medium, provided the original work is properly cited.

The license is subject to the *Beilstein Journal of Nanotechnology* terms and conditions: (http://www.beilstein-journals.org/bjnano)

The definitive version of this article is the electronic one which can be found at: doi:10.3762/bjnano.5.121

BEILSTEIN JOURNAL OF NANOTECHNOLOGY

Enhanced photocatalytic hydrogen evolution by combining water soluble graphene with cobalt salts

Jing Wang, Ke Feng*, Hui-Hui Zhang, Bin Chen, Zhi-Jun Li, Qing-Yuan Meng, Li-Ping Zhang, Chen-Ho Tung and Li-Zhu Wu*

Full Research Paper

Open Access

Address:
Key Laboratory of Photochemical Conversion and Optoelectronic Materials, Technical Institute of Physics and Chemistry & University of Chinese Academy of Sciences, the Chinese Academy of Sciences, Beijing 100190, P. R. China

Email:
Ke Feng* - kefeng@mail.ipc.ac.cn; Li-Zhu Wu* - lzwu@mail.ipc.ac.cn

* Corresponding author

Keywords:
cobalt salts; earth-abundant catalyst; photocatalysis; photocatalytic hydrogen evolution; water-dispersible sulfonated-graphene

Beilstein J. Nanotechnol. **2014,** *5,* 1167–1174.
doi:10.3762/bjnano.5.128

Received: 07 February 2014
Accepted: 02 July 2014
Published: 29 July 2014

This article is part of the Thematic Series "Photocatalysis".

Guest Editor: R. Xu

© 2014 Wang et al; licensee Beilstein-Institut.
License and terms: see end of document.

Abstract

There is tremendous effort put in the pursuit for cheap and efficient catalysts for photocatalytic hydrogen evolution systems. Herein, we report an active catalyst that uses the earth-abundant element cobalt and water-dispersible sulfonated graphene. The photocatalytic hydrogen evolution activity of the catalyst was tested by using triethanolamine (TEOA) as electron donor and eosin Y (EY) as the photosensitizer under LED irradiation at 525 nm. Hydrogen was produced constantly even after 20 h, and the turnover number (TON) reached 148 (H_2/Co) in 4 h with respect to the initial concentration of the added cobalt salts was shown to be 5.6 times larger than that without graphene.

Introduction

Photocatalytic hydrogen evolution from water-splitting is a long-standing goal for researchers since it can help to supply the growing worldwide energy demand not only environmentally friendly but also sustainably [1-4]. Platinum, the most efficient hydrogen evolution co-catalyst, is rare and expensive, which limits its availability [5]. Hence, developing photocatalytic systems that rely only on earth-abundant elements are desired for making hydrogen a competitive alternative energy source. In recent years, systems based on iron complexes, nickel complexes or molybdenum complexes have been reported as promising candidates for catalyzing the hydrogen evolution [6-15]. Cobalt-based catalysts are particularly attractive catalysts that are easily obtained, environmentally benign and rely on earth-abundant elements [16]. Molecular cobalt catalysts [17], such as polypyridyl complexes [18,19], oxime complexes [20], have been proven to be efficient in the photocatalytic production of hydrogen, and the turnover number (TON) has become higher upon introducing more appropriate ligands.

Besides, cobalt-based heterogeneous structures are also of interest [21,22]. A hybrid Co_h–CdTe artificial catalyst for photocatalytic hydrogen evolution [23], for example, was simply constructed in situ from earth-abundant cobalt salts and CdTe quantum dots.

As a new carbon material with large surface area and excellent electrical properties, graphene has raised much attention since 2004 [24-33]. Specifically, graphene has been involved in photocatalytic hydrogen production systems [34], such as TiO_2-(N)RGO-Pt [35-38], g-C_3N_4-RGO-Pt [39], CdS-RGO-Pt [40-43], MoS_2-NRGO [44,45], EY-RGO-Pt [46] and $BiVO_4$-RGO-Ru/$SrTiO_3$:Rh [47] (RGO: reduced graphene oxide; EY: eosin Y). Graphene enhances the catalytic efficiency of hydrogen evolution remarkably. By using transient photovoltage and photocurrent techniques [48-50], the function of graphene was examined. More recently, our group has demonstrated the efficient forward electron-transfer mediated by graphene in terms of the unique spectroscopic property of photosensitizer EY [51]. The result stimulated us to explore graphene-based hydrogen evolution systems with earth-abundant co-catalysts.

In the present work, we report a new water-soluble graphene–cobalt-based hydrogen evolution system, showing a 5.6 times higher efficiency than that of the same system without graphene. Herein, sulfonated-graphene (G-SO_3), being water-soluble and partially reduced [52,53], serves as a great platform [41,51] to support the catalysts. With TEOA (triethanolamine) as an electron donor, EY as a photosensitizer, $Co(TEOA)_2^{2+}$ is formed in situ and adsorbed at the surface or around the G-SO_3 when cobalt salts and G-SO_3 are introduced into the hydrogen evolution system. Upon irradiation by visible light (525 nm LEDs as light source) for 4 h, the system is able to produce hydrogen with a TON up to 148 with the initial concentration of cobalt salts added. And hydrogen constantly evolves even after 20 h irradiation.

Results and Discussion

Fourier transform infrared spectroscopy (FTIR) is employed to characterize GO and G-SO_3. As shown in Figure 1, compared to GO, G-SO_3 has typical absorptions at 1177, 1123 and 1037 cm^{-1}, which are assigned to $\nu_{S\text{-}O}$ and $\nu_{S\text{-}phenyl}$ confirming the modification of sulfanilic acid on graphene sheets [53]. Meanwhile, peaks attributed to C=O in carboxylic acid and carbonyl moieties ($\nu_{C=O}$ at 1720 cm^{-1}), C–OH (ν_{C-OH} at 1365 cm^{-1}) decrease sharply, implying a partial reduction of GO [54].

X-ray photoelectron spectroscopy (XPS) measurements were performed to confirm the differences between GO and G-SO_3. Five different peaks centered at 284.5, 285.9, 286.6, 287.7 and 288.9 eV appear in the C1s deconvolution spectrum of GO, corresponding to C=C/C–C in aromatic rings, C–OH (hydroxy), C–O–C (epoxy), C=O (carbonyl), and C(O)O (carboxyl) groups, respectively [55]. For G-SO_3, the peak centered at 284.6 eV becomes narrower, suggesting the partial restoration of the π-electron network in G-SO_3. Other oxygen-containing carbon peaks, decreased sharply, indicating GO is reduced efficiently.

Further, Raman spectra and X-ray diffraction (XRD) patterns of GO and G-SO_3 are compared in Figure 2. GO and G-SO_3 both show the characteristic D band and G band at 1350 cm^{-1} and 1597 cm^{-1}, but the enhanced I_D/I_G ratio for G-SO_3 indicates the functionalization and reduction of GO. As confirmed by the XRD patterns, after reduction and functionalization, the *d*-spacing becomes wider since the angle 2θ shifted to the left from 8.85° to 6.92°. The decreased intensity, meanwhile, manifests a more disordered structure in G-SO_3. As a result, the obtained G-SO_3 is both reduced and functionalized, which guarantees not only its high conductivity for electron transfer, but also its great dispersibility to act as a platform to anchor catalysts.

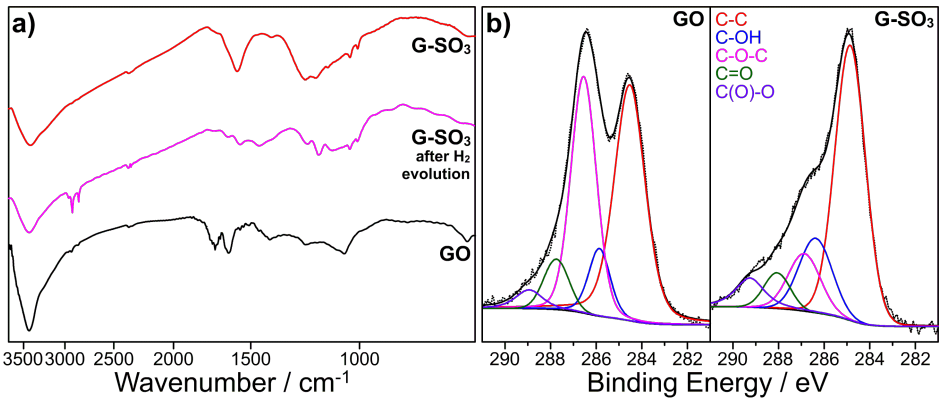

Figure 1: FTIR (a) and XPS (b) spectra of GO, G-SO_3 and G-SO_3 after photocatalytic hydrogen evolution

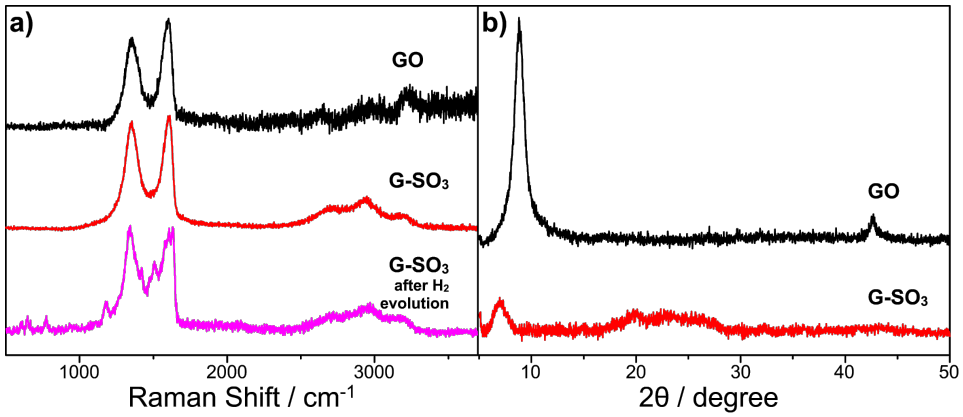

Figure 2: Raman (a) and XRD (b) spectra of GO (black), G-SO_3 (red) and G-SO_3 after photocatalytic hydrogen evolution (purple).

The photocatalytic hydrogen evolution was evaluated under irradiation at 525 nm by using TEOA as a sacrificial donor and EY as a photosensitizer, while cobalt salts and G-SO_3 were added to serve as a catalyst in the reaction system (Figure 3). It is proposed that Co^{2+} forms a $Co(TEOA)_2^{2+}$ complex in the presence of TEOA [56]. No significant amounts of hydrogen were detected in the absence of either irradiation or the photosensitizer EY, indicating that hydrogen was produced through the photochemical reaction. Evidently, $Co(TEOA)_2^{2+}$ complexes can function as catalysts to reduce protons to hydrogen, similar to the observations of Sun and coworkers [57]. When G-SO_3 was introduced, the amount of hydrogen obviously increased. Because our previous work [51] has demonstrated that G-SO_3 acts as an electron mediator of EY and platinum nanoparticles co-catalyst, we consider that in the current study the electron transfer process from the EY radical anion ($EY^{\bullet -}$) to G-SO_3 or in situ formed-$Co(TEOA)_2^{2+}$ would be facilitated. Similar to the storage phenomenon observed in carbon nanotubes, a small fraction of the electrons may get stored in graphene sheets, thus making graphene an electron reservoir to continuously provide electrons to the catalytic center [58-60]. The positive synergetic effect consequently enhances the photocatalytic activity for hydrogen evolution of the system. To examine any counter anion effects, we further used four different kinds of cobalt salts in our photocatalytic hydrogen evolution system: cobalt chloride, cobalt nitrate, cobalt perchlorate and cobalt acetate. The amounts of evolved hydrogen in each system did not differ much, indicating that the catalytic behavior is independent of the anions used. The results also manifest the formation of $Co(TEOA)_2^{2+}$ catalysts in the systems.

The pH value of the solution greatly influences the hydrogen evolution process of the system. The system performed well over a wide range (pH 8–12), reaching a maximal turnover at pH 10.86 (Supporting Information File 1, Figure S1). However, when pH value was below 7.2, there was no detectable hydrogen produced from the system. This pH-dependency is due to a

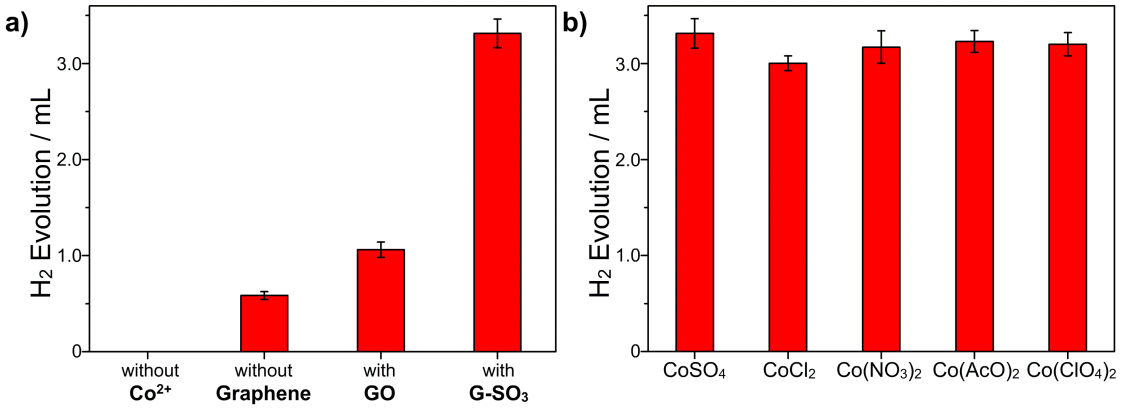

Figure 3: Photocatalytic hydrogen evolution with different graphene (a) and cobalt salts (b) at pH 10.86 in H_2O after 4 h; sample concentration: Co^{2+} (2.0×10^{-4} mol/L), graphene (0.04 mg/mL), EY (4.0×10^{-4} mol/L) and TEOA (0.2 mol/L).

number of factors: in acidic medium, the protonation of TEOA inevitably results in a poor electron-donating ability and less $Co(TEOA)_2^{2+}$ catalyst is formed. In a basic solution, the graphene dispersion was more stable and the light absorption of EY is stronger but the concentration of protons is too low.

To optimize the hydrogen evolution system, four sets of experiments were carried out: varying the concentration of $CoSO_4$, G-SO_3, EY and TEOA used while keeping a constant concentration of the other three components at pH 10.86. The results of these experiments are shown in Figure 4. With the addition of G-SO_3, even at low concentrations, the amount of hydrogen evolution showed a remarkable increase and reached a maximum of 3.31 mL, which is 5.6 times larger than that of the system without G-SO_3. Further increasing the concentration of G-SO_3 resulted in a decrease in the amount of hydrogen generated. This phenomenon happened in many other reported works, which can be explained by the light shielding effect of graphene [61-63]. Varying the concentration of $CoSO_4$, a similar tendency was observed. The concentration of EY also exercises a great influence on catalytic performance of the system. The amount of hydrogen evolution increases with the concentration of EY linearly when the concentration of EY is below 0.4 mM. After a further increase of the EY concentration to 0.8 mM or 1.6 mM, however, the amount of hydrogen still increases but at a relatively slower rate. This is because self-quenching and shield-effects inevitably decrease the ability of EY to act as the photosensitizer [64]. As for the electron donor TEOA, the highest hydrogen evolution efficiency was obtained at a concentration of 0.2 M. Figure S2 in Supporting Information File 1 shows the kinetic curve of the photocatalytic hydrogen evolution under the optimized conditions at pH 10.86 (the concentration of $CoSO_4$, G-SO_3, EY and TEOA are 2.0×10^{-4} mol/L, 0.04 mg/mL, 4.0×10^{-4} mol/L and 0.2 mol/L, respectively). The total amount of hydrogen evolved under LED irradiation at 525 nm was about 3.31 mL (148 μmol) and the TON reached 148 with respect to the initial concentration of cobalt. More hydrogen was produced from the system after prolonged irradiation times but at a slower rate. The reason for the decreased rate at longer irradiation times is attributed to the decomposition of EY. As described in our previous work [51], EY decomposes to fluorescein, which has a lower absorption but a higher stability. To confirm the result in the current study, we carried out control experiments that used fluorescein as photosensitizer

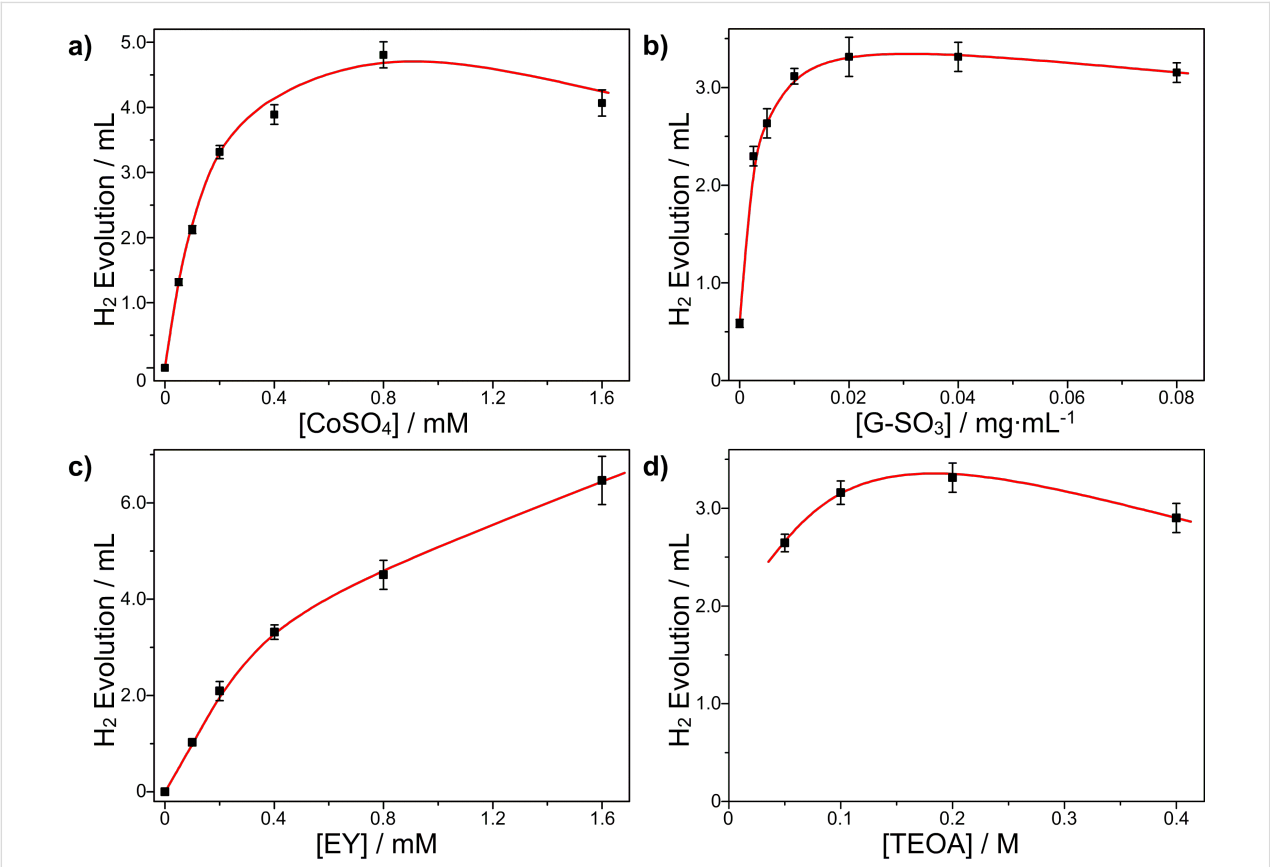

Figure 4: Photocatalytic hydrogen evolution as a function of the $CoSO_4$ (a), G-SO_3 (b), EY (c) and TEOA (d) concentration at pH 10.86 in H_2O after 4 h; other sample concentration: $CoSO_4$ (2.0×10^{-4} mol/L), G-SO_3 (0.04 mg/mL), EY (4.0×10^{-4} mol/L) and TEOA (0.2 mol/L).

for hydrogen evolution under the identical condition. As shown in Supporting Information File 1, Figure S2, the rate of hydrogen evolution is the same as that of the EY system after 1 h of irradiation.

It is worth noting that after irradiation, a black magnetic precipitate was observed and adsorbed on the magnetron in both cases with or without G-SO_3. When rinsed with acetone more than three times, the precipitation was visualized by TEM (transmission electron microscopy). As shown in Figure 5, in the absence of G-SO_3 nanoparticles aggregated in size of about hundreds nanometers. Each particle is composed of lots of small nanoparticles of several nanometers in diameter. The lattice fringes in the HRTEM (high resolution TEM) images suggest a well-defined crystal structure. The lattice spacing of about 0.191 and 0.203 nm can be assigned to the (101) and (002) planes of metallic cobalt Co, space group P_{63}/mmc (JCPDS card 05-0727). When G-SO_3 was added, the TEM images exhibited much difference. Firstly, nanoparticles were formed but dispersed on G-SO_3 sheets instead. Secondly, the sizes of the nanoparticles were smaller. The HRTEM image also showed the lattice fringes, and the lattice spacing (0.191 and 0.203 nm) is consistent with those observed in the system without G-SO_3. This phenomenon indicated that G-SO_3 provides a platform to support cobalt catalysts, and at the same time G-SO_3 avoids the aggregation of the catalyst to some extent. These results are consistent with the better performance and the higher hydrogen evolution from the system with G-SO_3.

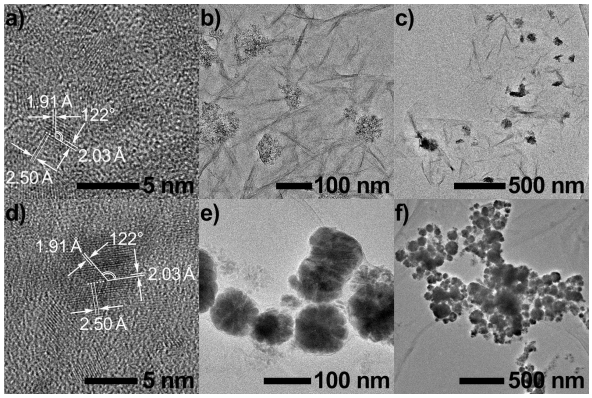

Figure 5: The TEM images nanoparticles after irradiation with (a–c) or without (d–f) G-SO_3.

As mentioned above, the TEM results showed that cobalt metal nanoparticles may form during the process in both cases. XPS and ICP-MS (inductively coupled plasma mass spectrometry) were used to further investigate the magnetic precipitates obtained after the hydrogen evolution reaction. XPS spectra of the precipitates with or without G-SO_3 showed the same peak pattern and location in the range from 776 to 810 eV, corresponding to the Co 2p orbital (Supporting Information File 1, Figure S3). The cobalt lines in the spectra, however, were assigned to cobalt(II) [65], not to cobalt(0). This is different from the TEM results and in contrast to the grown cobalt metal nanoparticles on graphene [66]. ICP-MS measurements were carried out by using the precipitates obtained from the system, which gave a cobalt content of 11.1% (with graphene) and 45.0% (without graphene), respectively. Either of these results was much higher than that calculated from XPS (3.8% and 20.8%). In consideration of the fact that XPS probes only a few nanometers below the surface, the discrepancy was tentatively interpreted to be because of Co^{2+} complexes around the cobalt metal particles, which hinder the effective detection of Co metal in XPS but allows its measurement with ICP-MS. In addition, FTIR spectra of G-SO_3 (Figure 1a, purple line) showed a typical C–H stretching vibration at 2918 cm^{-1} after photocatalytic hydrogen evolution, which apparently comes from the catalytic $Co^{II}(TEOA)_2$ species on the surface of G-SO_3.

Cyclic voltammetry (CV) spectra were used to investigate the hydrogen evolution system (Figure 6). And the results showed that $Co(TEOA)_2{}^{2+}$ complex was active for electrocatalytic hydrogen evolution in 0.2 M K_2SO_4 and 0.4 M TEOA aqueous solution. The $Co^{II}(TEOA)_2/Co^{I}(TEOA)_2$ reduction band peaked at about −1.1 V (vs SCE), and is followed by a rapid rise in current at −1.25 V (vs SCE). This increase of current, accompanied by the evolution of bubbles, can be attributed to the catalytic generation of hydrogen from the aqueous solution [67]. In order to verify that $Co(TEOA)_2{}^{2+}$ is responsible for the catalysis, control experiments were performed at room temperature. When the 0.2 M K_2SO_4 aqueous solution or 0.2 M K_2SO_4 and 0.4 M TEOA aqueous solution were studied, no catalytic current appeared until the potential was over −1.5 V (vs SCE). When G-SO_3 was added, no new peak emerged, but the catalytic current intensity increased by about 20%. The observation implied that in the presence of G-SO_3, electron transfer processes become faster, which results in a higher activity toward electrocatalytic hydrogen evolution. Analogously, G-SO_3 is important for enhancing the performance of photocatalytic hydrogen evolution. For photocatalytic hydrogen evolution systems, the photosensitizer EY is often reduced by TEOA to form $EY^{\bullet-}$ radical anions. Since the oxidation potential of $EY^{\bullet-}$ (−1.05 V vs NHE) [68] is more negative than that of $Co^{II}(TEOA)_2/Co^{I}(TEOA)_2$ couple, an electron transfer from $EY^{\bullet-}$ to cobalt-center is thermodynamically feasible and initiates the whole hydrogen evolution process.

Taking into consideration all results of the TEM, XPS, ICP–MS and CV measurements, the photocatalytic process in this work can be described in Scheme 1. When all the components

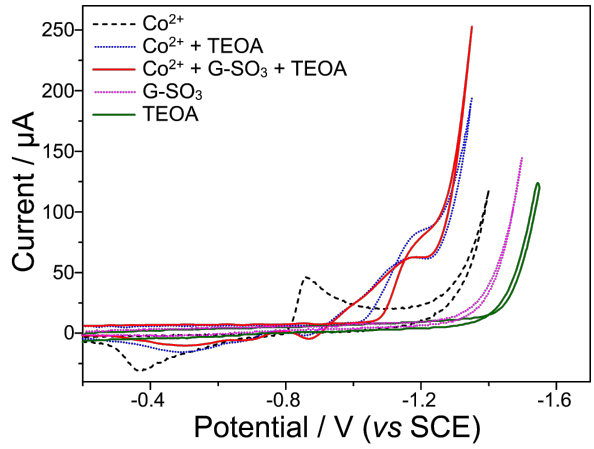

Figure 6: CV spectra of the 4.0×10^{-3} mol/L $CoSO_4$ + 0.2 mol/L K_2SO_4 solution (black), 4.0×10^{-3} mol/L $CoSO_4$ + 0.4 mol/L TEOA + 0.2 mol/L K_2SO_4 solution (blue), 4.0×10^{-3} mol/L $CoSO_4$ + 0.4 mol/L TEOA + 0.04 mg/mL G-SO_3 solution + 0.2 mol/L K_2SO_4 (red), 0.04 mg/mL G-SO_3 solution + 0.2 mol/L K_2SO_4 (purple) and 0.4 mol/L TEOA + 0.2 mol/L K_2SO_4 solution (green).

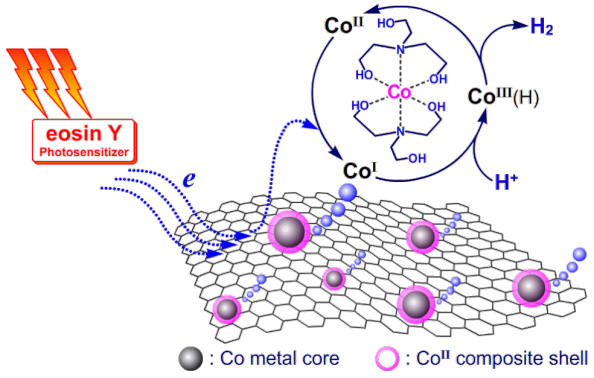

Scheme 1: Schematic illustration of the photocatalytic hydrogen evolution process.

(TEOA, EY, G-SO_3, $CoSO_4$) were added into the reaction system, $Co^{II}(TEOA)_2$ complexes were formed in situ and are at well-adsorbed or surround the G-SO_3. In fact, not all of the $Co^{II}(TEOA)_2$ complexes were on the surface of G-SO_3, because ICP-MS measurements gave a cobalt content of 11.1%, which was much lower than the feeding ratio of 22.8%. Upon irradiation, the electrons of the $EY^{\bullet-}$ radical anion generated from EY and TEOA, transfer to G-SO_3 or directly to $Co^{II}(TEOA)_2$ to initiate the catalytic hydrogen evolution. Since graphene is an ideal electron acceptor and/or electron reservoir, an efficient multi-electron transfer toward the catalytic center $Co^{II}(TEOA)_2$ takes place. Regarding the reports about photocatalytic hydrogen evolution systems based on molecular cobalt complexes in the literature [20], it could be speculated that in the present work the reduction of $Co^{II}(TEOA)_2$ to $Co^{I}(TEOA)_2$ occurs firstly. $Co^{I}(TEOA)_2$, on the one hand, can be protonated to form $Co^{III}(TEOA)_2H$ hydride, which reacts with another hydride to eliminate hydrogen or further protonated to release hydrogen and $Co^{III}(TEOA)_2$, which is subsequently reduced to $Co^{II}(TEOA)_2$ for the next catalytic circulation. On the other hand, the protonated $Co^{III}(TEOA)_2H$ can also be reduced further to yield $Co^{II}(TEOA)_2H$ hydride, which experienced the above cycle for hydrogen evolution. Specifically, if the $Co^{I}(TEOA)_2$ species is not protonated at low concentrations of protons in the system, it can be reduced further to $Co^{0}(TEOA)_2$ [69]. Since there are ligands around $Co^{0}(TEOA)_2$, this $Co^{0}(TEOA)_2$ species can be protonated to form $Co^{II}(TEOA)_2H$ that would either eliminate hydrogen as discussed above or release ligands to form metallic cobalt. The obtained metallic cobalt may function as nucleation center anchoring other cobalt-catalysts.

Conclusion

In summary, we introduce a new water-soluble graphene-cobalt-based hydrogen evolution system. With TEOA as the electron donor, EY as the photosensitizer, $Co(TEOA)_2^{2+}$ formed in situ from cobalt salts and TEOA on the surface of G-SO_3 or around it as the initial catalyst, the effective hydrogen evolution system is established. By using 525 nm LEDs as the light source, this system shows a 5.6 times higher efficiency than that of the same system without G-SO_3, and the hydrogen can continually evolve even after 20 h. With TEM, ICP-MS, and XPS measurements the magnetic precipitation after irradiation is confirmed to be Co metal surrounded by Co^{2+} species. CV results indicate the redox potential for the $Co^{II}(TEOA)_2/Co^{I}(TEOA)_2$, manifesting the feasible electron transfer process thermodynamically. The effects of the pH value, as well as the concentration of G-SO_3, $CoSO_4$ and TEOA were investigated in detail not only to optimize the catalytic activity for hydrogen evolution but also to understand the reaction mechanism. The enhanced activity of the photocatalytic system makes it attractive to design and synthesize new catalysts by using graphene and earth-abundant metal salts for the photocatalytic H_2 production.

Supporting Information

Supporting Information File 1

Experimental part.
[http://www.beilstein-journals.org/bjnano/content/supplementary/2190-4286-5-128-S1.pdf]

Acknowledgements

This work was supported by the Ministry of Science and Technology of China (2014CB239402, 2013CB834505 and 2013CB834804), the National Natural Science Foundation of

China (21372232, 21090343, 91027041, 21390404 and 51373193), and the Chinese Academy of Sciences.

References

1. McKone, J. R.; Lewis, N. S.; Gray, H. B. *Chem. Mater.* **2013,** *26,* 407–414. doi:10.1021/cm4021518
2. Armaroli, N.; Balzani, V. *Angew. Chem., Int. Ed.* **2007,** *46,* 52–66. doi:10.1002/anie.200602373
3. Cook, T. R.; Dogutan, D. K.; Reece, S. Y.; Surendranath, Y.; Teets, T. S.; Nocera, D. G. *Chem. Rev.* **2010,** *110,* 6474–6502. doi:10.1021/cr100246c
4. Armaroli, N.; Balzani, V. *ChemSusChem* **2011,** *4,* 21–36. doi:10.1002/cssc.201000182
5. Harinipriya, S.; Sangaranarayanan, M. V. *Langmuir* **2002,** *18,* 5572–5578. doi:10.1021/la025548t
6. Li, Z.-J.; Wang, J.-J.; Li, X.-B.; Fan, X.-B.; Meng, Q.-Y.; Feng, K.; Chen, B.; Tung, C.-H.; Wu, L.-Z. *Adv. Mater.* **2013,** *25,* 6613–6618. doi:10.1002/adma.201370283
7. Han, Z.; Qiu, F.; Eisenberg, R.; Holland, P. L.; Krauss, T. D. *Science* **2012,** *338,* 1321–1324. doi:10.1126/science.1227775
8. Nippe, M.; Khnayzer, R. S.; Panetier, J. A.; Zee, D. Z.; Olaiya, B. S.; Head-Gordon, M.; Chang, C. J.; Castellano, F. N.; Long, J. R. *Chem. Sci.* **2013,** *4,* 3934–3945. doi:10.1039/c3sc51660a
9. Wen, F.; Li, C. *Acc. Chem. Res.* **2013,** *46,* 2355–2364. doi:10.1021/ar300224u
10. Ran, J.; Zhang, J.; Yu, J.; Jaroniec, M.; Qiao, S. Z. *Chem. Soc. Rev.* **2014,** in press. doi:10.1039/c3cs60425j
11. Kong, D.; Cha, J. J.; Wang, H.; Lee, H. R.; Cui, Y. *Energy Environ. Sci.* **2013,** *6,* 3553–3558. doi:10.1039/c3ee42413h
12. Du, P.; Eisenberg, R. *Energy Environ. Sci.* **2012,** *5,* 6012–6021. doi:10.1039/C2EE03250C
13. Thoi, V. S.; Sun, Y.; Long, J. R.; Chang, C. J. *Chem. Soc. Rev.* **2013,** *42,* 2388–2400. doi:10.1039/c2cs35272a
14. Wang, M.; Sun, L. *ChemSusChem* **2010,** *3,* 551–554. doi:10.1002/cssc.201000062
15. Wang, F.; Wang, W.-G.; Wang, H.-Y.; Si, G.; Tung, C.-H.; Wu, L.-Z. *ACS Catal.* **2012,** *2,* 407–416. doi:10.1021/cs200458b
16. Losse, S.; Vos, J. G.; Rau, S. *Coord. Chem. Rev.* **2010,** *254,* 2492–2504. doi:10.1016/j.ccr.2010.06.004
17. Natali, M.; Luisa, A.; Iengo, E.; Scandola, F. *Chem. Commun.* **2014,** *50,* 1842–1844. doi:10.1039/c3cc48882a
18. Bachmann, C.; Guttentag, M.; Spingler, B.; Alberto, R. *Inorg. Chem.* **2013,** *52,* 6055–6061. doi:10.1021/ic4004017
19. Guttentag, M.; Rodenberg, A.; Bachmann, C.; Senn, A.; Hamm, P.; Alberto, R. *Dalton Trans.* **2013,** *42,* 334–337. doi:10.1039/c2dt31699d
20. Dempsey, J. L.; Brunschwig, B. S.; Winkler, J. R.; Gray, H. B. *Acc. Chem. Res.* **2009,** *42,* 1995–2004. doi:10.1021/ar900253e
21. Huang, J.; Mulfort, K. L.; Du, P.; Chen, L. X. *J. Am. Chem. Soc.* **2012,** *134,* 16472–16475. doi:10.1021/ja3062584
22. Cao, S.-W.; Liu, X.-F.; Yuan, Y.-P.; Zhang, Z.-Y.; Fang, J.; Loo, S. C. J.; Barber, J.; Sum, T. C.; Xue, C. *Phys. Chem. Chem. Phys.* **2013,** *15,* 18363–18366. doi:10.1039/c3cp53350f
23. Li, Z.-J.; Li, X.-B.; Wang, J.-J.; Yu, S.; Li, C.-B.; Tung, C.-H.; Wu, L.-Z. *Energy Environ. Sci.* **2013,** *6,* 465–469. doi:10.1039/C2EE23898E
24. Chen, D.; Zhang, H.; Liu, Y.; Li, J. *Energy Environ. Sci.* **2013,** *6,* 1362–1387. doi:10.1039/c3ee23586f
25. Li, D.; Kaner, R. B. *Science* **2008,** *320,* 1170–1171. doi:10.1126/science.1158180
26. Novoselov, K. S.; Geim, A. K.; Morozov, S. V.; Jiang, D.; Zhang, Y.; Dubonos, S. V.; Grigorieva, I. V.; Firsov, A. A. *Science* **2004,** *306,* 666–669. doi:10.1126/science.1102896
27. Loh, K. P.; Bao, Q.; Ang, P. K.; Yang, J. *J. Mater. Chem.* **2010,** *20,* 2277–2289. doi:10.1039/b920539j
28. Bolotin, K. I.; Sikes, K. J.; Jiang, Z.; Klima, M.; Fudenberg, G.; Hone, J.; Kim, P.; Stormer, H. L. *Solid State Commun.* **2008,** *146,* 351–355. doi:10.1016/j.ssc.2008.02.024
29. Stoller, M. D.; Park, S.; Zhu, Y.; An, J.; Ruoff, R. S. *Nano Lett.* **2008,** *8,* 3498–3502. doi:10.1021/nl802558y
30. Park, S.; Ruoff, R. S. *Nat. Nanotechnol.* **2009,** *4,* 217–224. doi:10.1038/nnano.2009.58
31. Huang, X.; Qi, X.; Boey, F.; Zhang, H. *Chem. Soc. Rev.* **2012,** *41,* 666–686. doi:10.1039/c1cs15078b
32. Liu, Y.; Dong, X.; Chen, P. *Chem. Soc. Rev.* **2012,** *41,* 2283–2307. doi:10.1039/c1cs15270j
33. Xu, C.; Xu, B.; Gu, Y.; Xiong, Z.; Sun, J.; Zhao, X. *Energy Environ. Sci.* **2013,** *6,* 1388–1414. doi:10.1039/c3ee23870a
34. Xie, G.; Zhang, K.; Guo, B.; Liu, Q.; Fang, L.; Gong, J. R. *Adv. Mater.* **2013,** *25,* 3820–3839. doi:10.1002/adma.201301207
35. Zhang, X.-Y.; Li, H.-P.; Cui, X.-L.; Lin, Y. *J. Mater. Chem.* **2010,** *20,* 2801–2806. doi:10.1039/b917240h
36. Fan, W.; Lai, Q.; Zhang, Q.; Wang, Y. *J. Phys. Chem. C* **2011,** *115,* 10694–10701. doi:10.1021/jp2008804
37. Pei, F.; Liu, Y.; Xu, S.; Lü, J.; Wang, C.; Cao, S. *Int. J. Hydrogen Energy* **2013,** *38,* 2670–2677. doi:10.1016/j.ijhydene.2012.12.045
38. Jiang, B.; Tian, C.; Pan, Q.; Jiang, Z.; Wang, J.-Q.; Yan, W.; Fu, H. *J. Phys. Chem. C* **2011,** *115,* 23718–23725. doi:10.1021/jp207624x
39. Xiang, Q.; Yu, J.; Jaroniec, M. *J. Phys. Chem. C* **2011,** *115,* 7355–7363. doi:10.1021/jp200953k
40. Fang, Z.; Wang, Y.; Song, J.; Sun, Y.; Zhou, J.; Xu, R.; Duan, H. *Nanoscale* **2013,** *5,* 9830–9838. doi:10.1039/c3nr03043a
41. Lv, X. J.; Fu, W. F.; Chang, H. X.; Zhang, H.; Cheng, J. S.; Zhang, G. J.; Song, Y.; Hu, C. Y.; Li, J. H. *J. Mater. Chem.* **2012,** *22,* 1539–1546. doi:10.1039/c1jm14502a
42. Khan, Z.; Chetia, T. R.; Vardhaman, A. K.; Barpuzary, D.; Sastri, C. V.; Qureshi, M. *RSC Adv.* **2012,** *2,* 12122–12128. doi:10.1039/c2ra21596a
43. Li, Q.; Guo, B.; Yu, J.; Ran, J.; Zhang, B.; Yan, H.; Gong, J. R. *J. Am. Chem. Soc.* **2011,** *133,* 10878–10884. doi:10.1021/ja2025454
44. Xiang, Q.; Yu, J.; Jaroniec, M. *J. Am. Chem. Soc.* **2012,** *134,* 6575–6578. doi:10.1021/ja302846n
45. Maitra, U.; Gupta, U.; De, M.; Datta, R.; Govindaraj, A.; Rao, C. N. R. *Angew. Chem., Int. Ed.* **2013,** *52,* 13057–13061. doi:10.1002/anie.201306918
46. Min, S. X.; Lu, G. X. *J. Phys. Chem. C* **2011,** *115,* 13938–13945. doi:10.1021/jp203750z
47. Iwase, A.; Ng, Y. H.; Ishiguro, Y.; Kudo, A.; Amal, R. *J. Am. Chem. Soc.* **2011,** *133,* 11054–11057. doi:10.1021/ja203296z
48. Kaniyankandy, S.; Rawalekar, S.; Ghosh, H. N. *J. Phys. Chem. C* **2012,** *116,* 16271–16275. doi:10.1021/jp303712y
49. Lightcap, I. V.; Kamat, P. V. *J. Am. Chem. Soc.* **2012,** *134,* 7109–7116. doi:10.1021/ja3012929
50. Cao, A.; Liu, Z.; Chu, S.; Wu, M.; Ye, Z.; Cai, Z.; Chang, Y.; Wang, S.; Gong, Q.; Liu, Y. *Adv. Mater.* **2010,** *22,* 103–106. doi:10.1002/adma.200901920
51. Zhang, H.-H.; Feng, K.; Chen, B.; Meng, Q.-Y.; Li, Z.-J.; Tung, C.-H.; Wu, L.-Z. *Catal. Sci. Technol.* **2013,** *3,* 1815–1821. doi:10.1039/c3cy00098b

52. Huang, W.; Ouyang, X.; Lee, L. J. *ACS Nano* **2012,** *6,* 10178–10185. doi:10.1021/nn303917p
53. Si, Y.; Samulski, E. T. *Nano Lett.* **2008,** *8,* 1679–1682. doi:10.1021/nl080604h
54. Stankovich, S.; Dikin, D. A.; Piner, R. D.; Kohlhaas, K. A.; Kleinhammes, A.; Jia, Y.; Wu, Y.; Nguyen, S. T.; Ruoff, R. S. *Carbon* **2007,** *45,* 1558–1565. doi:10.1016/j.carbon.2007.02.034
55. Ganguly, A.; Sharma, S.; Papakonstantinou, P.; Hamilton, J. *J. Phys. Chem. C* **2011,** *115,* 17009–17019. doi:10.1021/jp203741y
56. Hughes, M. N.; Rutt, K. J. *J. Chem. Soc. A* **1968,** *0,* 2788–2790. doi:10.1039/j19680002788
57. Dong, J. F.; Wang, M.; Li, X. Q.; Chen, L.; He, Y.; Sun, L. C. *ChemSusChem* **2012,** *5,* 2133–2138. doi:10.1002/cssc.201200490
58. Kamat, P. V. *J. Phys. Chem. Lett.* **2011,** *2,* 242–251. doi:10.1021/jz101639v
59. Williams, G.; Seger, B.; Kamat, P. V. *ACS Nano* **2008,** *2,* 1487–1491. doi:10.1021/nn800251f
60. Kongkanand, A.; Kamat, P. V. *ACS Nano* **2007,** *1,* 13–21. doi:10.1021/nn700036f
61. Zhu, M.; Li, Z.; Xiao, B.; Lu, Y.; Du, Y.; Yang, P.; Wang, X. *ACS Appl. Mater. Interfaces* **2013,** *5,* 1732–1740. doi:10.1021/am302912v
62. Zhou, J.; Tian, G.; Chen, Y.; Meng, X.; Shi, Y.; Cao, X.; Pan, K.; Fu, H. *Chem. Commun.* **2013,** *49,* 2237–2239. doi:10.1039/c3cc38999e
63. Mou, Z.; Yin, S.; Zhu, M.; Du, Y.; Wang, X.; Yang, P.; Zheng, J.; Lu, C. *Phys. Chem. Chem. Phys.* **2013,** *15,* 2793–2799. doi:10.1039/c2cp44270a
64. Valdes-Aguilera, O.; Neckers, D. C. *Acc. Chem. Res.* **1989,** *22,* 171–177. doi:10.1021/ar00161a002
65. Biesinger, M. C.; Payne, B. P.; Grosvenor, A. P.; Lau, L. W. M.; Gerson, A. R.; Smart, R. S. C. *Appl. Surf. Sci.* **2011,** *257,* 2717–2730. doi:10.1016/j.apsusc.2010.10.051
66. Bai, S.; Shen, X.; Zhu, G.; Li, M.; Xi, H.; Chen, K. *ACS Appl. Mater. Interfaces* **2012,** *4,* 2378–2386. doi:10.1021/am300310d
67. Sun, Y.; Bigi, J. P.; Piro, N. A.; Tang, M. L.; Long, J. R.; Chang, C. J. *J. Am. Chem. Soc.* **2011,** *133,* 9212–9215. doi:10.1021/ja202743r
68. Sharma, G. D.; Balraju, P.; Kumar, M.; Roy, M. S. *Mater. Sci. Eng., B* **2009,** *162,* 32–39. doi:10.1016/j.mseb.2009.01.033
69. Stubbert, B. D.; Peters, J. C.; Gray, H. B. *J. Am. Chem. Soc.* **2011,** *133,* 18070–18073. doi:10.1021/ja2078015

License and Terms

This is an Open Access article under the terms of the Creative Commons Attribution License (http://creativecommons.org/licenses/by/2.0), which permits unrestricted use, distribution, and reproduction in any medium, provided the original work is properly cited.

The license is subject to the *Beilstein Journal of Nanotechnology* terms and conditions: (http://www.beilstein-journals.org/bjnano)

The definitive version of this article is the electronic one which can be found at: doi:10.3762/bjnano.5.128